TUNABLE MICROWAVE FILTERS USING FERROELECTRIC THIN FILMS

by

XU WANG

A thesis submitted to the Faculty of Engineering
University of Birmingham
For the degree of

DOCTOR OF PHILOSOPHY

School of Electronic, Electrical and
Computer Engineering
University of Birmingham
Birmingham, B15 2TT
United Kingdom
October 2009

SYNOPSIS

Frequency agile microwave devices based on Barium Strontium Titanate (BST) thin films have gained a lot of interest in recent years. The frequency agility of the ferroelectric devices is based on the external DC electric field controlled permittivity of BST thin film. In this research work, several tunable microwave filters incorporating BST thin film varactors operating in a frequency range between 1 GHz and 25 GHz are designed, tested and analysed.

In the thesis, the motivation for developing frequency agile devices is reviewed and several technologies for tunable microwave filters are surveyed and compared. An introduction to the background of ferroelectric materials and microwave properties of BST thin films is given. Recent progress on the BST varactor and filters reported in the literature is reviewed and compared with this work. Theoretical fundamentals for microwave filter design are outlined as well.

The filters presented in this work are designed in a coplanar waveguide configuration on MgO or high resistivity silicon substrates. Integrated or discrete BST varactors in either interdigital or parallel plate configuration are employed as tuning elements. The filters design starts from Chebyshev prototype filter synthesis, and follows by full wave electromagnetic (EM) simulation by Sonnet. The multilayer BST filters are fabricated in house and tested using a network analyser. The measurement results of these filters are analysed and compared well with the EM simulation. The experimental performance shows that BST integrated filters have miniaturised size and large tuning range at a DC bias less than 15 V, and the filters with discrete BST varactors have a low insertion loss.

A lumped element lowpass filter incorporating integrated meander line inductors and BST parallel plate capacitors is implemented on a high resistivity silicon substrate. 5 µm × 5 µm or 10 µm × 10 µm $Ba_{0.25}Sr_{0.75}TiO_3$ thin film varactors are used as tuning elements. The filter loss factors including the metal loss and BST loss are discussed. A tunability of 32.1 % of a BST lowpass filter is recorded at 15 V. The lowpass filter can be treated as a switch, with 18 dB isolation at around 25 GHz.

A combline bandpass filter employing line elements shorted at one end and loaded by BST varactors at the opposite end as resonators is implemented on a MgO substrate. The $Ba_{0.6}Sr_{0.4}TiO_3$ thin film parallel plate capacitors are 5 µm × 5 µm in size. Each resonator can be independently biased, which enables performance optimisation of the fabricated filter. Etching of BST film is required to contact the bottom electrode. A two pole filter measured shows a reasonable tuning from about 8 GHz to 12 GHz with 10 V bias of only one resonator. The other resonator fails to tune as the top and bottom electrodes are shorted.

Two pole and four pole coupled resonator bandpass filters with discrete BST or GaAs varactors as tuning elements are implemented in a frequency range of 1 - 3 GHz. BST interdigital capacitors, BST parallel plate varactors, or GaAs varactors are integrated into a microwave laminate circuit in a hybrid manner. A full set of measurement results is given. The BST tuning technique is compared directly with the semiconductors in an application environment for the first time. The filters based on BST parallel plate capacitors show an insertion loss in line with the GaAs filters, which is also the lowest insertion loss of BST filters ever reported.

Future work on improving the BST film and metal film loss at tens of gigahertz range is also discussed.

To My Dad and Mom

ACKNOLEDGEMENTS

I would like to express my sincere gratitude to my supervisor Prof. Mike Lancaster, for providing me the opportunity to study in the Emerging Device Technology (EDT) Research Group, for generously guiding me throughout the research work, for constant encouragement, quick reply, and full support of my study here. He has a wide range of research interest, understands deep but expresses concisely. I benefit a lot from our meetings and his comments on my thesis and papers.

I would also like to thank my co-supervisor Dr. Frederick Huang for many helpful advices on device design and simulation, and correction of part of the thesis. I am also grateful to Dr. Tim Jackson for his support on material fabrication and I appreciate his correction of the thesis and papers very much. Special thanks go to my co-partner Dr. Peng Bao, who fabricates all the ferroelectric devices in this project, for his hard work on material optimisation and device fabrication, as well as many interesting ideas and discussion.

I would like to particularly thank Dr. Yi Wang and Dr. Guoyong Zhang for so much beneficial discussion and help in device design and measurement, and for generously sharing their experience. I also thank Donna Holdom and Dr. Maolong Ke for technical support on device fabrication, and Clifford Ansell for manufacturing copper boxes for the devices. I am also grateful to all my past and present colleagues in the EDT group for their advice, participation, and help from time to time.

The project is a joint work with Heriot-Watt University and Cranfield University. I appreciate the meetings and discussion with Dr. Jiasheng Hong, Dr. Young-Hoon Chun, Dr. Paul Kirby, Arne Luker, Robert Wright from the two universities. I also appreciate the financial support from the UK Engineering and Physics Science Research (EPSRC) scholarship.

Lastly and most importantly, I would like to acknowledge my parents. Love and trust from you encouraged me in the past years. I could not have completed this thesis without you.

CONTENTS

CHAPTER 1

INTRODUCTION

This chapter presents the motivation for developing frequency agile microwave devices. Competing technologies for frequency agile devices are reviewed and compared. Finally, the thesis organisation is outlined.

1.1 Microwave frequencies

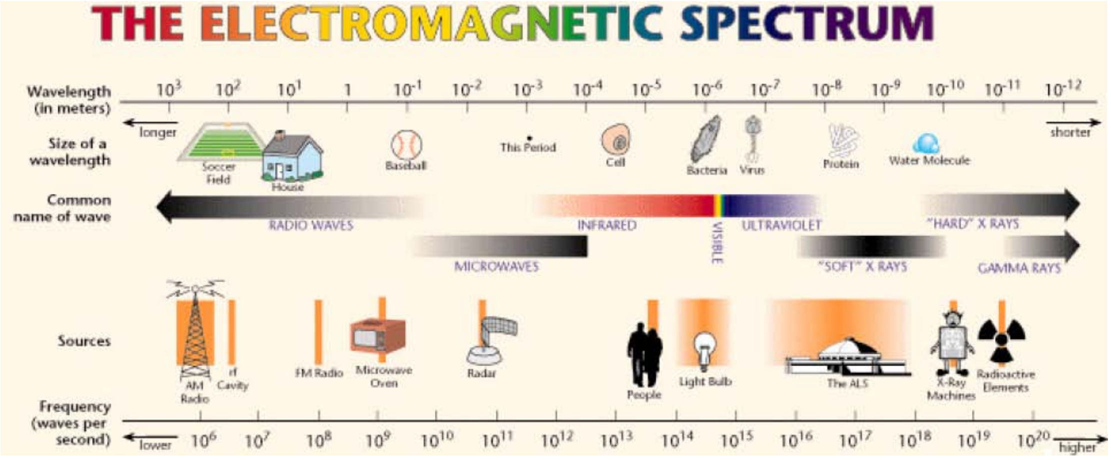

Fig.1- 1 The electromagnetic spectrum (taken from [1])

The term microwave describes electromagnetic waves in the frequency range of 0.3 GHz to 300 GHz [2], corresponding to a free space electrical wavelength λ of 1 m to 1 mm. The free space electrical wavelength λ is related to the frequency f as $\lambda = c/f$, where c is velocity of light in vacuum and is 3×10^8 m/s. As shown in the electromagnetic spectrum in Fig.1- 1, radio frequency (RF) waves have longer electromagnetic wavelength than the microwaves. Above the microwaves in frequency are the infrared radiation, visible light, ultraviolet spectrum, x-rays, and gamma rays.

Microwave frequencies include largely three bands: the ultra-high-frequency (UHF) band of

0.3 GHz to 3 GHz, the super-high-frequency (SHF) band of 3 GHz to 30 GHz, and the extremely-high-frequency (EHF) band of 30 GHz to 300 GHz. The UHF band is widely used for transmission of television signals, mobile phones, wireless local area network (WLAN), and bluetooth. The SHF band is also known as centimetre band as the wavelength ranging from 10 cm to 1 cm. The EHF band corresponds to a wavelength on the order of millimetres, so this frequency range is also called millimetre waves. The letter band designation of the microwave frequencies defined by IEEE standard 521-2002 is given in Table 1 - 1.

Designation	Frequency	Wavelength
UHF-band	0.3 - 1.0 GHz	100 - 30 cm
L-band	1 - 2 GHz	30 - 15 cm
S-band	2 - 4 GHz	15.0 - 7.5 cm
C-band	4 - 8 GHz	7.50 - 3.75 cm
X-band	8 - 12 GHz	3.75 - 2.50 cm
Ku-band	12 - 18 GHz	2.50 - 1.67 cm
K-band	18 - 27 GHz	1.67 - 1.11 cm
Ka-band	27 - 40 GHz	1.11 - 0.75 cm
V-band	40 - 75 GHz	7.5 - 4.0 mm
W-band	75 - 110 GHz	4.0 - 2.7 mm

Table 1 - 1 Radar frequency letter band nomenclature (IEEE standard 521-2002) [3]

1.2 Motivation

This thesis describes tunable microwave filters based on ferroelectric materials. The electric field dependent permittivity of ferroelectric materials is the key to obtain frequency agility. The interest on tunable filters is motivated by the increasing demand for reconfigurable communication systems in recent years.

Nowadays, high speed, high data rate communication systems are already an integral part of our lives. Microwave filters, which provide functions such as rejecting undesirable frequencies in microwave receivers and transmitters, and channelising or combining different frequency signals in multiplexers and demultiplexers, are the essential components in radars, cellular and satellite communication systems [4]. A tunable filter can replace switched filters bank with a single component, and can provide size and weight reduction and better channel selectivity, which makes it favourable for reconfigurable systems [5]. Tunable filters, together with tunable matching networks, tunable phase shifters, frequency agile antennas, and tunable power amplifiers, are the essential components to form multimode and multiband microwave devices. Such devices have found widespread applications in reconfigurable wireless and cellular communication systems, frequency agile radars, satellite communication, and cognitive radios. The main application areas are described as follows.

Multifunctional microwave devices are highly desirable in wireless communication systems due to their ability to cover different communication standards with a single device [6]. The number of wireless systems and standards has increased rapidly over the past decades. Different regions of the world also tend to use different standards and operate at different frequencies. Therefore, mobile terminals with reprogrammable operation frequency and mode are favourable to support global roaming and to be compatible with new services [7]. For instance, the GSM (global system for mobile communications) networks operate at 800 MHz, 900 MHz, 1800 MHz, and 1900 MHz frequency bands. A quad-band mobile phone covering the four GSM frequencies enables international roaming and is a standard now [8]. In addition, the third generation (3G) wireless systems, which are based on the international mobile telecommunication-2000 (IMT-2000) standards, have been launched and will coexist with the current systems. Hence, RF front ends which could combine different types of systems are in demand. An example of a receiver supporting GSM and W-CDMA (wide band code division multiple access) is discussed in [9].

Multimode and multiband devices have also found applications in military defense systems. A frequency agile system with capability to sense interference and switch to a different frequency is proposed for naval target control purpose [10]. For the satellite communication, a satellite which carries multiple frequency transponders serving different markets and various needs is desirable as the payload cost is shared [8].

A newly emerged reconfigurable system is a cognitive radio [11]. A cognitive radio is a smart system which is aware of available bands and changes its transmission parameters correspondingly to adapt to the environment and to avoid interference [12]. A cognitive radio is expected to use the frequency spectrum efficiently and solve the current problem of the overcrowded frequency spectrum [13]. An example of a cognitive WiMAX (worldwide interoperability for microwave access) framework is given in [14].

1.3 Microwave tunable filters

Before discussing various technologies for frequency agility, some terms describing the performance of a tunable filter is introduced here.

(1) Tunability or relative tunability

The tunability n or relative tunability n_r of a tunable bandpass filter is defined as

$$\mathrm{n} = \frac{f_{\max}}{f_{\min}} \tag{1.1}$$

$$\mathrm{n_r} = \frac{f_{\max} - f_{\min}}{f_{\max}} \times 100\% \tag{1.2}$$

where $f_{\max}$, $f_{\min}$ are the maximum and minimum centre frequency of the filter respectively. For ferroelectric tunable filters, relative tunability is usually defined as

$$\mathrm{n_r} = \frac{f(0) - f(\mathrm{V})}{f(0)} \tag{1.3}$$

where $f(0)$ and $f(\mathrm{V})$ are the centre frequency of the filter at zero bias and with maximum bias respectively. A large tunability or a wide tuning bandwidth is usually desirable in frequency agile applications.

(2) Loss

In RF front ends, bandpass filters are normally placed before the low noise amplifier to block out-of-band interfering signals. Low loss is an essential requirement for such filters to maintain good receiver noise figure and selectivity [15]. The insertion loss (IL) is a measure of the filter loss performance, which is often expressed in dB as [16]

$$\mathrm{IL} = 10\log \mathrm{P_{LR}} \ \ \mathrm{dB}$$

where P_{LR} is the power loss ratio of a network, defined as incident power divided by the actual power delivered to the load. A power loss ratio of 50 % is equivalent to - 3 dB insertion loss.

The quality factor Q of a resonator circuit is defined as [2]

$$Q = \omega \frac{\text{average energy stored}}{\text{average energy dissipated}} \qquad (1.4).$$

Resonator Q is a measure of the frequency selectivity and loss performance. For a filter consisting of resonators, a higher resonator Q implies a lower loss and better frequency selectivity of the filter. The resonator quality factor Q can be evaluated as [2]

$$Q = \frac{\omega_0 L}{R} = \frac{1}{\omega_0 RC}$$

for a series RLC resonant circuit, and

$$Q = \frac{R}{\omega_0 L} = \omega_0 RC$$

for a parallel RLC resonant circuit, where $\omega_0 = 1/\sqrt{LC}$ is the resonant frequency.

(3) Tuning speed

The tuning speed of a tunable filter refers to the delay time required by the filter to change between two frequencies or two states. A tuning speed over 1 GHz/μs is required in modern communication systems [17].

(4) Linearity

In a linear system, the output signal has the same frequency as the input signal, it only differs from the amplitude and phase. However, practical microwave devices are generally nonlinear and exhibit intermodulation distortion (IMD). For instance, for input signals comprised of two closely spaced frequencies ω_1 and ω_2, the output signals of a nonlinear device consist of fundamental frequencies ω_1 and ω_2, harmonics $n\omega_1$ and $n\omega_2$, and intermodulation products $\pm m\omega_1 \mp n\omega_2$, where m and n are integer. The third order intermodulation products $2\omega_1$-ω_2 and

$2\omega_2$-ω_1 are located close to the fundamental frequencies, which can cause in-band distortion of the output signals, hence are the ones of most concern. As shown in Fig.1- 2, the third order intercept point (IP3) is defined as the input power in decibels where the extrapolations of the output power as a function of the input power for fundamental and third order intermodulation signals intersect. IP3 is a convenient quantitative measure of the nonlinearity of a device.

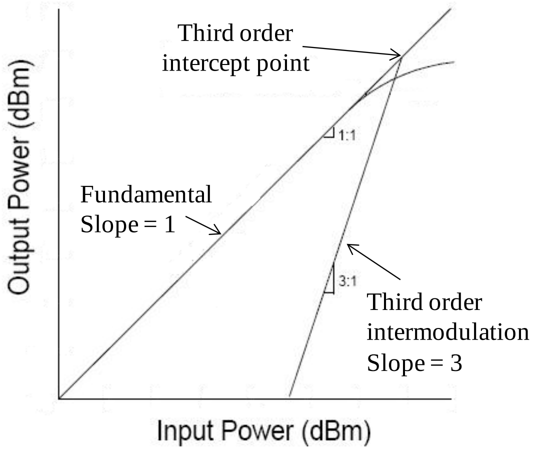

Fig.1- 2 The definition of the third order intercept point (IP3).

(5) RF power handling capability

Power handling capability of a RF/microwave device is the ability to transmit high microwave power level without breakdown or unacceptable intermodulation distortion of the in-band signals. A large power handling capability is required for filters in applications such as wireless or radio base station transmitters and diplexers, satellite output filters and multiplexers, and transmitters in radar systems [18].

In addition to the above, other performance parameters such as operating frequency, power consumption, tuning voltage as well as many others specify the tuning technology requirements. Several technologies realising frequency agility will be discussed in the following section.

1.4 Competing technologies

The frequency agility of a tunable filter can be achieved either in digital domain, in the analog domain, or in a combination of both. For the sake of this dissertation, discussions of tunable filters are referred to analog tuning unless otherwise stated. There are various technologies to accomplish frequency agility. One is by changing either the length and/or the inductive or capacitive loading of a resonator [19]. The resonance frequency of a resonator circuit can be expressed as [2]

$$f_0 = \frac{1}{2\pi\sqrt{\mathrm{LC}}} \tag{1.5}$$

where L and C are the equivalent inductance and capacitance of the resonator unit, regardless the circuit configuration or implementation. Technologies for frequency agile devices for microwave applications include mechanical tuning, ferrites, varactor diodes, micro-electro-mechanical systems (MEMS), and ferroelectric thin film technologies.

Mechanically tunable filters are the earliest type of tunable filters [20]. The design procedure of some mechanically tunable filters comprised of coaxial or waveguide resonators is discussed in [21]. They offer very good power handling capability and low insertion loss at a low cost. However, these filters are bulky and their tuning speed is quite slow (tuned manually if not combined with a remotely controlled motor [19]) and are therefore cumbersome. Their applications include the long-distance communication or radar systems where filter characteristics of large power handling capability as well as low loss are of the first importance [19], [21].

Ferrites are materials consisting of a mixing of metallic oxides and have a general chemical composition $\mathrm{MO{\cdot}Fe_2O_3}$, where M is a divalent metal such as manganese (Mn), magnesium (Mg), iron (Fe), zinc (Zn), or nickel (Ni). [16]. Ferrites exhibit anisotropic magnetic properties under a static magnetic field, which arises from the magnetic dipole moments associated with the unpaired electron spin [2], [16]. The permeability of ferrites is not a single scalar quantity but a tensor dependent on magnetic bias. Microwave tunable filters and phase shifters based on ferrites have been used for many years [22-25], and are reviewed in [19], [26]. The filters based on single crystal yttrium-iron-garnet (YIG) spheres have been proved the most popular type among these magnetically tunable filters, and are termed as YIG filters [21]. YIG filters are typically used as preselectors in the receiver frond-ends and microwave spectrum analysers [21]. YIG filters are controlled by the change of ferromagnetic resonance frequency with an externally applied DC magnetic field [27]. These filters feature a multi-octave tuning range and high power handling capability, however, they are large in size and their tuning speed is slow, in the microseconds range per gigahertz, limiting their use in certain areas [19]. They can have high power consumption as the magnetic field used for tuning is produced from a current.

Although mechanically and magnetically tunable filters have admirable features such as low loss, wide tuning bandwidth and large power handling capability, many modern communication systems require a tuning speed more than 1 GHz/μs [17], which exceeds the switching time capability of both filters. Furthermore, both mechanically tunable filters and YIG filters are bulky, not suitable to integrate with the planar monolithic microwave integrated circuits (MMICs). Currently, the frequency agility of microwave devices is generally achieved by using varactors which have variable capacitance as a function of the applied electric field. Electronically tunable filters based on semiconductor varactors, MEMS varactors and BST varactors are introduced below.

Semiconductor diodes have found a great variety of applications in microwave engineering. The varactor diode is a type of semiconductor diode which relies on the variable capacitance as a function of the applied bias voltage. The operation of a varactor diode is based on changing the depletion layer width of the p-n junction under a reverse bias voltage, which has the same effect of changing the distance between the two plates of a capacitor. The depletion layer width increases in proportional with the square root of the reverse bias voltage across the diode, therefore the junction capacitance is inversely proportional to the square root of the voltage. Abrupt or hyperabrupt varactor diodes, made by controlling the doping concentration in the active region, offer higher capacitance tuning ratio than ordinary p-n junction diodes [28].

Gallium Arsenide (GaAs) varactors have lower parasitic resistance and higher Q than their silicon counterparts, hence they are more favourable in microwave tuning applications [17]. Typical capacitance tuning curves of GaAs hyperabrupt junction varactor diodes with a tuning slope of 1.0 is shown in Fig.1- 3. Varactor diodes have the advantages of high tunability, compact size (~ μm), and fast tuning speed (~ GHz/μs). As a consequence, varactor diodes have been the state of art for building tunable filters and have been widely used in ESM receivers [17], [29]. However, the high tunability of a varactor diode often comes at a price of poor linearity and lower quality factor [8]. Furthermore, as the Q of a varactor diode is inversely proportional with frequency, the Q of a varactor diode degrades significantly with frequency and results a poor Q at frequencies above 10 GHz [30]. For instance, the GaAs varactor MV30009 from MDT Ltd. has a Q of 2000 specified at 50 MHz and this is reduced to only 10 at 10 GHz [31]. In addition, varactor diodes suffer from junction noise and poor power handling as a result of the tiny capacitor area.

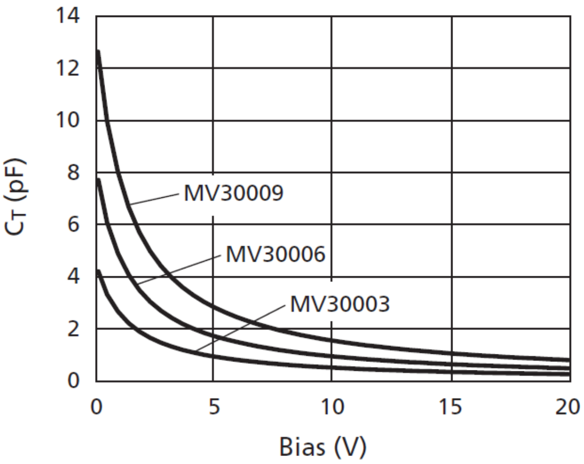

Fig.1- 3 Typical capacitance-voltage curves of GaAs hyperabrupt junction varactor diodes with a tuning slope of 1.0 from MDT Ltd. (picture taken from [31]).

Another promising candidate for tunable filters in future generations of communication systems is radio frequency micro-electro-mechanical systems (RF MEMS). These emerged in the 1990s [32-34]. The first RF MEMS switch demonstrated an ON state insertion loss less than 0.5 dB and an OFF state isolation greater than 35 dB up to 45 GHz; the first RF MEMS varactor demonstrated a capacitance ratio of 2.9 by altering the overlap between the interdigital fingers [32]. RF MEMS based filters can be divided into two general types: digital or analogue. MEMS switches are used for the digital type and large tuning range (20 % - 60 %) can be obtained [15], [35]. The switching function is accomplished by the physical movement of a component actuated by electrostatic [33], [36], [37], electrostictive, piezoelectric [38] or electrothermal [39] forces. Tunable filters based on MEMS varactors can be tuned continuously, although the tunability is limited to less than 15 % [40]. The MEMS varactor is typically implemented in a metal-air-metal bridge configuration and the capacitance is tuned by changing the distance between the two plates [40], [41].

The electrostatic force actuated MEMS switches and varactors have the merit of small size (~ 10^2 µm), low loss in the microwave region (less than 0.5 dB up to 100 GHz for switches [6]), high linearity, and can handle higher RF power levels than a varactor diode [42]. Although an actuation voltage of 20 - 100 V is often required, the power consumption is low, as no DC current flowing through the device [6]. Moreover, the micro-machining process to fabricate MEMS is compatible with the state of art MMIC technology, which enables batch fabrication for cost reduction and provides potentials to produce a system-on-a-chip. Because of these advantages there has arisen tremendous interest in the RF MEMS devices during the past two decades. However, the requirements of hermetic packaging and reliability issues have hindered their widespread use in industry. In addition, the MEMS devices exhibit a moderate tuning speed (2 - 100 µs), which is not adequate for many applications in phase array radar systems [8].

Ferroelectrics have been widely proposed as an alternative component for tunable circuits since the 1980s [43]. The dielectric constant of ferroelectric materials decreases substantially with the applied electric field, which is the key for tuning applications. The most intensively studied ferroelectric material in this application is Barium Strontium Titanate (BST). The dielectric constant of BST thin films reported is in the range of 10^2 - 10^3 at room temperature. The high dielectric constant of BST film results in a very high energy density capacitor. BST thin film varactors in both interdigital and parallel plate configurations have been used to demonstrate tunable filter, phase shifters [44], [45], tunable matching networks [46] and delay lines [47]. BST thin film varactors are compact (as a result of high dielectric constant), offer a good tunability and fast tuning speed (~ ns), and have low power consumption [48]. BST varactors with interdigital electrodes are easy to fabricate and offer good linearity and BST parallel plate capacitors exhibit a high capacitance density and high tunability at low bias voltage. BST capacitors with relative tunability greater than 50 % were obtained at DC bias voltage less than 5 V [49-51]. In addition, ferroelectric devices can be fabricated on a variety of substrates including silicon using standard semiconductor manufacturing process, which provides possibilities to integrate with MMICs. The relatively high loss of room temperature microwave devices based on BST varactors has been a significant drawback limiting their microwave applications [52]. However, intensive research effort has been made to improve the quality factors of BST varactors [53-55]. The best to date is Vorobiev [30] who has presented a circular BST parallel plate capacitor with a Q of 100 at 10 GHz.

Some important parameters and technologies for tunable devices are shown in Table 1 - 2. None of the technologies is perfect and choosing strongly depends on the particular system requirements, with a trade off between the performance of the suitable technology as well as cost, ease of integration, size and weight, reliability, and repeatability. In practical cases, two or more techniques can be implemented in one application. Lugo [56] has reported a bandpass filter with simultaneous frequency and bandwidth control using both ferroelectric varactors and cantiliever MEMS switches. The filter centre frequency was tuned continuously from 30 GHz to 35 GHz controlled by ferroelectric varactors. The filter bandwidth was independently controlled for a ratio of 2:1 by the MEMS switches.

Tuning methods	Mechanical	YIG	GaAs varactor	RF MEMS	BST thin film
Tunability	10-20%[57]	multi-octave	3:1	< 2:1	2 - 3:1
unloaded Q	> 1000	> 500	10 - 40[a]	very high[b]	20 - 100[a]
Insertion loss (dB)	0.5 - 2.5	3 - 8	2 - 10	2 - 8	3 - 10
Tuning voltage (V)	NA		< 15	20 - 100	5 - 20[c]
Tuning speed (GHz/ms)	very low	0.5 – 2.0	10^3	10^2 [31]	10^6
Power handling	very high[58]	2 W	~ mW	1 - 2 W	~ mW
Power consumption	high	high	medium	low	low
Linearity (IP3 : dBm)	> 60	< 30	15 - 25	> 65	30 - 55
Size / Weight	large	large	small	small	small
Integration	difficult	difficult	good	good	good

Table 1 - 2 Comparison of competing technologies for building microwave tunable filters. [a] at 10 GHz. [b] for MEMS switch. [c] for BST varactor in parallel plate configuration.

1.5 Thesis organisation

The concern of this thesis is devoted to the ferroelectric tuning technology. Ferroelectric materials have an electric field dependent permittivity and can be used in frequency agile microwave devices. This dissertation presents tunable microwave lowpass and bandpass filters based on BST thin film varactors. The design procedure of the filters is addressed in detail with full wave electromagnetic simulation performed. The fabrication process of the BST devices is also described. The measurement results of the filters are analysed and compared with the simulation. A brief outline of the thesis organisation is given below.

Chapter 2 starts from reviewing the history, fundamental characteristics and various applications of ferroelectric materials. This is followed by the discussion of the microwave properties of BST thin films, together with fabrication issues such as deposition methods, substrate and metallisation choice, and measurement techniques. BST thin film varactors in the interdigital and parallel plate configurations are discussed. A survey of the BST varactors reported in the literature is presented and compared with the varactors made in this work. Recent progress of ferroelectric tunable filters are also reviewed, and a survey of other people's work on BST room temperature bandpass filters is provided and compared with our filters.

Chapter 3 provides theoretical fundamentals for the microwave filters designed in chapters 4, 5 and 6. The filters presented in this work are all based on Chebyshev prototypes in a coplanar waveguide configuration. In chapter 3, characteristics of single and multilayer substrate coplanar waveguides are calculated analytically using a conformal mapping technique. General filter synthesis procedure for Chebyshev lowpass and bandpass filters is outlined. The design method for coupled resonator filters using a coupling matrix concept is also addressed here. In addition, lumped elements such as meander line inductors and ferroelectric varactors are modelled and discussed as well.

In chapter 4 a seventh order lumped element tunable lowpass filter incorparating integrated BST varactors is presented. The filter was implemented in a coplanar waveguide configuration on a high resistivity silicon substrate. The filter size was 1.8 mm × 0.9 mm and had a multilayer structure. The tuning elements, $Ba_{0.25}Sr_{0.75}TiO_3$ thin film parallel plate varactors, were 5 µm × 5 µm or 10 µm × 10 µm in size and 500 nm thick. A lowpass filter incorporating 5 µm square BST varactors demonstrated a - 10 dB cut-off frequency of 18.52 GHz at zero bias, and tuned to 24.47 GHz upon 15 V bias voltage, showing 32.1 % tuning. Several lowpass filters were fabricated and tested in house, with meander line inductors and BST varactors of different sizes. The filters with 5 µm square BST varactors covered a cut-off frequency range from 11 GHz to 25 GHz, and the filters with 10 µm square varactors covered from 4 GHz to 8 GHz.

In chapter 5 two pole and three pole combline bandpass filters incorporating integrated BST varactors are presented. These filters were implemented in a coplanar waveguide configuration on MgO substrates. The filters consisted of coupled resonators which were comprised of line elements shorted to ground at one end and loaded with 5 μm × 5 μm BST parallel plate capacitors at the other end. Each resonator could be independently biased. $Ba_{0.6}Sr_{0.4}TiO_3$ thin film was used in this design. The filters were designed and analysed by full wave electromagnetic simulation. The fabrication procedure of the multilayer filters and the problems encountered during the process of etching BST film were addressed. The two pole filter is 1.6 mm × 4 mm and the three pole filter 2.3 mm × 4 mm. A two pole filter measurement demonstrated a reasonable tuning of only one resonator from 8 GHz to 12 GHz with 10 V bias, whereas the other resonator showed no tuning with bias as a result of short circuit between the top and bottom metal layers. The bandpass filters showed a zero bias insertion loss above 8 dB. The losses contributed from the metal and BST films were analysed and separated.

Two pole and four pole combline tunable bandpass filters incorporating discrete BST varactors are presented in chapter 6. The filter circuits were implemented in a coplanar waveguide configuration on duroid 5870 laminate. Discrete BST intergiditial capacitors (IDCs) or BST parallel plate capacitors were fabricated in house, characterised using an impedance analyser, and assembled into the filter circuits in a hybrid manner. The same filters were also made using commercially available GaAs varactors to give a direct comparison between the BST and semiconductor tuning techniques in an application environment. These varactors performed as tuning elements in the filters. The two pole BST IDC filter was tuned from a centre frequency of 1.55 GHz and an insertion loss of 3.7 dB at zero bias, to 2.02 GHz and 1.1 dB with 65 V bias, which made a figure of merit (FoM) of 0.87 dB^{-1}. The two pole BST parallel plate filter was tuned from 2.32 GHz at zero bias to 2.52 GHz at 45 V bias, with an insertion loss of 1.4 dB to 1.3 dB correspondingly. The filter showed a FoM of 0.41 dB^{-1}. The two pole GaAs filter showed the largest tuning range from 0.94 GHz to 2.44 GHz with 14 V bias and a FoM of 3.84 dB^{-1}, as a result of the high tunability of the GaAs varactors. The four pole filters showed a tuning range close to that of the two pole ones with the same kind of varactors. The BST filters demonstrated a loss performance in line with the GaAs filters in the gigahertz range.

Finally, the thesis is concluded in the last chapter and direction for future work is also presented.

1.6 Summary

In this chapter the motivation to developing microwave tunable filters was described and some characteristic parameters of tunable filters were introduced. The current and promising technologies for frequency agile devices were discussed and compared. At the end, the thesis organisation was introduced and the following chapters were overviewed.

References

[1] http://safetycenter.navy.mil/acquisition/RFR.

[2] D. M. Pozar, Microwave Engineering, 2nd ed. New York, USA, John Wiley & Sons, Inc., 1998.

[3] Radio Frequency Band Designations, http://www.radioing.com/eengineer/index.html.

[4] K. Chang, "Microwave passive and antenna components", in *Handbook of microwave and optical components*. vol. 1: John Wiley & Sons, Inc., 1989.

[5] J. Nath, D. Ghosh, J. P. Maria, A. I. Kingon, W. Fathelbab, P. D. Franzon, and M. B. Steer, "An electronically tunable microstrip bandpass filter using thin-film Barium-Strontium-Titanate (BST) varactors", *IEEE Transactions on Microwave Theory and Techniques,* vol. 53, no. 9, pp. 2707-2712, 2005.

[6] S.-J. Park, "High-Performance RF-MEMS Tunable Filters", Doctor of Philosophy thesis, Electrical Engineering, The University of Michigan, 2008

[7] J. Ryynanen, S. Lindfors, K. Stadius, and K. A. I. Halonen, "Integrated circuits for multiband multimode receivers", *Circuits and Systems Magazine,* vol. 6, no. 2, pp. 5-16, 2006.

[8] J. Nath, "Design and characterization of frequency agile RF and microwave devices using ferroelectrics", Doctor of Philosophy thesis, Electrical Engineering, North Carolina State University, 2006

[9] J. Ryynanen, K. Kivekas, J. Jussila, L. Sumanen, A. Parssinen, and K. A. I. Halonen, "A single-chip multimode receiver for GSM900, DCS1800, PCS1900, and WCDMA", *IEEE Journal of Solid-State Circuits,* vol. 38, no. 4, pp. 594-602, 2003.

[10] M. Owens, "Frequency agile system for naval target control": http://www.dtic.mil/dtic, 2005.

[11] J. Mitola and G. Q. Maguire, "Cognitive radio: making software radios more personal", *IEEE Personal Communications,* vol. 6, no. 4, pp. 13-18, 1999.

[12] A. F. Molisch, L. J. Greenstein, and M. Shafi, "Propagation Issues for Cognitive Radio", *Proceedings of the IEEE,* vol. 97, no. 5, pp. 787-804, 2009.

[13] NTIA, "The radio spectrum frequency allocations": http://www.ntia.doc.gov/osmhome/allochrt.pdf, 2003.

[14] A. E. Leu, B. L. Mark, and M. A. McHenry, "A Framework for Cognitive WiMAX With Frequency Agility", *Proceedings of the IEEE,* vol. 97, no. 4, pp. 755-773, 2009.

[15] R. M. Young, J. D. Adam, C. R. Vale, T. T. Braggins, S. V. Krishnaswamy, C. E. Milton, D. W. Bever, L. G. Chorosinski, C. Li-Shu, D. E. Crockett, C. B. Freidhoff, S. H. Talisa, E. Capelle, R. Tranchini, J. R. Fende, J. M. Lorthioir, and A. R. Tories, "Low-loss bandpass RF filter using MEMS capacitance switches to achieve a one-octave tuning range and independently variable bandwidth", in *IEEE MTT-S International Microwave Symposium Digest*2003, pp. 1781-1784 vol.3.

[16] R. E. Collin, Foundations for Microwave Engineering, McGraw-Hill, 1992.

[17] I. C. Hunter and J. D. Rhodes, "Electronically tunable microwave bandpass filters", *IEEE Transactions on Microwave Theory and Techniques,* vol. 82, no. 9, pp. 1354-1360, 1982.

[18] Y. Ming, "Power-handling capability for RF filters", *Microwave Magazine,* vol. 8, no. 5, pp. 88-97, 2007.

[19] J. Uher and W. J. R. Hoefer, "Tunable microwave and millimeter-wave band-pass

filters", *IEEE Transactions on Microwave Theory and Techniques,* vol. 39, no. 4, pp. 643-653, 1991.

[20] A. G. Fox, "An Adjustable Wave-Guide Phase Changer", *Proceedings of the IRE,* vol. 35, no. 12, pp. 1489-1498, 1947.

[21] G.L.Matthaei, L.Young, and E.M.T.Jones, Microwave filters, impedance matching networks, and coupling structures, Artech House, 1980.

[22] F. Reggia and E. G. Spencer, "A New Technique in Ferrite Phase Shifting for Beam Scanning of Microwave Antennas", *Proceedings of the IRE,* vol. 45, no. 11, pp. 1510-1517, 1957.

[23] H. Brand and N. Krause, "Tunable millimetre-wave ferrite bandpass filter with reduced biasing field", *Electronics Letters,* vol. 13, no. 19, pp. 576-578, 1977.

[24] G. Leon, R. R. Boix, and F. Medina, "Tunability and bandwidth of microstrip filters fabricated on magnetized ferrites", *Microwave and Wireless Components Letters,* vol. 14, no. 4, pp. 171-173, 2004.

[25] J. Krupka, A. Abramowicz, and K. Derzakowski, "Magnetically tunable filters for cellular communication terminals", *IEEE Transactions on Microwave Theory and Techniques,* vol. 54, no. 6, pp. 2329-2335, 2006.

[26] J. D. Adam, L. E. Davis, G. F. Dionne, E. F. Schloemann, and S. N. Stitzer, "Ferrite devices and materials", *IEEE Transactions on Microwave Theory and Techniques,* vol. 50, no. 3, pp. 721-737, 2002.

[27] P. S. Carter, "Magnetically-tunable microwave filters using single-crystal yttrium-iron-garnet resonators", *IRE Transactions on Microwave Theory and Techniques*, no. pp. 252-260, 1960.

[28] Varactor / varicap diode, www.radio-electronics.com.

[29] C. B. Hofmann and A. R. Baron, "Wideband ESM receiving systems-Part I", *Microwave J.,* vol. 23, no. 9, pp. 24-34, Sep,1980.

[30] A. Vorobiev, P. Rundqvist, K. Khamchane, and S. Gevorgian, "Silicon substrate integrated high Q-factor parallel-plate ferroelectric varactors for microwave/millimeterwave applications", *Applied Physics Letters*, vol. 83, no. 15, pp. 3144-3146, 2003.

[31] Microwave Device Technology Ltd., http://www.microwavedevicetechnology.com.

[32] L. E. Larson, R. H. Hackett, M. A. Melendes, and R. F. Lohr, "Micromachined microwave actuator (MIMAC) technology-a new tuning approach for microwave integrated circuits", in *Microwave and Millimeter-Wave Monolithic Circuits Symposium, 1991. Digest of Papers, IEEE 1991*1991, pp. 27-30.

[33] A. Dec and K. Suyama, "Micromachined electro-mechanically tunable capacitors and their applications to RF IC's", *IEEE Transactions on Microwave Theory and Techniques,* vol. 46, no. 12, pp. 2587-2596, 1998.

[34] C. L. Goldsmith, Y. Zhimin, S. Eshelman, and D. Denniston, "Performance of low-loss RF MEMS capacitive switches", *Microwave and Guided Wave Letters,* vol. 8, no. 8, pp. 269-271, 1998.

[35] K. Entesari and G. M. Rebeiz, "A 12-18-GHz Three-Pole RF MEMS Tunable Filter", *IEEE Transactions on Microwave Theory and Techniques,* vol. 53, no. 8, pp. 2566-2571, 2005.

[36] Y. Jun-Bo and C. T. C. Nguyen, "A high-Q tunable micromechanical capacitor with movable dielectric for RF applications", in *Electron Devices Meeting Technical Digest*2000, pp. 489-492.

[37] T. K. K. Tsang and M. N. El-Gamal, "Micro-electromechanical variable capacitors for

RF applications", in *the 45th Midwest Symposium on Circuits and Systems*2002, pp. 25-28.

[38] J. Y. Park, Y. J. Yee, H. J. Nam, and J. U. Bu, "Micromachined RF MEMS tunable capacitors using piezoelectric actuators", in *IEEE MTT-S International Microwave Symposium Digest*2001, pp. 2111-2114.

[39] Z. Feng, H. Zhang, K. C. Gupta, W. Zhang, V. M. Bright, and Y. C. Lee, "MEMS-based series and shunt variable capacitors for microwave and millimeter-wave frequencies", *Sensors and Actuators A: Physical,* vol. 91, no. pp. 256-265, 2001.

[40] A. Abbaspour-Tamijani, L. Dussopt, and G. M. Rebeiz, "Miniature and tunable filters using MEMS capacitors", *IEEE Transactions on Microwave Theory and Techniques,* vol. 51, no. 7, pp. 1878-1885, 2003.

[41] K. Hong-Teuk, P. Jae-Hyoung, K. Yong-Kweon, and Youngwoo Kwon, "Low-loss and compact V-band MEMS-based analog tunable bandpass filters", *Microwave and Wireless Components Letters,* vol. 12, no. 11, pp. 432-434, 2002.

[42] E. Marsan, J. Gauthier, M. Chaker, and K. Wu, "Tunable microwave device: status and perspective", in *IEEE-NEWCAS Conference*2005, pp. 279-282.

[43] A.K.Tagantsev, V.O.Sherman, K.F.Astafiev, J.Venkatesh, and N.Setter, "Ferroelectric materials for microwave tunable applications", *Journal of Electroceramics,* vol. 11, no. pp. 5-66, 2003.

[44] D. Kuylenstierna, E. Ash, A. Vorobiev, T. Itoh, and S. Gevorgian, "X-band Left Handed Phase Shifter using Thin Film $Ba_{0.25}Sr_{0.75}TiO_3$ Ferroelectric Varactors", in *the 36th European Microwave Conference*2006, pp. 847-850.

[45] K. B. Kim, T. S. Yun, J. C. Lee, M. Chaker, C. S. Park, and K. Wu, "Integration of microwave phase shifter with BST varactor onto TiO/sub 2//Si wafer", *Electronics Letters,* vol. 43, no. 14, 2007.

[46] L. Y. V. Chen, R. Forse, D. Chase, and R. A. York, "Analog tunable matching network using integrated thin-film BST capacitors", in *IEEE MTT-S International Microwave Symposium Digest*2004, pp. 261-264.

[47] D. Kuylenstierna, A. Vorobiev, P. Linner, and S. Gevorgian, "Ultrawide-band tunable true-time delay lines using ferroelectric varactors", *IEEE Transactions on Microwave Theory and Techniques,* vol. 53, no. 6, pp. 2164-2170, 2005.

[48] P. Bao, T. J. Jackson, X. Wang, and M. J. Lancaster, "Barium strontium titanate thin film varactors for room-temperature microwave device applications", *Journal of Physics D: Applied Physics,* vol. 41, no. p. 063001, 2008.

[49] A. Tombak, F. Tito Ayguavives, J. P. Maria, G. T. Stauf, A. I. Kingon, and A. Mortazawi, "Low voltage tunable barium strontium titanate thin film capacitors for RF and microwave applications", in *IEEE MTT-S International Microwave Symposium Digest*2000, pp. 1345-1348 vol.3.

[50] T. Ayguavives, A. Tombak, J. P. Maria, G. T. Stauf, C. Ragaglia, J. Roeder, A. Mortazawi, and A. I. Kingon, "Physical properties of (Ba,Sr)TiO_3 thin films used for integrated capacitors in microwave applications", in *Proceedings of the12th IEEE International Symposium on Applications of Ferroelectrics*2000, pp. 365-368.

[51] R. York, A. Nagra, E. Erker, T. Taylor, P. Periaswamy, J. Speck, S. Streiffer, and O. Auciello, "Microwave integrated circuits using thin-film BST", in *Proceedings of the 12th IEEE International Symposium on Applications of Ferroelectrics*2000, pp. 195-200 vol. 1.

[52] O. G. Vendik, E.K.Hollmann, A. B. Kozyrev, and A. M. Prudan, "Ferroelectric tuning

of planar and bulk microwave devices", *Journal of Superconductivity,* vol. 12, no. pp. 325-338, 1999.

[53] M. S. Tsai, S. C. Sun, and T.-Y. Tseng, "Effect of bottom electrode materials on the electrical and reliability characteristics of (Ba, Sr)TiO_3 capacitors", *IEEE Transactions on Electron Devices,* vol. 46, no. 9, pp. 1829-1838, 1999.

[54] A. Vorobiev, P. Rundqvist, K. Khamchane, and S. Gevorgian, "Microwave loss mechanisms in $Ba_{0.25}Sr_{0.75}TiO_3$ thin film varactors", *Journal of Applied Physics,* vol. 96, no. 8, pp. 4642-4649, 2004.

[55] D. Ghosh, B. Laughlin, J. Nath, A. I. Kingon, M. B. Steer, and J. P. Maria, "Tunable high-quality-factor interdigitated (Ba, Sr)TiO_3 capacitors fabricated on low-cost substrates with copper metallization", *Thin Solid Films,* vol. 496, no. 2, pp. 669-673, 2006.

[56] C. Lugo, G. Wang, J. Papapolymerou, Z. Zhao, X. Wang, and A. T. Hunt, "Frequency and Bandwidth Agile Millimeter-Wave Filter Using Ferroelectric Capacitors and MEMS Cantilevers", *IEEE Transactions on Microwave Theory and Techniques,* vol. 55, no. 2, pp. 376-382, 2007.

[57] W. Sichak and H. Augenblick, "Tunable Waveguide Filters", *Proceedings of the IRE,* vol. 39, no. 9, pp. 1055-1059, 1951.

[58] H. L. Bachman and H. A. Wheeler, "Evacuated Waveguide Filter for Suppressing Spurious Transmission from High-Power S-Band Radar", *IRE Transactions on Microwave Theory and Techniques,* vol. 7, no. 1, pp. 154-162, 1959.

CHAPTER 2

FERROELECTRIC MATERIALS AND DEVICES

This chapter covers the history, fundamental properties, fabrication issues, measurement techniques and applications of ferroelectric materials, with emphasis on ferroelectric thin films for microwave applications. Ferroelectric microwave devices are reviewed and surveys of BST varactors and bandpass filters are presented.

2.1 History and applications

Ferroelectric materials, which are a subset of piezoelectric and pyroelectric materials, exhibit an electric field re-orientable spontaneous polarisation in a certain temperature range. The spontaneous polarisation is highly temperature dependent and disappears above a phase transition temperature T_{ph}, where the material is said to be in the paraelectric phase. When the temperature decreases below T_{ph}, the crystal structure exhibits a slight deformation, the centre of positive charge and negative charge does not coincide, thus electric dipoles are formed and spontaneous polarisation appears in the ferroelectric phase [1].

In the paraelectric phase, the polarisation is proportional to the external electric field. In the ferroelectric phase, the polarisation does not return back to zero when the external field is zero and exhibits remanent polarisation P_r. A coercive field E_c is needed to bring the polarisation back to zero [1]. Hence a polarisation-electric field (P-E) hysteresis loop is observed in ferroelectric phase. The polarisation as a function of electric field of the ferroelectric material in ferroelectric and paraelectric phases is shown in Fig.2- 1.

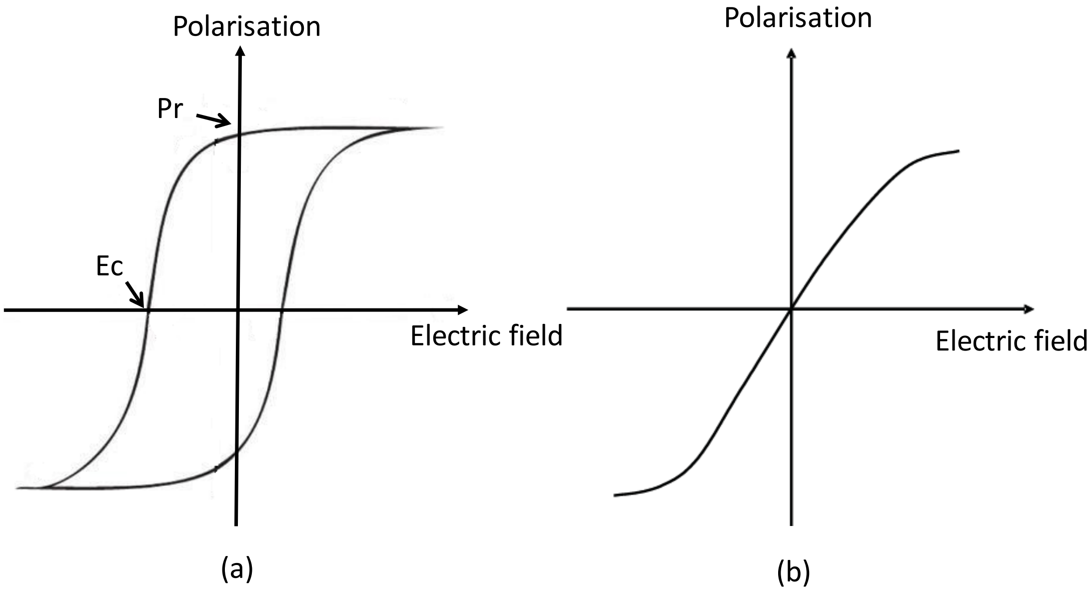

(a) (b)

Fig.2- 1 Polarisation versus electric field of the ferroelectrics in the ferroelectric phase (a) and the paraelectric phase (b)

Ferroelectricity was first discovered by Joseph Valasek in 1921 (40 years after Pierre Curie and Jacques Curie discovered piezoelectricity in 1880 [2]) during an investigation of the dielectric properties of Rochelle salt ($NaKC_4H_4O_6{\cdot}4H_2O$) [3]. He demonstrated the polarisation hysteresis with electric field in Rochelle salt and the dependence of the hysteresis loop on temperature. The term “ferroelectricity” (instead of “Seignette-electricity” or “Rochelle-electricity” in the early literature) was used to describe the spontaneous electric polarisation of Rochelle salt in analogy to the spontaneous magnetic polarisation of ferromagnetics, although most ferroelectrics did not have iron in their lattice. Other ferroelectric materials, potassium dihydrogen phosphate (KDP) and its isomorphs, were not found until 1935. This was followed by the discovery of barium titanate ($BaTiO_3$) as a new class of ferroelectric material by Von Hippel (America), and Wul and Goldman (Russia), in the 1940s [4], [5]. Since then the number of known ferroelectric materials has rapidly proliferated, and there are about 600 known ferroelectric materials according to Landoldt and Börnstein [6].

Most of the useful ferroelectric materials belong to the perovskite family [1], which is characterised by the chemical formula ABO_3, for instance, barium titanate ($BaTiO_3$), strontium titanate ($SrTiO_3$), lead titanate ($PbTiO_3$), lead zirconate ($PbZrO_3$) and their solid solutions. Fig.2- 2 shows the cubic cell structure of ABO_3 type materials, with A^{2+} ions (green) at the apices, B^{4+} (blue) ions at the centre, and O^{2-} (red) ions at the face centres of the cube. It is well known that the ABO_3 structure permits variable compositions by substitution on A- or B- sites by radius compatible ions [7], [8]. When applying an electric field, both B^{4+} cations and O^{2-} anions shift from their equilibrium positions and form electric dipoles as shown in Fig.2- 3. In the paraelectric phase, the ions return to their initial equilibrium positions after the electric field is removed. When $T < T_{ph}$, a ferroelectric phase is exhibited, the ions undergo a spontaneous displacement in the absence of an electric field and remain permanently displaced [9].

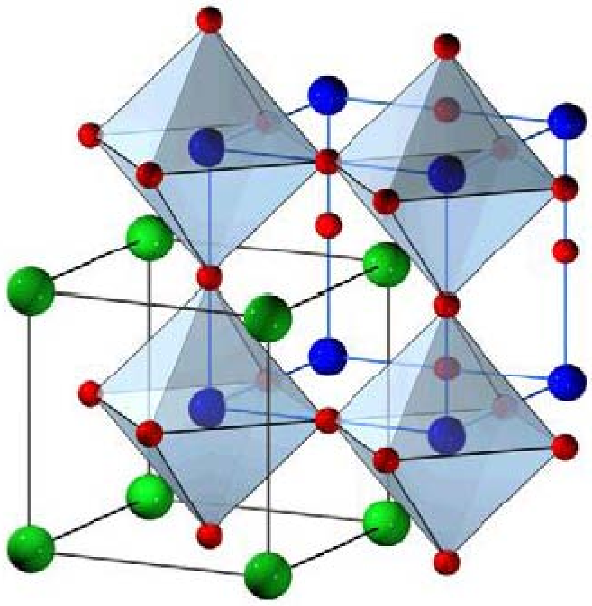

Fig.2- 2 Cubic Cell of ABO_3 type material (taken from [7])

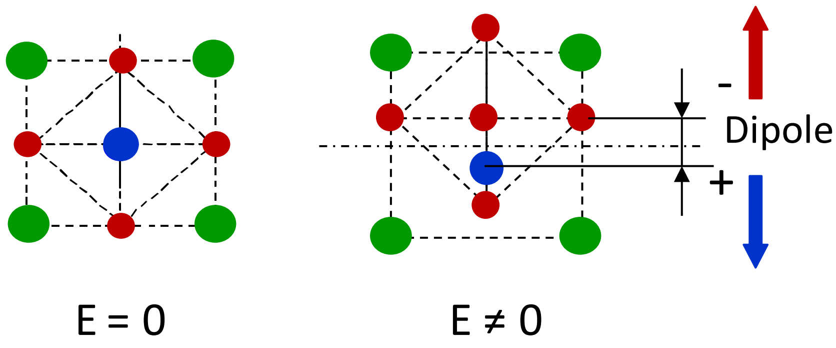

Fig.2- 3 Rearrangement of unit cell in response to an external electric field and formation of a dipole (taken from [10])

Bulk ferroelectrics have found a wide spread usage as dielectrics, piezoelectrics, pyroelectrics and ferroelectrics in the electronic industry for more than 50 years. Prominent examples include the widely used multilayer ceramic capacitors, which use barium titanate as dielectrics, and the positive temperature coefficient resistors (PTCRs) using appropriately doped barium titanate in thermistors and self-regulating heating systems [11]. Piezoelectric/pyroelectric ceramics are widely used in various sensing and actuating applications [1]. For instance, ultrasonic transducers, which use the piezoelectricity of lead zirconium titanate ceramics, are used in many sonar and depth sounding systems.

Applications of ferroelectrics in the form of thin films did not emerge until the 1980s [12]. The initial interest of developing ferroelectric thin films started in the late sixties, with the non-volatile memory as the main driving application [13-15], however, this attempt was frustrated due to the limitations of both material fabrication technology and device electronics at that time. The interest in ferroelectric thin films was renewed due to both the advance in thin film deposition techniques in the mid-eighties and the increasing requirement for miniaturised systems [16], [17]. The current and potential application domains of thin film ferroelectrics include memories, microsystems with pyroelectric and piezoelectric microsensors/actuators, and microwave tunable devices [15].

Non-volatile ferroelectric memory (FeRAM) might be one of the most attractive applications of ferroelectrics. FeRAM has a similar construction to conventional dynamic random access memory (DRAM), but uses a ferroelectric layer to achieve non-volatility. An electric field is used to switch, or “write”, each ferroelectric cell into either a positive or negative polarisation state, representing either “0” or “1” in binary encoding. FeRAM shows attractive features such as low power consumption compared with conventional DRAM and fast write speed over flash memory. FeRAMs have now become a commercially viable option as low density memories in smart cards [18]. Another important memory application is ferroelectric dynamic random access memory. The cell size and capacitor size can be progressively reduced by the use of high dielectric constant ferroelectrics as a replacement of SiO_2/Si_3N_4 in conventional DRAMs.

Ferroelectric thin films have also found applications in the recently emerged area of micro-electro-mechanical systems (MEMS) due to their strong piezoelectric and pyroelectric effect [19]. Ferroelectric films, typically PZT, can be deposited on the substrate prior to the microfabrication to add sensing and actuating functionalities to microdevices [15]. Various devices have been intensively researched during the past decade, such as accelerometers [20], micromotors [21], ultrasonic transducers for medical imaging [22] and sensors and actuators in atomic force microscopy (AFM) [23].

Ferroelectric thin film based microwave tunable devices have received intensive attention in recent years, and are the focus of this thesis. The material property that makes ferroelectric tuning possible is the electric field controlled dielectric constant. The basic concept was not new; being first proposed back in the 1960s [24], [25]. However, the difficulties of matching the reactance of the bulk ferroelectric varactors to the impedance of the rest of the circuit and the requirement for high tuning voltage impeded its development [26]. The interest was then moved to the development of thin film ferroelectrics on dielectric substrates, which provided suitable capacitance values and could be tuned at modest voltage levels. However, such samples suffered from a prohibitively high loss tangent [27]. The applications of ferroelectric thin films were only beginning to emerge from the late eighties [12]. This was in large part due to the advances in ferroelectric thin film deposition techniques [16], [17] and the ability to integrate ferroelectrics with semiconductor technologies [15], and perhaps also encouraged by the discovery of high-temperature superconducting oxides (i.e. YBCO), which had similar crystal structure (perovskite type) to ferroelectrics [28] and enabled further miniaturisation. Since then various ferroelectric varactors, tunable filters and resonators, phase shifters, tunable matching networks and delay lines have been demonstrated with high performance in the past decades.

$SrTiO_3$ (STO) and $Ba_xSr_{1-x}TiO_3$ (BST) thin films are two of the most popular ferroelectrics for electric tuning applications. The paraelectric phase is often preferred for microwave tuning applications because of the absence of hysteresis and lower dielectric loss [29]. STO, which is an incipient ferroelectric, is in the paraelectric phase at the boiling temperature of liquid nitrogen. The structure and processing compatibility of STO and high-temperature superconductors (HTS) has enabled a variety of cryogenic microwave devices since the 1990s [30-40]. However, STO has little tunability at room temperature. Application of such devices is limited as they need to be cooled down to cryogenic temperature. $Ba_xSr_{1-x}TiO_3$, which has good tunability and reasonable loss at room temperature, can overcome this problem. The

Curie temperature T_c of $Ba_xSr_{1-x}TiO_3$ can be continuously shifted from about 40 K to 385 K by tailoring the Ba to Sr ratio in the composition (see Fig.2- 4). Examples of the published BST thin film varactors and tunable filters will be summarised in sections 2.7 and 2.8.

An overview of the main application areas of ferroelectrics and the underlying behaviour exploited is given in Fig.2- 5. The microwave dielectric properties of ferroelectric materials will be discussed in the next section with emphasis on BST thin films.

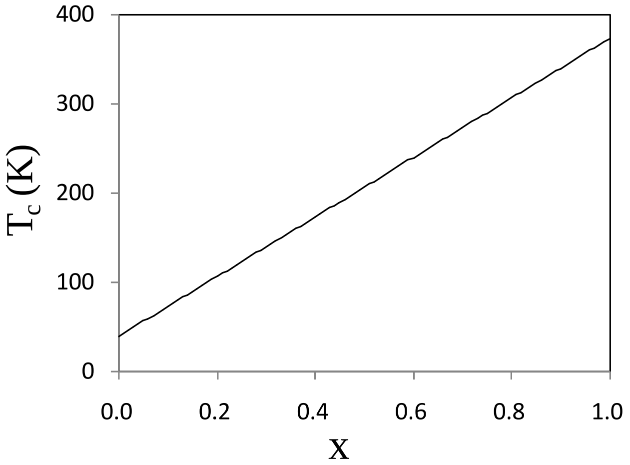

Fig.2- 4 Curie temperature (T_c) as a function of Ba concentration (x) for $Ba_xSr_{1-x}TiO_3$ [10]

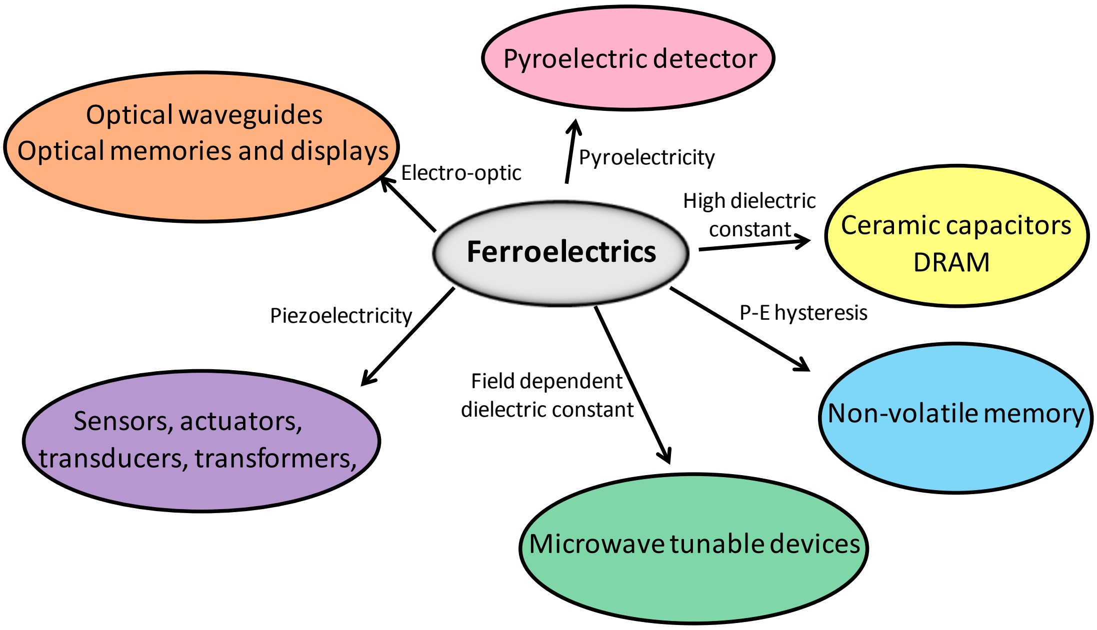

Fig.2- 5 Overview of major application areas for ferroelectric materials

2.2 Properties for microwave applications

The dielectric properties of ferroelectrics have been extensively studied since the 1950s [41]. Phenomenological models of the dielectric constant and loss tangent of ferroelectrics as functions of temperature, electric field and frequency were developed by Vendik [42]. These models have shown good agreement with experimental data and are valuable for understanding the dielectric properties of bulk ferroelectrics [27]. However, the dielectric properties of thin film ferroelectrics can differ from the single crystal of the same chemical composition in some substantial ways. Generally, the dielectric constant for thin films can be more than one order of magnitude lower and the loss tangent can be one order higher compared to the single crystal with the same composition [29]. An example of the temperature dependence of the permittivity of bulk and thin film BST is shown in Fig.2- 6 [43]. It should be noted that for the BST thin film the permittivity is substantially lower than the bulk and the sharp peak at the phase transition temperature is not observed. The size effect, or the presence of dead layers, the misfit strain and defects in thin films are considered as the sources of the deviation of properties from the bulk behaviour [29]. However, the theory of this deviation is not yet well understood.

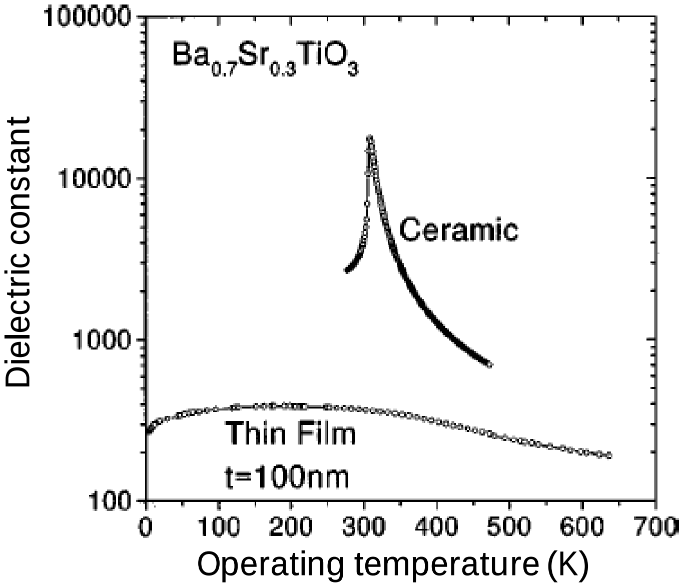

Fig.2- 6 Variation of the dielectric constant of a BST ceramic and thin film as a function of operating temperature (taken from [43])

The dielectric constant, tunability and loss performance of ferroelectric materials are the most important properties for microwave applications. It is clear that a high tunability and a low dielectric loss are favourable for high performance devices. The dielectric constant ε of ferroelectrics varies in response to an applied electric field, which is the basis of microwave applications. Tunability is a criterion to evaluate the electric field dependence of permittivity. There are two ways to define the tunability of a ferroelectric material, which are the tunability n defined as the ratio of the dielectric permittivity of the material at zero electric field to its permittivity under bias

$$n = \frac{\varepsilon(0)}{\varepsilon(E)} \tag{2.1}$$

and the relative tunability n_r defined as the relative change of the permittivity between zero bias and an electric field E with respect to its permittivity at zero bias

$$n_r = \frac{\varepsilon(0) - \varepsilon(E)}{\varepsilon(0)} = 1 - \frac{1}{n} \tag{2.2}$$

An example of a $Ba_{0.6}Sr_{0.4}TiO_3$ thin film interdigital capacitor made at Birmingham[1] is given in Fig.2- 7. The capacitance and relative tunability as a function of the applied electric field is shown in the figure. A relative tunability of 60 % (a tunability of 2.5) is achieved at 9 V/µm, measured at room temperature, 10 GHz. Recently Pervez [44] reported a BST thin film varactor in a parallel plate configuration with a tunability of 13.7 (90 %) at 400 V/µm, 100 MHz, which is the best tunability ever reported for BST varactors.

In the ferroelectric phase (or polar phase), the polarisation hysteresis results in hysteresis in the ε(V) curve, and the maximum ε may occur when the applied field $E = \pm E_c$ (the coercive field), not zero. This is called a butterfly shaped ε(V) curve in the ferroelectric phase [45] (see Fig.2- 8 (a)). The bi-valued capacitance at the same bias field in Fig.2- 7 indicates the material is in a ferroelectric phase. Clearly the paraelectric phase is preferred in microwave tunable applications as no hysteresis exhibited in the C(V) curve, whereas ferroelectrics in

---

[1] refers to the Emerging Device Technology Research Centre at the University of Birmingham

ferroelectric phase are primarily used in non-volatile FeRAMs.

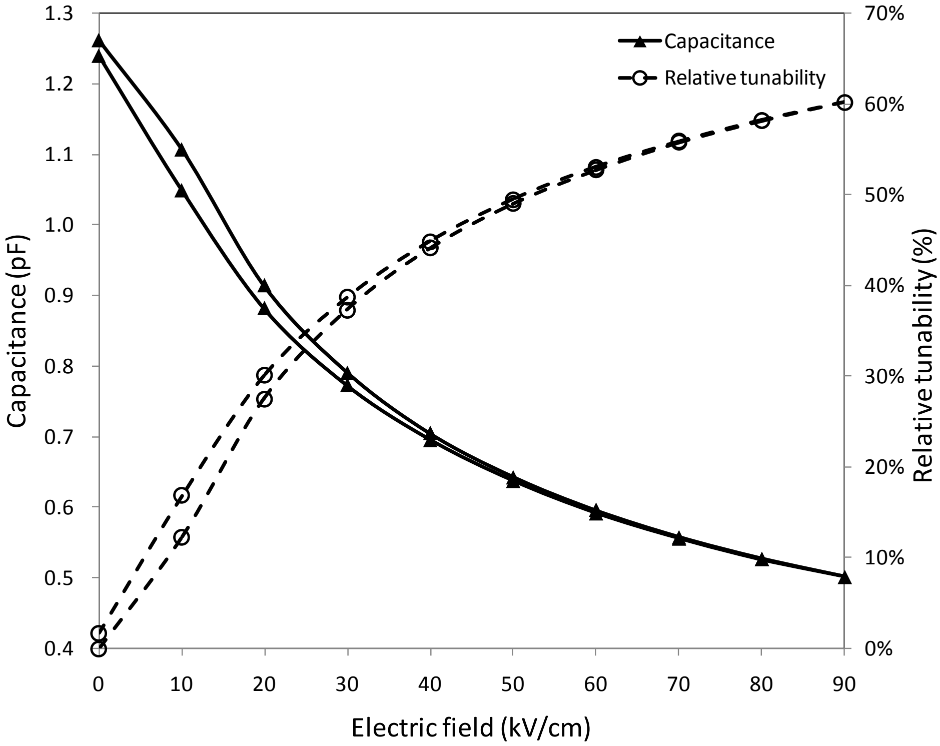

Fig.2- 7 Capacitance and relative tunability of a $Ba_{0.6}Sr_{0.4}TiO_3$ thin film interdigital capacitor (made at Birmingham) as a function of the applied electric field measured at room temperature and 10 GHz.

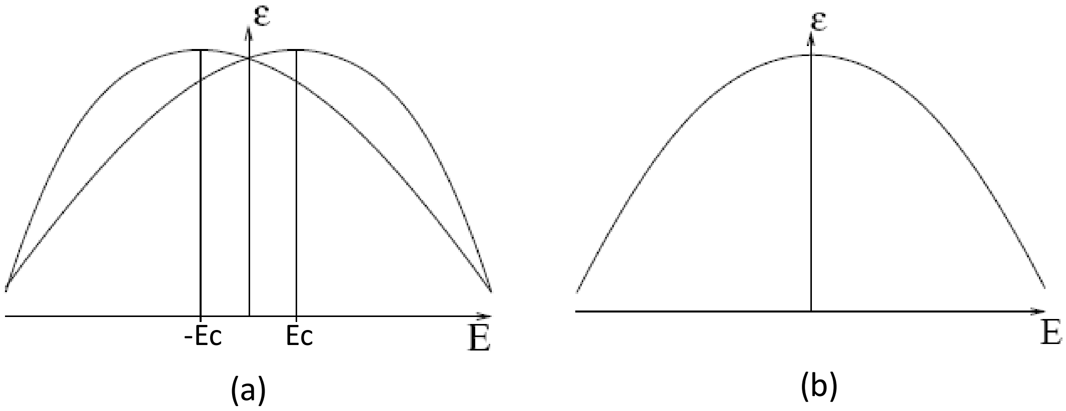

Fig.2- 8 Schematic curves of permittivity ε as a function of the electric field E in ferroelectric phase (a) and paraelectric phase (b) (taken from [9])

The permittivity ε of ferroelectric materials also changes with temperature as shown in Fig.2-

6. The temperature dependence of permittivity for temperature above the Curie temperature T_c can be modelled with the Curie-Weiss law [46]

$$\varepsilon(T) = \frac{C}{T - T_C} + \varepsilon_L \tag{2.3}$$

where C is the Curie constant, ε_L is about 30 and therefore negligible in most cases. It is obvious that the maximum ε occurs at around the Curie temperature T_c. Above this temperature, the permittivity decreases rapidly with the temperature increasing. The phase transition temperature T_{ph}, the Curie temperature T_c and maximum permittivity temperature T_m are not in principle the same and discussion of their relations can be found in [47].

The permittivity is actually complex, and can be written as

$$\varepsilon = \varepsilon' + i\varepsilon'' \tag{2.4}.$$

The loss tangent tanδ of a ferroelectric material can be written as

$$\tan\delta = \frac{\varepsilon''}{\varepsilon'} = \frac{1}{Q_{FE}} \tag{2.5}$$

where Q_{FE} is the quality factor of the material. The dielectric loss in ferroelectrics is also a crucial issue which should be taken into account in the device design. The measured or modelled dependence of loss tangent on electric field, temperature and composition has been reviewed in [41], [27], [48]. The sources of the ferroelectric loss are either intrinsic, associated with the interaction of the microwave field with the phonons, or extrinsic, due to the interaction between the microwave field and the defects [29]. The extrinsic loss often dominates the loss of ferroelectric thin films in practical conditions [45]. The reported measured loss tangent of room temperature BST thin films is in the range of 0.02 - 0.2 at microwave frequencies and usually decreases with electric field [49-53]. This is consistent with the theoretical predictions as most loss mechanisms suggest the loss tangent to be proportional to the permittivity, although not linearly proportional [29].

The frequency dependence of tanδ, differs from that of the permittivity, which is usually independent with frequency. The loss tangent is often found to be directly proportional to the frequency in the microwave region. This is because the charged defects under an ac electric field will convert part of the electromagnetic energy into acoustic energy [48]. However, the exact relation between tanδ and frequency is not yet well established. Some reports claim tanδ $\sim \omega^{1/3}$ [45], [54] and other reports a linear [55] or $\omega^{1/2}$ [56] dependence.

Generally, a high tunability is often accompanied by a high dielectric loss for many dielectrics [29]. This indicates that a design trade off between tunability and loss tangent of ferroelectric thin films is often required for microwave applications. A commutation quality factor (CQF or K) is defined to characterise the tuning and loss performance of ferroelectric material. It is convenient from a microwave engineering point of view and is indicative for choosing material with the optimal tradeoff between tunability and loss tangent. K is defined as follows

$$K = \frac{(n-1)^2}{n \tan\delta(U_1) \tan\delta(U_2)} \tag{2.6}$$

where U_1 and U_2 are the applied bias voltages in two states and n is the tunability. K is thus a function of the bias voltage.

The (Ba+Sr)/Ti ratio in BST should be as close to 1 as possible for optimal electrical properties at room temperature [57]. It is also found that, at room temperature, for Ba concentration from 0 % to 50 %, the tunability, loss tangent and CQF increases with the increasing of Ba content according to a model calculation [48]. $Ba_{0.5}Sr_{0.5}TiO_3$ has the maximum tunability and CQF, as well as the maximum loss tangent at room temperature. However, it should be noted that real films may exhibit quite different properties as a result of strains and defects.

The dependence of dielectric constant on film thickness is observed by many groups [58-60]. The measured dielectric constant decreases significantly with the thickness as shown in Fig.2- 9 (a) [58]. The decrease in dielectric constant can be effectively modelled by assuming the presence of a “dead layer” at the electrode/ferroelectric interface. The dead layer is considered as a thin dielectric layer with severely depressed dielectric constant and tunability. The dead layer is modelled as in series with the bulk like ferroelectrics as shown in Fig.2- 9 (b) so the decrease in dielectric constant follows the “series capacitor model” [59]. It is also observed from Fig.2- 9 (a) that the dielectric constant becomes less dependent on thickness at higher electric field [58].

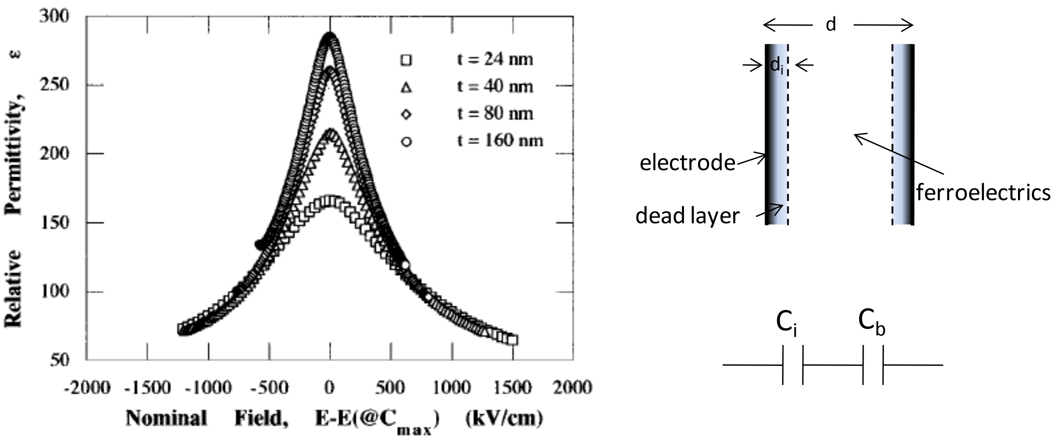

(a) (b)

Fig.2- 9 Thickness dependence of the relative permittivity versus nominal electric field (a) (taken from [58]) and modelling of the dead layer in a ferroelectric varactor (b). Nominal dc field is calculated using the maximal capacitance voltage as an offset (not zero bias).

In the series capacitor model, the effective capacitance of a ferroelectric varactor C_{eff} is given by

$$\frac{1}{C_{eff}} = \frac{1}{C_b} + \frac{1}{C_i} \tag{2.7}$$

where the subscripts i and b refer to the interface dead layer and the bulk like ferroelectrics parameters respectively. If the dead layer thickness d_i is independent of the total thickness d, then

$$\frac{d}{\varepsilon_{eff}} = \frac{d_b}{\varepsilon_b} + \frac{d_i}{\varepsilon_i} = \frac{d}{\varepsilon_b} + d_i\left(\frac{1}{\varepsilon_i} - \frac{1}{\varepsilon_b}\right) \tag{2.8}$$

where ε_{eff} is the effective dielectric constant, $d = d_b + d_i$, $\varepsilon_b \gg \varepsilon_i$. The term d/ε_{eff} is a linear function of d with gradient of $1/\varepsilon_b$ and y-axis intercept of d_i/ε_i [59]. This model is valid as long as the film is thicker than the presumed dead layer. As the film thickness increases the effect of the dead layer is smaller.

One problem that impedes the microwave applications of ferroelectrics is the temperature dependence of the dielectric constant. The dependence is especially strong for temperatures close to the phase transition temperature. One possible solution for this problem is incorporating a temperature stabilisation bias network [15]. The bias network consists of a voltage divider (a fixed capacitor in series with temperature sensitive capacitor usually using similar ferroelectrics) and a DC decoupling network. The capacitance changing with temperature can be compensated by the changing of the distributed voltage. However, this temperature stabilisation is obtained at the cost of requiring a higher tuning voltage.

Lifetime and reliability are also crucial issues in practical applications of ferroelectric devices. The most important failure mechanism is resistance degradation, which is characterised by a steady but pronounced increase of leakage current under a constant DC bias after a specific time. Detailed analysis and models of resistance degradation and other reliability issues can be found in [61].

In summary, the quality and dielectric property of BST thin films are complex functions of electric field, temperature, frequency, composition and film thickness. In addition, they also depend on the processing, e.g. deposition method, growth conditions, defect density, substrate and metallisation choices. A good understanding of these relationships is essential prior to the microwave applications of ferroelectrics becoming commercial.

2.3 BST deposition methods

There are various ways to grow BST films and each one has its merits and drawbacks. The method of choice is usually determined by the application, system requirement and cost. Generally, the deposition methods can be divided into three main categories, which are (i) physical vapor deposition (PVD) including electron beam evaporation, magnetron sputtering and pulsed laser deposition (PLD); (ii) chemical vapor deposition (CVD) including metallic organic CVD (MOCVD) and atomic layer deposition (ALD); (iii) chemical solution deposition (CSD) like sol-gel. The most popular deposition methods for BST thin films such as sol-gel, MOCVD, magnetron sputtering and PLD will be discussed as follows.

The Sol-gel process offers the advantages of low cost, good composition control and it does not require vacuum infrastructure. The precursor solution with the right concentration of cations should be prepared and deposited on the substrate by spin-coating, and this is repeated to reach the desired thickness. Then a low temperature heat treatment (300 - 400 °C) is performed to dehydrate the organic species and form an amorphous film. Finally, high temperature heat treatment (600 - 1100 °C) for densification and crystallization of the film is performed. The Sol-gel process has been investigated for preparation of high quality ferroelectric materials by many research groups [62-65]. A phase shifter made with a sol-gel BST thin film deposited on LAO is demonstrated in [66]. It has a 40.9 °/ dB figure of merit at 14.2 GHz, which is comparable to the BST thin film phase shifter of the same design grown using the PLD process.

Metal organic chemical vapor deposition (MOCVD) is a technique to grow epitaxial films on a substrate surface based on chemical reaction of metal organic gaseous precursors at high temperature. MOCVD offers the potential for large scale deposition, good composition control, highly uniform and highly conformal films on planar and high aspect ratio substrates [67], [68]. However, MOCVD process is limited by the availability of suitable precursors and process control difficulties [69]. A parallel plate capacitor with 71 % tuning at 9 V (which is 30 V/µm electric field) was reported using a $Ba_{0.7}Sr_{0.3}TiO_3$ film deposited by MOCVD technique [70]. The loss tangent of the film was in the range of 0.003 - 0.009 up to 500 MHz.

Magnetron sputtering is a versatile technique which can deposit conductive and insulating thin films onto metal or ceramic substrates. It is a vacuum process which physically removes portions of target material and deposits a thin layer onto the substrate surface. Sputtering can be either DC or RF depending on the nature of the target. DC power is used when the target is conducting, while RF can be used for both conducting and insulating targets. The principle of DC sputtering is shown in Fig.2- 10. The chamber is filled with argon gas at low pressure. When the target is connected to a negative high voltage, a glowing plasma forms just above the target surface, the plasma consists of electrons and positive argon ions in a high energy state. The ions are accelerated towards the negatively charged target and strike it. This causes the atoms of the target material to be ejected, and some of the atoms land on and bond with the substrate which is mounted in front of the target, building a thin film. The word “magnetron” refers to placing of a magnet behind the target, resulting a very high density of ions, which in turn increases the sputtering rate. At Birmingham, metal films of several hundred nanometres thick were deposited using the DC and RF magnetron sputtering system shown in Fig.2- 11.

Oxide materials such as BST can be only successfully grown by sputtering when the reactive sputtering technique is used. In reactive sputtering, a gas (e.g. O_2) is added to the argon introduced into the sputtering system. The quality and properties of BST thin films deposited by reactive sputtering depends on the substrate temperature, power and composition of target, pressure, ratio of partial pressure of Ar and O_2 [69].

The pulsed laser deposition (PLD) technique has been widely used to grow high quality ferroelectric films for microwave application. As shown in Fig.2- 12, a high power pulsed laser beam is focused on a spot of the target surface to strike the target. The high energy density vaporises the target material and a plume of material is transported towards and deposited on the heated substrate facing the target. This process can occur in vacuum or in the presence of a reactive background gas, such as oxygen, which is commonly used in oxide deposition to fully oxygenate the deposited films, as in reactive sputtering. The background gas pressure, the substrate to target distance, laser energy and frequency, and substrate temperature have important effects on the BST thin film composition, microstructure and properties. To produce high quality BST thin films for microwave applications, intensive research effort has been made to clarify the correlation between the deposition conditions and film properties, and to optimise the growth conditions [71-73]. Compared with vacuum evaporation and sputtering, PLD has a higher maximum deposition rate although slowing down of the deposition rate from the maximum is often required to obtain high quality films. The deposition temperature is relatively low as a result of high ionic content in laser plumes and high particle velocity [71]. PLD is appropriate for deposition of complex oxide materials as a result of stoichiometric transfer of the complex materials to thin films [74]. The PLD process is also best suited to deposition on small (1 cm^2) substrate. Deposition over large areas is possible but technically challenging. So for commercial processes or larger area devices the previously discussed deposition processes are more suitable. One major drawback PLD process suffers is the formation of droplet or particulate production due to the melting or fracture of the target surface. This problem may be tackled by a careful control of the laser energy just above the ablation threshold [71]. All the BST thin films used in this work were deposited by PLD process. A photo of the PLD system at Birmingham is shown in Fig.2- 13.

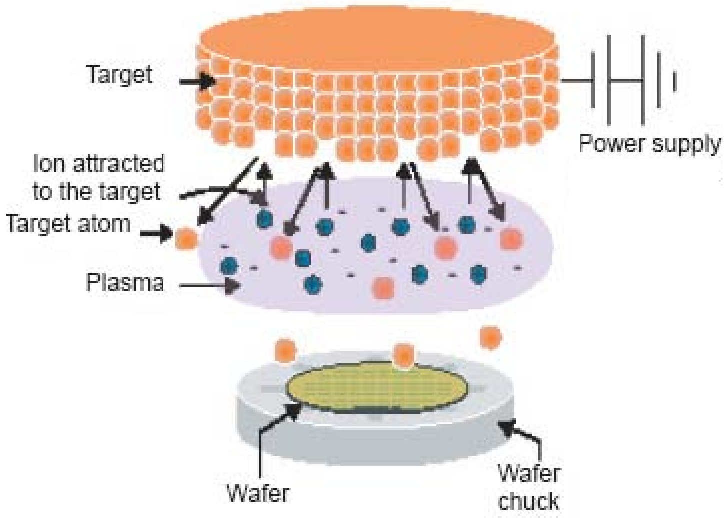

Fig.2- 10 Principle of DC magnetron sputtering (taken from [75])

Fig.2- 11 DC and RF magnetron sputtering equipment at Birmingham

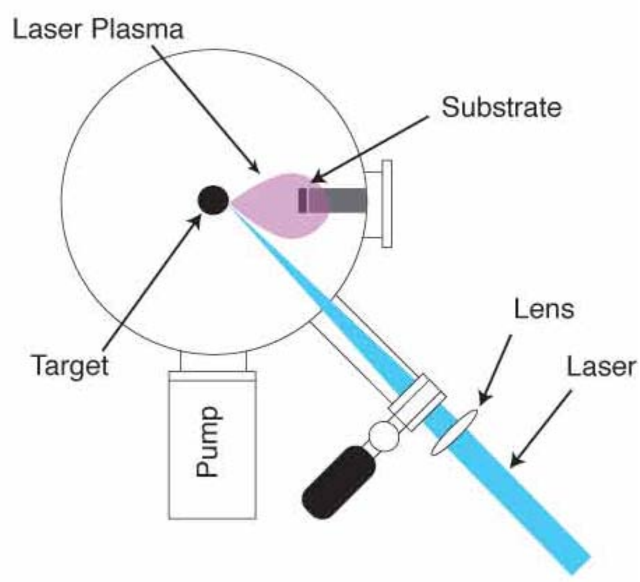

Fig.2- 12 Schematic of PLD deposition chamber (taken from [76])

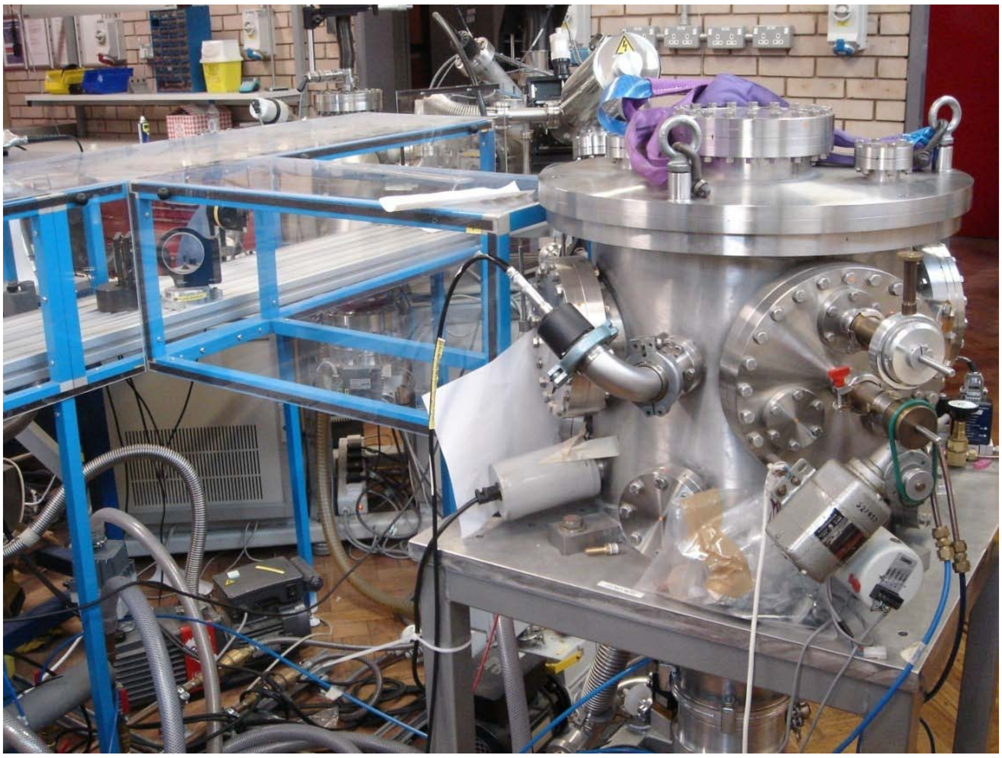

Fig.2- 13 Pulsed laser deposition chamber at Birmingham

2.4 Microwave characterisation techniques of ferroelectric thin films

The properties (real and imaginary parts of permittivity and tunability) of ferroelectric thin films at microwave frequencies can be extracted by several methods, characterised as varactor methods, transmission line methods and resonance methods. At microwave frequencies, usually the devices cannot be modelled as lumped elements due to the presence of various parasitic effects, hence distributed models are often required. A good calibration prior to the measurement is also essential for accurate extraction of the dielectric properties of ferroelectric thin films.

In the resonance method, where a transmission line resonator is patterned on the BST thin film [77] or interrupted by a BST gap capacitor [78], the permittivity and loss tangent of the BST thin film are calculated from the measured resonant frequency and unloaded quality factor. This method can give a precise extraction of the loss tangent especially for low loss material [48]. However, the resonance method can only give information at one frequency point and the frequency dependent dielectric properties of the BST thin film are not available.

Parallel plate or planar varactors are commonly used structures to characterise the dielectric properties of BST thin film as functions of frequency and electric field. One port reflection data or two port S-parameters are often measured using a vector network analyser. The extraction of dielectric properties of BST film is complicated at microwave frequencies because the loss from electrodes and lead strips is also important and parasitic inductance and capacitance will affect the apparent capacitance. The parasitic and peripheral circuit effect can be removed either by additional structures [79], [80] or by evaluation of electric models [49], [81], [82].

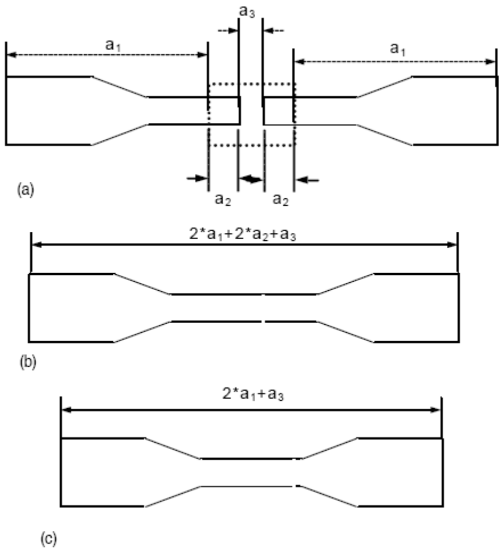

Fig.2- 14 capacitor (a), through line 1 (b), and through line 2 (c) (taken from [79])

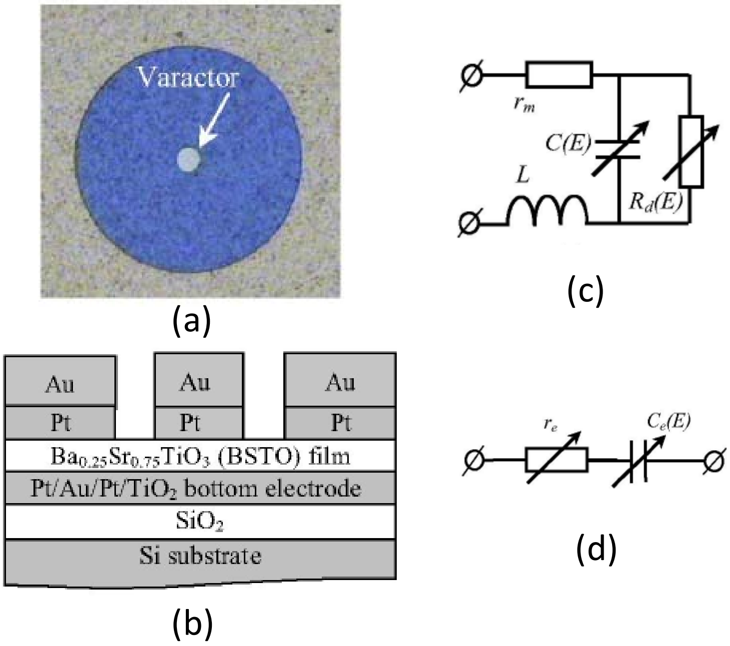

Fig.2- 15 Top view (a), cross sectional view (b), physics based equivalent circuit (c) and its representation circuit (d) of a circular parallel plate varactor (taken from [81])

For a parallel plate capacitor, an electrode size as small as several microns is often required as a result of the high dielectric constant of ferroelectrics and small film thickness. Otherwise, a large capacitance will lead to an equivalent short circuit at microwave frequency. A simple two port measurement technique has been reported in reference [79]. The BST parallel plate capacitor was embedded in a transmission line and two “through lines” were used to de-embed the effect of the transmission line as shown in Fig.2- 14. The capacitance and loss tangent were extracted from the measured responses for up to 12 GHz. The extracted capacitance showed little dispersion with frequency and a tunability of 2.4 was achieved at 15 V. The extracted loss tangent was less than 0.012 up to 10 GHz.

For a relatively simple structure, circuit modelling methods can be used to remove the parasitic inductance and series resistance in the test structure. An example of using a circuit model to characterise the BST thin film in a circular parallel plate capacitor was given by Vorobiev [81]. The capacitor had a simple layout as shown in Fig.2- 15 (a) and (b) and its circuit model and simplified model were shown in Fig.2- 15 (c) and (d). The test structure offered minimised losses and parasitic inductance from the electrodes which helped to determine the loss from BST thin film. The large capacitance between the outer circular top plate and the bottom plate was equivalent to a short circuit in the microwave region and allowed a DC bias to be applied. The parasitic inductance and negative calibration inductance was removed. The extracted capacitance showed little dispersion up to 25 GHz. The loss of the BST thin film was separated from the electrode loss and the BST loss tangent was reported to be around 0.02 up to 25 GHz.

The extraction of dielectric properties in the microwave region using interdigital capacitor (IDC) structures is more difficult because of the presence of various parasitic effects. Conformal mapping based models are often used to extract the permittivity [83]. Knowledge of the geometry of interdigital fingers, the thickness of the BST thin film and substrate, and the permittivity of the substrate is required to calculate the dielectric constant of BST film. The permittivity can also be determined by comparing the experimental results with a set of full wave electromagnetic simulation results [84].

Transmission line structures, particularly the coplanar waveguide (CPW), can be also used to determine the properties of BST thin film. The impedance of the transmission line should be close to 50 Ω to reduce the signal reflection. The transmission line can be modelled using full wave simulation, or, it can be analysed using an equivalent circuit model [77]. The propagation constant γ ($\gamma = \alpha + i\beta$ where α is the attenuation constant and β is the phase constant) and the line impedance Z_0 are determined from the ABCD-parameters calculated from the measured S-parameters. The permittivity of BST thin film is calculated from the effective permittivity using the conformal mapping method.

It should be noted that the characterisation methods discussed above are not complete but emphasis is placed on BST thin films in the microwave region. Examples of simple characterisation methods based on BST parallel plate capacitors are given. More detailed discussions and comparisons of different extraction methods can be found in [29], [41], [48], [77].

2.5 Substrate choice

BST thin films have been deposited on oxide single crystal substrate such as sapphire (Al_2O_3) [85-87], magnesium oxide (MgO) [88], lanthanum aluminate ($LaAlO_3$) [89] and strontium titanate ($SrTiO_3$) [90], as well as silicon wafers [51], [91] and metallised substrates [70], [92]. The dielectric properties and crystal structure of BST films may change greatly when grown on different substrates due to different internal stress and interface conditions. The dielectric constant, loss tangent, coefficient of thermal expansion (CTE) and lattice parameter are the most important parameters defining the substrate properties. These parameters, together with the cost, size and availability should be judiciously considered to choose the substrate material. Substrates with dielectric constant of low temperature dependence and low loss tangent are favourable for fabrication of high performance microwave devices. Single crystal substrates with a lattice parameter matched to that of the BST film, enable epitaxial growth and high quality films [48]. The CTE of the substrate should be as close to the film's CTE as possible [69]. The BST thin film is typically deposited at a temperature of several hundred degrees centigrade [51], [84], [93]. During the cooling or annealing process, a large difference between CTE of substrate and BST film will cause compressive or tensile strain at the film/substrate interface and result in roughening or cracking of the BST film [48], [69]. However, single crystal substrates are expensive and not available in large scale, which impedes development into the commercial markets.

High resistivity silicon (> 5000 Ω·cm) is a promising alternative substrate which overcomes the loss problems of conventional silicon at microwave and millimetre wave range. The integration of BST thin films with silicon substrates provides the possibility to integrate with the popular monolithic microwave integrated circuits (MMICs) and hence reduces the cost from a manufacturing point of view. However, the high resistivity may be degraded due to the high temperature required for BST deposition. The surface charge accumulation at the Si/SiO_2 interface can form a thin conductive layer which also reduces the effective resistivity of the substrate. One possible solution is micromachining or etching away the substrate beneath the transmission line. Alternatively, surface passivation methods can be used to minimise the substrate loss [94], [95]. Several groups have demonstrated BST varactors on silicon substrates successfully [45], [51], [70], [91].

BST thin films deposited on metallised substrates will be discussed in the following section.

2.6 Metallisation choice

The choice of metallisation should be carefully considered during the design of ferroelectric devices. The device performance strongly depends on the quality of the electrode, not only for reducing the ohmic loss, but also for initiating high quality BST thin films for devices in the parallel plate configuration.

At microwave/millimetre frequencies, the metal loss from the electrodes often contributes significantly to the total loss. This is because at high frequency, the electric current is confined within a ‘skin’ at the surface of a conductor. The decrease in current density versus depth is known as the skin effect. The skin depth is a measure of the distance over which the current falls to 1/e of its original value beneath the surface of a semi-infinite planar conductor. The skin depth is defined as [96]

$$\delta = \frac{1}{\sqrt{\pi f \mu \sigma}} \tag{2.9}$$

where μ is the permeability and σ is the conductivity of the metal, and f is the frequency of interest. The conductivity and skin depth at 20 GHz of several common metal materials are listed in Table 2- 1. It is clear that metals with a high conductivity will have a small skin depth. Fig.2- 16 shows the skin depth of these metals in the microwave frequency range. The skin depth falls with increasing frequency, indicating a greater current concentration near the surface at higher frequency and potentially higher loss from the metal. The current density J in an infinitely thick, semi-infinite planar conductor decreases exponentially with the depth (d) from the surface, as follows

$$J = J_0 e^{(-d/\delta)} \tag{2.10}$$

where δ is the skin depth and J_0 is the current density at the surface. At a depth $d = 3\delta$ the current is $1/e^3$ (about 0.05) times the current at the surface, which means 95 % of current flows through the top three skin depths of the metal. This is why a metal thickness of three times the skin depth at operating frequency is often used to avoid aggravating the current crowding. It can be seen from Table 2- 1 that at 20 GHz, three times the skin depth means a thickness of 1.4 µm for silver, 3.5 µm for platinum and 8.1 µm for titanium.

It is clear that a thick metal layer with a high conductivity is desired to reduce metal loss. However, in the microfabrication, a metal layer of several microns thickness might be difficult to pattern because of the high aspect ratio of narrow, closely spaced stripes. The cost, availability and ease of patterning issues should be considered for metallisation choice. Platinum, gold and silver are the most commonly used electrodes in thin film oxides based devices because they are in most cases non-reactive in contact with oxides and their large work functions provide Schottky contacts hence have small leakage [67], [92]. BST devices with copper metallisation have also been successfully demonstrated [97], [98].

For devices based on ferroelectric parallel plate capacitors, deposition of the BST film onto a metallised substrate is required and this is more challenging. The choice of bottom metallisation must meet two requirements; one is to enable growth of high quality BST films while the other is having a high conductivity at microwave frequencies. However, it is difficult to find a material which fulfils these two criteria. High conductivity metals which provide good microwave loss performance usually can’t support BST films of high quality. Electrodes such as platinum and strontium ruthenate ($SrRuO_3$) which are compatible with BST films have a poor conductivity [99]. In addition, the bottom electrodes have to endure a high temperature (typically above 650 °C) and oxidizing atmosphere during the BST deposition, and remain stable, smooth and adherent to the substrate [100].

Material	**Conductivity (S/m) at 20°C**	**Skin depth (μm) at 20 GHz**
Silver	6.173×10^{7}	0.453
Gold	4.098×10^{7}	0.556
Platnium	0.952×10^{7}	1.153
Aluminum	3.816×10^{7}	0.576
Chromium	3.846×10^{7}	0.574
Copper	5.813×10^{7}	0.467
Nickel	1.449×10^{7}	0.935
Titanium	0.175×10^{7}	2.690

Table 2- 1 The conductivity and skin depth at 20 GHz of several common metals [101]

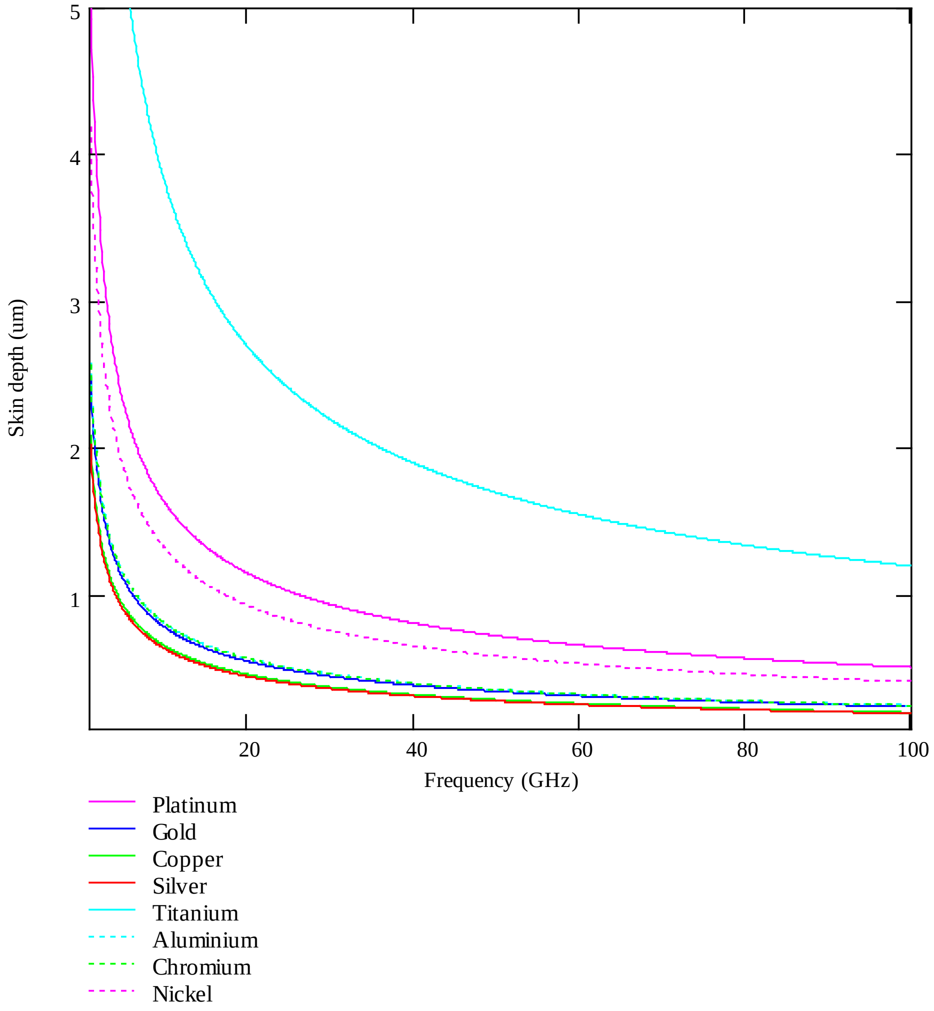

Fig.2- 16 Skin depth of several common metals versus frequency

Pt [70], [102], Ir [103], Ru [103], Cu [97], Au [92] and $SrRuO_3$ [104] are the electrodes that have been tried as bottom electrode of BST devices. Pt is the most popular bottom electrode material because of its stability against oxidisation and relatively high conductivity compared with oxide electrodes [48]. Pt also has a lattice parameter (a = 0.3924 nm) close to that of BST with 25 % Ba concentration and initiates quasi-epitaxial growth of BST film [9]. In addition, the high work function of Pt (5.65 eV) results in a low leakage current [80]. However, careful treatment is required during the deposition, annealing and cooling process. The difference in CTE between Pt and the substrate can cause strain at the electrode/substrate interface and roughen the electrode. A slow cooling procedure can help to resolve this problem [48]. Another problem is that the step near the edge of the patterned bottom electrode may cause a short circuit in the parallel plate structure [48]. Thicker BST films or a ramp at the electrode edge can help to prevent such problems. In addition, beneath the Pt layer, a thin adhesion layer such as Ti, TiO_2, Cr, SiO_2 and IrO_2 is often used to enhance adhesion to substrate. In the case of devices on silicon substrate, a thin SiO_2 layer is often used as a barrier against oxygen diffusion.

The thickness of the Pt bottom electrode is usually in the range of 50 - 200 nm which is much smaller than its skin depth in gigahertz range. This inevitably leads to high current concentration in the electrode and inferior the total loss performance of the device. One possible solution is to deposit a thicker gold layer between two platinum layers as both larger thickness and better conductivity result in lower loss [51].

2.7 Ferroelectric varactors

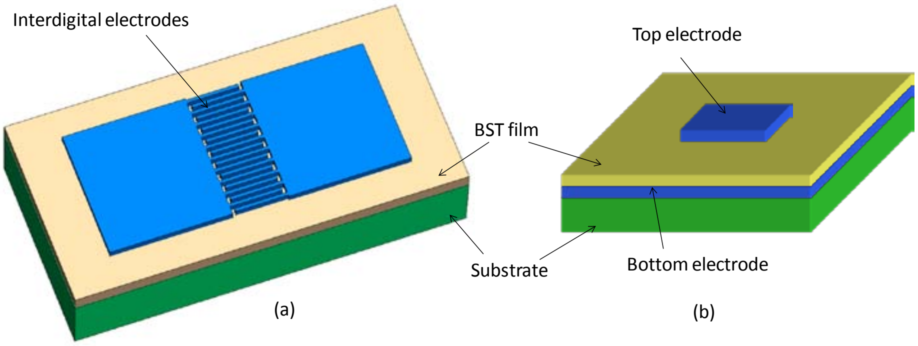

Fig.2- 17 Schematics of a BST interdigital (a) and parallel plate (b) capacitor

Ferroelectric varactors are the core elements of ferroelectric tunable filters, phase shifters and tunable matching networks. Interdigital and parallel plate are two common configurations of ferroelectric varactors, both utilizing the property that the dielectric constant of the BST thin film can be altered by applying a DC voltage, thus tuning the capacitance. The schematic layouts of the two types of varactors are shown in Fig.2- 17.

Interdigital capacitors (IDCs) have a simple fabrication process because only single step photolithography is required. The BST thin film is deposited directly on the substrate and the top metal layer is then defined on the film surface. A capacitance range of 0.1 - 10 pF can be obtained by simply changing the number of fingers, the length of fingers and the gap between the fingers. However, IDCs typically require a bias voltage as high as 40 - 400 V depending of the space between the fingers. The tunability of interdigital capacitor is usually smaller than that in the parallel plate configuration for a given bias voltage because part of the electric field is in air thus is not effectively tuned and the electrodes of IDC are at least a factor of 10 further apart than that of the parallel plate capacitor. In addition, it is difficult to extract the material properties directly and empirical formula and full wave electromagnetic simulation are often required.

Although the IDC is popular due to its relatively simple fabrication, the high bias voltage requirement impedes the application of IDC in all but specific systems. In practical applications, the parallel plate capacitor is more attractive because it is compact and requires a low bias voltage. BST parallel plate capacitors have a very high energy density as a result of the high dielectric constant of the BST thin film. A capacitance of 1 pF can be comprised of an parallel plate area of 25 - 100 μm^2 corresponding to a capacitance density of 40 -10 $fF/\mu m^2$. The tuning voltage for a parallel plate capacitor is usually below 30 V, which is much smaller than that of interdigital ones. For example, a bandpass filter using BST parallel plate capacitors shows 57 % tuning of the centre frequency with the application of 6 V bias [100]. The low bias voltage not only eliminates the need for a DC transformer but also provides possibility to integrate with semiconductor technologies. However, the processing of BST parallel plate capacitors is more complicated. In the parallel plate configuration, the BST thin film is typically grown on metallised substrate with adhesion layers. One key problem in the multilayer structure is the difference in thermal expansion coefficient and lattice parameter of different layer, as discussed in previous section. This difference can lead to substantial misfit strain on the BST/electrode or electrode/substrate interface and can roughen or cause hillocks in the BST film or electrodes [48]. In addition, two or more steps of photolithography are required to define the top and bottom electrodes and micron-level lithography is often required for capacitances less than 1 pF. These fabrication issues make the production of high Q varactor challenging.

Despite the fabrication difficulties, BST IDC with a Q of 30 at 20 GHz [67] and BST parallel plate capacitor with a Q of 50 at 40 GHz [51] have been reported. These values are comparable or better than semiconductor analogs at the same frequency range. Tunability and Q are often tradeoffs in BST varactor design. The optimal tradeoff between the tunability and Q can be characterised by the commutation quality factor defined in equation (2.6) [27].

RF power handling capability, which is the ability to transmit high microwave power levels without unacceptable degradation of signals due to intermodulation distortion, is another important feature of tunable devices. The amount of intermodulation distortion (IMD) is related to the DC bias voltage required as follows [99]

$$\mathrm{IMD} \propto \frac{V_{RF}}{V_{DC}} \tag{2.11}$$

where V_{RF} is the amplitude of the RF signal and V_{DC} is bias voltage required for tuning. High power handling capability can be achieved at a cost of higher tuning voltage. For example, interdigital capacitors typically have higher power handling capability and better linearity than parallel plate capacitors [67]. Optimal tradeoff between power handling and DC bias required (or tunability) can be made by simply adjusting the gap between fingers in the interdigital configuration. A ferroelectric gap capacitor with improved IMD and simultaneous high tunability at low bias voltage was presented in [52]. Separate high resistance DC bias electrodes were fabricated in the gap to enhance the DC electric field. The IMD performance of the gap capacitor with this bias structure was improved by 6 dB over a conventional structure with the same tunability.

The substrate material, BST composition and deposition method, electric field, tunability, Q and CQF of several published BST capacitors in both interdigital and parallel plate configuration are summarised in Table 2- 2. The BST capacitor made in this work (discussed in appendix A) is also included in Table 2- 2, having a CQF of 235 at 2 GHz, which is comparable to or better than other published results. It should be noted that the CQF of a ferroelectric varactor depends on both the electric field and operating frequency. A higher electric field leads to higher tunability thus higher CQF. Q will be considerably degraded in the high gigahertz region and so will the CQF.

Reference	Capacitor configuration /Substrate	Ba/Sr ratio /Deposition method	Bias(V)/ Electric field(V/μm)	Capacitance (pF)	Permittivity	Relative tunability	Q	CQF
Kirchoefer et al. 1998 [53]	interdigital /LaAlO3	50:50 PLD	0~40 0~8	3.4~1.0	2700~700	70.6%	13~17	**374.4**
							at 2 GHz	
Nash et al. 2005 [105]	interdigital /Sapphire	25:75 magnetron sputtering	0~35 0~7	0.63~0.55	NA	21%	100~250	**461.8**
							at 1 MHz	
Ouaddari et al. 2005 [49]	interdigital /Alumina	50:50 PLD	0~35 0~4.4	NA	620~520	15%	14.3	**5.4**
							at 6 GHz	
Kenney et al. 2006 [106]	interdigital /Sapphire	57:43 CCVD[2]	0~80 0~40	NA	NA	61%	74~27	**1906**
							at 2.4 GHz	
Vendik et al. 2003 [107]	Microstrip gap/Alumina	NA	0~150 0~15	0.35~0.19	NA	45.7%	22.7~58.8	**514.7**
							at 4 GHz	
Marsan et al. 2005 [102]	Parallel plate /Alumina	50:50 PLD	0~19 0~34	2.9~0.9	NA	71%	14~13	**309**
							at 1 GHz	
Tombak et al. 2002 [70]	Parallel plate /Silicon	70:30 MOCVD	0~9 0~130	65.0~19.2	200~60	71%	20	**677.6**
							at 300 MHz	
Vorobiev et al. 2003 [51]	Parallel plate /HR silicon	25:75 PLD	0~25 0~83.3	2.2~1.4	150~75	40%	180~240	**8977**
							at 1MHZ	
this work	Parallel plate /HR silicon	25:75 PLD	0~13 0~32.5	1.63~1.14	738~514	30%	45.5~40.0	**235**
							at 2GHz	

Table 2- 2 A comparison between several published BST varactors and the BST varactor made in this work.

---

[2] CCVD stands for combustion chemical vapor-phase deposition.

2.8 Ferroelectric tunable filters

Various ferroelectric thin film (BST or STO) tunable filters have been reported by several research groups and companies. These filters can be classified as many different types: they are based on a lumped element or distributed line approach or a combination; they are implemented in a coplanar waveguide or a microstrip configuration; they have single or multi metal layer structure; and they use ferroelectric varactors in integrated or discrete form.

For a tunable filter, the tuning range, bandwidth and filter insertion loss are the important parameters describing the filter performance. These parameters can be characterised as the figure of merit (FoM) and different tunable filters can be compared in terms of FoM. The FoM of a tunable filter is defined as [108]

$$F = \frac{\omega_2 - \omega_1}{\sqrt{\Delta\omega_1 \Delta\omega_2}} \frac{1}{\sqrt{IL_1 IL_2}} \quad dB^{-1} \tag{2.12}$$

where ω_1, ω_2 are the centre frequency of two states, $\Delta\omega_1$, $\Delta\omega_2$ are the bandwidth and IL_1, IL_2 are the insertion loss at the pass band in two states. The FoM of some reported BST filters will be given in Table 2- 3 and the FoM of our BST filters will be given in chapter 6. The maximum available FoM of a tunable filter based on ferroelectric varactors is related to the filter order N and the commutation quality factor K of the ferroelectric capacitor and is determined as [109]

$$F = \frac{1}{8.68N} \sqrt{K} \quad dB^{-1} \tag{2.13}$$

The FoM is electric field dependent. At higher electric field, the tunability is larger and so is the FoM. FoM is also frequency dependent. At higher frequency, the loss from both BST and metal is increased and leads to a lower FoM. When comparing FoM of different filters, the operating frequency and electric field must be taken into account.

Keis [110] reported a 20 GHz tunable filter using a BST thick film (5 mm thick) gap capacitors on a MgO substrate. The filter was based on a symmetrical fin-line topology in a rectangular waveguide. The width and length of the capacitor gap was 0.05 mm and 0.5 mm respectively, which gave a capacitance of 0.4 pF at zero bias, tuned to 0.15 pF with 400 V bias (which is 8 V/µm electric field), at 20 GHz. The centre frequency could be tuned 1.8 GHz (which is 9 %) from 20 GHz with a 3.5 % 3dB fractional bandwidth. The filter had an insertion loss better than 3.5 dB and reflection loss better than 20 dB in the tuning range. This was one of the first reported BST thick film tunable filters at room temperature.

Pleskachev [109] reported tunable microstrip filters using ferroelectric thin film capacitors. The filters were based on short circuit or open circuit resonators with BST or STO thin films on an alumina substrate. The ferroelectric capacitors were formed by 10 µm wide gaps in the microstrip lines. 4 µm thick copper metallisation was used. The 3-pole bandpass filter based on a short circuit resonator and BST gap capacitors was measured at room temperature. The centre frequency tuned from 4.4 GHz to 4.7 GHz at 150 V (which is 15 V/µm electric field), with a 15 - 8 dB insertion loss at passband. The figure of merit of the measured filter was 0.34 dB^{-1}. The 2-pole bandpass filter based on open circuit resonator and STO film was measured at 77 K. The figure of merit was 0.17 dB^{-1}.

Tan [38] reported a planar tunable HTS filter with a patterned $Ba_{0.1}Sr_{0.9}TiO_3$ thin film on a $LaAlO_3$ substrate. The YBCO thin film was first patterned to form a negative image for BST thin film deposition. After the BST film deposition, the remaining YBCO and unwanted BST film were removed, leaving the BST thin film with desired pattern. A YBCO conducting layer was then deposited and patterned using conventional photolithography and wet etching. The 3-pole microstrip filter was comprised of open loop resonators with BST gap capacitors between the two ends. At 77 K, the filter was measured to have a centre frequency of 11.74 GHz when in the unbiased state and the centre frequency increased to 11.93 GHz (tuned 1.6 %) under 200 V (which corresponds to an electric field of 2 V/µm). The insertion loss of the filter was 1.6 dB at zero bias and 0.35 dB at 200 V. The low insertion loss demonstrated the potential of achieving low loss microwave tunable devices using ferroelectric materials. The filter had a figure of merit of 0.51 dB^{-1}.

Subramanyam [111] presented a novel ferroelectric varactor shunt switch in coplanar waveguide configuration on a high resistivity silicon substrate. The switch consisted of a CPW line loaded by a shunt varactor. The ferroelectric varactor had the highest capacitance at zero bias, resulting in signals shunted to the ground and the output port isolated from the input port (i.e. off-state). Applying a bias voltage drove the capacitance of the varactor to its lowest value and allowed signals to pass through from the input to output ports (on-state). The capacitor area was 5 × 15 μm^2. The switch had an isolation (difference in insertion loss of on-state and off-state) of 16.6 dB at 45 GHz and the on-state insertion loss is 7.1 dB at 9.5 V bias (which corresponds to an electric field of 23.75 V/µm). The switching speed of the varactor shunt switch was tested. The rise and fall times for the device were estimated to be approximately 43 ns.

Tombak [100] reported third order and fifth order lumped element lowpass filters. The filters consisted of BST parallel plate capacitors and coil inductors connected by bond wires. The quality factor of a 65 pF BST varactor was 63 at 45 MHz, which was comparable to the commercially available varactor diode of similar capacitance and frequency. The third order lowpass filter had an insertion loss of 0.8 dB and the 3 dB cut-off frequency was tuned 30 % from 120 to 170 MHz with 0 - 9 V DC bias (which is 30 V/µm electric field). The reflection was better than 10 dB for all biasing conditions. The fifth order lowpass filter had about 2 dB insertion loss and a return loss better than 7 dB with a 40 % tunability by application of 0 - 9 V bias. The IP3 point of the third order and fifth order filter was 24 dBm and 22 dBm at 0 V respectively. A similar tunable bandpass filter was reported as well and the results are included in the summary in Table 2- 3.

Various BST bandpass filters at room temperature have been reported recently and some of the best results are summarised in Table 2- 3 in terms of electric field required, centre frequency, bandwidth, tunability, passband insertion loss and reflection, and figure of merit. Interdigital or parallel plate capacitors are used in integrated or discrete manner. Intermodulation distortion (IMD) is compared as well in terms of the IP3 points. Filters using interdigital capacitors exhibit higher IP3 than those using parallel plate capacitors. This is in large part because the interdigital configuration enables RF field to spread over large volumes [99]. The electrode gap is typically 3 - 20 µm and length of finger 0.1 - 0.4 mm, whereas the dimensions of parallel plate capacitors are of the order of microns. Another reason is that IMD is inversely related to DC bias voltage as shown in equation (2.11). Interdigital capacitors which require higher bias result in lower IMD compared with parallel plate capacitors.

It should be noted that filters using discrete BST varactors have lower insertion loss. At microwave frequencies, the metal loss becomes pronounced in ferroelectric thin film devices as a result of the small metal thickness. The filters using discrete BST varactors usually have much thicker transmission lines and the metal loss is considerably reduced. Discrete BST varactors are assembled on the circuit using silver epoxy or bond wires.

A tunable bandpass filter using discrete BST varactors demonstrated in this work is also included in Table 2- 3. It has a FoM of 0.87 dB^{-1} at an electric field of 6.5 V/μm, which is much higher than other published filters.

Reference	Capacitor configuration/ Integration	Bias voltage (V)/ Electric field (V/μm)	Centre frequency (GHz)/ Tunablility	Band width (before bias)	Insertion loss(dB)/ minimum return loss (dB)	IP3 (dBm)	Top metal/ Filter order	FoM (dB^{-1})
Tombak, et al. 2003[100]	parallel plate/ discrete	0~6/ 0~20	0.176~0.276/ 56.8%	40%	3/ 7	19	Pt/ 3	**0.35**
Pleskachev, et al. 2004[109]	gap/ integrated	0~150/ 0~15	4.40~4.65/ 5.7%	3%	15~8/ NA	NA	Cu/ 3	**0.34**
Kuylenstierna, et al. 2006[112]	parallel plate/ integrated	0~13/ 0~43.3	40~50/ 25 %	25%	9.5~9.0/ 4.5	NA	Au/Pt/ 1	**0.097**
Papapolymerou, et al. 2006[113]	planar/ integrated	0~30/ NA	11.5~14/ 22%	14%	5.4~3.3/ 10	31	Cu/Pt/ 2	**0.322**
Subramanyam, et al. 2001[114]	gap/ integrated	0~100/ 0~4	16.69~17.17/ 3%	2%	8.1~5.3/ NA	NA	Au/ 2	**0.22**
Lugo, et al. 2007[115]	planar/ integrated	1~40/ NA	34.0~37.5/ 10.3%	9.6%	9.0~2.7/ 4	NA	Ti/Au/Pt/ 2	**0.207**
Nath, et al. 2005[105]	interdigital/ integrated	0~200/ 0~40	2.44~2.88/ 18%	24.6%	5.1~3.3/ 13	41	Cu/ 3	**0.155**
Nath, et al. 2006[98]	interdigital/ discrete	0~130/ 43.3	2.14~2.61/ 22%	18%	4.9~2.9/ 11	32	Cu/ 2	**0.292**
this work	interdigital/ discrete	0~65/ 0~6.5	1.55~2.02/ 30.3%	15.5%	3.7~1.1/ 15	NA	Ag/ 2	**0.87**

Table 2- 3 A comparison of published BST thin film bandpass filters at room temperature

2.9 Other ferroelectric devices

The phase shifter is one of the simplest microwave components using ferroelectrics. A continuously variable phase shifter is the most critical component of phased array antennas. Phase shifters can be implemented in different ways, such as a switched line phase shifter, a lowpass/highpass phase shifter, a reflection type or a loaded line phase shifter. The first two types typically use switches whereas the latter two can produce continuous phase tuning using variable capacitors. The most desirable features of a phase shifter are large phase shift ΔΦ and low insertion loss. Subsequently, the figure of merit of a phase shifter is defined as the phase shift divided by loss

$$\mathrm{FoM} = \frac{\Delta\Phi}{\mathrm{IL}_{\mathrm{dB}}} \qquad (2.14).$$

FoM is related to the commutation quality factor K of the loaded varactor as follows [116]

$$\mathrm{FoM} = 6.6\sqrt{\mathrm{K}} \qquad (2.15).$$

Coplanar waveguide transmission lines on top of $Ba_{0.5}Sr_{0.5}TiO_3$ thin film/MgO substrate were made at Birmingham and functioned as phase shifters [117]. The correlation between the microwave performance of the device and the operating temperature, the microstructure of BST thin film were investigated. A FoM of 12.5 °/dB was obtained with optimised grown conditions. Acikel [118] reported a phase shifter comprised of a CPW line periodically loaded with ST parallel plate capacitors. The circuit provided 240° of phase shift with an insertion loss of 3 dB at 10 GHz under 17.5 V DC bias. A figure of merit of 93 °/dB was achieved at 6.3 GHz, which is the best reported figure of merit for a BST phase shifter.

In addition, voltage controlled oscillators [119], tunable matching networks [120] and delay lines [121] utilizing the electric field dependent dielectric constant of ferroelectric materials have been also reported by many research groups.

2.10 Summary

The fundamentals of ferroelectric thin films were presented in this chapter and fabrication issues such as deposition methods, choice of substrate and metallisation were discussed. Understanding of these fundamentals was essential for the designing and optimising of ferroelectric tunable devices. Published results of ferroelectric varactors and tunable filters were reviewed and compared in detail. In addition, recent progress on BST thin film varactors for room temperature microwave applications is reviewed [48]. In the next chapter models of the coplanar waveguide transmission line will be presented and the general microwave filter synthesis procedure will be introduced.

References

[1] Y. Xu, Ferroelectric Materials and Their Applications, North-Holland, 1991.

[2] W.D.Kingery, H.K.Bowen, and D.R.Uhlman, Introduction to Ceramics. New York, USA, John Wiley and Sons, 1960.

[3] J. Valasek, "Piezo-Electric and Allied Phenomena in Rochelle Salt", *Physical Review,* vol. 17, no. 4, pp. 475-481, 1921.

[4] A. V. Hippel, R.G.Breckenridge, F.G.Chesley, and L. Tisza, "High dielectric constant ceramics", *Industrial and Engineering Chemistry,* vol. 38, no. 11, pp. 1097-1109, 1946.

[5] B.Wul and J.M.Goldman, *C.R.Acad.Sci.URSS,* vol. 51, no. p. 21, 1946.

[6] "Complex perovskite-type oxides", in *Landoldt-Bornstein: oxides*. vol. 28, K.H.Hellwege and A.M.Hellwege, Eds. Springer-Verlag, 1990.

[7] D. Czekaj, E. Jaszczyszyn, T. Orkisz, L. Kozielski, Lisiiiska-Czekaj, E. Federowicz, and J. Modelski, "Synthesis and Basic Properties of Ferroelectric Thin Films. Methods Materials and Novel Applications", in *International Conference on Microwaves, Radar & Wireless Communications*2006, pp. 692-699.

[8] B.Jaffe, W.R.Cook, and H.Jaff, Piezoelectric ceramics. London, Academic Press, 1971.

[9] P. Rundqvist, "(Ba,Sr)TiO_3 ferroelectric thin films for microwave applications", Doctor of Philosophy thesis, Department of Microtechnology and Nanoscience, Chalmers University of Technology, 2006

[10] S. Zubko, "Ferroelectrics:Physics and microwave applications", *Visiting seminar,* no. 2007.

[11] C.A.Randall, R.E.Newnham, and L.E.Cross, "History of the first ferroelectric oxide, BaTiO3", Materials Research Institute, The Pennsylvania State University.

[12] M. Daglish and T. Kemmitt, "Ferroelectric thin films - research, development and commercialisation", *IPENZ Transactions,* vol. 27, no. pp. 21-24, 2000.

[13] D. W. Chapman, "Some Thin-Film Properties of a New Ferroelectric Composition", *Journal of Applied Physics,* vol. 40, no. 6, pp. 2381-2385, 1969.

[14] M. H. Francombe, "The Research Status and Device Potential of Ferroelectric Thin Films", *IEEE Transactions on Sonics and Ultrasonics,* vol. 19, no. 2, pp. 199-212, 1972.

[15] N. Setter, D. Damjanovic, L. Eng, G. Fox, S. Gevorgian, S. Hong, A. Kingon, H. Kohlstedt, N. Y. Park, G. B. Stephenson, I. Stolitchnov, A. K. Taganstev, D. V. Taylor, T. Yamada, and S. Streiffer, "Ferroelectric thin films: Review of materials, properties, and applications", *Journal of Applied Physics,* vol. 100, no. 10, p. 109901, 2006.

[16] J.B.Blum and S.R.Gurkovich, "Sol-gel-derived PbTiO3", *Journal of Materials Science,* vol. 20, no. pp. 4479-4483, 1985.

[17] K.D.Budd, S.K.Dey, and D.A.Payne, "Sol-gel processing of lead titanate (PbTiO3), lead zirconate (PbZrO3), PZT, and PLZT thin films", *British Ceramic Proceedings,* vol. 36, no. p. 107, 1985.

[18] S. Baik, N. Setter, and O. Auciello, "Preface: Science of ferroelectric thin films and application to devices", *Journal of Applied Physics,* vol. 100, no. p. 051501, 2006.

[19] R. W. Whatmore, Q. Zhang, Z. Huang, and R. A. Dorey, "Ferroelectric thin and thick films for microsystems", *Materials Science in Semiconductor Processing,* vol. 5, no.

2-3, pp. 65-76, 2002.

[20] Y. Nemirovsky, A. Nemirovsky, P. Muralt, and N. Setter, "Design of novel thin-film piezoelectric accelerometer", *Sensors and Actuators A: Physical,* vol. 56, no. 3, pp. 239-249, 1996.

[21] M. A. Dubois and P. Muralt, "PZT thin film actuated elastic fin micromotor", *IEEE Transactions on Ultrasonics, Ferroelectrics and Frequency Control,* vol. 45, no. 5, pp. 1169-1177, 1998.

[22] P. Muralt and J. Baborowski, "Micromachined Ultrasonic Transducers and Acoustic Sensors Based on Piezoelectric Thin Films", *journal of electroceramics,* vol. 12, no. 1, pp. 101-108, 2004.

[23] F. Toru and W. Shunji, "Feedback positioning cantilever using lead zirconate titanate thin film for force microscopy observation of micropattern", *Applied Physics Letters,* vol. 68, no. 4, pp. 467-468, 1996.

[24] M. J. Kenneth, "Variation of Dielectric Constant with Voltage in Ferroelectrics and Its Application to Parametric Devices", *Journal of Applied Physics,* vol. 33, no. 9, pp. 2826-2831, 1962.

[25] M. DiDomenico, D. A. Johnson, and R. H. Pantell, "Ferroelectric Harmonic Generator and the Large-Signal Microwave Characteristics of a Ferroelectric Ceramic", *Journal of Applied Physics,* vol. 33, no. 5, pp. 1697-1706, 1962.

[26] D. Dimos and C. H. Mueller, "Perovskite thin films for high-frequency capacitor applications", *Annual Review of Materials Science,* vol. 28, no. 1, pp. 397-419, 1998.

[27] O. G. Vendik, E.K.Hollmann, A. B. Kozyrev, and A. M. Prudan, "Ferroelectric tuning of planar and bulk microwave devices", *Journal of Superconductivity,* vol. 12, no. pp. 325-338, 1999.

[28] G. David, C. P. John, A. B. James, and H. O. Ronald, "Characterization of a tunable thin film microwave $YBa_2Cu_3O_{7-x}/SrTiO_3$ coplanar capacitor", *Applied Physics Letters,* vol. 63, no. 22, pp. 3078-3080, 1993.

[29] A.K.Tagantsev, V.O.Sherman, K.F.Astafiev, J.Venkatesh, and N.Setter, "Ferroelectric materials for microwave tunable applications", *Journal of Electroceramics,* vol. 11, no. pp. 5-66, 2003.

[30] D. Galt, J. C. Price, J. A. Beall, and T. E. Harvey, "Ferroelectric thin film characterization using superconducting microstrip resonators", *IEEE Transactions on Applied Superconductivity,* vol. 5, no. 2, pp. 2575-2578, 1995.

[31] F. A. Miranda, C. H. Mueller, C. D. Cubbage, K. B. Bhasin, R. K. Singh, and S. D. Harkness, "HTS/ferroelectric thin films for tunable microwave components", *IEEE Transactions on Applied Superconductivity,* vol. 5, no. 2, pp. 3191-3194, 1995.

[32] A. T. Findikoglu, Q. X. Jia, X. D. Wu, G. J. Chen, T. Venkatesan, and D. W. Reagor, "Tunable and adaptive bandpass filter using a nonlinear dielectric thin film of $SrTiO_3$", *Applied Physics Letters,* vol. 68, no. 12, pp. 1651-1653, 1996.

[33] G. Subramanyam, F. Van Keuls, and F. A. Miranda, "A K-band tunable microstrip bandpass filter using a thin-film conductor/ferroelectric/dielectric multilayer configuration", *Microwave and Guided Wave Letters,* vol. 8, no. 2, pp. 78-80, 1998.

[34] G. Subramanyam, F. Van Keuls, and F. A. Miranda, "A novel K-band tunable microstrip bandpass filter using a thin film HTS/ferroelectric/dielectric multilayer configuration", in *IEEE MTT-S International Microwave Symposium Digest*1998, pp. 1011-1014.

[35] F. A. Miranda, G. Subramanyam, F. W. van Keuls, R. R. Romanofsky, J. D. Warner, and C. H. Mueller, "Design and development of ferroelectric tunable microwave

components for Ku- and K-band satellite communication systems", *IEEE Transactions on Microwave Theory and Techniques,* vol. 48, no. 7, pp. 1181-1189, 2000.

[36] G. Subramanyam, A. Zaman, N. Mohsina, F. W. Van Keuls, F. A. Miranda, and R. R. Romanofsky, "A narrow-band ferroelectric tunable bandpass filter for K-band applications", in *Asia-Pacific Microwave Conference*2000, pp. 938-941.

[37] B. H. Moeckly and Y. Zhang, "Strontium titanate thin films for tunable $YBa_2Cu_3O_7$ microwave filters", *IEEE Transactions on Applied Superconductivity,* vol. 11, no. 1, pp. 450-453, 2001.

[38] C. Y. Tan and C. K. Ong, "Planar tunable HTS microwave filter with patterned ferroelectric thin film", *Supercondctor Science and Technology,* vol. 19, no. pp. 212-216, 2006.

[39] I. Wooldridge, C. W. Turner, P. A. Warburton, and E. J. Romans, "Electrical tuning of passive HTS microwave devices using single crystal strontium titanate", *IEEE Transactions on Applied Superconductivity,* vol. 9, no. 2, pp. 3220-3223, 1999.

[40] A. T. Findikoglu, Q. X. Jia, and D. W. Reagor, "Superconductor/ nonlinear-dielectric bilayers for tunable and adaptive microwave devices", *IEEE Transactions on Applied Superconductivity,* vol. 7, no. 2, pp. 2925-2928, 1997.

[41] M.J.Lancaster, J.Powell, and A.Porch, "Thin-film ferroelectric microwave devices", *Supercondoctor Science and Technology,* vol. 11, no. pp. 1323-1334, 1998.

[42] O. G. Vendik, "Dielectric nonlinearity of the displacive ferroelectrics at UHF", *Ferroelectrics,* vol. 12, no. pp. 85-90, 1976.

[43] T. M. Shaw, Z. Suo, M. Huang, E. Liniger, R. B. Laibowitz, and J. D. Baniecki, "The effect of stress on the dielectric properties of barium strontium titanate thin films", *Applied Physics Letters,* vol. 75, no. 14, pp. 2129-2131, 1999.

[44] N. K. Pervez, P. J. Hansen, and R. A. York, "High tunability barium strontium titanate thin films for rf circuit applications", *Applied Physics Letters,* vol. 85, no. 19, pp. 4451-4453, 2004.

[45] A. Vorobiev, P. Rundqvist, K. Khamchane, and S. Gevorgian, "Microwave loss mechanisms in $Ba_{0.25}Sr_{0.75}TiO_3$ thin film varactors", *Journal of Applied Physics,* vol. 96, no. 8, pp. 4642-4649, 2004.

[46] M. J. Lancaster, J.Powell, and A.Porch, "Thin-film ferroelectric microwave devices", *Supercondoctor Science and Technology,* vol. 11, no. pp. 1323-1334, 1998.

[47] O. G. Vendik and S. P. Zubko, "Ferroelectric phase transition and maximum dielectric permittivity of displacement type ferroelectrics ($Ba_xSr_{1-x}TiO_3$)", *Journal of Applied Physics,* vol. 88, no. 9, pp. 5343-5350, 2000.

[48] P. Bao, T. J. Jackson, X. Wang, and M. J. Lancaster, "Barium strontium titanate thin film varactors for room-temperature microwave device applications", *Journal of Physics D: Applied Physics,* vol. 41, no. p. 063001, 2008.

[49] M. Ouaddari, S. Delprat, F. Vidal, M. Chaker, and Ke Wu, "Microwave characterization of ferroelectric thin-film materials", *IEEE Transactions on Microwave Theory and Techniques,* vol. 53, no. 4, pp. 1390-1397, 2005.

[50] D. Ghosh, B. Laughlin, J. Nath, A. I. Kingon, M. B. Steer, and J. P. Maria, "Tunable high-quality-factor interdigitated (Ba, Sr)TiO_3 capacitors fabricated on low-cost substrates with copper metallization", *Thin Solid Films,* vol. 496, no. 2, pp. 669-673, 2006.

[51] A. Vorobiev, P. Rundqvist, K. Khamchane, and S. Gevorgian, "Silicon substrate integrated high Q-factor parallel-plate ferroelectric varactors for microwave/millimeterwave applications", *Applied Physics Letters,* vol. 83, no. 15, pp.

3144-3146, 2003.

[52] Y. Yong-Kyu, K. Dongsu, M. G. Allen, J. S. Kenney, and A. T. Hunt, "A reduced intermodulation distortion tunable ferroelectric capacitor-architecture and demonstration", *IEEE Transactions on Microwave Theory and Techniques*, vol. 51, no. 12, pp. 2568-2576, 2003.

[53] S. W. Kirchoefer, J. M. Pond, A. C. Carter, W. Chang, K. K. Agarwal, J. S. Horwitz, and D. B. Chrisey, "Microwave properties of $Sr_{0.5}Ba_{0.5}TiO_3$ thin-film interdigitated capacitors", *Microwave and Optical Technology Letters*, vol. 18, no. 3, pp. 168-171, 1998.

[54] O. G. Vendik and A.N.Rogachev, "Electrostriction mechanism of microwave losses in a ferroelectric film and experimental", *Technical Physics Letters*, vol. 25, no. pp. 702-704, 1999.

[55] C.-Y. Kang, S. F. Karmanenko, I. G. Mironenko, A. A. Semenov, A. I. Dedyk, A. A. Ivanov, P. J. Beljavski, and U. V. Pavlova, "The investigation of dielectric characterisitic of (Ba, Sr)TiO_3 thin films in millimeter wavelength range", *Integrated Ferroelectrics*, vol. 86, no. 1, pp. 131 - 140, 2006.

[56] J. C. Booth, I. Takeuchi, and K.-S. Chang, "Microwave-frequency loss and dispersion in ferroelectric $Ba_{0.3}Sr_{0.7}TiO_3$ thin films", *Applied Physics Letters*, vol. 87, no. 8, p. 082908, 2005.

[57] C. B. Parker, "Size effects and reliability of (Ba,Sr)TiO3 thin films", PhD thesis thesis, NCSU, 2002

[58] B. Cem, S. K. Streiffer, I. K. Angus, and R. Waser, "The dielectric response as a function of temperature and film thickness of fiber-textured (Ba,Sr)TiO_3 thin films grown by chemical vapor deposition", *Journal of Applied Physics*, vol. 82, no. 5, pp. 2497-2504, 1997.

[59] L. J. Sinnamon, R. M. Bowman, and J. M. Gregg, "Investigation of dead-layer thickness in $SrRuO_3/Ba_{0.5}Sr_{0.5}TiO_3$/Au thin-film capacitors", *Applied Physics Letters*, vol. 78, no. 12, pp. 1724-1726, 2001.

[60] P. Padmini, T. R. Taylor, M. J. Lefevre, A. S. Nagra, R. A. York, and J. S. Speck, "Realization of high tunability barium strontium titanate thin films by rf magnetron sputtering", *Applied Physics Letters*, vol. 75, no. 20, pp. 3186-3188, 1999.

[61] C. B. Parker, "Size effects and reliability of (Ba,Sr)TiO3 thin films", Ph.D thesis thesis, North Carolina State University, 2002

[62] G. Velu, J. C. Carru, E. Cattan, D. Remiens, X. Melique, and D. Lippens, "Deposition of Ferroelectric BST Thin Films by Sol Gel Route in View of Electronic Applications", *Ferroelectrics*, vol. 288, no. pp. 59-69, 2003.

[63] C. W. Law, K. Y. Tong, K. L. Wong, J. H. Li, and K. Li, "Electrical characteristics of MIS capacitors with BST thin films deposited on n-Si(100) by the sol-gel method", in *Proceeding of Electron Devices Meeting*, Hong Kong, 1998, pp. 54-57.

[64] D. M. Tahan, L. C. Klein, and A. Safari, "Processing and dielectric property evaluation of barium strontium titanate thin films prepared by a sol-gel technique", in *Proceedings of the Tenth IEEE International Symposium on Applications of Ferroelectrics*1996, pp. 483-486.

[65] V. O. Sherman, T. Yamada, A. Noeth, N. Setter, M. Mandeljc, B. Malic, M. Kosec, and M. Vukadinovic, "Microwave phase shifters based on sol-gel derived $Ba_{0.3}Sr_{0.7}TiO_3$ ferroelectric thin films", in *European Microwave Conference*2007, pp. 1295-1298.

[66] F. W. Van Keuls, C. H. Mueller, R. R. Romanofsky, J. D. Warner, F. A. Miranda, S. B. Majumder, M. Jain, A. Martinez, R. S. Katiyar, and H. Jiang, "Evaluation of Chemical

Solution Deposited $Ba_xSr_{1-x}TiO_3$ Thin Films on $LaAlO_3$ in Tunable Microwave Devices", *Integrated Ferroelectrics,* vol. 42, no. 1, pp. 207-217, 2002.

[67] J. Nath, "Design and characterization of frequency agile RF and microwave devices using ferroelectrics", Doctor of Philosophy thesis, Electrical Engineering, North Carolina State University, 2006

[68] M. Shimizu, M. Okaniwa, H. Fujisawa, and H. Niu, "Ferroelectric properties of $Pb(Zr,Ti)O^3$ thin films prepared by low-temperature MOCVD using $PbTiO_3$ seeds", *Journal of the European Ceramic Society,* vol. 24, no. 6, pp. 1625-1628, 2004.

[69] D. Ghosh, "Tunable Microwave Devices using BST (Barium Strontium Titanate) and Base Metal Electrodes", Doctor of Philosophy thesis, North Carolina State University, 2005

[70] A. Tombak, J. P. Maria, F. Ayguavives, Zhang Jin, G. T. Stauf, A. I. Kingon, and A. Mortazawi, "Tunable barium strontium titanate thin film capacitors for RF and microwave applications", *Microwave and Wireless Components Letters,* vol. 12, no. 1, pp. 3-5, 2002.

[71] T. J. Jackson and S. B. Palmer, "Oxide superconductor and magnetic metal thin film deposition by pulsed laser ablation: a review", *Journal of Physics D: Applied Physics,* vol. 27, no. 8, pp. 1581-1594, Aug 1994.

[72] L. Goux, M. Gervais, F. Gervais, C. Champeaux, and A. Catherinot, "Pulsed laser deposition of ferroelectric BST thin films on perovskite substrates: an infrared characterization", *International Journal of Inorganic Materials,* vol. 3, no. 7, pp. 839-842, 2001.

[73] S. K. Dey, P. Majhi, J. S. Horwitz, S. W. Kirchoefer, and W. J. Kim, "Microstructure evolution of Pulsed Laser-Deposited (Ba, Sr)TiO_3 films on MgO for microwave applications", *International Journal of Applied Ceramic Technology,* vol. 2, no. pp. 59-63, 2005.

[74] L. L. López, J. Portelles, J. M. Siqueiros, G. A. Hirata, and J. McKittrick, "$Ba_{0.5}Sr_{0.5}TiO_3$ thin films deposited by PLD on SiO_2/Si RuO_2/Si and Pt/Si electrodes", *Thin Solid Films,* vol. 373, no. 1-2, pp. 49-52, 2000.

[75] M. Wiora, "Magnetron sputtering of thin film", University of California, Santa Barvara. A report on http://www.nanotech.ucsb.edu/ 2004.

[76] D. B. Chrisey and G. K. Hubler, Pulsed Laser Deposition of Thin Films, John Wiley & Sons, 1994.

[77] P. M. Suherman, T. J. Jackson, and M. J. Lancaster, "Comparison of Techniques for Microwave Characterization of BST Thin Films", *Microwave Theory and Techniques, IEEE Transactions on,* vol. 55, no. 2, pp. 397-401, 2007.

[78] D. Galt, J. C. Price, J. A. Beall, and T. E. A. H. T. E. Harvey, "Ferroelectric thin film characterization using superconducting microstrip resonators", *Applied Superconductivity, IEEE Transactions on,* vol. 5, no. 2, pp. 2575-2578, 1995.

[79] X. Zhu, D.-Y. Chen, J. Zhang, J. D. Phillips, and A. Mortazawi, "Characterization of thin film BST tunable capacitors using a simple two port measurement technique", in *Microwave Symposium Digest, 2005 IEEE MTT-S International*2005, p. 4 pp.

[80] B. Acikel, "High performance barium strontium titanate varactor technology for low cost circuit applications", Doctor of Philosophy thesis, University of California, Santa Barbara, 2002

[81] A. Vorobiev, D. Kuylenstierna, P. Rundqvist, and S. Gevorgian, "Broadband Microprobe Characterization of the Ferroelectric Films and Varactors", in *36th European Microwave Conference*2006, pp. 843-846.

[82] P. Rundqvist, A. Vorobiev, S. Gevorgian, and K. Khamchane, "Non-Destructive Microwave Characterization of Ferroelectric Films on Conductive Substrates", *Integrated Ferroelectrics,* vol. 60, no. pp. 1-19, 2004.

[83] S. S. Gevorgian, T. Martinsson, P. L. J. Linner, and E. L. Kollberg, "CAD models for multilayered substrate interdigital capacitors", *Microwave Theory and Techniques, IEEE Transactions on,* vol. 44, no. 6, pp. 896-904, 1996.

[84] E. A. Fardin, K. Ghorbani, and A. S. Holland, "Low Cost Interdigital BST Varactors for Tunable Microwave Applications", in *IEEE TENCON*2005, pp. 1-4.

[85] B. Acikel, L. Yu, A. S. Nagra, T. R. Taylor, P. J. Hansen, J. S. Speck, and R. A. York, "Phase shifters using (Ba,Sr)TiO_3 thin films on sapphire and glass substrates", in *IEEE MTT-S International Microwave Symposium Digest*2001, pp. 1191-1194.

[86] Y. Liu, A. S. Nagra, E. G. Erker, P. Periaswamy, T. R. Taylor, J. Speck, and R. A. York, "$BaSrTiO_3$ interdigitated capacitors for distributed phase shifter applications", *Microwave and Guided Wave Letters,* vol. 10, no. 11, pp. 448-450, 2000.

[87] K. Dongsu, C. Yoonsu, M. Ahn, M. G. Allen, J. Stevenson Kenney, and P. Marry, "2.4 GHz continuously variable ferroelectric phase shifters using all-pass networks", *Microwave and Wireless Components Letters,* vol. 13, no. 10, pp. 434-436, 2003.

[88] P. M. Suherman, T. J. Jackson, Y. Koutsonas, R. A. Chakalov, and M. J. Lancaster, "On-wafer microwave characterization of ferroelectric thin film phase shifters", in *IEEE MTT-S International Microwave Symposium Digest*2004, pp. 265-268.

[89] Y. L. Cheng, N. Chong, Y. Wang, J. Z. Liu, H. L. W. Chan, and C. L. Choy, "Microwave Characterization of BST Thin Films on LAO Interdigital Capacitor", *Integrated Ferroelectrics,* vol. 55, no. pp. 939-946, 2003.

[90] D. Wang, Y. Wang, J. Dai, H. Chan, and C. Choy, "Substrate effect on in-plane ferroelectric and dielectric properties of $Ba_{0.7}Sr_{0.3}TiO_3$ thin films", *journal of electroceramics,* vol. 16, no. 4, pp. 587-591, 2006.

[91] M. Al Ahmad, M. Brunet, S. Payan, D. Michau, M. Maglione, and R. Plana, "Wide-Tunable Low-Field Interdigitated Barium Strontium Titanate Capacitors", *Microwave and Wireless Components Letters,* vol. 17, no. 11, pp. 769-771, 2007.

[92] A. Vorobiev, J. Berge, and S. Gevorgian, "Thin Film $Ba_{0.25}Sr_{0.75}TiO_3$ Varactors on Au Bottom Electrode for Microwave Applications", in *36th European Microwave Conference*2006, pp. 839-842.

[93] J. Nath, D. Ghosh, J. Maria, M. B. Steer, A. Kingon, and G. T. Stauf, "Microwave properties of bst thin film interdigital capacitors on low cost alumina substrates", in *the 34th European Microwave Conference*2004, pp. 1497-1500.

[94] H. S. Gamble, B. M. Armstrong, S. J. N. Mitchell, Y. Wu, V. F. Fusco, and J. A. C. Stewart, "Low-loss CPW lines on surface stabilized high-resistivity silicon", *Microwave and Guided Wave Letters,* vol. 9, no. 10, pp. 395-397, 1999.

[95] D. Kuylenstierna, M. Norling, A. Vorobiev, K. Reimann, D. Lederer, J. P. Raskin, and S. Gevorgian, "Performance of Coplanar Waveguides on Surface Passivated Highly Resistive Silicon Covered by Ferroelectric Thin Film", in *IEEE/MTT-S International Microwave Symposium*2007, pp. 2055-2058.

[96] T. K. Ishii, Handbook of Microwave Technology, Volume 1, Components and Devices, Academic Press, Inc., 1995.

[97] W. Fan, B. Kabius, J. M. Hiller, S. Saha, J. A. Carlisle, O. Auciello, R. P. H. Chang, and R. Ramesh, "Materials science and integration bases for fabrication of $(Ba_xSr_{1-x})TiO_3$ thin film capacitors with layered Cu-based electrodes", *Journal of Applied Physics,* vol. 94, no. 9, pp. 6192-6200, 2003.

[98] J. Nath, W. M. Fathelbab, P. G. Lam, D. Ghosh, S. Aygiin, K. G. Gard, J. P. Maria, A. I. Kingon, and M. B. Steer, "Discrete Barium Strontium Titanate (BST) Thin-Film Interdigital Varactors on Alumina: Design, Fabrication, Characterization, and Applications", in *IEEE MTT-S International Microwave Symposium Digest*2006, pp. 552-555.

[99] C. H. Mueller, R. R. Romanofsky, and F. A. Miranda, "Ferroelectric thin film and broadband satellite systems", *IEEE Potentials*, vol. 20, no. 2, pp. 36-39, 2001.

[100] A. Tombak, J. P. Maria, F. T. Ayguavives, Zhang Jin, G. T. Stauf, A. I. Kingon, and A. Mortazawi, "Voltage-controlled RF filters employing thin-film barium-strontium-titanate tunable capacitors", *IEEE Transactions on Microwave Theory and Techniques*, vol. 51, no. 2, pp. 462-467, 2003.

[101] D.M.Pozar, Microwave Engineering, 2nd ed. New York, USA, John Wiley & Sons, Inc., 1998.

[102] E. Marsan, J. Gauthier, M. Chaker, and K. Wu, "Tunable microwave device: status and perspective", in *IEEE-NEWCAS Conference*2005, pp. 279-282.

[103] M. S. Tsai, S. C. Sun, and T.-Y. Tseng, "Effect of bottom electrode materials on the electrical and reliability characteristics of (Ba, Sr)TiO_3 capacitors", *IEEE Transactions on Electron Devices,* vol. 46, no. 9, pp. 1829-1838, 1999.

[104] A. J. Hartmann, M. Neilson, R. N. Lamb, K. Watanabe, and J. F. Scott, "Ruthenium oxide and strontium ruthenate electrodes for ferroelectric thin-films capacitors", *Applied Physics A: Materials Science & Processing,* vol. 70, no. 2, pp. 239-242, 2000.

[105] J. Nath, D. Ghosh, J. P. Maria, A. I. Kingon, W. Fathelbab, P. D. Franzon, and M. B. Steer, "An electronically tunable microstrip bandpass filter using thin-film Barium-Strontium-Titanate (BST) varactors", *IEEE Transactions on Microwave Theory and Techniques,* vol. 53, no. 9, pp. 2707-2712, 2005.

[106] J. S. Kenney, Y. Yong Kyu, A. Minsik, M. G. Allen, Zhiyong Zhao, Xiaoyan Wang, A. Hunt, and Dongsu Kim, "Low-voltage ferroelectric phase shifters from L- to C-band and their applications", in *IEEE Aerospace Conference*2006.

[107] I. Vendik, O. Vendik, V. Pleskachev, and M. Nikol'ski, "Tunable microwave filters using ferroelectric materials", *IEEE Transactions on Applied Superconductivity,* vol. 13, no. 2, pp. 716-719, 2003.

[108] V. Pleskachev and I. Vendik, "Figure of Merit of Tunable Ferroelectric Planar Filters", in *the 33rd European Microwave Conference*2003, pp. 191-194.

[109] V. Pleskachev and I. Vendik, "Tunable microwave filters based on ferroelectric capacitors", in *15th International Conference on Microwaves, Radar and Wireless Communications*2004, pp. 1039-1043.

[110] V. N. Keis, A. B. Kozyrev, M. L. Khazov, J. Sok, and J. S. Lee, "20 GHz tunable filter based on ferroelectric (Ba,Sr)TiO_3 film varactors", *Electronics Letters,* vol. 34, no. 11, pp. 1107-1109, 1998.

[111] G. Subramanyam and F. Ahamed, "RF performance characteristics of a novel ferroelectric varactor shunt switch", in *the 48th Midwest Symposium on Circuits and Systems*2005, pp. 619-622.

[112] D. Kuylenstierna, A. Vorobiev, and S. Gevorgian, "40 GHz lumped element tunable bandpass filters with transmission zeros based on thin $Ba_{0.25}Sr_{0.75}TiO_3$ (BST) film varactors", in *Topical Meeting on Silicon Monolithic Integrated Circuits in RF Systems,* 2006, pp. 342-345.

[113] J. Papapolymerou, C. Lugo, Z. Zhiyong, X. Wang, and A. Hunt, "A Miniature Low-Loss Slow-Wave Tunable Ferroelectric BandPass Filter From 11-14 GHz", in

*IEEE MTT-S International Microwave Symposium Digest*2006, pp. 556-559.

[114] G. Subramanyam, N. Mohsina, A. Al Zaman, F. Miranda, F. Van Keuls, R. Romanofsky, and J. Warner, "Ferroelectric thin-film based electrically tunable Ku-band coplanar waveguide components", in *IEEE MTT-S International Microwave Symposium Digest*2001, pp. 471-474.

[115] C. Lugo, G. Wang, J. Papapolymerou, Z. Zhao, X. Wang, and A. T. Hunt, "Frequency and Bandwidth Agile Millimeter-Wave Filter Using Ferroelectric Capacitors and MEMS Cantilevers", *IEEE Transactions on Microwave Theory and Techniques*, vol. 55, no. 2, pp. 376-382, 2007.

[116] I. B. Vendik, O. G. Vendik, and E. L. Kollberg, "Criterion for a Switching Device as a Basis of Microwave Switchable and Tunable Components", in *29th European Microwave Conference*1999, pp. 187-190.

[117] P. M. Suherman, T. J. Jackson, Y. Y. Tse, I. P. Jones, R. I. Chakalova, M. J. Lancaster, and A. Porch, "Microwave properties of $Ba_{0.5}Sr_{0.5}TiO_3$ thin film coplanar phase shifters", *Journal of Applied Physics*, vol. 99, no. 10, p. 104101, 2006.

[118] B. Acikel, T. R. Taylor, P. J. Hansen, J. S. Speck, and R. A. York, "A new high performance phase shifter using $Ba_xSr_{1-x}TiO_3$ thin films", *Microwave and Wireless Components Letters*, vol. 12, no. 7, pp. 237-239, 2002.

[119] A. Victor, J. Nath, D. Ghosh, B. Boyette, J. P. Maria, M. B. Steer, A. I. Kingon, and G. T. Stauf, "A voltage controlled oscillator using barium strontium titanate (BST) thin film varactor", in *Radio and Wireless Conference*2004, pp. 91-94.

[120] L. Y. V. Chen, R. Forse, D. Chase, and R. A. York, "Analog tunable matching network using integrated thin-film BST capacitors", in *IEEE MTT-S International Microwave Symposium Digest*2004, pp. 261-264.

[121] D. Kuylenstierna, A. Vorobiev, P. Linner, and S. Gevorgian, "Ultrawide-band tunable true-time delay lines using ferroelectric varactors", *IEEE Transactions on Microwave Theory and Techniques*, vol. 53, no. 6, pp. 2164-2170, 2005.

CHAPTER 3

MICROWAVE FILTER THEORY

In this chapter the characteristics of single and multilayer substrate coplanar waveguides are presented. The general microwave filter synthesis procedure is outlined and in particular, the design method for coupled resonator filters is reviewed. These analyses provide the theoretical basis for the lowpass and bandpass filters based on the coplanar waveguide configuration presented in chapters 4, 5 and 6.

3.1 Coplanar waveguide

Coplanar waveguide (CPW), microstrip and stripline are the most commonly used planar transmission lines for microwave integrated circuits (MICs) and monolithic microwave integrated circuits (MMICs) [1]. Coplanar waveguide was invented by C. P. Wen in 1969 [2]. CPW consists of a conductor strip separated from a pair of ground planes, lying on the same plane, on top of a dielectric substrate, as shown in Fig.3- 1.

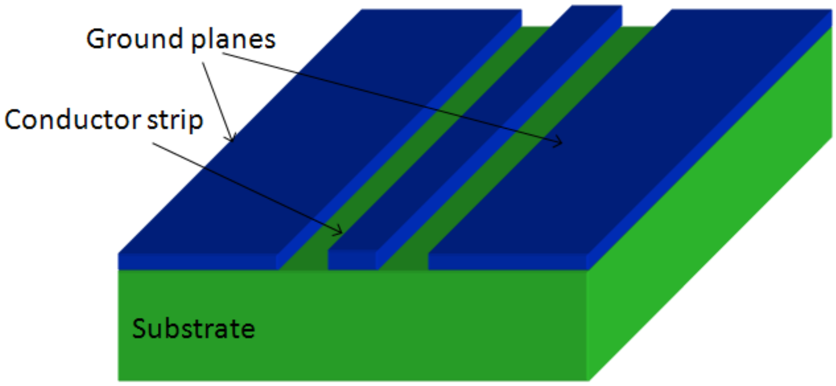

Fig.3- 1 Sketch of coplanar waveguide structure

CPW has several advantages over other planar transmission lines. Unlike microstrip and stripline, in which, for a certain characteristic impedance, the line width is often determined by a fixed substrate thickness, the characteristic impedance of CPW is mainly determined by the slot-to-strip width ratio and is less dependent on the substrate thickness. Hence different line widths can be chosen by keeping appropriate slot-to-strip width ratio for a given line impedance. This offers the potential to make a very compact circuit [3]. However, in practical conditions, the circuit size has to be traded off with the line loss, as narrow lines can be quite lossy. In addition, CPW has great isolation or low cross coupling because of the screening effect of the in-plane grounds. CPW also eliminates the need for via holes and backside plating as the ground is in the same plane as the signal line and this lends itself to surface mounting of devices.

However, CPW suffers from parasitic wave modes such as the slotline mode and surface wave leakage [4-6]. Such parasitic modes can be detrimental if the circuit is not properly designed. Crossover bonding wires or air bridges between the two ground planes may be used to balance the unequal potentials of the ground planes and suppress the unwanted modes.

3.1.1 Characteristic impedance and effective permittivity

Although CPW is a non-TEM structure, the quasi-TEM approximation has proved a good representation of its characteristic properties. The lateral configuration of a CPW is shown in Fig.3- 2. The strip width is 2s and the slot width is g. t and h represents the thickness of the conductor and substrate respectively. ε_r denotes the relative permittivity of the substrate. The transverse dimension of CPW 2(s+g), should be small compared to the wavelength and substrate thickness. In this case, the slots can be modelled as magnetic walls. Conformal mapping techniques can be used to give the close formed analytical expressions of effective permittivity and characteristic impedance [1]. In the analysis, the conductor strips are also assumed to have zero thickness. The quasi-TEM approximation is applicable only when the conductor and dielectric (substrate) are homogeneous and have low loss.

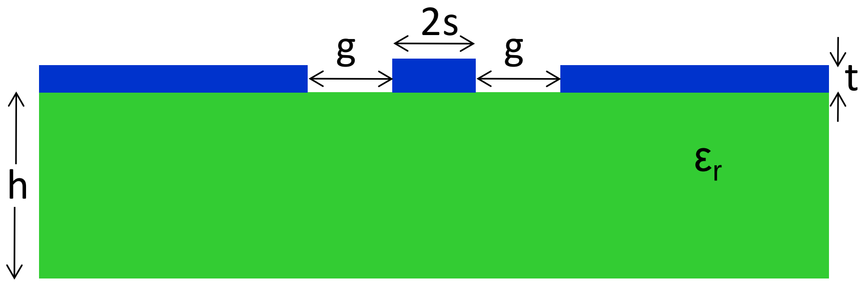

Fig.3- 2 Coplanar waveguide configuration

The analysis is based on the partial capacitance technique and the validity of this approach is well established for CPW [7]. The effective permittivity ε_e and characteristic impedance Z_0 of the unshielded CPW shown in Fig.3- 2 can be expressed as [8]

$$\varepsilon_e = 1 + \frac{\varepsilon_r - 1}{2} \frac{K(k_1)}{K(k_1')} \frac{K(k_0')}{K(k_0)} \tag{3.1}$$

$$Z_0 = \frac{30\pi}{\sqrt{\varepsilon_e}} \frac{K(k_0')}{K(k_0)} \tag{3.2}$$

where K is the complete elliptic integral of the first kind and is defined as

$$K(k) = \int_0^{\pi/2} \frac{d\theta}{\sqrt{1 - k^2 \sin^2 \theta}} \tag{3.3}$$

and $K'(k) = K(k')$, $k' = \sqrt{1-k^2}$. The factors k_0 and k_1 are given by

$$k_0 = \frac{s}{s+g}$$

$$k_1 = \frac{\sinh(\pi s / 2h)}{\sinh(\pi (s+g)/2h)}.$$

Fig.3- 3 shows the characteristic impedance Z_0 as functions of strip width 2s and slot width g for a duroid 5870 substrate of ε_r = 2.33, h = 0.787 mm, calculated using the above equations. The squares represent the characteristic impedance Z_0 as a function of the strip width 2s from 0.2 mm to 6 mm for a fixed slot width of g = 0.1 mm. The dots represent Z_0 as a function of g

from 0.01 mm to 0.3 mm for a fixed 2s = 4 mm. As observed from the figure, Z_0 increases with the decreasing of the strip width or with the increasing of the gap. This is expected as more field is confined between the central strip and ground plane for a wider strip or smaller gap, which results in a smaller impedance.

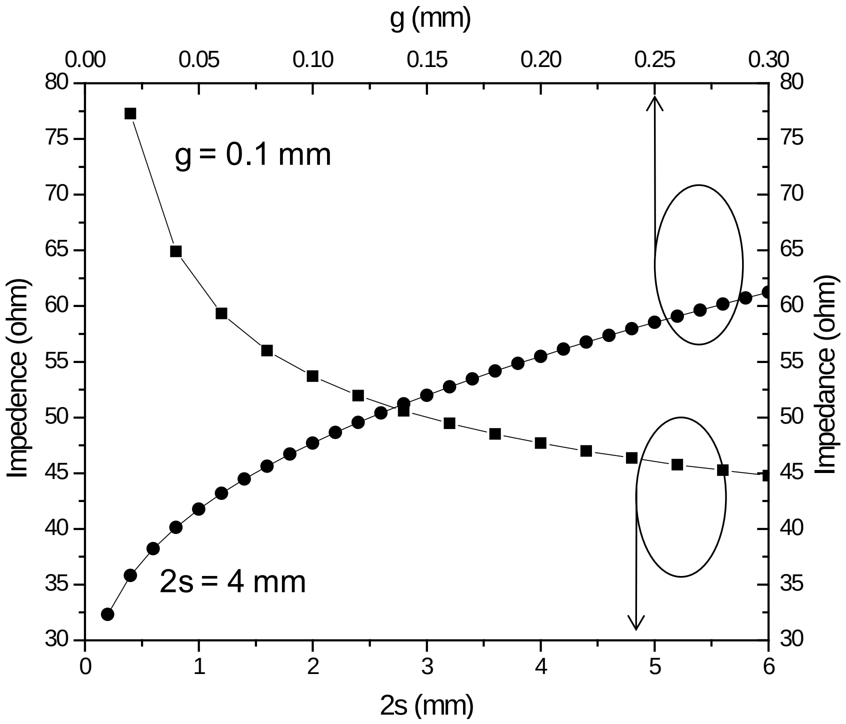

Fig.3- 3 Characteristic impedance of CPW lines on Rogers RT/duroid 5870 laminate ($\varepsilon_r = 2.33$, h = 0.787 mm) as functions of strip width 2s (—■—) for a fixed gap g = 0.1 mm and slot width g (—●—) for a fixed strip width 2s = 4 mm.

3.1.2 Multilayer substrate coplanar waveguide

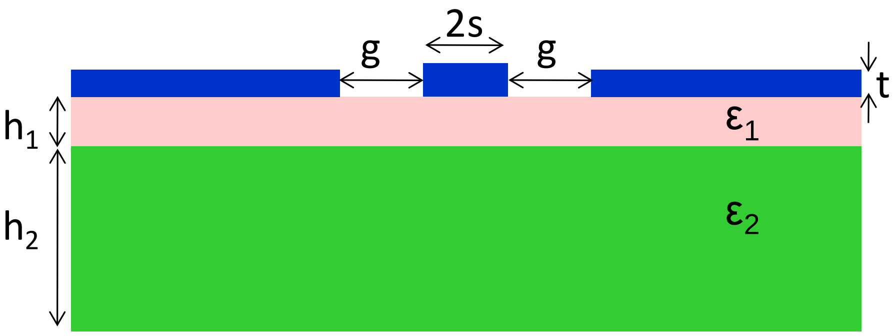

Fig.3- 4 Multilayer coplanar waveguide configuration

Most work in this thesis uses a multilayer coplanar waveguide configuration, where the conductor is on top of a ferroelectric thin film and substrate. The lateral dimensions of a multilayer CPW are shown in Fig.3- 4. The ferroelectric layer has a permittivity of ε_1 and thickness of h_1, and the substrate has a permittivity of ε_2 and thickness of h_2. The effective permittivity is a combination of the permittivity of the air above, the ferroelectric layer and the substrate, and is dependent on the CPW geometry.

The effective permittivity ε_e and characteristic impedance Z_0 of the multilayer CPW shown in Fig.3- 4 can be expressed as [8]

$$\varepsilon_e = 1 + \frac{q_1(\varepsilon_1 - \varepsilon_2)}{2} + \frac{q_2(\varepsilon_2 - 1)}{2} \tag{3.4}$$

and

$$Z_0 = \frac{30\pi}{\sqrt{\varepsilon_e}} \frac{K(k_0')}{K(k_0)} \tag{3.5}$$

where filling factor q_i for ferroelectric layer (i = 1) and substrate (i = 2) are given by

$$q_i = \frac{K(k_i)}{K(K_i')} \frac{K(K_0')}{K(k_0)} \tag{3.6}.$$

K is the complete elliptic integral of the first kind as defined in equation (3.3), and

$$k_0 = \frac{s}{s+g}$$

$$k_i = \frac{\sinh(\pi s / 2h_i)}{\sinh(\pi(s+g)/2h_i)}.$$

When the ferroelectric layer thickness (h_1) is extremely small compared with the line dimensions (s or g), some computational difficulties may be encountered when trying to evaluate the dielectric filling factor of ferroelectric layer. In this case, the limiting form [9]

$$q_i = \frac{\pi}{\ln(16) + \pi g / h_i} \frac{K(k_0')}{K(k_0)} \tag{3.7}$$

can be employed. It is accurate to better than 1 % for $2s/h_i > 1$.

Using the above equations, the slot width g as a function of the strip width 2s can be found for the 50 Ω CPW lines on ferroelectric/silicon substrate, with $\varepsilon_1 = 400$ or 600, $\varepsilon_2 = 11.7$, $h_1 = 400$ nm, $h_2 = 0.5$ mm, as shown in Fig.3- 5. As mentioned previously, a narrower strip can be used as long as a smaller slot is chosen appropriately to achieve 50 Ω impedance. The impedance is also affected by the permittivity of the ferroelectric. For a given strip width, a smaller gap would be required for a lower permittivity of the ferroelectric to keep the impedance 50 Ω. This is because the field is less concentrated in the ferroelectrics when a smaller permittivity is exhibited.

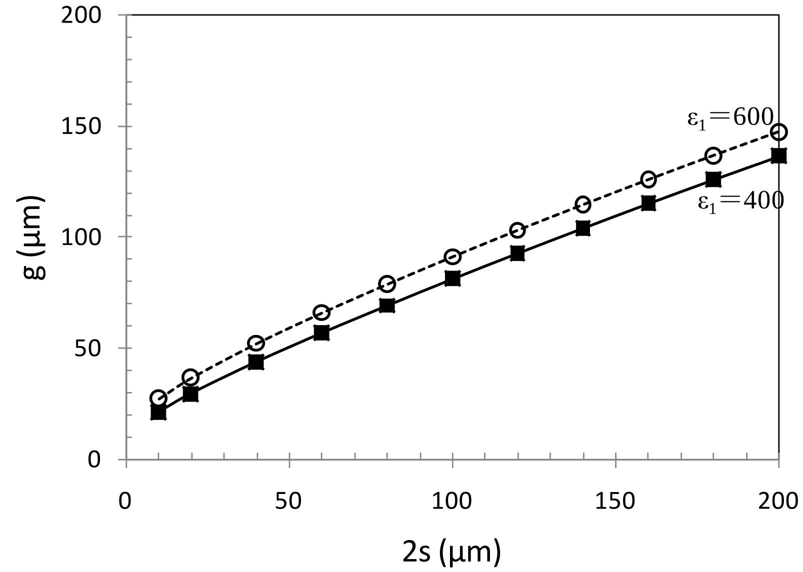

Fig.3- 5 The slot width g versus strip width 2s curve for a 50 Ω CPW on a ferroelectric/silicon substrate for ferroelectric films of permittivity $\varepsilon_1 = 600$ (--○--) or 400 (—■—).The thickness of the ferroelectric layer is 400 nm.

CPW lines used in the ferroelectric lowpass filters presented in chapter 4 are calculated and listed in Table 3- 1. In the calculation, the thickness of the ferroelectric layer and silicon substrate is 400 nm and 0.5 mm, the permittivity of the ferroelectric and silicon is 400 and 11.7 respectively. The simulated results using Sonnet [10] are also included in Table 3- 1 for comparison. In the simulation, the conductors are assumed to have zero thickness and infinite conductivity, the length of the CPW line is 1 mm and the cell size is 5 μm. The simulated results are obtained at 10 GHz. It can be seen that the results calculated using the equations (3.4) to (3.7) agree well with the simulated data with an average difference of 4 %. The finite width of the ground plane in the simulation might be one reason for the discrepancy.

In some applications it is necessary to provide shielding of a microwave circuit. The effect of shielding on CPW line characteristics is negligible when the shield dimensions are large [1]. The analytical calculations of CPWs with different shield arrangements can be found in [8] and will not be presented here for clarity.

2s (µm)	g (µm)	Z_c (Ω) Calculation	Z_c (Ω) Sonnet simulation
120	100	51.35	49.99
200	150	51.67	48.93

Table 3- 1 The characteristic impedance of CPW lines obtained from conformal mapping calculation and electromagnetic full wave simulation using Sonnet

3.1.3 Guided wavelength, phase velocity and electrical length

The phase velocity ν_p of the wave propagating on a lossless TEM transmission line, including a coplanar transmission line, is obtained from

$$\nu_p = \frac{1}{\sqrt{\varepsilon_e \varepsilon_0 \mu}} = \frac{c_0}{\sqrt{\varepsilon_e}} \tag{3.8}$$

where $c_0 = 3\times10^8$ m/s is the velocity of light in vacuum and ε_e is the effective dielectric constant of the coplanar waveguide.

The guided wavelength of the quasi-TEM mode of CPW is

$$\lambda_g = \frac{\lambda_0}{\sqrt{\varepsilon_e}} = \frac{c_0}{f}\frac{1}{\sqrt{\varepsilon_e}} \tag{3.9}$$

where λ_0 is the free space wavelength and *f* is the frequency of interest. The propagation constant β can be expressed as

$$\beta = \frac{2\pi}{\lambda_g} \qquad (3.10).$$

The electrical length θ, in radians, for a given physical length *l* of transmission line is defined by

$$\theta = \beta l \tag{3.11}$$

3.2 Microwave filter design

A filter is typically a two port network which rejects unwanted signal frequencies and permits good transmission of wanted frequencies [11]. Typical frequency responses of filters include lowpass, highpass, bandpass and bandstop characteristics.

The majority of filters are designed using the insertion loss method, whereby the amplitude response of the filter is approximated by the network synthesis methods. Filters can be classified into categories by the terms of locations of transmission zeros and poles of the transfer functions, e.g. Butterworth, Chebyshev, or Elliptic function. Both Butterworth and Chebyshev type filters have no finite frequency transmission zeros, sometimes referred as all-pole filters [12]. The Butterworth filter has a maximally flat passband. The Chebyshev filter has steeper attenuation over the Butterworth filter beyond the cut-off frequency by allowing ripples in passband. The Elliptic function filter has ripples in both passband and stopband. Although the Elliptic function filter has the steepest cut-off, such a filter is complex in practical realisation and is not widely used. All the filters in this thesis are based on Chebyshev prototype filters. A typical Chebyshev response filter, which has equal-ripple passband and maximally flat stopband, is depicted in Fig.3- 6.

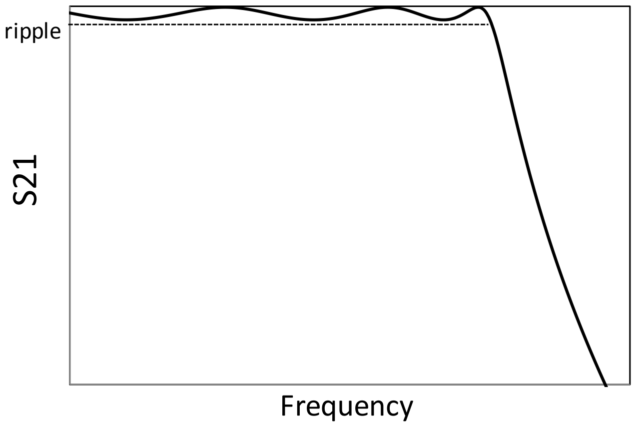

Fig.3- 6   A typical Chebyshev lowpass filter response.

3.2.1 Lowpass prototype filter

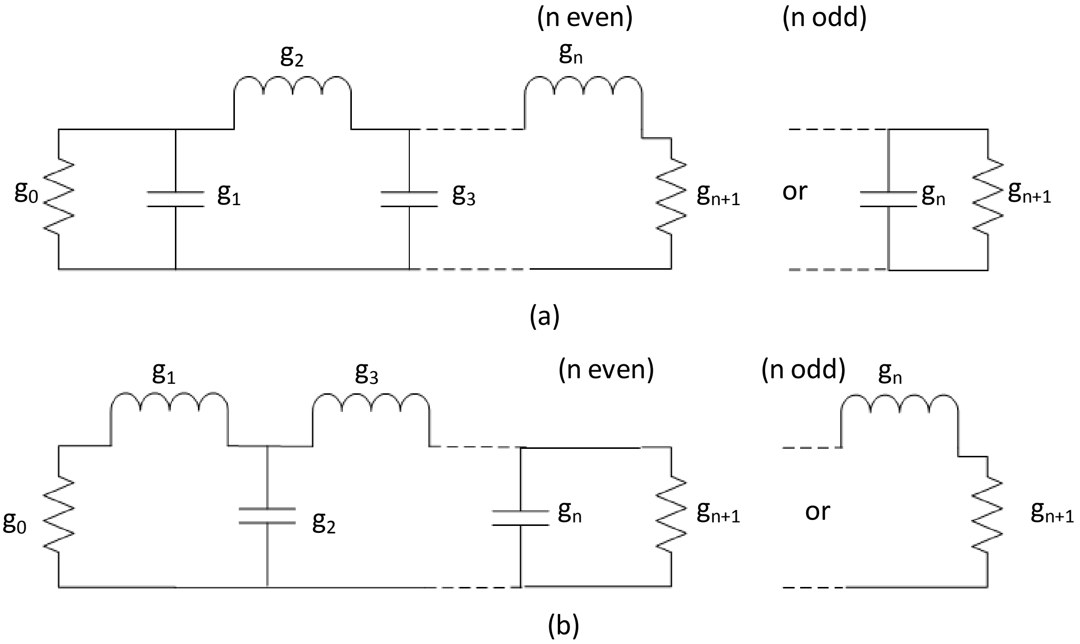

Fig.3- 7 A lowpass prototype filter (a) and its dual (b)

The general synthesis procedure usually commences from a lumped element lowpass prototype filter. A lowpass prototype filter and its dual are shown in Fig.3- 7. A Chebyshev response lowpass prototype filter is chosen in this work. For an n-order lossless passive filter network, the amplitude-squared transfer function can be expressed as

$$\left|S21(j\Omega)\right|^2 = \frac{1}{1+\varepsilon^2 T_n^2(\Omega)} \tag{3.12}$$

where Ω represents an angular frequency variable of a lowpass prototype filter which has a cut-off frequency at $\Omega = \Omega_c$ for $\Omega_c = 1$ (rad/s), ε is the ripple constant and is related to a given passband ripple L_{Ar} in dB by

$$\varepsilon = \sqrt{10^{\frac{L_{Ar}}{10}} - 1} \tag{3.13}$$

$T_n(\Omega)$ is a Chebyshev function of the first kind of order n, which is defined as

$$T_n(\Omega) = \begin{cases} \cos(n\cos^{-1}\Omega) & |\Omega| \le 1 \\ \cosh(n\cosh^{-1}\Omega) & |\Omega| \ge 1 \end{cases} \qquad (3.14).$$

The element values of the prototype filters shown in Fig.3- 7 are normalised to make the source resistance or conductance equal to one ($g_0 = 1$) and the cut-off angular frequency to be unity ($\Omega_c = 1$ rad/s). The normalised element values (g-values) for an n-order Chebyshev lowpass prototype filter with a passband ripple L_{Ar} (dB) can be calculated as follows

$$\begin{aligned} & g_0 = 1 \\ & g_1 = \frac{2a_1}{\gamma} \\ & g_i = \frac{4a_{i-1}a_i}{b_{i-1}g_{i-1}} \qquad i = 2,3,\cdots n \\ & g_{n+1} = \begin{cases} 1 & \text{for n odd} \\ \coth^2(\frac{\beta}{4}) & \text{for n even} \end{cases} \end{aligned} \qquad (3.15)$$

where

$$\begin{aligned} & \beta = \ln\left(\coth\frac{L_{Ar}}{17.37}\right) \\ & \gamma = \sinh\left(\frac{\beta}{2n}\right) \\ & a_i = \sin\frac{(2i-1)\pi}{2n} \qquad i = 1,2,\cdots n \\ & b_i = \gamma^2 + \sin^2\left(\frac{i\pi}{n}\right) \qquad i = 1,2,\cdots n \end{aligned} .$$

3.2.2 Frequency and element transformations

The normalised lowpass prototype filter can be mapped to a practical frequency domain ω where lowpass, highpass, bandpass or bandstop response can be exhibited. In addition to the frequency transformation, impedance scaling is required to shift the source impedance from the $g_0 = 1$ normalisation to a desired impedance Z_0. The frequency transformation from a lowpass prototype to a practical lowpass filter with a cut-off frequency ω_c is given by

$$\Omega=\left(\frac{\Omega_c}{\omega_c}\right)\omega \qquad (3.16).$$

The element transformation is accomplished by applying (3.16) together with the impedance scaling to a desired source impedance Z_0, which can be expressed by

$$\begin{aligned} L &= \left(\frac{\Omega_c}{\omega_c}\right)Z_0 g \quad \text{with g representing the inductance} \\ C &= \left(\frac{\Omega_c}{\omega_c}\right)\frac{g}{Z_0} \quad \text{with g representing the capacitance} \end{aligned} \qquad (3.17).$$

The lowpass prototype can be transformed to a bandpass response with a passband (ω_2-ω_1) by

$$\Omega=\frac{\Omega_c}{FBW}\left(\frac{\omega}{\omega_0}-\frac{\omega_0}{\omega}\right) \qquad (3.18)$$

with

$$\begin{aligned} FBW &= \frac{\omega_2-\omega_1}{\omega_0} \\ \omega_0 &= \sqrt{\omega_1\omega_2} \end{aligned}$$

where ω_1 and ω_2 indicate the lower and upper passband edge angular frequency, ω_0 denotes the centre angular frequency and FBW is the fractional bandwidth. The inductive or capacitive element g in the lowpass prototype will transform to a series or parallel LC resonant circuit respectively in the bandpass filter as shown in Fig.3- 8.

The elements for the series LC resonator circuit are expressed by

$$\begin{cases} L_s = \left(\dfrac{\Omega_c}{FBW\omega_0}\right)Z_0 g \\ C_s = \left(\dfrac{FBW}{\omega_0\Omega_c}\right)\dfrac{1}{Z_0 g} \end{cases} \quad \text{with g representing the inductance} \qquad (3.19).$$

The parallel LC resonator circuit are expressed by

$$\begin{cases} C_p = \left(\dfrac{\Omega_c}{FBW\omega_0}\right)\dfrac{g}{Z_0} \\ L_p = \left(\dfrac{FBW}{\omega_0\Omega_c}\right)\dfrac{Z_0}{g} \end{cases} \quad \text{with g representing the capacitance} \qquad (3.20).$$

It should be noted that $\omega_0 L_s = 1/\omega_0 C_s$ and $\omega_0 L_p = 1/\omega_0 C_p$.

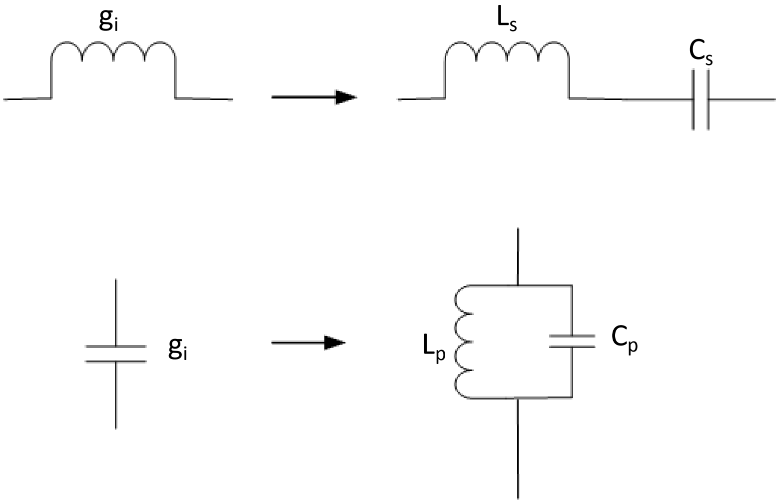

Fig.3- 8 Basic element transformation from a lowpass prototype to a bandpass filter

3.2.3 Immittance inverters

The lowpass or bandpass filters generated above have both series and shunt elements and may be difficult to realise in practice [11]. Immittance inverters can be used to transform these elements to equivalent forms which use only series or shunt elements. Immittance inverters are either impedance (K) or admittance (J) inverters. The K inverters can be used to transform shunt connected elements to series connected elements, whereas the J inverters transform series connected elements to shunt elements [12]. The symbolised K and J inverter are shown in Fig.3- 9.

An idealised impedance inverter is a two port network which has a unique property at all frequencies. If an impedance inverter is terminated in an impedance Z_L at one end, the impedance Z_{in} seen looking in at the other end is

$$Z_{in} = \frac{K^2}{Z_L} \tag{3.21}$$

where K is the characteristic impedance of the inverter and is real. Therefore the inverter has a phase shift of ±90° or an odd multiple of it. Likewise, if an admittance inverter is terminated in an admittance Y_L at one end, the admittance Y_{in} seen looking in at the other end is

$$Y_{in} = \frac{J^2}{Y_L} \tag{3.22}$$

where J is real and is the characteristic admittance of the inverter.

A quarter wavelength transmission line with appropriate characteristic impedance is a simplest form of K or J inverter. Besides, other implementations which can produce a phase shift of some odd multiple of ±90° can be also used as immittance inverters. Examples of practical implementations of inverters can be found in [12].

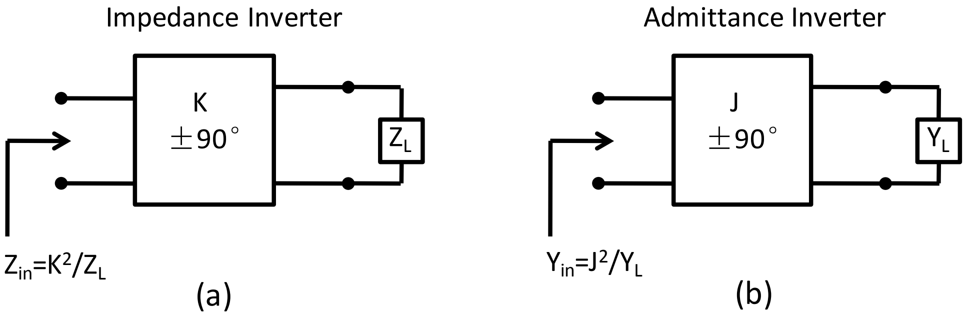

Fig.3- 9 Symbolised impedance (a) and admittance inverter (b) [13]

3.2.4 Filters using immittance inverters

By making use of the immittance inverters, the prototype circuits in Fig.3- 7 can be converted to either of the equivalent form in Fig.3- 10. The new element values such as Z_0, Y_0, Z_{n+1}, Y_{n+1}, L_{ai}, C_{ai} can be chosen arbitrarily and remain identical in response to the original prototypes, providing that the immittance inverter parameters $K_{i,i+1}$ and $J_{i,i+1}$ are specified following the relations

$$\begin{cases} K_{0,1} = \sqrt{\dfrac{Z_0 L_{a1}}{g_0 g_1}} \\ K_{i,i+1}\big|_{i=1 \text{ to } n-1} = \sqrt{\dfrac{L_{ai} L_{a(i+1)}}{g_i g_{i+1}}} \\ K_{n,n+1} = \sqrt{\dfrac{L_{an} Z_{n+1}}{g_n g_{n+1}}} \end{cases} \qquad \begin{cases} J_{0,1} = \sqrt{\dfrac{Y_0 C_{a1}}{g_0 g_1}} \\ J_{i,i+1}\big|_{i=1 \text{ to } n-1} = \sqrt{\dfrac{C_{ai} C_{a(i+1)}}{g_i g_{i+1}}} \\ J_{n,n+1} = \sqrt{\dfrac{C_{an} Y_{n+1}}{g_n g_{n+1}}} \end{cases} \tag{3.23}$$

where the g_i values are defined as for the lowpass prototype filter discussed earlier.

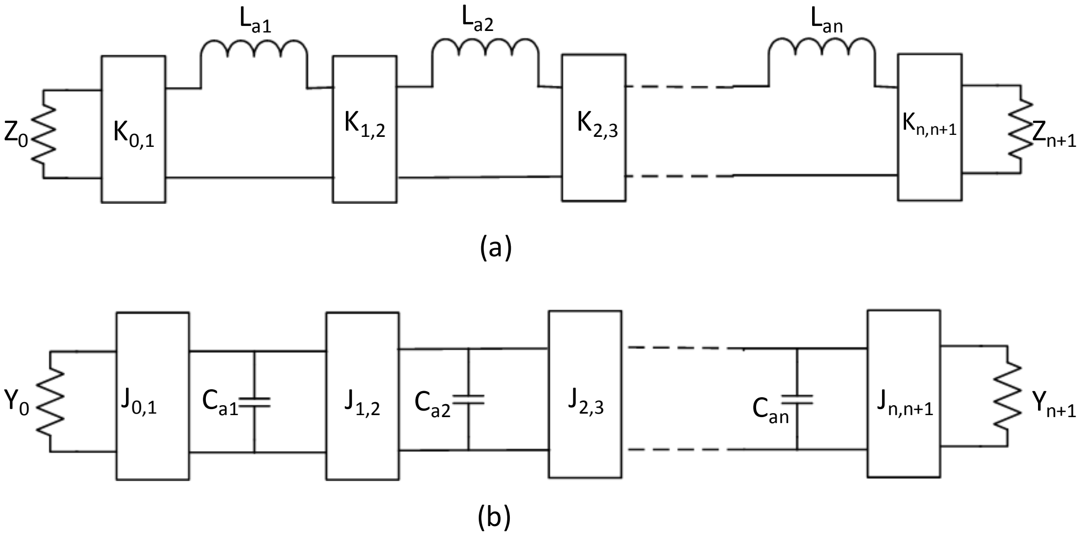

Fig.3- 10 Lowpass filter using impedance (a) or admittance (b) inverters

By applying the element transformation defined in equation (3.19) and (3.20) to equation (3.23), the lowpass prototype filters can be easily transformed to bandpass filters with immittance inverters. Fig.3- 11 (a) illustrates a bandpass filter with K inverters and only series resonators, whereas the filter in Fig.3- 11 (b) consists of J inverters and only shunt parallel resonators. The K/J inverters can be expressed as

$$\begin{cases} K_{0,1}=\sqrt{\dfrac{Z_0 FBW\omega_0 L_{s1}}{\Omega_c g_0 g_1}} \\ K_{i,i+1}\Big|_{i=1\text{ to }n-1}=\dfrac{FBW\omega_0}{\Omega_c}\sqrt{\dfrac{L_{si}L_{s(i+1)}}{g_i g_{i+1}}} \\ K_{n,n+1}=\sqrt{\dfrac{FBW\omega_0 L_{sn} Z_{n+1}}{\Omega_c g_n g_{n+1}}} \\ C_{si}\Big|_{i=1\text{ to }n}=\dfrac{1}{\omega_0^2 L_{si}} \end{cases} \qquad \begin{cases} J_{0,1}=\sqrt{\dfrac{Y_0 FBW\omega_0 C_{p1}}{\Omega_c g_0 g_1}} \\ J_{i,i+1}\Big|_{i=1\text{ to }n-1}=\dfrac{FBW\omega_0}{\Omega_c}\sqrt{\dfrac{C_{pi}C_{p(i+1)}}{g_i g_{i+1}}} \\ J_{n,n+1}=\sqrt{\dfrac{FBW\omega_0 C_{pn} Y_{n+1}}{\Omega_c g_n g_{n+1}}} \\ L_{pi}\Big|_{i=1\text{ to }n}=\dfrac{1}{\omega_0^2 C_{pi}} \end{cases} \qquad (3.24)$$

In this way identical resonators can be cascaded together with appropriate K/J inverters to realise practical filters.

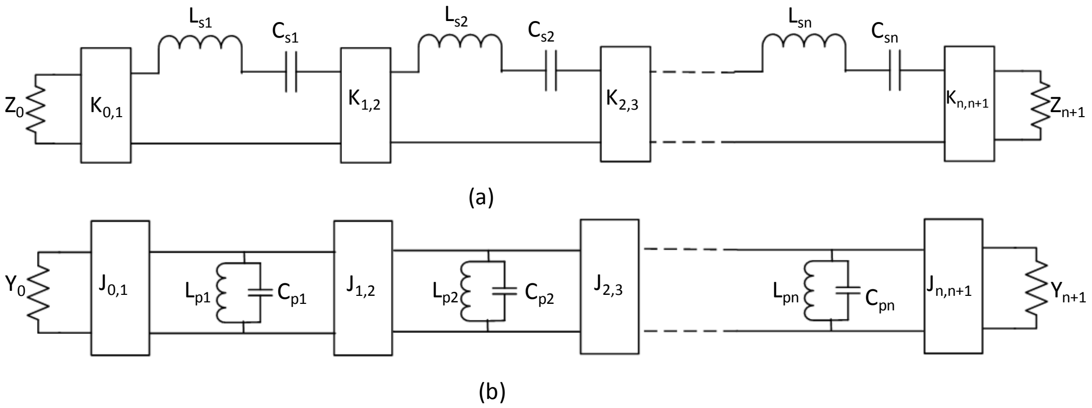

Fig.3- 11 Bandpass filters with series resonators only using impedance inverters (a) and shunt resonators only using admittance inverters (b)

The lumped LC resonators can be replaced by distributed resonators as long as they have an equal reactance/susceptance slope parameter [12]. The reactance slope parameter, χ, of a resonator regardless its form can be defined as [12]

$$\chi=\frac{\omega_0}{2}\frac{dX(\omega)}{\omega}\Big|_{\omega=\omega_0} \qquad (3.25)$$

where X(ω) is the reactance of the resonator. The susceptance slope parameter, b, is defined as [12]

$$b = \frac{\omega_0}{2}\frac{dB(\omega)}{d\omega}\bigg|_{\omega=\omega_0} \tag{3.26}$$

where $B(\omega)$ is the susceptance of the resonator. Ideally the reactance/susceptance of the distributed resonator should be equal to that of the lumped LC resonator at all frequencies. However, in practice, this is normally only valid near resonance, which is sufficient for narrow band filters. For a LC series resonator,

$$\chi = \frac{\omega_0}{2}\frac{d}{\omega}\left(\omega L - \frac{1}{\omega C}\right)\bigg|_{\omega_0} = \omega_0 L = \frac{1}{\omega_0 C} \qquad (3.27).$$

For a LC parallel resonator, the dual of the series resonator,

$$b = \frac{\omega_0}{2}\frac{d}{\omega}\left(\omega C - \frac{1}{\omega L}\right)\bigg|_{\omega_0} = \omega_0 C = \frac{1}{\omega_0 L} \qquad (3.28).$$

Hence, by replacing $\omega_0 L_{si}$ and $\omega_0 C_{pi}$ in equation (3.24) with the general terms χ_i and b_i as defined by (3.27) and (3.28), the J/K inverters can be generated by

$$\begin{cases} K_{0,1} = \sqrt{\dfrac{Z_0 FBW \chi_1}{\Omega_c g_0 g_1}} \\ K_{i,i+1}\big|_{i=1 \text{ to } n-1} = \dfrac{FBW}{\Omega_c}\sqrt{\dfrac{\chi_i \chi_{i+1}}{g_i g_{i+1}}} \\ K_{n,n+1} = \sqrt{\dfrac{FBW \chi_n Z_{n+1}}{\Omega_c g_n g_{n+1}}} \\ \chi_i = \dfrac{\omega_0}{2}\dfrac{dX_i(\omega)}{\omega}\bigg|_{\omega=\omega_0} \end{cases} \qquad \begin{cases} J_{0,1} = \sqrt{\dfrac{Y_0 FBW b_1}{\Omega_c g_0 g_1}} \\ J_{i,i+1}\big|_{i=1 \text{ to } n-1} = \dfrac{FBW}{\Omega_c}\sqrt{\dfrac{b_i b_{i+1}}{g_i g_{i+1}}} \\ J_{n,n+1} = \sqrt{\dfrac{FBW b_n Y_{n+1}}{\Omega_c g_n g_{n+1}}} \\ b_i = \dfrac{\omega_0}{2}\dfrac{dB_i(\omega)}{d\omega}\bigg|_{\omega=\omega_0} \end{cases} \tag{3.29}$$

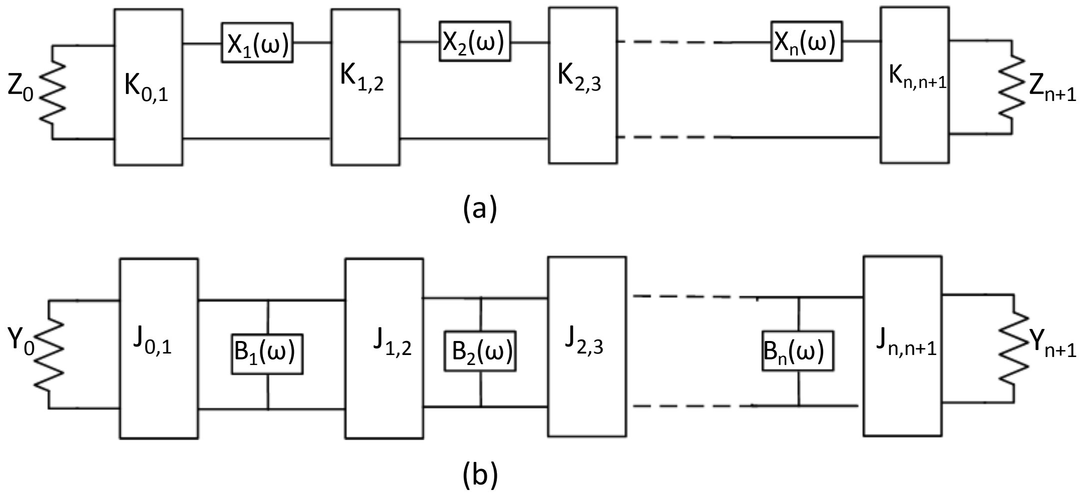

Fig.3- 12 Generalised bandpass filter circuits using impedance (a) and admittance (b) inverters

3.2.5 Coupled resonator filter

Coupled resonator filters can be also represented by the circuits shown in Fig.3- 12 and the J/K inverters represent the coupling. A general technique to design the coupled resonator circuit is briefly outlined as follows. A more detailed analysis of the theory of the coupled resonator circuits can be found in [12].

An n-coupled resonator filter topology can be represented by terms of coupling coefficients M_{ij} and external quality factors Q_e despite the physical structure of the resonator or the type of coupling. Coupling coefficient M_{ij} defines the coupling strength between the i-th and j-th resonators. m_{ij} is the so-called normalised coupling coefficient, defined as

$$m_{ij} = \frac{M_{ij}}{FBW}$$

where FBW is the fractional bandwidth of the filter. A general coupling matrix [m] is comprised of the normalised coupling coefficients and is an n×n reciprocal matrix (i.e., $m_{ij}=m_{ji}$). For a synchronously tuned filter (i.e. all the resonators have the same resonant frequency), the diagonal entries m_{ii} of the coupling matrix is zero.

The external quality factor Q_{ei} ($i = 1, n$) denotes the coupling strength of the input/output resonators to the ports. q_{ei} is the scaled external quality factor, defined as

$$q_{ei} = Q_{ei}FBW \quad \text{for } i = 1, n.$$

The frequency response of the filter can be synthesised from the general coupling matrix and the scaled external quality factors as follows

$$\begin{aligned} S21 &= \frac{2}{\sqrt{q_{e1}q_{en}}}[A]^{-1}_{n1} \\ S11 &= \pm\left(1-\frac{2}{q_{e1}}[A]^{-1}_{11}\right) \end{aligned} \tag{3.30}$$

with

$$\begin{aligned} A &= [q]+p[U]-j[m] \\ p &= j\frac{1}{FBW}\left(\frac{\omega}{\omega_0}-\frac{\omega_0}{\omega}\right) \end{aligned}$$

where p is the complex frequency transformation from the lowpass prototype to bandpass filter, [U] is the n×n unit or identity matrix, [q] is an n×n matrix with all entries zero, except for $q_{11}=1/q_{e1}$ and $q_{nn}=1/q_{en}$, q_{e1}, [m] is the general coupling matrix. The above formulation applies to coupled resonator filters regardless the type of coupling is electric, magnetic, or mixed.

The first step of designing a coupled resonator filter is to find the appropriate coupling coefficients M_{ij} and external quality factors Q_e for the desired filter characteristics. For an n-pole bandpass filter, the required M_{ij} and Q_e filter can be derived from its lowpass prototype filter as follows

$$Q_{e1} = \frac{g_0 g_1}{FBW} \tag{3.31}$$

$$Q_{en} = \frac{g_n g_{n+1}}{FBW} \tag{3.32}$$

$$M_{i,i+1} = \frac{FBW}{\sqrt{g_i g_{i+1}}} \quad \text{for i=1 to n-1} \tag{3.33}$$

where Q_{e1} and Q_{en} are the external quality factors of the resonators at the input and output ports, and $M_{i,i+1}$ are the coupling coefficients between the adjacent resonators. g_i is the element value of the lowpass filter prototype. n is the filter order and FBW is the fractional bandwidth of the passband.

After determining the required coupling coefficients and external quality factors, the next step for the filter design is to characterise the coupling coefficients and external quality factors in terms of physical structures.

In general, the coupling coefficient can be defined as the ratio of coupled energy to stored energy [12]

$$M = \frac{\iiint \varepsilon \underline{E}_1 \bullet \underline{E}_2 d\nu}{\sqrt{\iiint \varepsilon |\underline{E}_1|^2 d\nu \times \iiint \varepsilon |\underline{E}_2|^2 d\nu}} + \frac{\iiint \mu \underline{H}_1 \bullet \underline{H}_2 d\nu}{\sqrt{\iiint \mu |\underline{H}_1|^2 d\nu \times \iiint \mu |\underline{H}_2|^2 d\nu}} \tag{3.34}$$

where $\underline{E}$ and $\underline{H}$ represent the electric and magnetic field vectors, and subscript 1 and 2 denote resonators 1 and 2 respectively. The first term on the right hand side represents the electric coupling and the second term the magnetic coupling. It should be noted that the interaction of the coupled resonators is mathematically described by the dot product of their space vector fields, which gives either positive or negative sign of the coupling. A positive sign indicates the stored energy of the uncoupled resonators is enhanced by the coupling, whereas a negative sign indicates a reduction. The electric and magnetic coupling can therefore have the same or opposite effect depending whether they have the same sign or not. Obviously, it is difficult to identify the coupling coefficient using equation (3.34), which requires full knowledge of field distribution and space integral performance. Instead, the coupling coefficient can be found by the frequency response of two coupled resonators from the full wave electromagnetic simulation or experiment as follows.

The typical frequency response of two coupled resonators is shown in Fig.3- 13, irrespective of the type of coupling. Normally, the stronger the coupling between the resonators (the bigger the coupling coefficient), the larger the separation of the two split resonances and the deeper the trough in the middle. The coupling coefficient can be extracted from frequency response of the coupled resonators regardless of the type of coupling as [12]

$$\mathrm{M}_{\mathrm{ij}} = \pm \frac{f_2^2 - f_1^2}{f_2^2 + f_1^2} \tag{3.35}$$

where f_1 is the lower resonance frequency and f_2 is the upper resonance frequency.

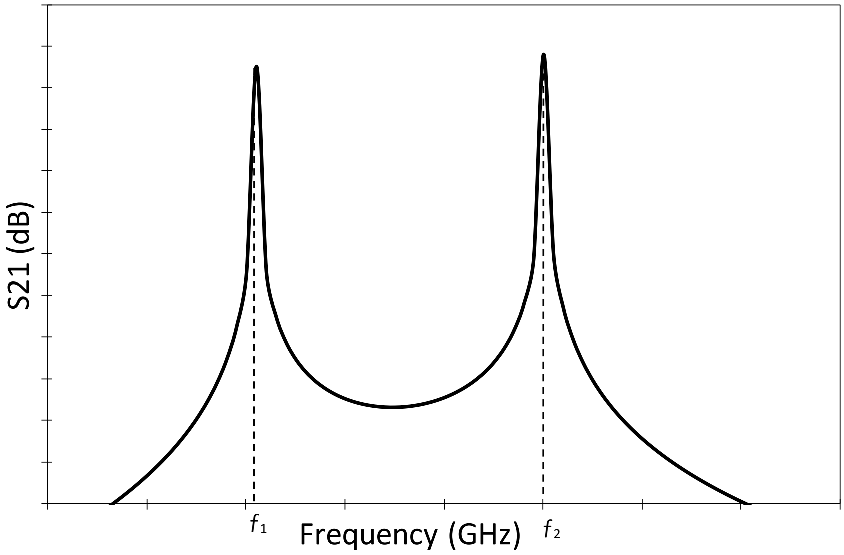

Fig.3- 13 Typical frequency response of two coupled resonators

The external Q_e can be also found from the frequency response of an external coupled resonator from simulation or measurement. The external input/output coupling are mainly realised by tapped line or coupled line structures. It should be noted that when extracting the external Q_e, the resonator is properly coupled to one port only. The other port should be very weakly coupled to the resonator, for instance, without using tapped line or a big gap for the coupled line structure at the other port, to reduce its effect on the extracting of the external Q_e. The typical frequency response of an input/output coupled resonator is shown in Fig.3- 14 and the external quality factor can be extracted as [12]

$$\mathrm{Q}_{\mathrm{e}} = \frac{\omega_0}{\Delta\omega_{3\mathrm{dB}}} = \frac{f_0}{f_{\mathrm{b}} - f_{\mathrm{a}}} \tag{3.36}$$

where $\Delta\omega_{3\mathrm{dB}}$ is the bandwidth for which the attenuation of S_{21} is 3 dB from that at resonance. The wider, or larger the bandwidth of the response is, the smaller the Q_e is, which also means a stronger external coupling to the input/output ports.

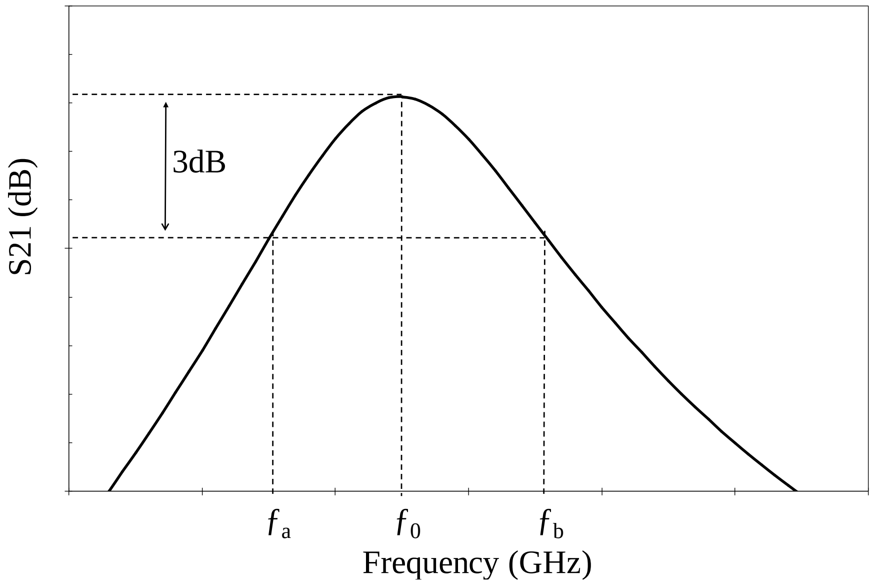

Fig.3- 14 Typical frequency response of an externally coupled resonator

These foregoing formulations will be used in chapter 5 and 6 to predict the performance of the coupled resonator bandpass filters.

3.2.6 Dissipation effect

Practical microwave filters are lossy and have finite quality factors. The unloaded quality factor Q of a component is defined as [14]

$$Q_u = \omega \frac{\text{average energy stored}}{\text{average energy dissipated}} \tag{3.37}$$

For lumped elements, if the loss resistance is modelled in series with the reactance, the unloaded Q is [14]

$$Q_u = \frac{\omega L}{R_s} = \frac{1}{\omega C R_s} \tag{3.38}$$

and if the loss resistance is in parallel with the reactance,

$$Q_u = \frac{R_p}{\omega L} = \omega C R_p \tag{3.39}$$

In the case of a resonator is comprised of a transmission line loaded a ferroelectric varactor, the energy is dissipated in the conductors, in the ferroelectric material, in the substrate dielectric, and by radiation. The total unloaded quality factor can be expressed as

$$\frac{1}{\mathrm{Q}}=\frac{1}{\mathrm{Q_c}}+\frac{1}{\mathrm{Q_{FE}}}+\frac{1}{\mathrm{Q_d}}+\frac{1}{\mathrm{Q_r}} \tag{3.40}$$

where $\mathrm{Q_c}$, $\mathrm{Q_{FE}}$, $\mathrm{Q_d}$ and $\mathrm{Q_r}$ stands for the conductor resistive loss, the ferroelectric loss, the dielectric loss of the substrate, and loss from the radiation respectively. The ferroelectric loss and dielectric loss are determined by the loss tangent of the ferroelectric material and the substrate dielectric respectively.

The unloaded quality factor $\mathrm{Q_u}$ denotes the intrinsic component quality and is different from the measured quality factor, or the loaded quality factor $\mathrm{Q_L}$, which also includes the loss associated with the external coupling $\mathrm{Q_e}$. The $\mathrm{Q_L}$ is expressed as [14]

$$\frac{1}{\mathrm{Q_L}}=\frac{1}{\mathrm{Q_u}}+\frac{1}{\mathrm{Q_e}} \tag{3.41}$$

The $\mathrm{Q_L}$ is assumed to be equal to $\mathrm{Q_u}$ in case of a very low external coupling [15]. The $\mathrm{Q_L}$ can be found by simulation or experimentally in terms of resonant frequency f_0 and 3 dB bandwidth $\mathrm{BW_{3dB}}$ of the resonator circuit, as stated below [14]

$$\mathrm{Q_L}=\frac{f_0}{\mathrm{BW_{3dB}}} \tag{3.42}$$

The $\mathrm{Q_u}$ can be related to the $\mathrm{Q_L}$ by the transmission coefficient $\mathrm{S_{21}}$ at the centre frequency as follows if the resonator is equally coupled at both the input and output ports [15]

$$\mathrm{Q_u}=\frac{\mathrm{Q_L}}{1-|\mathrm{S_{21}}(f_0)|}=\frac{\mathrm{Q_L}}{1-10^{-\mathrm{IL}/20}} \tag{3.43}$$

where IL is the transmission loss in dB at the centre frequency. Usually when the IL is more than 20 dB, the resonator can be regarded as weakly coupled [16].

The dissipation of a bandpass filter can be estimated from the quality factor of the resonators as follows [12]

$$\mathrm{IL}_{f_0} = 4.343\sum_{i=1}^{n} \frac{\Omega_c}{\mathrm{FBW}\,Q_i} g_i \ \mathrm{dB} \tag{3.44}$$

where IL_{f0} is the insertion loss in dB at the centre frequency of the filter, $\Omega_c = 1$, FBW is the fractional bandwidth of the filter and the Q_i are the unloaded quality factors of the resonators corresponding to element g_i.

3.3 Lumped element modelling

Lumped inductors and capacitors are analysed and modelled in this section. Both ferroelectric parallel plate and interdigital capacitors are used as the tuning elements of the filters discussed in chapters 4, 5 and 6. They are used in both integrated and discrete forms. The schematic layout of ferroelectric parallel plate and interdigital capacitors have been shown in Fig.2-17 in chapter 2. Meander line inductors are used in the ferroelectric lowpass filters discussed in chapter 4.

3.3.1 Parallel plate capacitor

In chapters 4 and 5, $5 \times 5\ \mu m^2$ and $10 \times 10\ \mu m^2$ square parallel plate capacitors are integrated in the ferroelectric lowpass and bandpass filters. For parallel plate capacitors, the calculation of the capacitance is quite straight forward. The capacitance of a square parallel plate capacitor is defined as

$$C = \frac{\varepsilon_0 \varepsilon_r l^2}{t} \tag{3.45}$$

In equation (3.45) the fringe effect has not been considered and ε_0, ε_r, l and t are the permittivity of free space, the relative permittivity of the ferroelectric thin film, the side of the square capacitor and the thickness of the ferroelectric thin film respectively. Examples of the capacitance as a function of the ferroelectric permittivity for capacitor sizes of $l = 5$ µm or 10 µm and t = 100 nm, 500 nm, 1000 nm are shown in Fig.3- 15. The solid lines and dashed lines represent $5 \times 5\ \mu m^2$ and $10 \times 10\ \mu m^2$ capacitors respectively. As can be seen, for capacitors size of 5 × 5 μm^2 and 10 × 10 μm^2, a capacitance range of 0.01 - 10 pF can be achieved for the ferroelectric permittivity in the range of 100 - 1000 and thickness between 100 nm and 1000 nm. For given capacitors size of 5 × 5 μm^2 or 10 × 10 μm^2, a fixed capacitance of 0.2 pF or 1 pF can be realised by different combination of permittivity and thickness, as shown in Fig.3- 16.

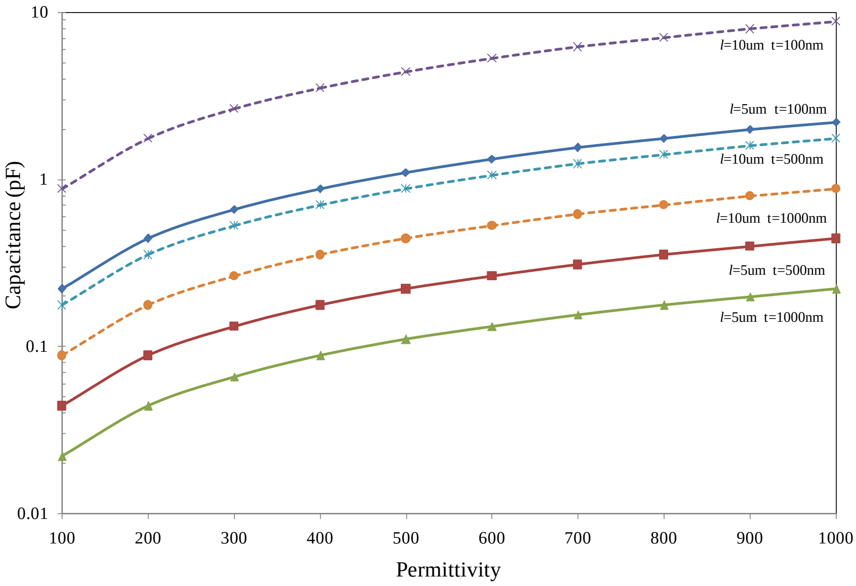

Fig.3- 15 Capacitance versus permittivity for 5 × 5 μm^2 (solid lines) and 10 × 10 μm^2 (dashed lines) capacitors with the ferroelectric thickness t = 100 nm, 500 nm and 1000 nm.

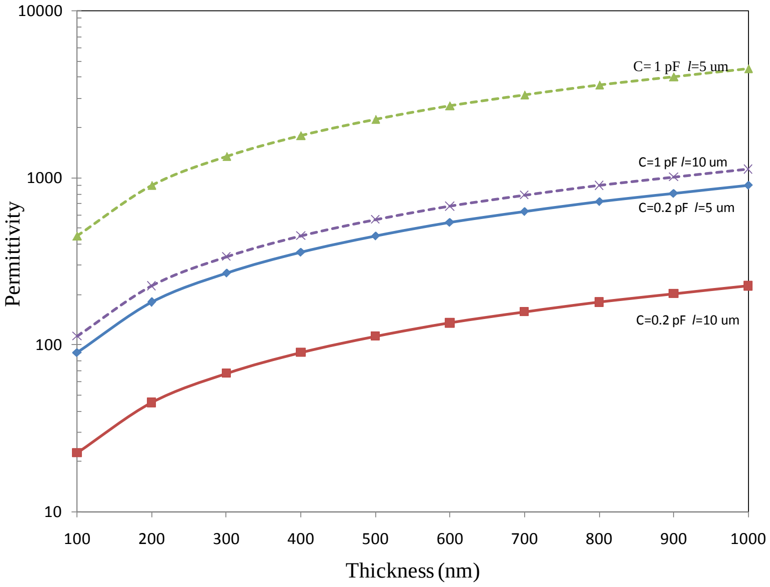

Fig.3- 16 Different ways to realise 0.2 pF (solid lines) and 1 pF (dashed lines) parallel plate capacitors

3.3.2 Interdigital capacitor

In chapter 6, interdigital capacitors (IDCs) are fabricated and mounted on duroid laminate bandpass filters in a hybrid manner. The capacitance of an IDC patterned on a ferroelectric thin film/substrate can be estimated from the following expression [17]

$$C = \frac{\varepsilon_0}{2}(n-\Delta)l + \frac{\varepsilon_0\varepsilon_2}{2}(n-\Delta)l + \frac{\varepsilon_0(\varepsilon_1-\varepsilon_2)(n-1)l}{0.882+\frac{g}{h_1}} \qquad (3.46)$$

where ε_1, ε_2 are the relative permittivity of ferroelectric layer and substrate respectively, l is the finger length, g is the gap between fingers and h_1 is the thickness of ferroelectric thin film. $\Delta = 0.5$ is a limiting value for n large [18]. The three terms on the right side of the equation refer to the capacitance contributed by the air, substrate and ferroelectric thin film respectively. 0.882 in the denominator of the third term accounts for the electric field at edges of the fingers and is derived by the conformal mapping technique [17], [18].

Alternatively, ferroelectric IDCs can be simulated by Sonnet and the lumped element SPICE model can be synthesised automatically from the electromagnetic analysis of the circuits as long as the circuit is small with respect to the wavelength [10]. The schematic layout of an IDC in Sonnet is shown in Fig.3- 17 (a) and a Π-model circuit is obtained from SPICE as shown in Fig.3- 17 (b). C_{12} represents the series capacitance between port 1 and 2, which is the capacitance of the IDC, and C_{10}, C_{20} represent the capacitance shunt to ground, which is parasitic.

IDCs with different finger number, finger length and gap are calculated analytically using equation (3.46) and also simulated by Sonnet for comparison. In the calculation, the permittivity of the ferroelectric layer and substrate are 500 and 9.8 respectively and the thickness of the ferroelectric is 500 nm. In the simulation the substrate is assumed to be 0.5 mm thick MgO. The calculated capacitance compares very well with the capacitance obtained by simulation as shown in Fig.3- 18.

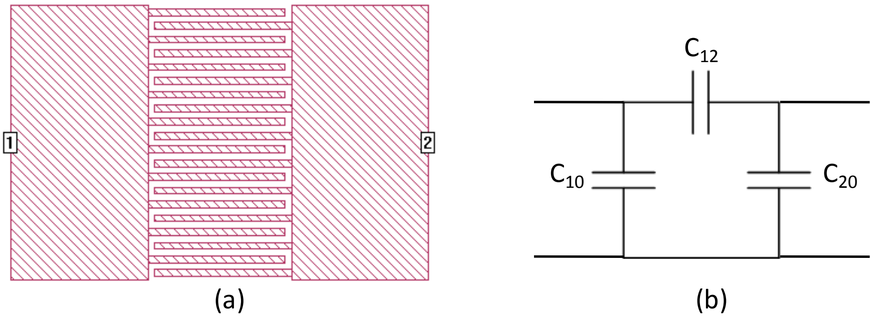

Fig.3- 17 A representative IDC layout in Sonnet (a) and its circuit model (b)

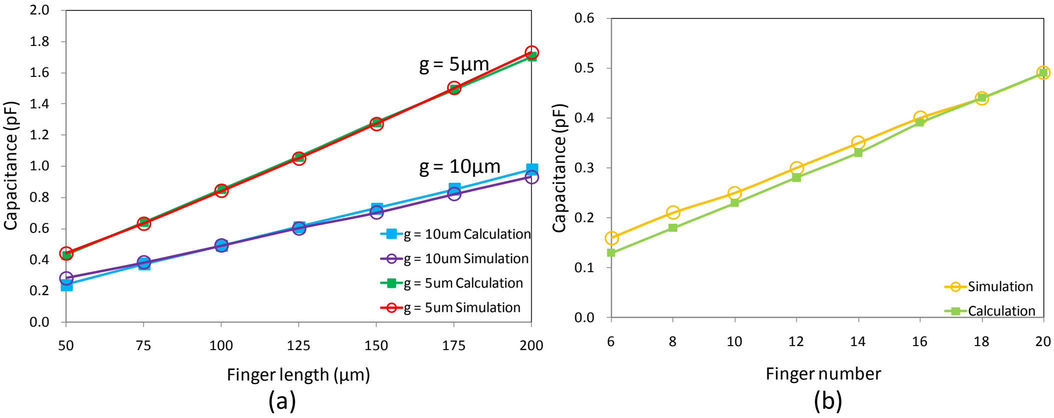

Fig.3- 18 Capacitance versus finger length for an IDC with 5 μm or 10 μm gap and 20 fingers (a) and capacitance versus finger number for an IDC with 10 μm gap, 100 μm finger length (b). The open circles represent results from simulation obtained at 1 GHz and the solid squares represent results calculated from equation (3.46).

3.3.3 Meander line inductor

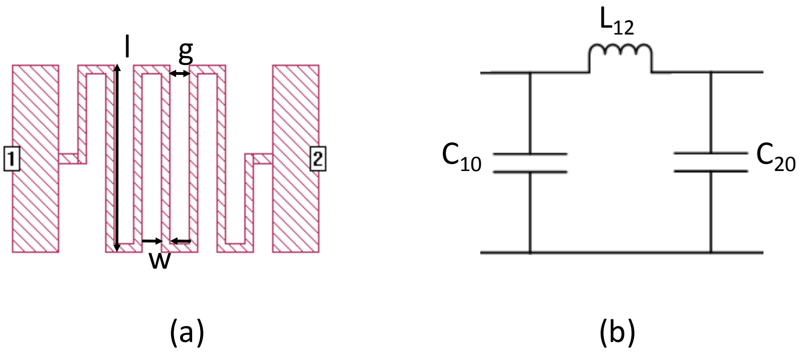

Fig.3- 19 A typical meander line inductor in Sonnet (a) and its equivalent circuit (b)

The meander and spiral are two common forms for making miniaturised thin film planar inductors. Although meander line inductors often exhibit larger size and lower quality factor compared with spiral inductors of the same inductance, they have the advantage of a simple process of fabrication as no vias are required [19]. Parameters defining a meander inductor are the length of the leg *l*, the distance between adjacent conductors g, the width of the conductor strip w and the number of turns as shown in Fig.3- 19 (a). A Π-model SPICE circuit (see Fig.3-19 (b)) can be obtained easily from Sonnet simulation, where the inductance of the meander line is represented by the series inductance L_{12}, and C_{10}, C_{20} refer to the parasitic capacitance shunt to ground. For example, a meander inductor with n = 6, *l* = 0.2 mm, w = 0.02 mm and g = 0.04 mm has been simulated and a series inductance of 0.98 nH is obtained at 1 GHz. Obviously, the inductance is proportional to the leg length *l*, the number of turns n and a closer gap will reduce the inductance as the mutual inductance between adjacent lines has a minus sign.

3.4 Summary

In this chapter single and multilayer coplanar waveguides were analysed using the quasi-TEM approximation and the conformal mapping technique. The general Chebyshev lowpass and bandpass filter synthesis procedure was reviewed. The general design method for coupled resonator filters was presented. The analytical calculation of the characteristics of CPW lines and filters will be used in chapters 4, 5 and 6 to predict the performance of the lowpass and bandpass tunable filters based on ferroelectric varactors. In addition, lumped capacitors and inductors were modelled and analysed. The next chapter will present a seventh order Chebyshev lowpass filter incorporating integrated ferroelectric varactors as tuning elements.

References

[1] R. E. Collin, Foundations for Microwave Engineering, McGraw-Hill, 1992.

[2] C. P. Wen, "Coplanar waveguide: a surface strip transmission line suitable for nonreciprocal gyromagnetic device applications", *IEEE Transactions on Microwave Theory and Techniques*, vol. 17, no. 12, pp. 1087-1090, 1969.

[3] R. N. Simons, Coplanar Waveguide Circuits, Components and Systems, 1st ed., Wiley-Interscience, 2001.

[4] L. Jongjoo, L. Heeseok, K. Woopoung, Jaehoon Lee, and Joungho Kim, "Suppression of coupled-slotline mode on CPW using air-bridges measured by picosecond photoconductive sampling", *Microwave and Guided Wave Letters,* vol. 9, no. 7, pp. 265-267, 1999.

[5] L. Chung-Yi, L. Yaozhong, and I. Tatsuo, "The effects of the coupled slotline mode and air-bridges on CPW and NLC waveguide discontinuities", *IEEE Transactions on Microwave Theory and Techniques,* vol. 43, no. 12, pp. 2759-2765, 1995.

[6] Y.-D. Lin and J.-W. Sheeen, "Surface wave leakage of coplanar waveguide with nearby back conductor plane", in *IEEE MTT-S Digest*1994, pp. 1704-1704.

[7] E. Carlsson and S. Gevorgian, "Conformal mapping of the field and charge distributions in multilayered substrate CPWs", *IEEE Transactions on Microwave Theory and Techniques,* vol. 47, no. 8, pp. 1544-1552, 1999.

[8] S. Gevorgian, L. J. P. Linner, and E. L. Kollberg, "CAD models for shielded multilayered CPW", *IEEE Transactions on Microwave Theory and Techniques,* vol. 43, no. 4, pp. 772-779, 1995.

[9] M. J. Lancaster, J.Powell, and A.Porch, "Thin-film ferroelectric microwave devices", *Supercondoctor Science and Technology,* vol. 11, no. pp. 1323-1334, 1998.

[10] "Sonnet User's Guide, Release 10": Sonnet Softerware, Inc., 2004.

[11] G.L.Matthaei, L.Young, and E.M.T.Jones, Microwave filters, impedance matching networks, and coupling structures, Artech House, 1980.

[12] J.-S. Hong and M. J. Lancaster, Microstrip Filters for RF/Microwave Applications, John Wiley & Sons,Inc., 2001.

[13] D. M. Pozar, Microwave Engineering, 2nd ed. New York, USA, John Wiley & Sons, Inc., 1998.

[14] T. K. Ishii, Handbook of Microwave Technology, Volume 1, Components and Devices, Academic Press, Inc., 1995.

[15] K. Leong, J. Mazierska, and J. Krupka, "Measurements of unloaded Q-factor of transmission mode dielectric resonators", in *IEEE MTT-S International Microwave Symposium Digest*1997, pp. 1639-1642.

[16] Y. Wang, "Supercondcting coplanar delay lines", Doctor of Philosophy thesis, Electronic, Electrical and Computer Engineering, The university of Birmingham, 2005

[17] H. T. Su, M. J. Lancaster, F. Huang, and F. Wellhofer, "Electrically tunable superconducting quasilumped element resonator using thin-film ferroelectrics", *Microwave and Optical Technology Letters*, vol. 24, no. 3, pp. 155-157, 2000.

[18] F. Huang, B. Avenhaus, and M. J. Lancaster, "Lumped-element switchable superconducting filters", *IEE Proceedings of Microwaves, Antennas and Propagation,* vol. 146, no. 3, pp. 229-233, 1999.

[19] G. Stojanovic, L. Zivanov, and M. Damjanovic, "Compact form of expressions for

inductance calculation of meander inductors", *Serbian Journal of Electrical Engineering,* vol. 1, no. 3, pp. 57-68, 2004.

CHAPTER 4

FERROELECTRIC LOWPASS FILTERS INCORPORATING INTEGRATED BST THIN FILM VARACTORS

This chapter describes a K-band tunable lowpass filter incorporating integrated thin film Barium Strontium Titanate (BST) varactors. The filter was implemented in a coplanar waveguide (CPW) configuration on a high resistivity silicon substrate using a seventh order Chebyshev lowpass filter prototype. Parallel plate BST capacitors as small as 5 µm × 5 µm were incorporated, and formed the tuning elements. The design procedure is addressed in detail with full wave electromagnetic (EM) simulation performed. The fabrication process including BST thin film deposition and two metal layers photolithography is described step by step. The measured results of the lowpass filter are presented, discussed and compared with simulations. In addition, several lowpass filters covering a wide frequency range, using different size inductors or capacitors, are presented as well. An improved layout aiming at reducing the loss of the bottom electrodes is also presented.

4.1 Filter design

Although no particular filter specification is given in this project, the project aims at developing advanced frequency agile microwave/millimetre-wave devices with miniaturised size, taking advantages of ferroelectric thin films. A tunable low pass filter is chosen as an example and discussed in this chapter.

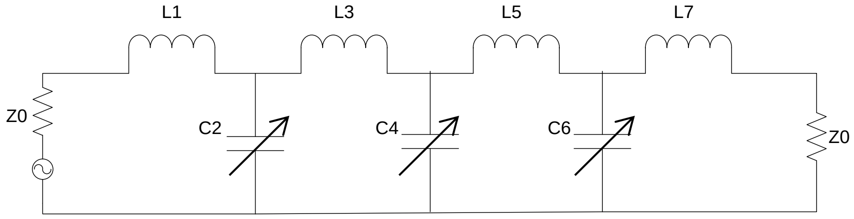

Fig.4- 1 The schematic circuit of a seventh order lowpass filter

The lowpass filter consists of inductors in series and variable capacitors shunted to ground as shown in Fig.4- 1. BST parallel plate capacitors were used as the shunt varactor, which were the tuning elements of the filter. The capacitance of a BST parallel plate capacitor changes with the application of an electric field. Hence, the cut-off frequency of the lowpass filter can be tuned by applying a DC bias. The capacitors use a parallel plate configuration, as discussed in chapter 2, which can benefit the circuit in terms of a very compact size, high tunability and low bias voltage requirement compared with interdigital structure. To have a useful capacitance in the microwave region, the size of the capacitors needs to be extremely small (dimension from several microns to tens of microns) due to the high dielectric constant of BST thin film, which substantially miniaturised the device size. Due to the small thickness of the film (< 1 μm) the capacitor can be approximated as parallel plate capacitor and its capacitance can be estimated without considering the fringe field effect, giving a capacitance of

$$C = \frac{\varepsilon_0 \varepsilon_r A}{t} \tag{4.1}$$

where ε_0, ε_r, A and t are permittivity of free space, the relative permittivity of the ferroelectric thin film, the over-lapping area of the electrodes and the thickness of ferroelectric thin film respectively. In practice, the area of the capacitor A is limited by the precision of photolithography which is in the microns range. 5 μm is almost the smallest line width that can be achieved with acceptable tolerance in the group at Birmingham. The thickness of the ferroelectric thin film is usually less than 1 μm. Typical values for the dielectric constant of BST thin films are usually in the range of 10^2 - 10^3 at room temperature [1-4]. As provided in the modelling of parallel plate capacitors in chapter 3, the capacitance C cannot be much less than 0.02 pF considering the above limiting factors.

Quasi-lumped meander line inductors were used to implement the series inductors. The size of the meander line inductors are required to be less than $\lambda_g/20$ at the operating frequency in order to be regarded as lumped elements. The guided wavelength is defined as below [5]

$$\lambda_g = \frac{c}{f_0}\frac{1}{\sqrt{\varepsilon_r}} \tag{4.2}$$

where c, ε_r and f_0 are velocity of light in vacuum, the effective relative permittivity and the frequency of interest respectively. The using of lumped elements reduces the size of the device compared with a distributed line approach.

The filter was to be implemented in a coplanar waveguide (CPW) configuration. The high resistivity silicon substrate was chosen to show the potential for integration with monolithic microwave integrate circuits (MMICs). The proposed lowpass filter layout is shown in Fig.4-2, where the yellow defines the top metal layer and blue defines the bottom metal and BST thin film is between these two metal layers. The overlap area of a narrow conductor track on the top layer and the shunt line in bottom layer forms the BST parallel plate capacitor. In this work two capacitor sizes were used, one 5 µm × 5 µm and the other 10 µm × 10 µm. The presence of the same ground plane in both top and bottom metal layers with the BST film between them provides a large capacitance, which is equivalent to a short circuit in microwave region but allows a DC bias to be applied between the top and bottom metal layers. When DC bias was applied to the CPW lines, the large capacitance of the ground planes was connected in series with the very small capacitance of the BST parallel plate capacitor, therefore shared very little DC voltage.

The initial filter synthesis was carried out using the design formulas provided in chapter 3. The appropriate g-values of a seventh order Chebyshev lowpass filter for a desired passband ripple L_{Ar} of 0.01 dB are listed in Table 4- 1.

g_0	g_1	g_2	g_3	g_4	g_5	g_6	g_7	g_8
1	0.797	1.392	1.748	1.633	1.748	1.392	0.797	1

Table 4- 1 Element values for Chebyshev lowpass prototype filter (for n = 7, L_{Ar} = 0.01 dB).

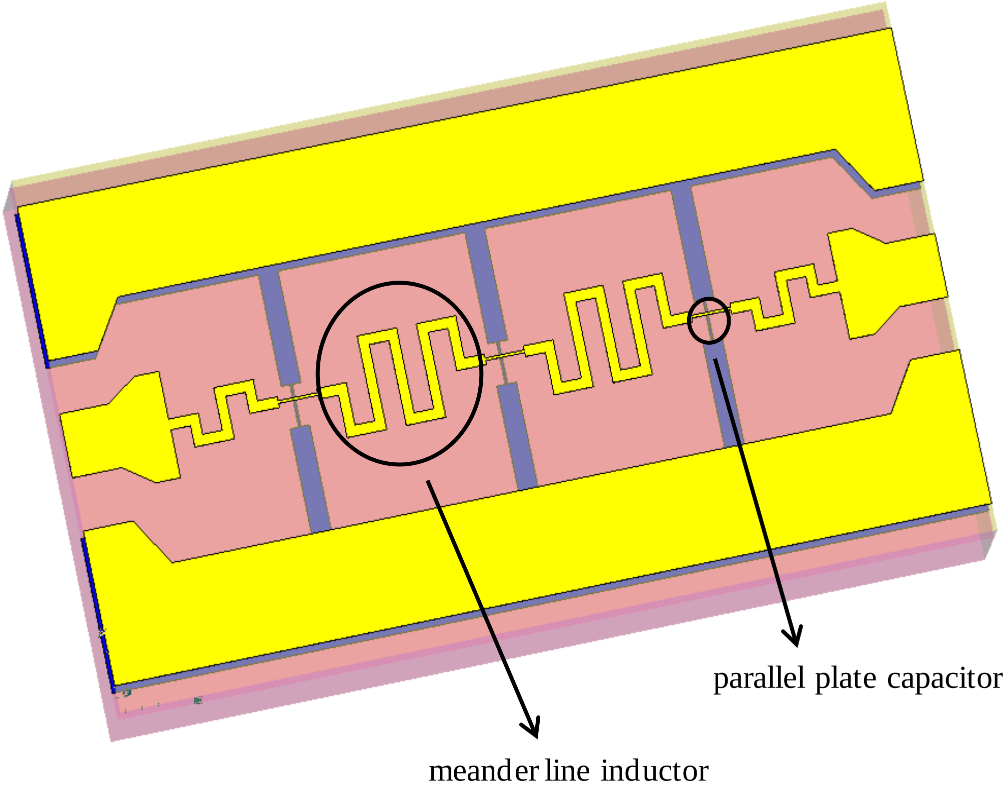

Fig.4- 2 The three dimensional view of a seventh order lowpass filter (1.8 mm × 0.9 mm). The yellow defines the top metal layer and blue defines the bottom metal, and BST thin film is between these two metal layers.

With these values a normalised source resistance/conductance of $g_0 = 1$ and a cut-off frequency $\Omega_c = 1$ are obtained. Transforming to the desired source impedance Z_0 and cut-off frequency ω_c can be accomplished by the following equations

$$L = \left(\frac{\Omega_c}{\omega_c}\right) Z_0 g \tag{4.3}$$

$$C = \left(\frac{\Omega_c}{\omega_c}\right)\frac{g}{Z_0} \tag{4.4}.$$

The cut-off frequency f_c can be derived from (4.4) as

$$f_c = \left(\frac{\Omega_c}{2\pi C}\right)\frac{g}{Z_0} \tag{4.5}.$$

As we already have a desired capacitance value C, the cut-off frequency f_c is derived from C using equation (4.5) and the inductance value L is then determined by f_c from equation (4.3). It can be seen from equation (4.5) that the scalable range of the cut-off frequency f_c is limited by the possible capacitance C. As discussed previously, the capacitance C of a BST parallel plate capacitor cannot be much less than 0.02 pF. Since the cut-off frequency f_c is inversely proportional to the capacitance C (as shown in (4.5)), the upper scalable range of the cut-off frequency is limited in this way by the BST capacitor dimensions and available permittivity of BST film. An upper available limit of f_c is also determined by the highest frequency at which the meander line inductor can be regarded as lumped element. As indicated previously, the size of the meander lines are required to be less than $\lambda_g/20$ to keep the lumped element approximation valid. Above a certain frequency, when the guided wavelength is shorter than several millimetres, the parasitic reactance of the meander lines becomes prominent, which makes the lumped element assumption inappropriate. In addition, the lower available range of f_c is limited by the practical inductance and capacitance range according to equations (4.3) and (4.4). Despite all the above limits, the lowpass filter can still be designed for a wide operating frequency range. Following from the relative permittivity and thickness of the BST thin films made at Birmingham, the capacitance is around 0.2 pF for a 5 µm × 5 µm BST parallel plate capacitor. If $Z_0 = 50$, on substituting $C_2 = C_6 = 0.2$ pF into formula (4.5) the cut-off frequency is found to be

$$f_c = 22.16\ \text{GHz}\ .$$

Scaling C_4 and the inductance to the cut-off frequency using formula (4.3) and (4.4) yields

$$C_4 = 0.235\ \text{pF}$$

$$L_1 = L_7 = 0.286\ \text{nH}$$

$$L_3 = L_5 = 0.628\ \text{nH}\ .$$

The schematic circuit containing the above calculated capacitance and inductance was simulated using Advanced Design Systems 2005A (ADS) [6]. Fig.4- 3 shows the schematic circuit of an ideal seventh order Chebyshev lowpass filter and its simulated response. The cut-off frequency of the lowpass filter can be tuned by the varying the capacitance of the ferroelectric varactor.

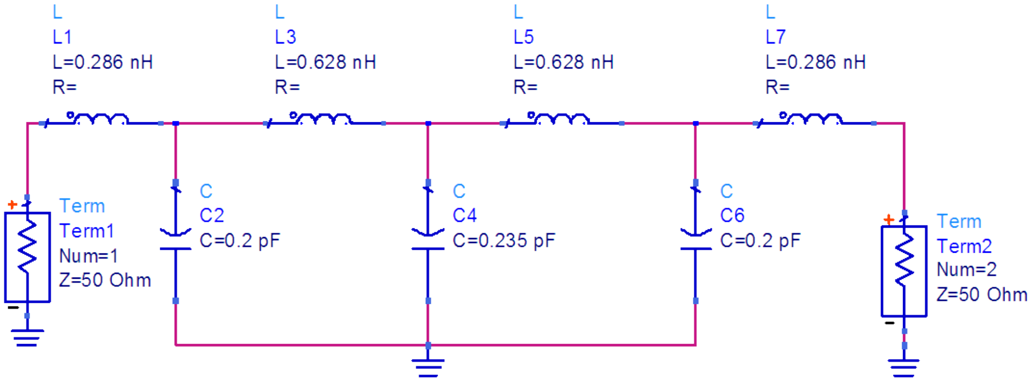

(a)

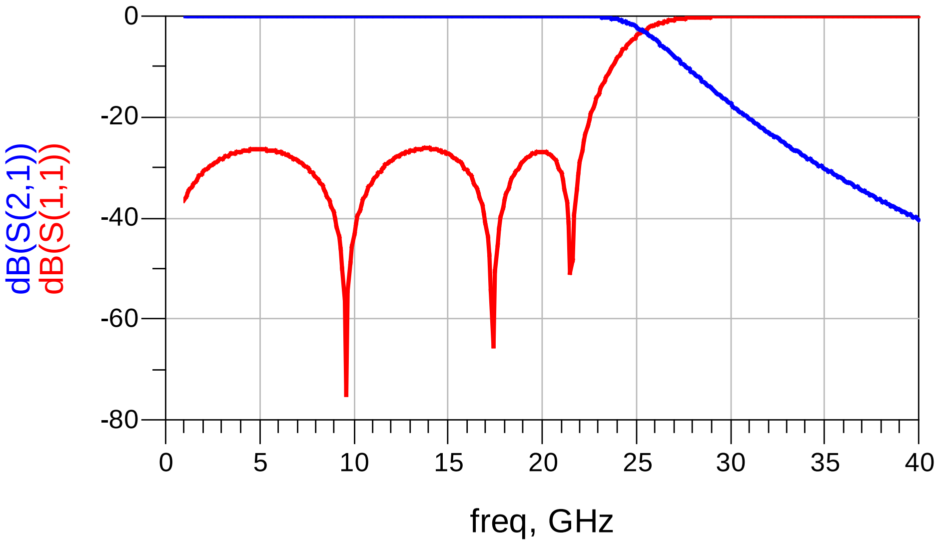

(b)

Fig.4- 3 The schematic circuit of an ideal seventh order Chebyshev lowpass filter (a) and its response simulated using ADS (b).

After the initial synthesis, an electromagnetic full wave simulation of the lowpass filter was performed using Sonnet em 10 [7]. The three dimensional view of the lowpass filter is already shown in Fig.4- 2. The line width of the meander line inductors was 20 µm and the space between two adjacent lines was 40 µm. The dimensions of the inductors were determined by simulation as discussed in chapter 3. The size of the inductors was smaller than $\lambda_g/20$ at the operating frequency (the guided wavelength was about 4 mm at 25 GHz). The line width of the narrow central conductor track in both top and bottom layers was 5 µm for 5 µm × 5 µm capacitor and 10 µm for 10 µm × 10 µm capacitor. The three shunt varactors were made the same size as the capacitance value of C_4 was close to that of C_2 and C_6. The width of the shunt straight line to ground in the bottom layer was 40 µm.

The CPW input/output lines were designed to have a characteristic impedance of 50 Ω at around 25 GHz, the impedance being calculated using a conformal mapping technique [8] as discussed in chapter 3. In order to match the dimensions of the microprobes used to measure the device, the width of the CPW signal line was tapered from 200 µm to 120 µm at the port interface and the gap between the signal line and (upper) ground plane was tapered from 150 µm to 100 µm. The area of the whole device was approximately 1.8 mm × 0.9 mm.

Fig.4- 4 shows the performance of the lowpass filter simulated using Sonnet without considering any loss factors. The thickness of the silicon substrate was 0.5 mm. The size of the BST parallel plate capacitor was 5 µm × 5 µm. The thickness of BST thin film was assumed to be 400 nm and the relative dielectric constant was assumed to be 300 at zero bias and 200 after tuning. The lowpass filter showed a wide tuning range with the changing of permittivity. The reflection was degraded for the filter with higher permittivity due to the circuit being not perfectly matched. The resonance at higher frequency was caused by the resonance of the ground plane.

Loss is an essential problem in BST devices at room temperature. Both dielectric loss and metal loss contribute significantly to the overall performance. As presented in chapter 2, the reported loss tangent of BST thin films at room temperature is in the range of 0.02 ~ 0.2 [4], [9-15] which makes the pursuit of high quality BST thin films crucial. As discussed in chapter 2, the quality of BST thin films is determined by various factors, including Ba concentration, growth conditions and the substrate. Recently a BST/Pt/Au parallel plate capacitor with a Q of 100 at 10 GHz was reported using $Ba_{0.25}Sr_{0.75}TiO_3$ thin film [4]. It is suggested that $Ba_{0.25}Sr_{0.75}TiO_3$ thin film has a lattice parameter close to that of Pt, enabling quasi-epitaxial growth of BST thin film [16]. Besides, $Ba_{0.25}Sr_{0.75}TiO_3$ has a phase transition temperature of 125 K so it is in paraelectric phase at room temperature [14]. The paraelectric phase is often preferred for microwave applications because of the absence of hysteresis and lower loss [17]. In this work, a $Ba_{0.25}Sr_{0.75}TiO_3$ thin film is also used and deposited by pulsed laser deposition (PLD).

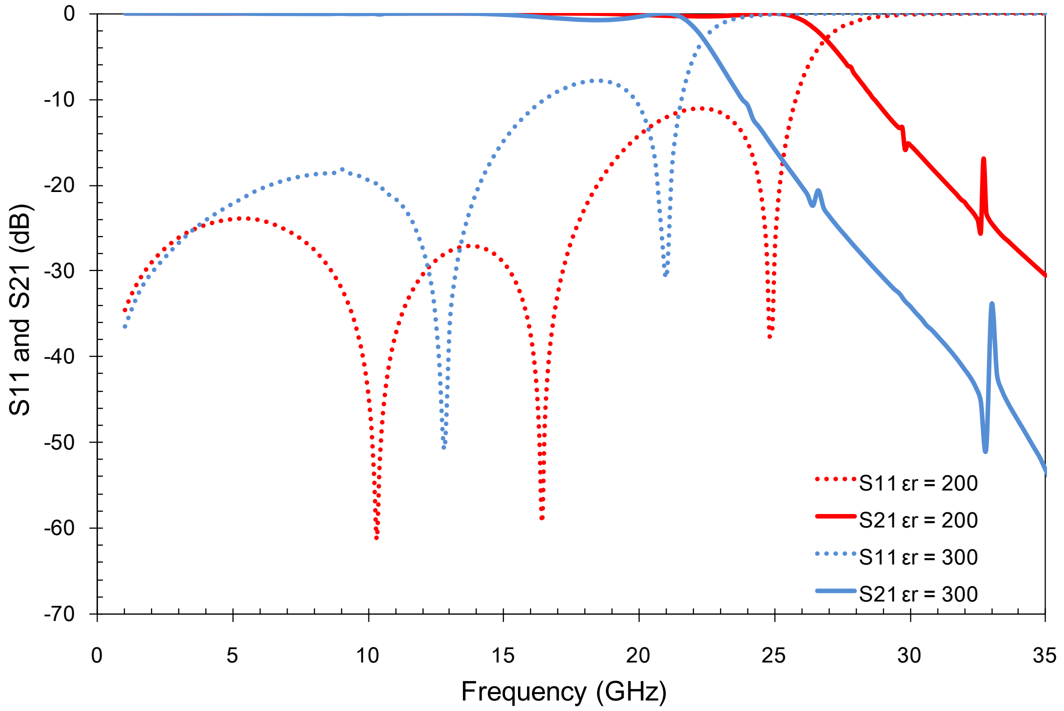

Fig.4- 4 The simulated performance of the lossless filter shown in Fig.4- 2. The parameters of the BST capacitor used in the simulation were 5 μm × 5 μm in size, 400 nm thickness, dielectric constant ε_r of 200 and 300.

However, the metal loss becomes dominant at higher frequencies. As discussed in chapter 2, platinum, gold, silver are the most commonly used electrodes in thin film oxide based devices because they are in most cases non-reactive upon contact with oxides and their large work functions provide Schottky contacts [16], [18]. For devices based on parallel plate capacitors, BST film is deposited on a metallised substrate. The bottom metallisation should enable growth of high quality BST films while having a good conductivity at microwave region. Platinum is of particular interest as bottom electrode because it is chemically compatible with the BST material and stable against oxidization [19], [20]. To minimize the loss from the electrode, a metal thickness of three times the skin depth at the operating frequency is required. As the skin depth of silver and platinum at 25 GHz is 410 nm and 1030 nm respectively, a metallisation thickness of several microns is required. However, it is difficult to pattern such thick, narrow and closely spaced metal strips due to the high aspect ratio. In addition, the residual stress which exists at the interface of the bottom electrode and the substrate is aggravated with the increased metal thickness and leads to a mechanically unstable bottom electrode [1]. In this work, 250 nm Pt/Au/Pt multilayer was chosen as bottom metal and a 400 nm thick silver layer was deposited as the top electrode.

The effect of the metal thickness on the filter insertion loss was verified using the full wave simulation of Sonnet. Sonnet models the metal loss using the concept of surface impedance [7]. This concept allows Sonnet to model real three-dimensional metal in two dimensions. This approximation is valid if the metal thickness is small with respect to the width of the line, the separation between lines, and the thickness of the dielectric. The total loss of the device consists of the loss from the top metal layer, the bottom metal layer, the BST thin films, the substrate and radiation loss. To investigate the effect of the metal thickness on the insertion loss, only the loss from the top metal layer, which is silver, is taken into account in the simulation. The insertion loss of the lowpass filter for different thickness of silver of 100 nm, 200 nm, 500 nm and 1000nm is shown in Fig.4- 5. The skin depth of silver is 410 nm at 25 GHz. As expected it was found that when the thickness of metal was smaller than the skin depth its loss performance degraded dramatically. The reflection is also distorted when the metal layer is too thin. It should be noted that in practical situations the metal loss will be even greater because the metal is not perfect.

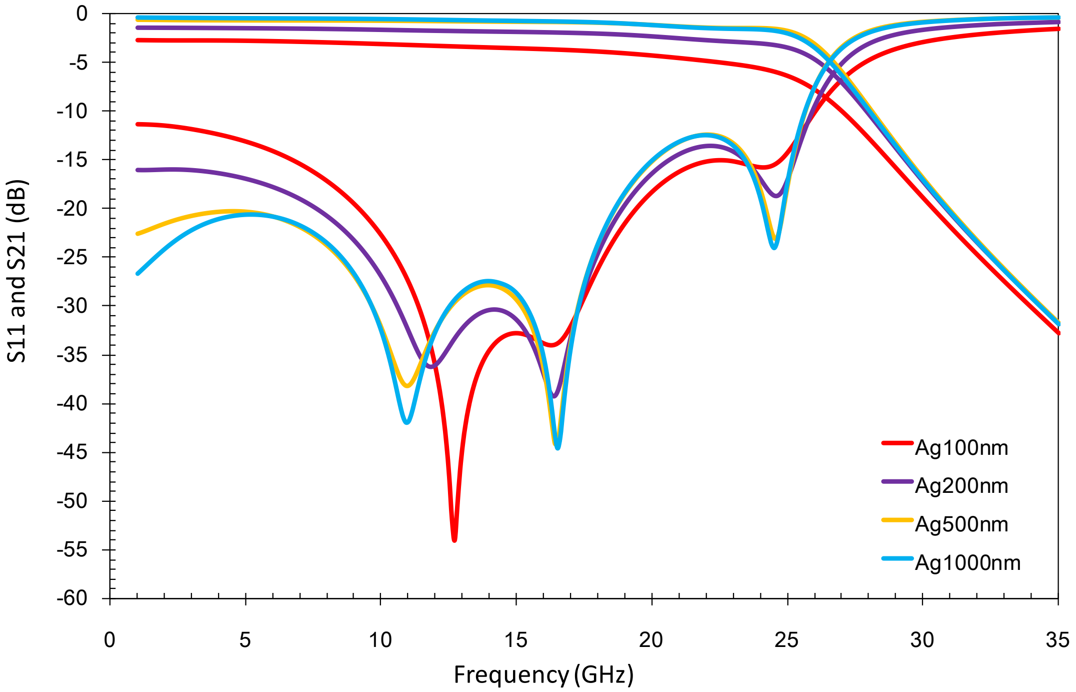

Fig.4- 5 Simulated insertion loss and reflection of the lowpass filter when top metal silver is 100 nm, 200 nm, 500 nm and 1000 nm thick.

4.2 Fabrication

A commercial Pt/Au/Pt/Ti/SiO2/Si template was used as the substrate. The total thickness of Pt/Au/Pt multilayer was about 250 nm measured by DEKTAK surface profiler. 500 nm SiO_2 was used as diffusion barrier and about 20 - 30 nm Ti as an adhesion layer. The thickness of the high resistivity (5000 Ω·cm) silicon substrate was 0.5 mm and the devices were fabricated on it following the process flow explained in Fig.4- 6. The Pt/Au/Pt multilayer was initially patterned by ion beam milling to form the bottom electrodes. After that, a $Ba_{0.25}Sr_{0.75}TiO_3$ thin film was deposited on the patterned bottom electrodes by pulsed laser deposition (PLD), using a laser fluence of 1.5 J/cm^2 at 5 Hz pulse rate with a substrate temperature of 750 °C. An oxygen pressure of 10^{-1} mbar was used in the deposition. After deposition, in-situ annealing was performed at 650 °C for one hour at about 800 mbar static oxygen pressure. These conditions had been shown previously to give the best microwave performance [21]. Finally, the top electrode, 400 nm thick silver, was deposited by RF magnetron sputtering and defined by ion beam milling to complete the fabrication. Fig.4- 6 (i) shows the cross-sectional view of the device.

A group of six lowpass filters involving 5 µm × 5 µm capacitors were fabricated on two 10 mm × 10 mm silicon samples, which were called sample A and sample B. On each sample the filters are numbered from 1 to 6 to distinguish them. The filters on the same sample differed from each other by the different inductance of the meander line inductors. Table 4- 2 gives the simulated inductance of the first and third meander line inductors (L_1 and L_3) in each filter. The inductance of the fifth and seventh inductors is equal to that of the third and first inductors as the circuit is symmetric. The second, fourth and sixth components of the filters are capacitors. In addition, three lowpass filters involving 10 µm × 10 µm capacitors but different size meander line inductors on a separate 10 mm × 10 mm sample were also tested.

Inductance (nH)	Filter Number				
	No.1	No.2	No.3	No.5	No.6
L_1	0.47	0.39	0.31	0.39	0.41
L_3	0.83	0.67	0.52	0.95	0.95

Table 4- 2 The simulated inductance of the meander lines

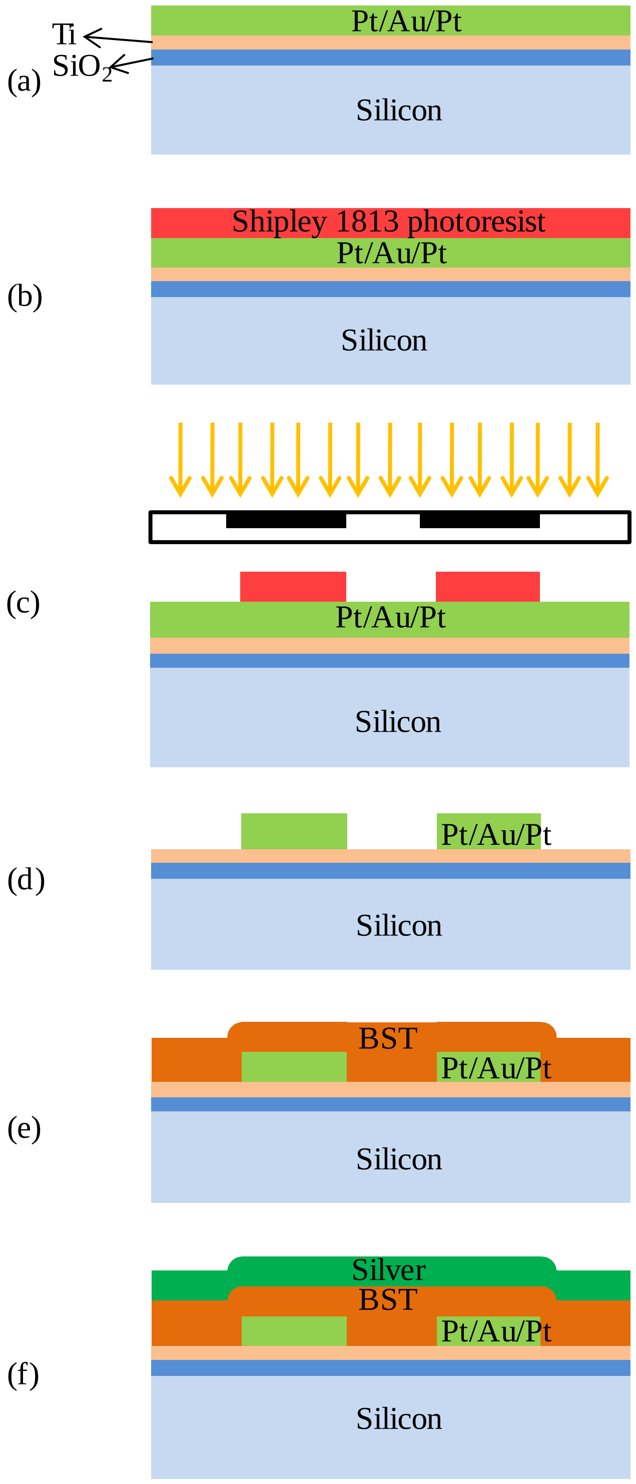
(a)
Ti
SiO2
Pt/Au/Pt
Silicon
(b)
Shipley 1813 photoresist
Pt/Au/Pt
Silicon
(c)
Pt/Au/Pt
Silicon
(d)
Pt/Au/Pt
Silicon
(e)
BST
Pt/Au/Pt
Silicon
(f)
Silver
BST
Pt/Au/Pt
Silicon

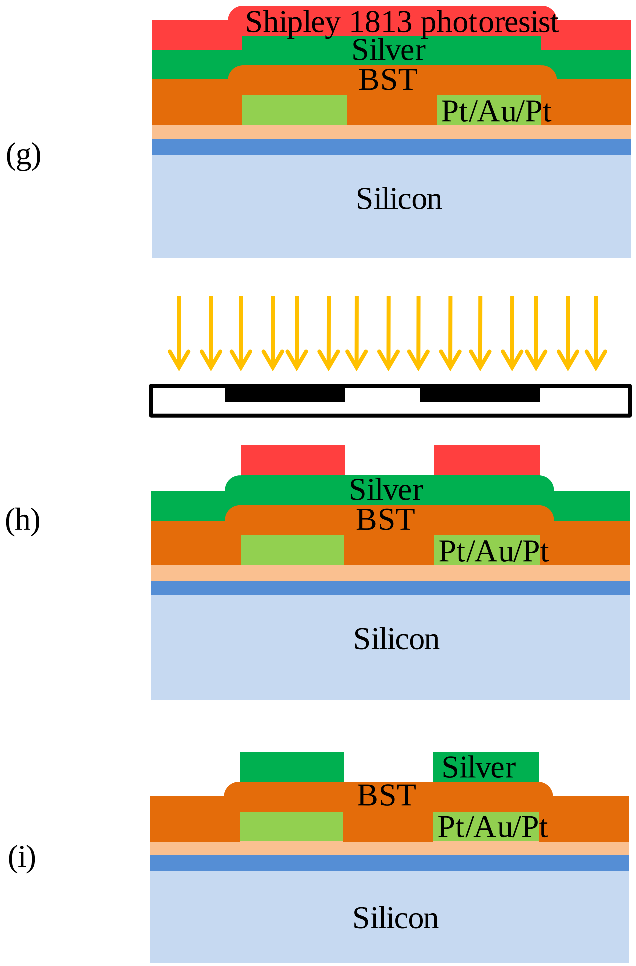

Fig.4- 6 The process flow showing the fabrication procedure of the BST lowpass filter on silicon substrate: silicon substrate with Pt/Au/Pt bottom metal layer (a); photoresist coating (b); UV exposure (c); patterning of bottom electrode by ion beam milling and removal of photoresist (d); BST thin film deposition by PLD (e); top metal layer deposition by RF magnetron sputtering (f); photoresist coating on top metal layer (g); UV exposure (h); patterning of top electrode by ion beam milling and removal of photoresist (i).

Fig.4- 7 shows a photograph and enlargement of one ferroelectric lowpass filter with 5 µm × 5 µm capacitors. The width of the narrow lines defining the capacitors was measured with an optical microscope as shown in Fig.4- 7 (b). The intended 5 µm lines were measured as 4.195 µm and 4.362 µm for the line in top and bottom layer respectively; this is a result of over-etching.

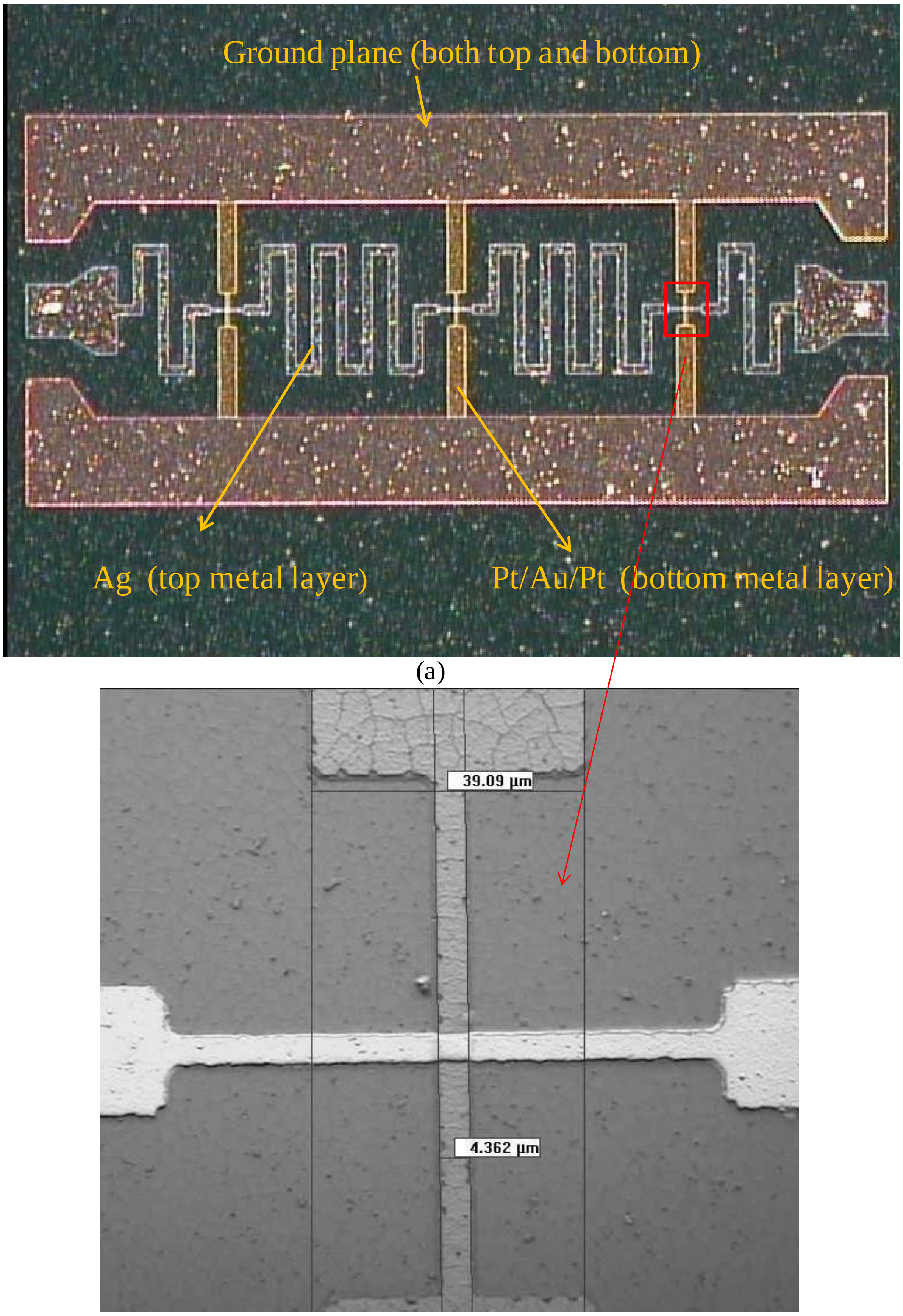

(a)

(b)

Fig.4- 7 Photograph of a ferroelectric lowpass filter on silicon substrate (a) and enlargement of the 5 µm × 5 µm parallel plate capacitor area (b).

4.3 Filter measurement

The ferroelectric lowpass filters were tested on a probe station using an Agilent E8361A PNA network analyser through ACP40-GSG-250 microprobes at frequencies up to 50 GHz. A two-port line-reflect-reflect-match (LRRM) calibration was performed using Wincal XE over a wide frequency range from 0.01 GHz to 50 GHz. The DC bias of up to 15 V was applied to the probes through external bias tees.

The measurement results of one ferroelectric lowpass filter involving 5 µm × 5 µm parallel plate capacitors are presented in Fig.4- 8. The 10 dB cut-off frequency shifts 6 GHz from 18.52 GHz at 0 V to 24.47 GHz at 15V (corresponding to an electric field of 37.5 V/µm), showing 32.1 % tuning. Above 15 V the leakage current increases quickly. The measured results show a cut-off frequency close to that of the design but have a high insertion loss. The metal loss is considered to be dominant, which will be discussed in section 4.4.

For frequencies close to 25 GHz, the lowpass filter can be treated as a switch. The bias determines the state of the switch, with 15 V corresponding to low loss (ON) and 0 V to high loss (OFF). The switch isolation is defined as the difference in insertion loss with and without bias. Fig.4- 9 shows the maximum isolation of the switch is 18 dB at 25 GHz with an insertion loss of 12 dB.

As mentioned previously, several lowpass filters covering a wide frequency range by using different size inductors and capacitors were also tested. Instead of showing the measured response of all the devices, Fig.4- 10 shows a summary of the 10 dB cut-off frequencies of the lowpass filters involving 5 µm × 5 µm and 10 µm × 10 µm capacitors versus bias voltage. In Fig.4- 10 ‘5umA_3’ means filter No.3 with 5 µm × 5 µm capacitors grown on sample A. ‘5umB_3’ has exactly the same layout as ‘5umA_3’ but on sample B.

Although the filters on silicon samples A and B had the same fabrication procedure, the measured performance of the same filter on different samples exhibits slightly different cut-off frequencies. Generally, the -10 dB cut-off frequency of lowpass filters on sample B is 2 - 4 GHz (about 15 % - 25 %) higher than the corresponding filters on sample A. One possible reason for this difference might be the different BST film thickness but this is not verified at present.

Alternatively, it could be that the BST fabrication technique is sensitive to various growth conditions, i.e. temperature, pressure, composition, crystal quality, thickness and defects concentration which have not been sufficiently well controlled in the growth process.

The different cut-off frequencies of the filters on the same sample are mainly caused by the different sized inductors. It can seen from Table 4- 2 that the inductors in lowpass filter No.3 have the smallest inductance values, as a result, the cut-off frequency of the lowpass filter No.3 is highest in both sample A and sample B. Cut-off frequencies of lowpass filters containing 10 µm × 10 µm capacitors are also summarised in Fig.4- 10. The much bigger capacitance of the 10 µm × 10 µm parallel plate capacitors leads to lower cut-off frequencies of the '10 um' filters compared with the '5 um' ones. The cut-off frequencies of the '5 um' filters cover from 11 GHz to 25 GHz and the '10 um' filters cover from 4 GHz to 8 GHz.

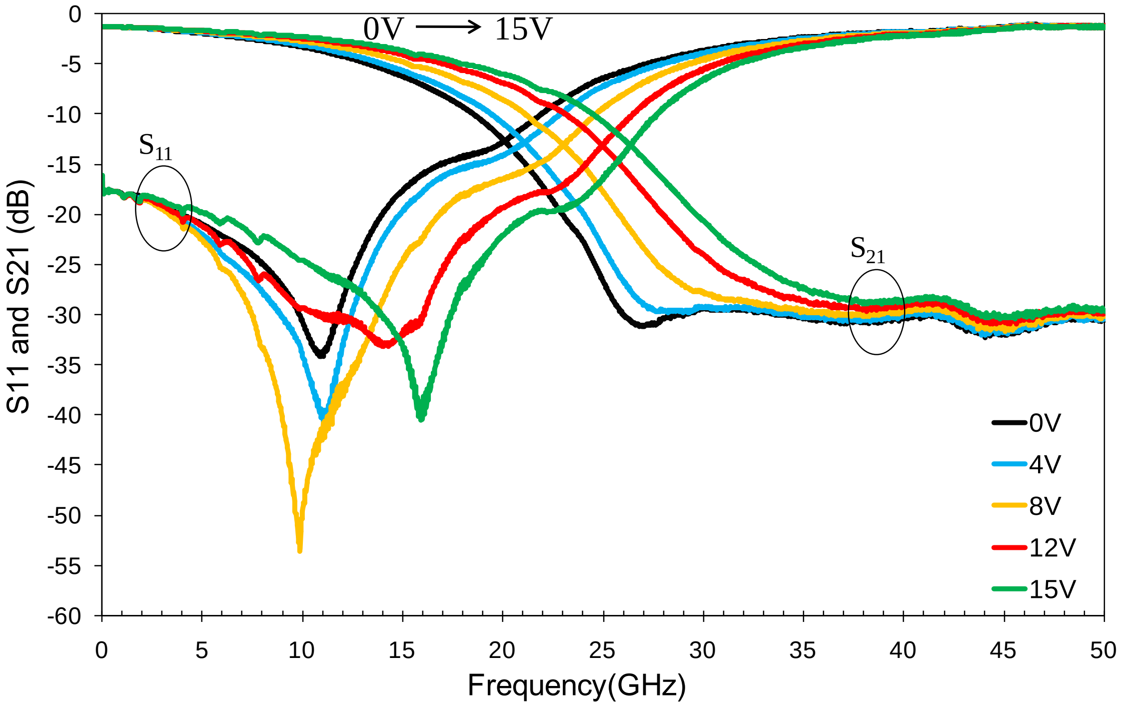

Fig.4- 8 Measured transmission and reflection of ferroelectric lowpass filter No.3 on sample B with 0 - 15 V bias.

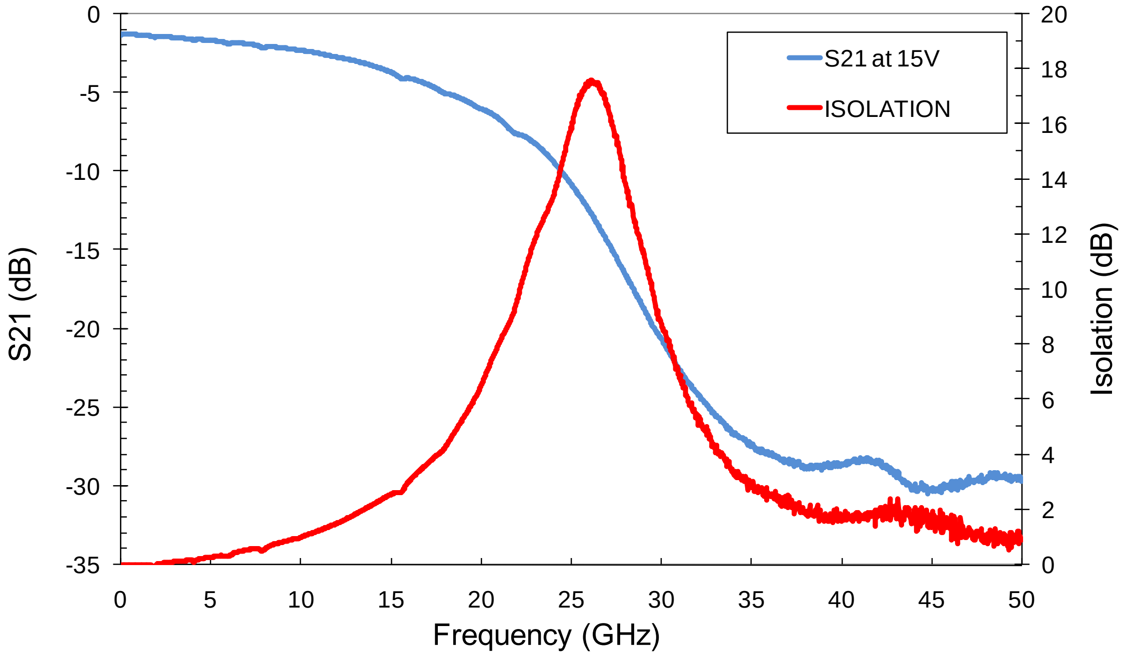

Fig.4- 9 Isolation and transmission response versus frequency of the lowpass filter No.3 on sample B (the same device as shown in Fig.4- 8) working as a switch near 25 GHz.

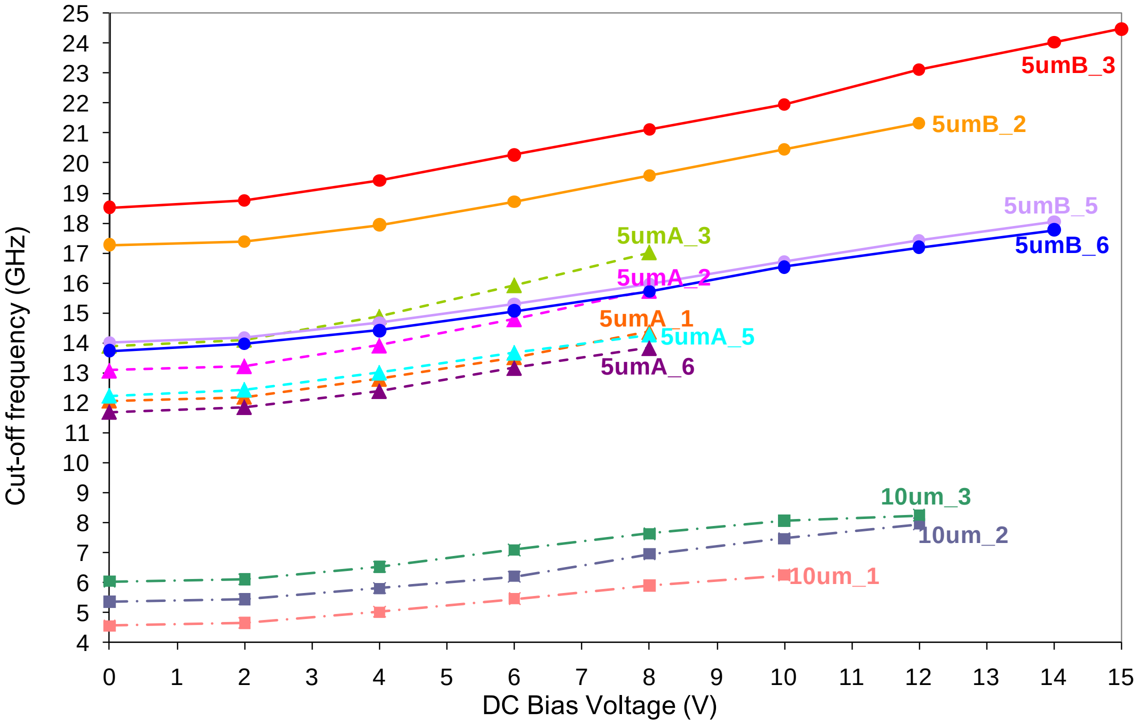

Fig.4- 10 Summary of the 10 dB cut-off frequencies of the lowpass filters with 5 μm × 5 μm capacitors on sample A (triangles) and B (dots), and filters with 10 μm × 10 μm capacitors (squares) as a function of DC bias voltage.

4.4 Discussion

The properties of BST and metal films were characterised experimentally using square varactors as described in appendix A. For the lowpass filter, the EM full wave simulation of the filter, using Sonnet, was compared with the experimental frequency sweep to extract the permittivity of the fabricated BST thin film. To compare the device as accurately as possible, the loss from the metal and BST film was carefully considered in the simulation. The conductivity of the metal was set to 64.3 % of its ideal case, according to appendix A. The thickness of top silver layer was chosen as 400 nm and the bottom metal was 250 nm platinum, which was a little different with the Pt/Au/Pt multilayer in practice. The size of the capacitor was set to 4 µm × 4 µm as it was closer to its actual size. The loss tangent of BST film was set to 0.1 and thickness to 400 nm. The extracted permittivity of BST thin film varies from 485 to 295 with 0 - 15 V bias. The EM full wave simulation using the above parameters compares well the experiments results despite small difference in S11 as shown in Fig.4- 11.

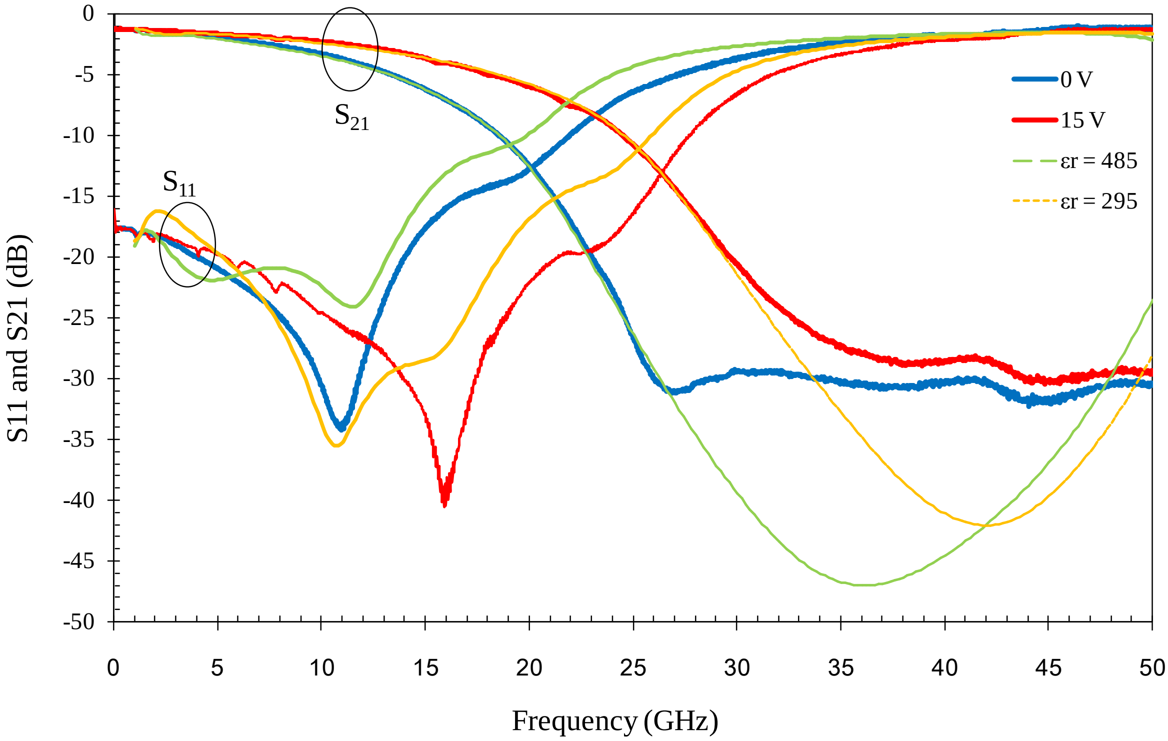

Fig.4- 11 The comparison between simulation and measurement of the lowpass filter. The dashed lines are the simulation results and the solid lines are the measurement results.

As discussed in appendix A, the BST loss is dominant in the total loss of a varactor. However, the situation is different for the lowpass filters, where the metal loss is significantly aggravated as a result of current crowding in the narrow lines, which also leads to a degraded power handling capability. A large current density concentrated in the meander lines and the narrow shunt lines in the bottom layer is shown in Fig.4- 12.

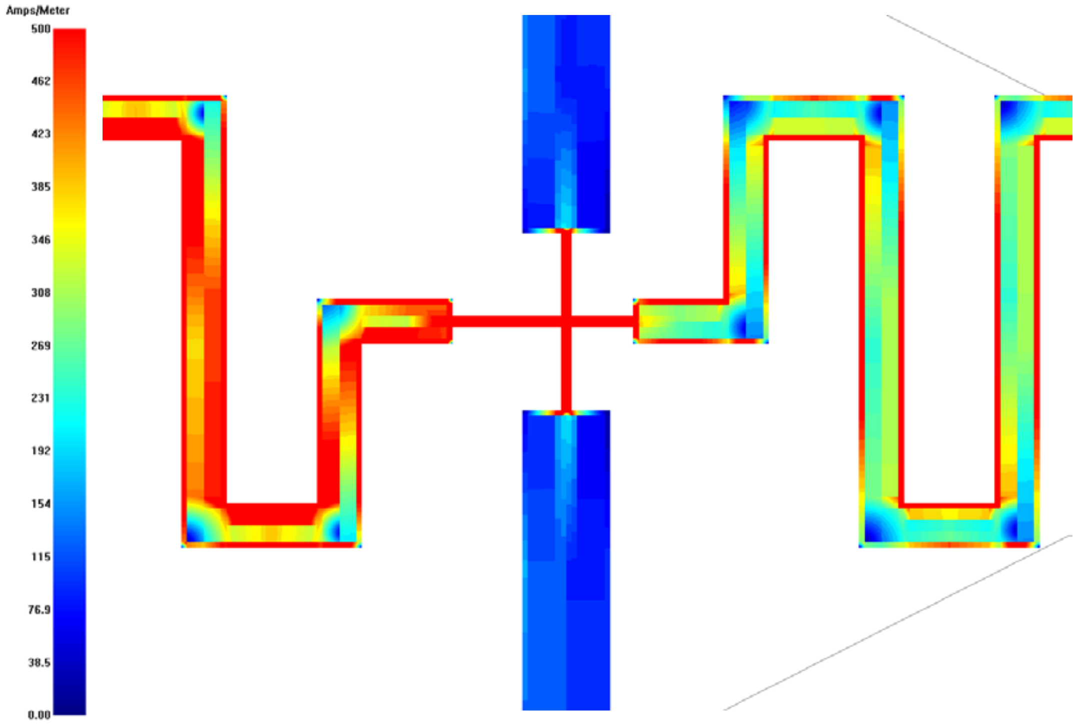

Fig.4- 12 Current crowding in the parallel plate capacitor area of the filter

The losses from different parts of the filter were investigated by full wave EM simulation. The simulated performance of the lowpass filter considering separated losses from top metal layer, which was 400 nm silver, bottom metal layer, which was 250 nm platinum, and BST film with $\tan\delta = 0.1$ respectively was shown in Fig.4- 13. The conductivity of metal was set to 64.3 % of its ideal value. The lossy filter, which considered all the above losses, and the lossless case were also shown in Fig.4- 13. The loss from silicon substrate and radiation loss was small in this case and not shown here. It can be seen that either the loss from top or bottom metal layer is comparable to or even worse than that of BST film, which is a result of the severe current crowding and the very small thickness (smaller than skin depth). The large current concentration in this small device (1.8 mm × 0.9 mm) makes metal loss dominant in the total loss. This also leaves room for improvement - thicker metal will ensure lower insertion loss.

The transmission zero at 42 GHz is caused by the resonance of the parallel plate capacitor and the inductance of the 40 μm wide shunt line to ground. The other resonance in lossless situation is caused by the resonance of ground plane at certain frequency and will not appear with loss.

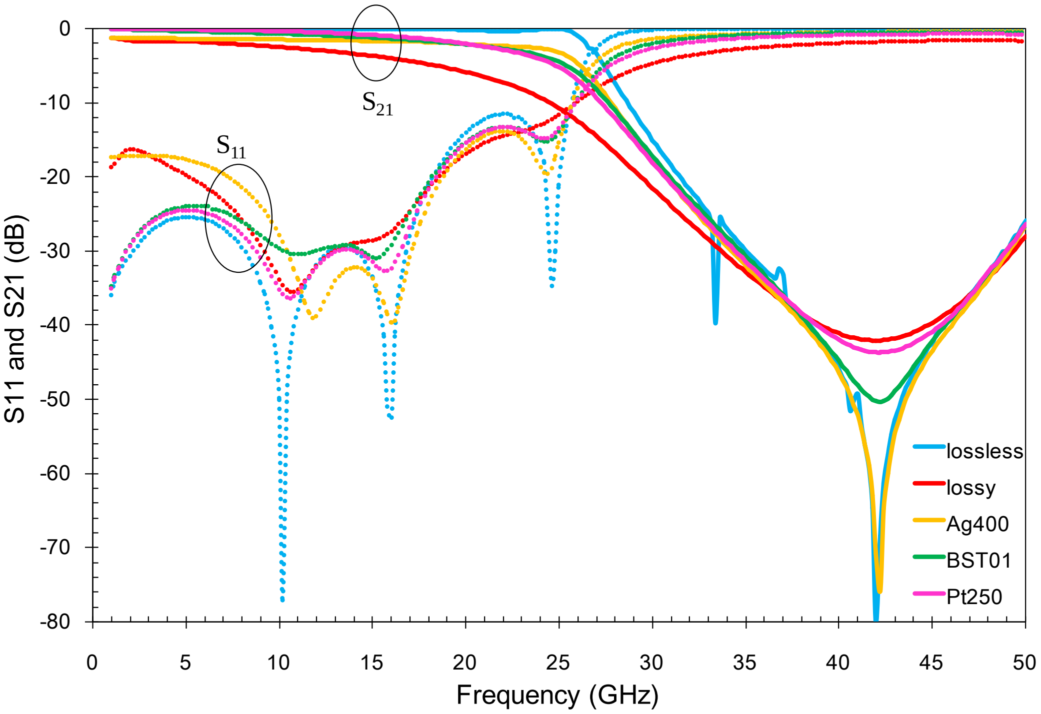

Fig.4- 13 The losses from top metal layer (400 nm thick silver), bottom metal layer (250 nm thick platinum), BST film (loss tangent of 0.1) compared with lossy (including all the above losses) and lossless situations. Solid lines represent S_{21} and dot lines S_{11}.

Except using thicker metals, the insertion loss of the filter can be also improved by modifying the filter layout. In the new layout, as shown in Fig.4- 14, the shunt lines in the bottom layer were moved to the upper layer where silver is used instead of platinum and the narrow central lines (i.e. 5 μm width lines) were removed. As silver has much higher conductivity than platinum and the top metal can be made thicker, the metal loss was expected to be reduced. In addition, mitered corners were used in the meander lines in order to reduce current reflection and hence achieved a much more uniform current distribution. The improvement in the simulated performance of the lowpass filter is shown in Fig.4- 15. The insertion loss is about 1 dB better at 25 GHz using the new layout. However, experimental verification of the filter in new layout is not available.

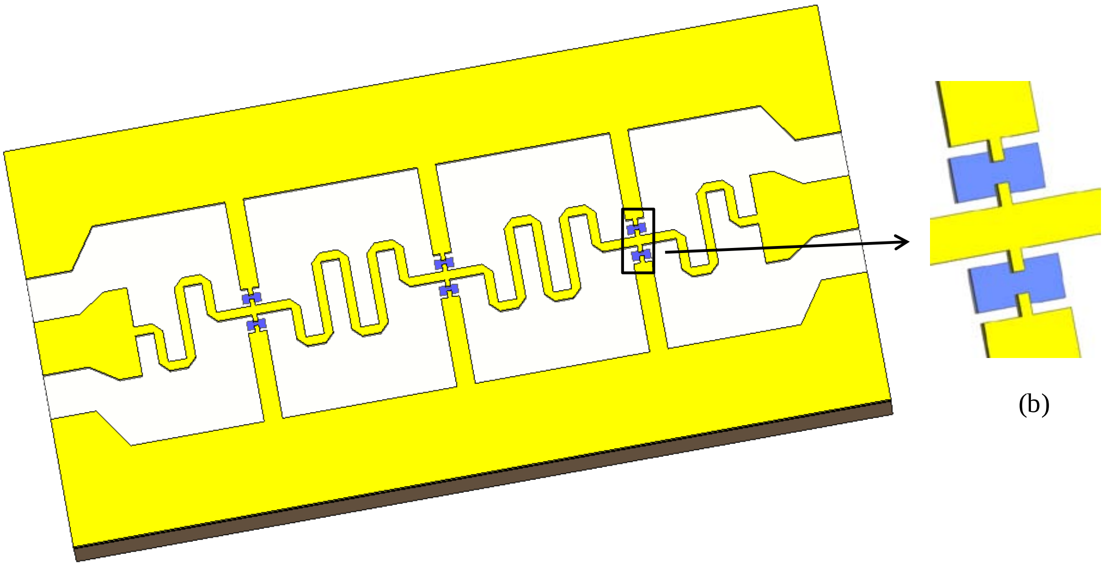

(a) (b)

Fig.4- 14 Layout of the modified lowpass filter (a) and enlarged view of the parallel plate capacitor area (b).

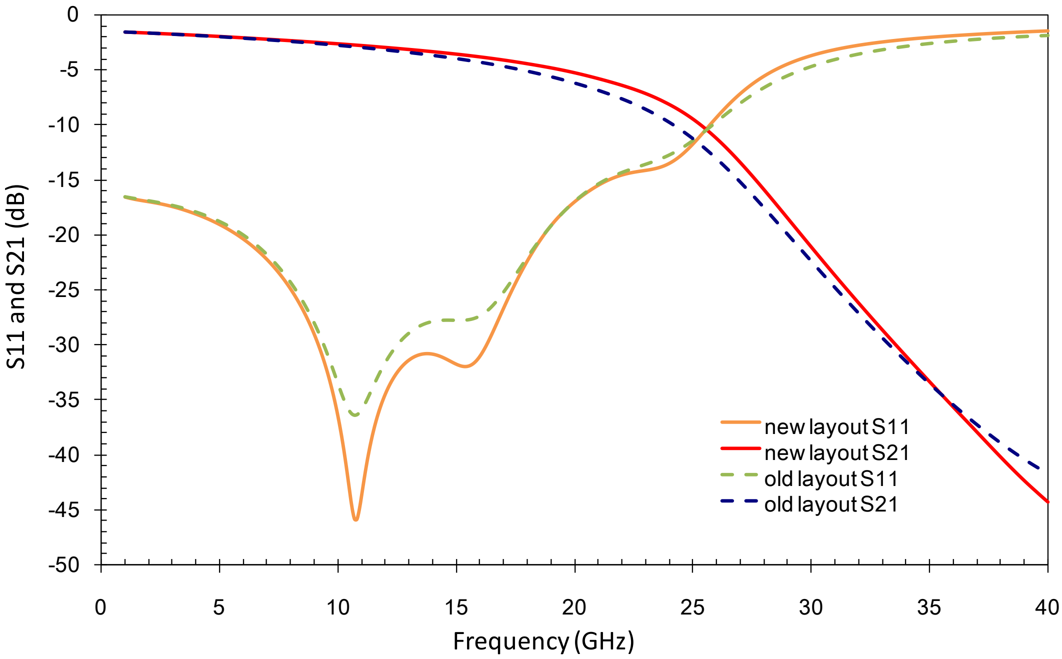

Fig.4- 15 The insertion loss improvement of the lowpass filter in the new layout. The Solid lines represent the filter in the modified layout while the dashed lines represent the old layout.

4.5 Summary

In this chapter a K-band BST lowpass filter on a high resistivity silicon substrate was demonstrated. The 10 dB cut-off frequency of the filter was tuned 32.1 % from 18.52 GHz at zero bias to 24.47 GHz with 15 V bias. Several lowpass filters covering a wide frequency operating range from 4 GHz to 25 GHz were demonstrated as well. The loss from metal and BST film were separated and analysed. Although the BST loss was more important in the varactors, the metal loss became dominant in the filters as a result of severe current crowding. A modified layout of the lowpass filter aiming at reducing the conductor loss was also suggested.

References

[1] A. Tombak, J. P. Maria, F. T. Ayguavives, Zhang Jin, G. T. Stauf, A. I. Kingon, and A. Mortazawi, "Voltage-controlled RF filters employing thin-film barium-strontium-titanate tunable capacitors", *IEEE Transactions on Microwave Theory and Techniques*, vol. 51, no. 2, pp. 462-467, 2003.

[2] J. Nath, D. Ghosh, J. P. Maria, A. I. Kingon, W. Fathelbab, P. D. Franzon, and M. B. Steer, "An electronically tunable microstrip bandpass filter using thin-film Barium-Strontium-Titanate (BST) varactors", *IEEE Transactions on Microwave Theory and Techniques,* vol. 53, no. 9, pp. 2707-2712, 2005.

[3] P. M. Suherman, T. J. Jackson, Y. Koutsonas, R. A. Chakalov, and M. J. Lancaster, "On-wafer microwave characterization of ferroelectric thin film phase shifters", in *IEEE MTT-S International Microwave Symposium Digest*2004, pp. 265-268.

[4] A. Vorobiev, P. Rundqvist, K. Khamchane, and S. Gevorgian, "Silicon substrate integrated high Q-factor parallel-plate ferroelectric varactors for microwave/millimeterwave applications", *Applied Physics Letters,* vol. 83, no. 15, pp. 3144-3146, 2003.

[5] T. K. Ishii, Handbook of Microwave Technology, Volume 1, Components and Devices, Academic Press, Inc., 1995.

[6] "Advanced Design System (ADS), Agilent Technoligies, Palo Alto, USA. http://eesof.tm.agilent.com".

[7] "Sonnet User's Guide, Release 10": Sonnet Softerware, Inc., 2004.

[8] S. S. Gevorgian, "Basic characteristics of two layered substrate coplanar waveguides", *Electronics Letters,* vol. 30, no. 15, pp. 1236-1237, 1994.

[9] M. Ouaddari, S. Delprat, F. Vidal, M. Chaker, and Ke Wu, "Microwave characterization of ferroelectric thin-film materials", *IEEE Transactions on Microwave Theory and Techniques,* vol. 53, no. 4, pp. 1390-1397, 2005.

[10] D. Ghosh, B. Laughlin, J. Nath, A. I. Kingon, M. B. Steer, and J. P. Maria, "Tunable high-quality-factor interdigitated (Ba, Sr)TiO_3 capacitors fabricated on low-cost substrates with copper metallization", *Thin Solid Films,* vol. 496, no. 2, pp. 669-673, 2006.

[11] Y. Yong-Kyu, K. Dongsu, M. G. Allen, J. S. Kenney, and A. T. Hunt, "A reduced intermodulation distortion tunable ferroelectric capacitor-architecture and demonstration", *IEEE Transactions on Microwave Theory and Techniques,* vol. 51, no. 12, pp. 2568-2576, 2003.

[12] S. W. Kirchoefer, J. M. Pond, A. C. Carter, W. Chang, K. K. Agarwal, J. S. Horwitz, and D. B. Chrisey, "Microwave properties of $Sr_{0.5}Ba_{0.5}TiO_3$ thin-film interdigitated capacitors", *Microwave and Optical Technology Letters,* vol. 18, no. 3, pp. 168-171, 1998.

[13] M. S. Tsai, S. C. Sun, and T.-Y. Tseng, "Effect of bottom electrode materials on the electrical and reliability characteristics of (Ba, Sr)TiO_3 capacitors", *IEEE Transactions on Electron Devices,* vol. 46, no. 9, pp. 1829-1838, 1999.

[14] A. Vorobiev, P. Rundqvist, K. Khamchane, and S. Gevorgian, "Microwave loss mechanisms in $Ba_{0.25}Sr_{0.75}TiO_3$ thin film varactors", *Journal of Applied Physics,* vol. 96, no. 8, pp. 4642-4649, 2004.

[15] B. Acikel, "High performance barium strontium titanate varactor technology for low

cost circuit applications", Doctor of Philosophy thesis, University of California, Santa Barbara, 2002

[16] A. Vorobiev, J. Berge, and S. Gevorgian, "Thin Film $Ba_{0.25}Sr_{0.75}TiO_3$ Varactors on Au Bottom Electrode for Microwave Applications", in *36th European Microwave Conference*2006, pp. 839-842.

[17] A.K.Tagantsev, V.O.Sherman, K.F.Astafiev, J.Venkatesh, and N.Setter, "Ferroelectric materials for microwave tunable applications", *Journal of Electroceramics*, vol. 11, no. pp. 5-66, 2003.

[18] J. Nath, "Design and characterization of frequency agile RF and microwave devices using ferroelectrics", Doctor of Philosophy thesis, Electrical Engineering, North Carolina State University, 2006

[19] C. H. Mueller, R. R. Romanofsky, and F. A. Miranda, "Ferroelectric thin film and broadband satellite systems", *IEEE Potentials*, vol. 20, no. 2, pp. 36-39, 2001.

[20] P. Bao, T. J. Jackson, X. Wang, and M. J. Lancaster, "Barium strontium titanate thin film varactors for room-temperature microwave device applications", *Journal of Physics D: Applied Physics*, vol. 41, no. p. 063001, 2008.

[21] P. Suherman, T. Jackson, Y. Tse, and M. Lancaster, "Temperature Dependent Dielectric Properties of Coplanar Phase Shifters Fabricated from $Ba_{0.5}Sr_{0.5}TiO_3$ Thin Films", *Ferroelectrics*, vol. 335, no. pp. 69-78, 2006.

CHAPTER 5

FERROELECTRIC BANDPASS FILTERS INCORPORATING INTEGRATED BST THIN FILM VARACTORS

Following from the ferroelectric lowpass filters based on Barium Strontium Titanate (BST) thin film varactors described in the previous chapter, a novel implementation of combline bandpass filters incorporating integrated BST thin film varactors will be presented in this chapter. Two pole and three pole BST bandpass filters were implemented in a coplanar waveguide configuration on MgO substrates, incorporating 5 µm × 5 µm BST parallel plate capacitors as tuning elements. The filter synthesis and full wave electromagnetic (EM) simulation are described in detail in this chapter. The fabrication procedure of the multilayer filters and the problems encountered during the etching process of BST film are also presented. Measurement results of a two pole BST bandpass filter demonstrated reasonable tuning with bias application.

5.1 Theory of combline filter

As shown in Fig.5- 1, a combline filter is comprised of several coupled resonators. The resonators consist of line elements which are shorted to ground at one end and terminated with a variable capacitor at the opposite end. The resonator lines are significantly less than quarter wavelength long at resonant frequency due to the contribution from the lumped capacitance. The larger the loaded capacitor, the shorter the transmission line is, hence a more compact filter. The presence of the loading capacitor also broadens the stopband because the second passband occurs when the resonator line elements are somewhat over a half wavelength long [1], [2]. Coupling between the resonators can be achieved by the way of fringing fields. The input/output couplings are realised in two typical structures: the parallel coupled lines as shown in Fig.5- 1, and the tapped lines, which will be used in this work.

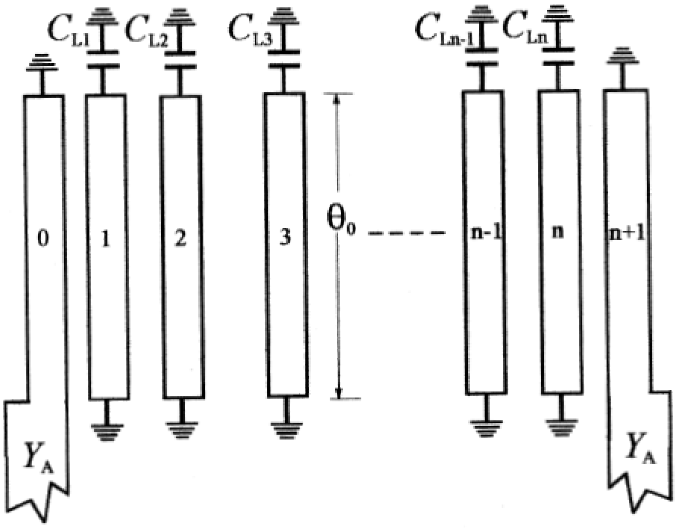

Fig.5- 1 General structure of combline bandpass filter (taken from [2])

5.2 Design considerations

5.2.1 Filter synthesis

Although no particular specification is set for this project, the project pursues microwave filters with miniaturised size, wide tuning bandwidth at low bias voltage, and low loss for applications in future generation of communication systems. Novel combline ferroelectric bandpass filters incorporating integrated BST varactors were designed and discussed in this chapter.

The filter was designed in a coplanar waveguide (CPW) configuration. CPW eases the mounting of shunt resonator as the ground is in the same plane as the signal lines and eliminates the needs for drilling holes compared with microstrip configuration [3]. A proposed 3-pole BST bandpass filter is shown in Fig.5- 2, where the top metal layer is shown in green and the bottom metal is in pink. BST thin film is sandwiched between the two metal layers. The resonator consists of a distributed transmission line element which is shorted to ground at one end and loaded with a BST parallel plate capacitor at the other end. The resonator line is 200 µm wide but narrowed to only 5 µm wide to form the top plate of the BST parallel plate capacitor. The slot in the bottom electrode is designed to tolerate possible mis-alignment between the two metal layers, hence keeping the BST capacitors size as designed, which is 5 µm × 5 µm. The overlap area of the ground in the top metal layer and the bottom electrode forms a large capacitance as BST film is sandwiched between the two layers. This large capacitance is equivalent to short circuit in the microwave region and is in parallel with the 5 µm × 5 µm BST capacitor for DC signals. The DC bias is applied to the top and bottom electrodes. To bias the bottom electrode, the BST film on top of the bottom electrode (outside the top metal region) is required to be etched out. Each resonator can be independently biased as the bottom electrodes are separated from each other. A tapped line input/output coupling structure is used to excite the resonators, which saves space compared with the parallel coupled structure [4]. The coupling between the resonators is realised by fringing fields, and in this case, the coupling is reduced to achieve the appropriate coupling strength using a short.

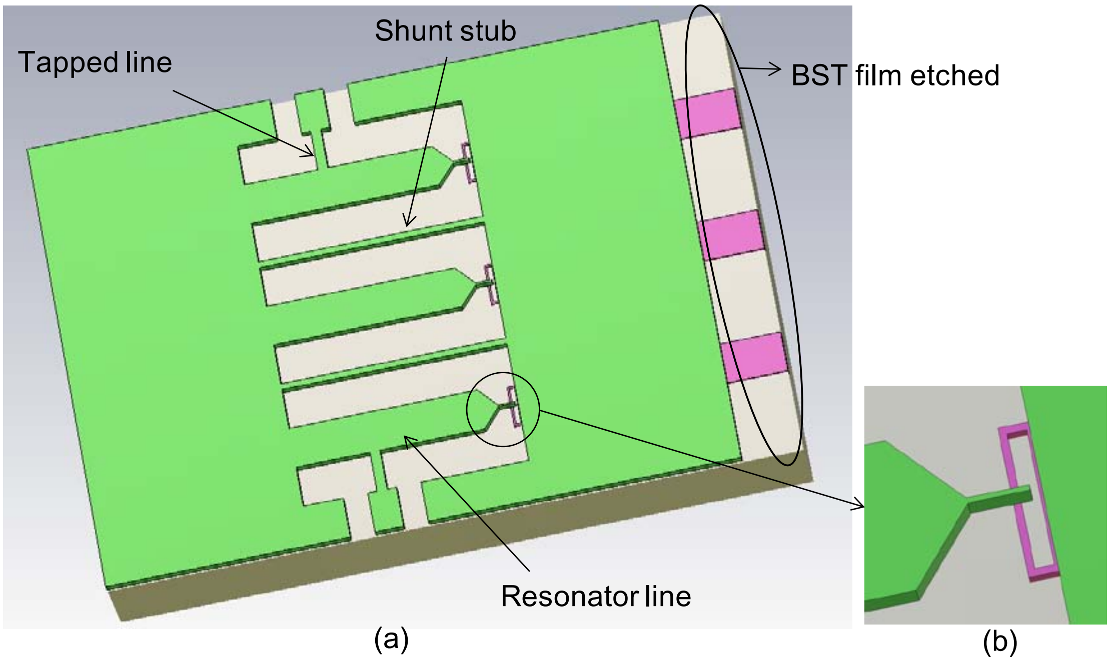

Fig.5- 2 A 3-pole BST bandpass filter (a) and the enlarged view of the BST parallel plate capacitor area (b); the top electrode is shown in green and the bottom electrode in pink, BST thin film is sandwiched between the two metal layers (this figure is not to scale).

The combline filters can be designed directly from the Chebyshev low-pass filter prototype using the concept of coupling matrix. The element values (g_i) for a 2-pole and a 3-pole Chebyshev filter for 0.02 dB ripple are calculated using the formulas provided in chapter 3 and given in Table 5- 1. The required coupling coefficients and external quality factors for a n-pole bandpass filter can be derived from the following equations [2] as

$$Q_{e1} = \frac{g_0 g_1}{FBW} \tag{5.1}$$

$$Q_{en} = \frac{g_n g_{n+1}}{FBW} \tag{5.2}$$

$$M_{i,i+1} = \frac{FBW}{\sqrt{g_i g_{i+1}}} \qquad \text{for i=1 to n-1} \tag{5.3}$$

where Q_{e1} and Q_{en} are the external quality factors of the resonators at the input and output, and $M_{i,i+1}$ are the coupling coefficients between the adjacent resonators. n is the filter order and FBW is the fractional bandwidth of the passband. The desired coupling coefficients and external quality factors for a 2-pole, 5 % fractional bandwidth (FBW) bandpass filter and a 3-pole, 9 % FBW bandpass filter are calculated and also shown in Table 5- 1.

Filter order	ripple (dB)	FBW	Return loss (dB)	g_0	g_1	g_2	g_3	g_4	Q_e	M_{12}	M_{23}
2	0.02	5%	23.38	1	0.539	0.471	1.145		10.786	0.099	
3	0.02	9%	23.38	1	0.723	1.039	0.723	1	8.037	0.104	0.104

Table 5- 1 The synthesis parameter values for a 2-pole and a 3-pole bandpass filter.

5.2.2 Investigating the resonant frequency

After determining the required coupling matrix for the desired filtering characteristic, the next step for the filter design is to characterise the coupling coefficients M_{ij} and external quality factors Q_e in terms of physical structures, which can be done by full wave electromagnetic (EM) simulation using Sonnet [5]. In the simulations, the metals were assumed to be lossless as a simplification. The dielectric constant of MgO substrate was 9.7 and the thickness of the substrate was 0.5 mm. The thickness of BST film was assumed to be 0.5 μm.

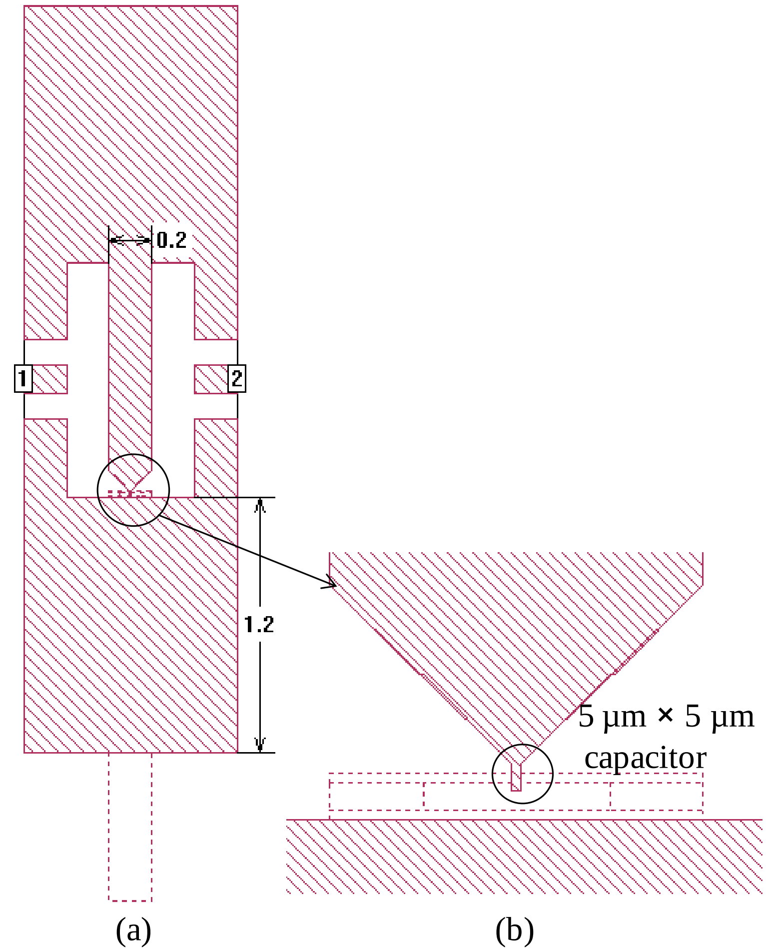

Fig.5- 3 The layout of a single resonator (a) and the enlarged part of the 5 µm × 5 µm capacitor area (b). The solid lines define the top metal electrodes and the dotted lines define the bottom electrodes (pictures taken from Sonnet).

Before M_{ij} and Q_e characterisation, a single resonator was first simulated in Sonnet as shown in Fig.5- 3. The length of the resonator line was 1.07 mm. The resonator line was 0.2 mm wide but narrowed to only 5 µm wide. The overlap area of the BST parallel plate capacitor is 5 µm × 5 µm. The bias line in the bottom metal line is 0.2 mm wide and 1.9 mm long with a 0.1 mm × 0.015 mm window at one end. The two upper ground planes are 1.2 mm × 1 mm in size.

The simulated resonant frequency of a single resonator as a function of the BST film dielectric constant was investigated and is shown in Fig.5- 4. The dielectric constant of the BST film was assumed to change from 100 to 1500 in steps of 100. The resonant frequency of the resonator decreases steadily from 18.1 GHz to 6.5 GHz with the increasing of BST film dielectric constant from 100 to 1500. The electrical length of the resonator line at each resonant frequency changes correspondingly from 57.3° to 27.2°, which is significantly less than 90°. The electrical length of a transmission line is defined as follows [6]

$$\theta = \beta l = \frac{2\pi f \sqrt{\varepsilon_r}}{c} l \tag{5.4}$$

where f is the resonant frequency, ε_r is the effective relative permittivity, c is the velocity of light in vacuum and l is the length of the resonator line. The electrical length of the resonator line decreases with the increasing of the loaded capacitance.

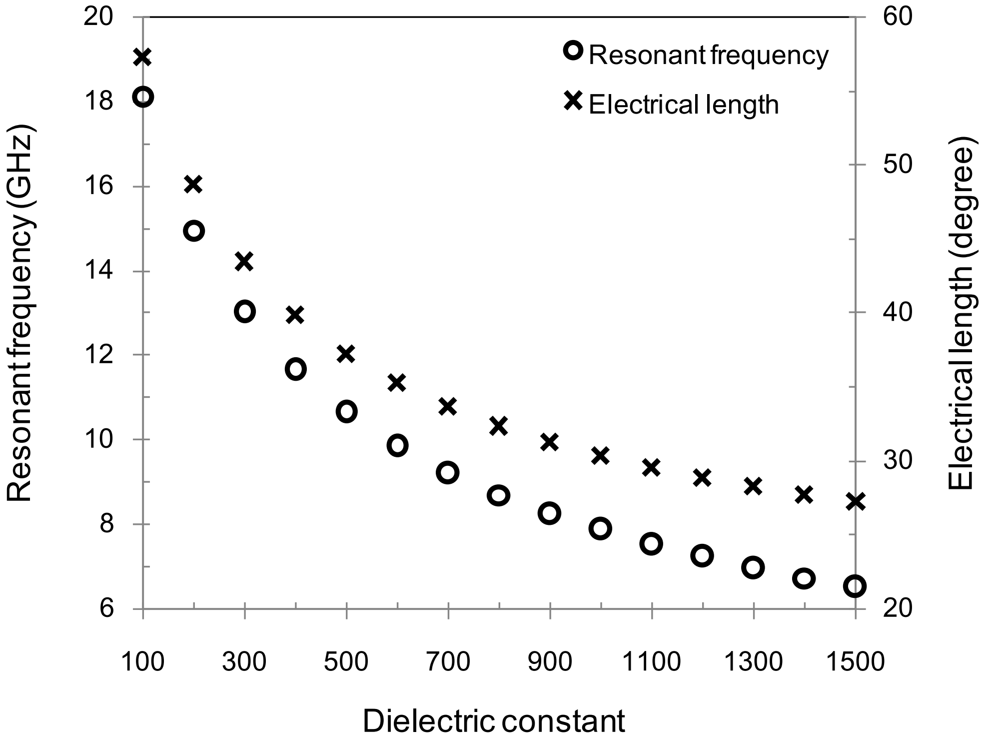

Fig.5- 4 The simulated resonant frequency of a single resonator (circles) and the electrical length of the resonator line (crosses) as a function of the dielectric constant of BST film in the range from 100 to 1500.

5.2.3 Investigating the external coupling

To extract the external quality factor Q_e, a resonator properly coupled to one port by tapped line is constructed in Sonnet, as shown in Fig.5- 5. The other port is weakly coupled to avoid its effect on the external Q_e. The tapped line is 0.2 mm long, 0.05 mm wide and its position is controlled by the distance d between the tapped line and the virtual ground. The tapped line is always centred at the port interface signal line. The two upper ground planes are 1.2 mm × 1 mm in size and are not shown in complete in the figure.

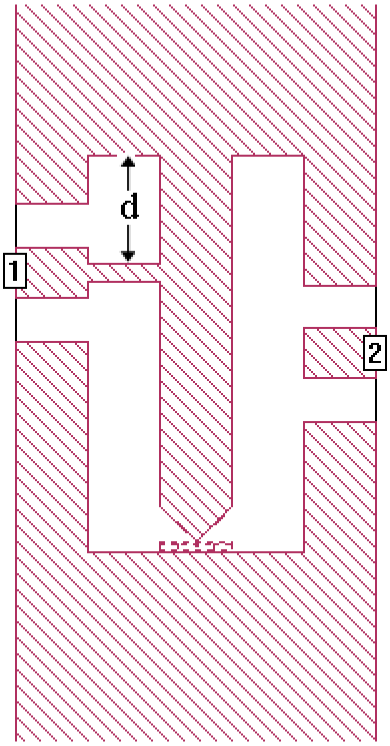

Fig.5- 5 The layout of an external coupled resonator (figure taken from Sonnet).

The coupling strength of the tapped lines is controlled by the position of the tapped line and declines with moving towards to the virtual ground [2]. The smaller the distance d is, the weaker the input/output coupling is, which is represented by the larger external quality factor. For a fixed BST film dielectric constant of 500, the simulated transmission of an external coupled resonator as a function of different tapped line position is shown in Fig.5- 6.

The external quality factor can be extracted from the transmission as [2]

$$Q_e = \frac{\omega_0}{\Delta\omega_{3dB}} = \frac{f_0}{f_2 - f_1} \tag{5.5}$$

where ω_0 is the resonant frequency, $\Delta\omega_{3dB}$ is the bandwidth for which the attenuation for S_{21} is 3 dB from that at the resonance peak. The larger the bandwidth is, the smaller the external Q_e

value, which also means a stronger coupling. The extracted Q_e versus different tapped line positions for a fixed BST film dielectric constant of 500 is shown in Table 5- 2. The external coupling strength is reduced considerably (external Q_e value from 7.5 to 16.7) with the tapped line moving close to the ground (d decreasing from 0.4 mm to 0.2 mm). In the filter simulation which will be given later, a tapped line distance of 0.3 mm is chosen to implement the 2-pole filter, which gives an external Q_e of 10.7 for a BST film dielectric constant of 500. For the 3-pole filter, a distance of 0.38 mm is chosen and an external Q_e of 8.0 is achieved. The achieved external quality factors are very close to that of specified in Table 5- 1 (a desired Q_e of 10.786 for the 2-pole filter and 8.037 for the 3-pole filter). The resonant frequency shifts slightly with the tapped line positions.

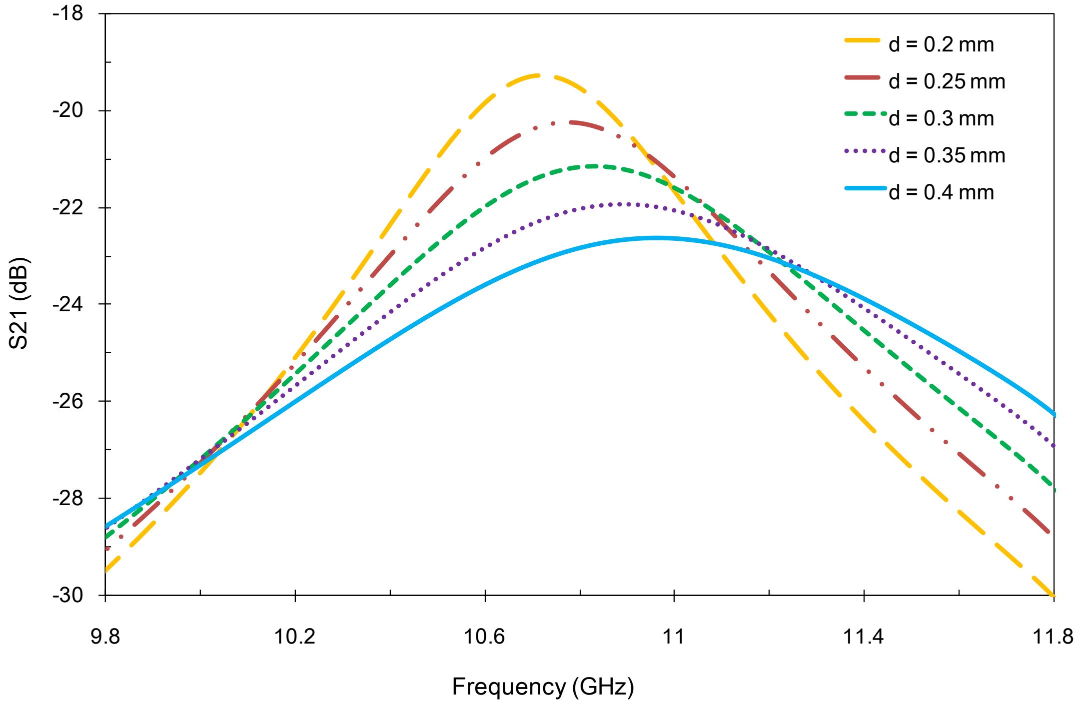

Fig.5- 6 The simulated S_{21} of the external coupled resonator for the tapped line to virtual ground distance d changing from 0.2 mm to 0.4 mm at a step of 0.05 mm. The BST film dielectric constant is 500.

d	0.2	0.25	0.3	0.35	0.38	0.4
Q_e	16.7	13.2	10.7	8.9	8.0	7.5

Table 5- 2 The external quality factor (Q_e) for different tapped line to ground distance (d) when the dielectric constant of BST film is fixed to 500.

In addition, the external coupling is also related to the dielectric constant of the BST film as the tapped line is directly connected with the resonator and the BST capacitor. The extracted external Q_e as a function of the BST film dielectric constant is shown in Fig.5- 7, for a tapped line to ground distance d fixed to 0.3 mm. The external Q_e value increases from 7.2 to 17.8, which corresponds to a reduced external coupling strength, with the BST film dielectric constant increasing from 100 to 1500.

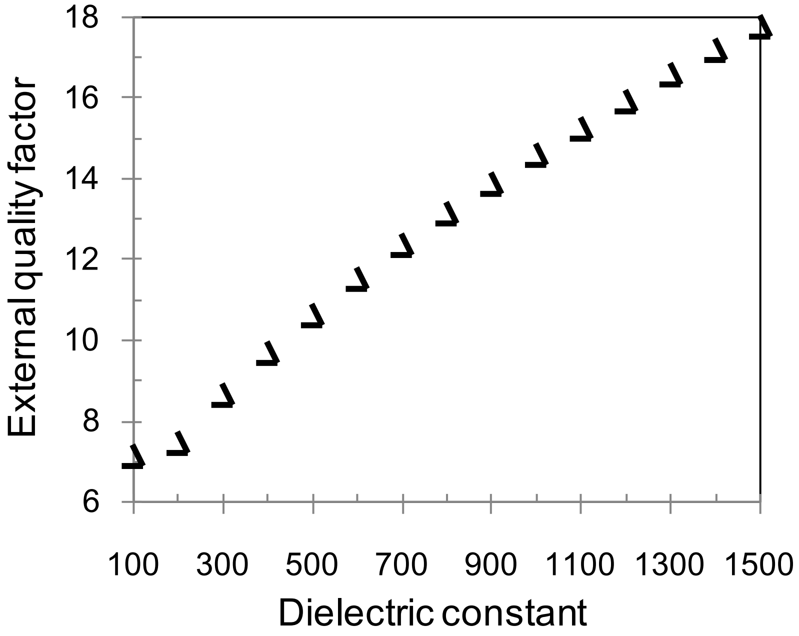

Fig.5- 7 The extracted external quality factor versus the dielectric constant of BST film in the range from 100 to 1500 at a step of 100 for a fixed tapped line position d of 0.3 mm.

5.2.4 Investigating the coupling coefficient

The layout of two coupled resonators is shown in Fig.5- 8, with a shunt short between ground planes to weaken the coupling between the two resonators. The two upper ground planes are 1.6 mm × 1.2 mm in size and are not shown complete in the figure. The short is 1.1 mm long. The distance from the resonator line to the short is 0.2 mm.

As mentioned in chapter 3, the coupling coefficient can be extracted from the frequency response of the coupled resonators as [2]

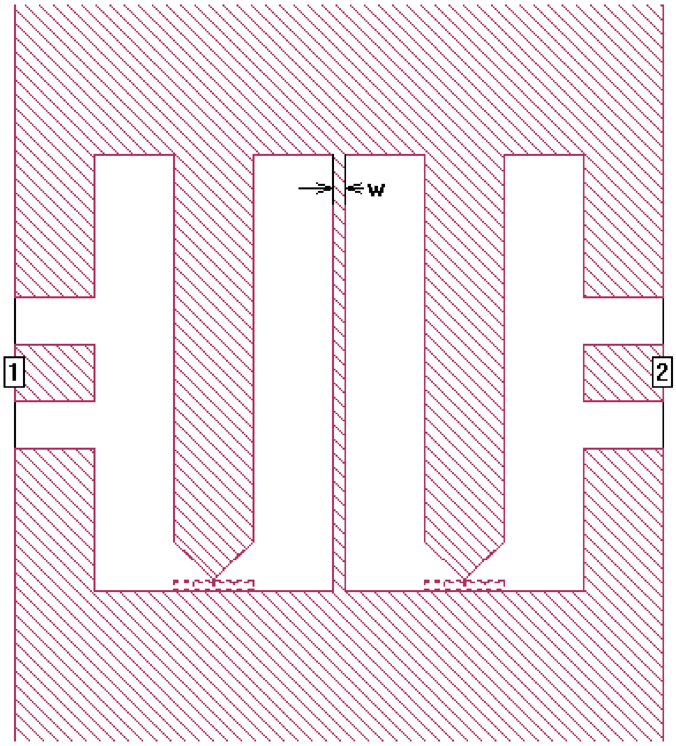

Fig.5- 8 The layout of two coupled resonators in the presence of a short (figure taken from Sonnet).

$$M_{ij} = \pm \frac{f_2^2 - f_1^2}{f_2^2 + f_1^2} \tag{5.6}$$

where f_1 is the lower resonant frequency and f_2 is the upper resonant frequency. The magnitude of the coupling coefficient determines the separation between the two split resonance peaks. Normally the stronger coupling between the resonators is (bigger the coupling coefficient), the larger the separation of the two split resonances and the deeper the trough in the middle is. A coupling coefficient of 0.2 was acquired without the presence of the short, which was much larger than the required coupling coefficients listed in Table 5- 1. This coupling between the two resonators can be significantly depressed by a short and its strength can be controlled by the width of the short. The simulated transmission of the coupled resonators as a function of the short width w is shown in Fig.5- 9, with a BST permittivity of 500. A wider short leads to a smaller coupling, which corresponds to a transmission response with closer peaks in Fig.5- 9. The extracted coupling coefficient decreases from 0.13 to 0.06 with the short width increasing from 0.005 mm to 0.1 mm, as shown in Fig.5- 10. A short width of 0.03 mm is chosen to implement both the 2-pole and 3-pole BST filters, which gives a coupling coefficient of 0.1 and this is very close to that of the required coupling coefficients listed in Table 5- 1. The coupling coefficient does not change with the dielectric constant of the BST film.

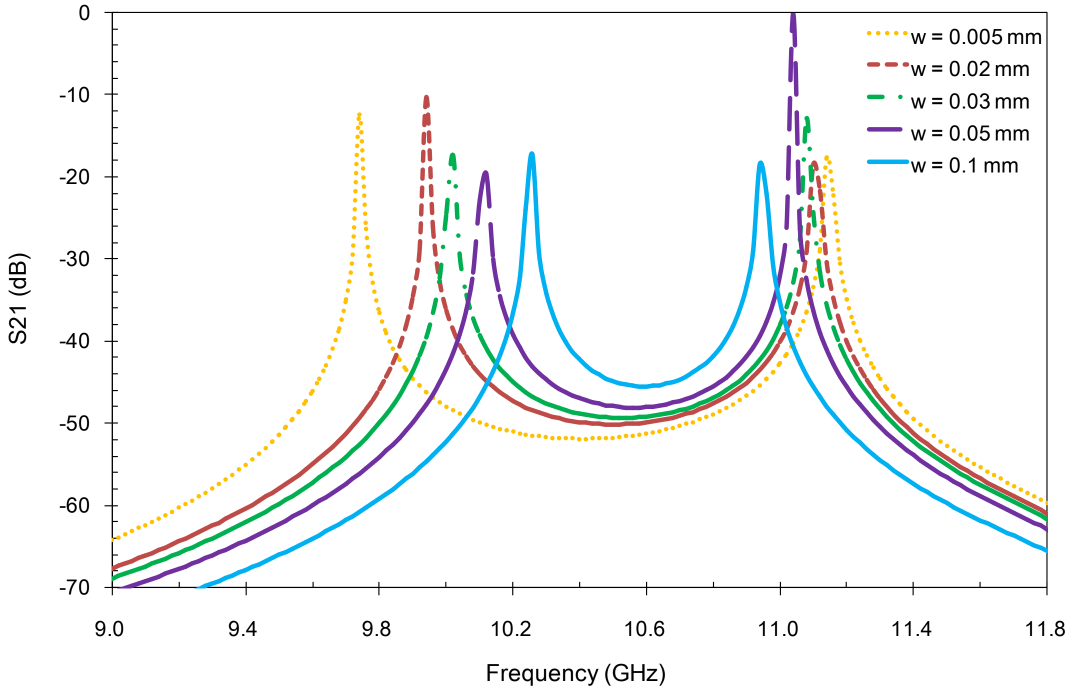

Fig.5- 9 The simulated S_{21} of the coupled resonators shown in Fig.5- 8 for a short width of 0.005 mm, 0.02 mm, 0.03 mm, 0.05 mm and 0.1mm respectively. The BST film dielectric constant is 500.

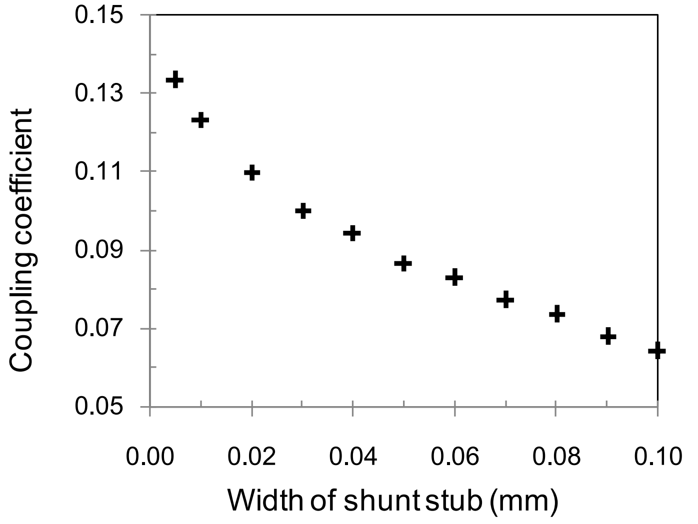

Fig.5- 10 The coupling coefficient as a function of the width of the short for a BST film dielectric constant of 500.

5.3 Completed filter design

A 2-pole filter with the tapped line to ground distance of 0.3 mm and a short of 0.03 mm wide was constructed and simulated in Sonnet. The CPW input/output lines were designed to have a characteristic impedance of around 50 Ω. The width of the signal line was 0.14 mm and the gap between the signal line and the ground was 0.12 mm, which also matched the dimensions of the microprobes used in the measurement. The size of the 2-pole filter was approximately 1.6 mm × 4 mm. The simulated response of the 2-pole filter in a lossless assumption is shown Fig.5- 11 for the BST film dielectric constant changing from 200 to 1200. The filter is tuned from about 7.2 GHz for a BST film dielectric constant of 1200 to 15.4 GHz for a dielectric constant of 200. As can be seen in Fig.5- 11, the external coupling is too strong for the filters with BST dielectric constant of 200 and 300, and the external coupling is too weak for BST dielectric constant of 800 and 1200. This is because the filter is designed at a BST dielectric constant of 500 and the external coupling strength declines with the increasing of BST dielectric constant. The resonances outside the passband are caused by the resonance of the bias line in the bottom metal layer. The bottom electrode line behaves as a half wavelength resonator at 5.7 GHz, a full wavelength resonator at 11.95 GHz, and a 3/2 wavelength resonator at 18.45 GHz for a BST dielectric constant of 500. The current distribution of the 2-pole filter at 11.95 GHz and 18.45 GHz is shown in Fig.5- 12 and Fig.5- 13 respectively. As can be seen from Fig.5- 12, at 11.95 GHz, the bias line performs as an open circuited wavelength resonator which is equivalent to a parallel LC resonator circuit and it is connected in shunt configuration to the ports. These sharp peaks have a very high Q and are non-existent when loss factors are considered.

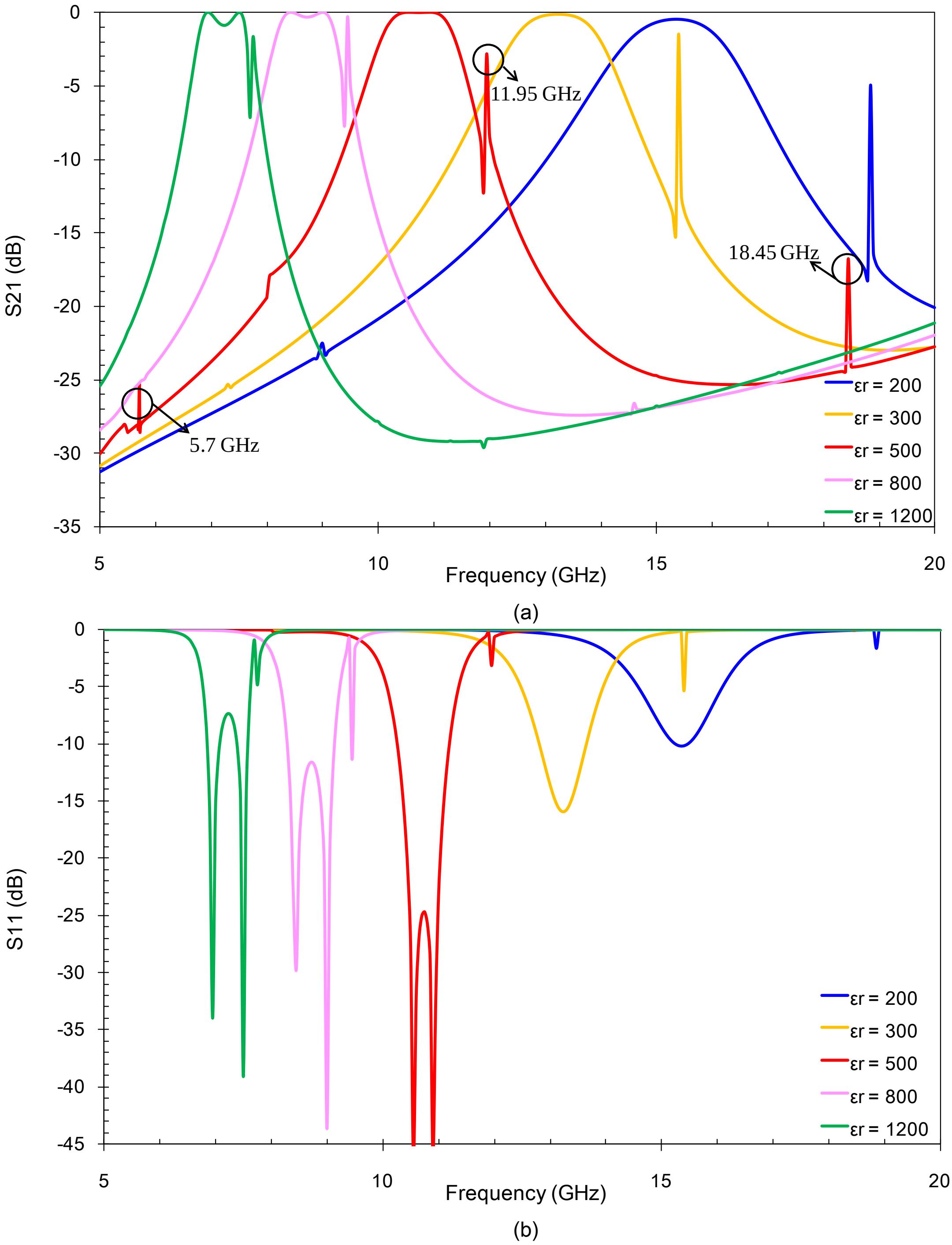

Fig.5- 11 The simulated transmission (a) and reflection (b) of a lossless 2-pole filter with BST film dielectric constant changing from 200 and 1200.

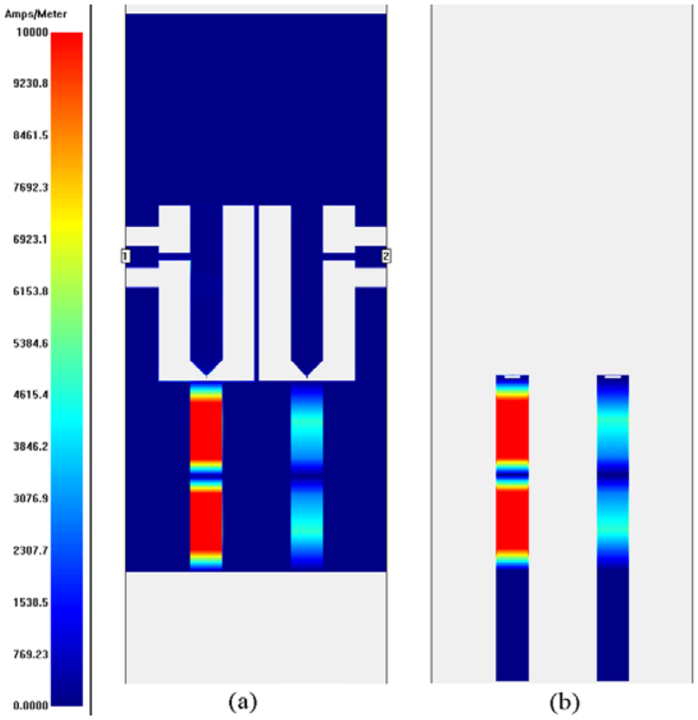

Fig.5- 12 The current distribution of the top metal layer (a) and bottom metal layer (b) of the 2-pole BST filter at 11.85 GHz, for a BST dielectric constant of 500.

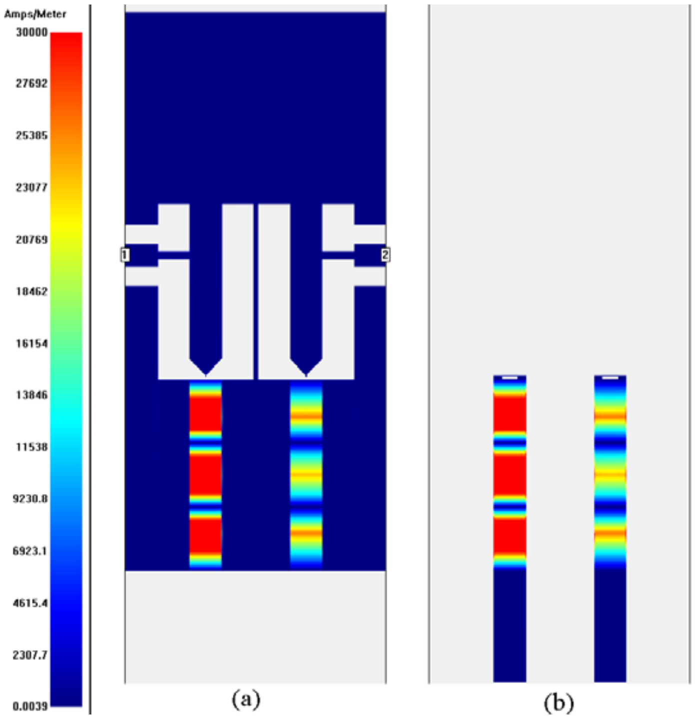

Fig.5- 13 The current distribution of the top metal layer (a) and bottom metal layer (b) of the 2-pole BST filter at 18.45 GHz, for a BST dielectric constant of 500.

A 3-pole filter was also designed with a tapped line to ground distance of 0.38 mm and shorts of 0.03 mm wide. The 3-pole filter has a size of approximately 2.3 mm × 4 mm. The simulated response of the 3-pole filter as a function of BST dielectric constant of 300, 500 and 800 is shown in Fig.5- 15. However, as the resonant frequency of the second resonator is slightly different from the first and third resonator, the 3-pole filter is not well matched and the return loss is worse than 5 dB. In practice, the poor matching could be improved by independently tuning each resonator since the bias lines are separated from each other. In the simulation, the independent tuning could be simulated using a dielectric brick having a dielectric constant different to the rest of the BST film. A dielectric brick, which is a solid volume of dielectric material embedded within a circuit layer, is used in Sonnet as an approximation of dielectric discontinuities [5]. For the 3-pole filter with a BST dielectric constant of 500, a dielectric brick with a size of 10 µm × 10 µm and a dielectric constant of 440 was embedded at the BST capacitor area of second resonator. The return loss can be improved to better than 19 dB in this way as shown in Fig.5- 14. For the 3-pole filter with a BST dielectric constant of 300 and 800, dielectric bricks can be used in a similar way to have good return loss.

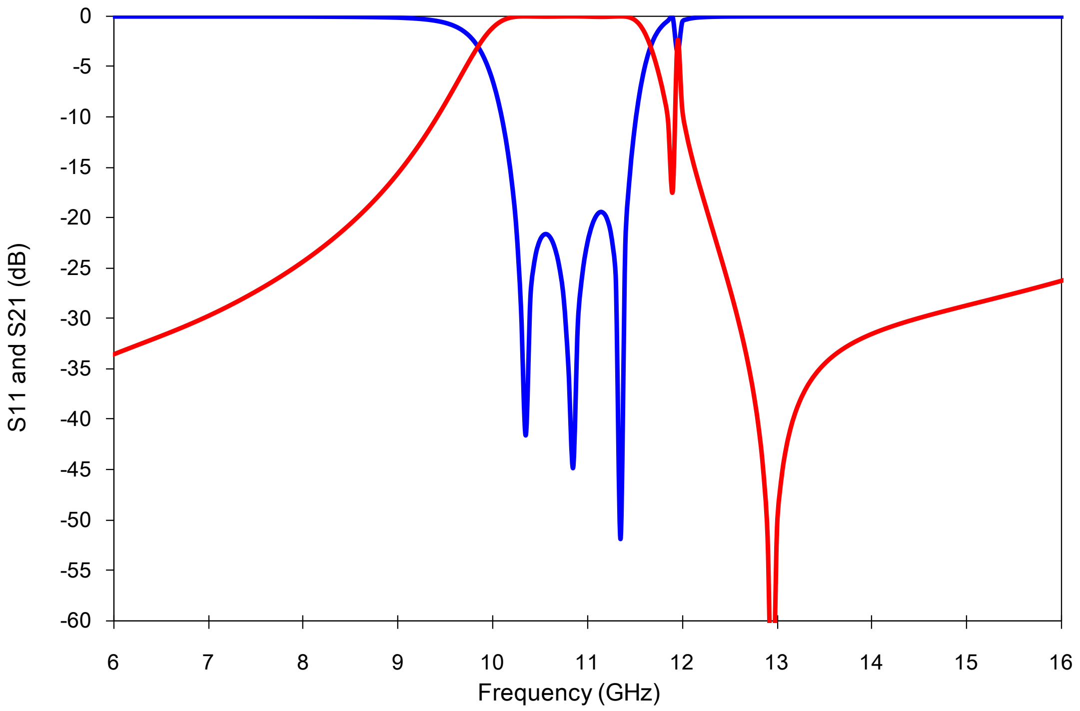

Fig.5- 14 A 3-pole BST filter uses a dielectric brick for good return loss. The dielectric constant of the BST film spreading the circuit area is 500. The dielectric brick embedded at the capacitor overlap area of the second resonator uses a dielectric constant of 440.

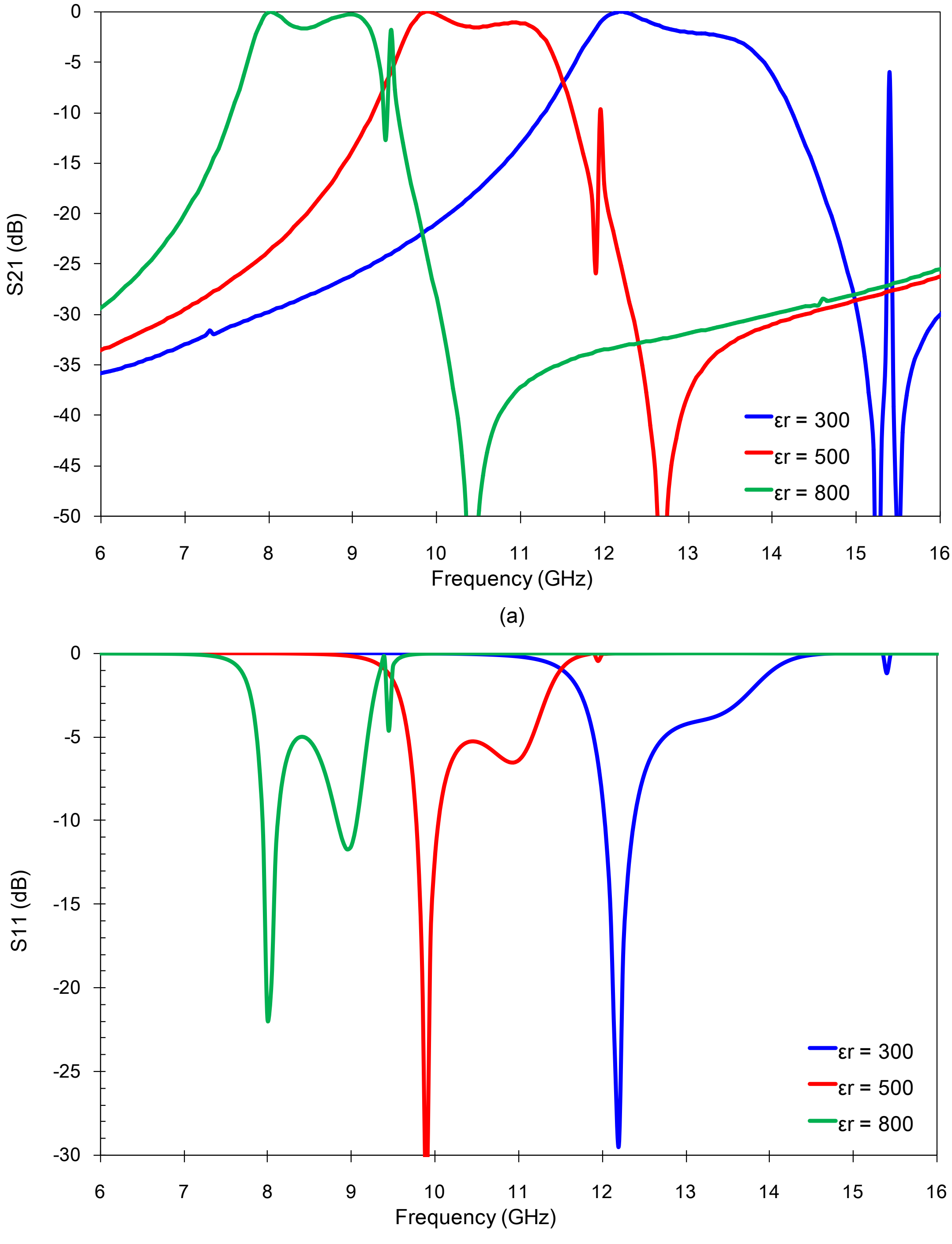

(a)

(b)

Fig.5- 15 The simulated transmission (a) and reflection (b) of a lossless 3-pole filter with BST dielectric constant of 300, 500 and 800.

5.4 Investigating quality factor and loss

The discussion above is based on a lossless assumption. However, practical room temperature integrated BST filters exhibit an insertion loss in the range of 3 - 8 dB at X- or Ku-band [7-9]. To evaluate the contribution of metal loss and dielectric loss separately, resonators with only loss from the top metal layer, or the bottom metal layer, or the BST film were simulated using Sonnet. The top and bottom electrode was assumed to be gold and platinum respectively. Metal with different thickness and BST film with different loss tangent were assumed in the resonator simulation. As discussed in chapter 3, the loaded quality factor of a resonator can be derived from the simulated transmission response as [6]

$$Q_L = \frac{\omega_0}{\Delta\omega_{3dB}} \tag{5.7}$$

where ω_0 is the resonant frequency, $\Delta\omega_{3dB}$ is the 3 dB attenuation bandwidth. The loaded Q includes the loss from the resonator as well as the effect of the external loading as [10]

$$\frac{1}{Q_L} = \frac{1}{Q_e} + \frac{1}{Q_u} \tag{5.8}$$

where Q_u is the unloaded quality factor of the resonator, and Q_e represents the effect from the external loading. When the resonator is weakly coupled, the loaded Q extracted from the simulation or measurement can be regarded as the unloaded Q [11]. The loaded quality factors of the resonators with different loss assumptions for a fixed BST dielectric constant of 500 are extracted from the simulations. As the resonators are weakly coupled (insertion loss is more than 25 dB), these Q_L can be used as unloaded Q of the resonators, as concluded in Table 5- 3.

Resonator	Top electrode Au thickness (nm)				Bottom electrode Pt thickness (nm)				BST loss tangent			
	300	500	1000	2000	300	1000	2000	3000	0.01	0.02	0.05	0.1
Q_u	20.2	32.8	56.1	55.3	31.1	94.6	138	148.8	112.7	58.7	23.2	10.7

Table 5- 3 A summary of the quality factors of the simulated resonators for different metal thickness or different BST film loss tangent, for a fixed BST dielectric constant of 500.

The metal loss can to be severe at microwave frequencies especially when the metal layer is thin and narrow lines are involved in the circuit. At high frequencies, the electric current in a conductor is not uniformly distributed but reinforced into the surface of the conductor, which is known as the skin effect. The skin effect increases the effective resistance of conductors at high frequency and degrades the loss performance of the circuits. The skin depth is a measure of the distance over which the current falls 1/e of its original value [6]. As discussed in chapter 2, most of the current (95 %) flows within the top three skin depth from the conductor surface. Therefore, a metal layer thickness less than about three times the skin depth at the operating frequency will aggravate the current crowding and lead to inferior loss performance. The skin depth of gold and platinum at 10 GHz is 780 nm and 1630 nm respectively. A resonator quality factor of 20.2 was extracted when the top electrode was assumed to be 300 nm thick gold. This can be increased to 56.1 by increasing the gold thickness to 1000 nm. Paper [12], [13] also presented BST capacitors with increased quality factors using thicker metallisation.

The loss mechanisms of BST thin films have been studied in [14], [15]. However, the conclusion is not straightforward, especially in the microwave region. As discussed in chapter 2, the loss tangent of BST film is electric field, frequency and temperature dependent, and also depends on lots of fabrication issues such as substrate choice, misfit strain, growth temperature, surface roughness and so on. For the state of art of BST thin film technology, BST capacitors with Q better than 100 at 1 MHz can be readily obtained [13], [16]. However, this is usually degraded at higher frequencies as the loss tangent of BST film is directly proportional to frequency in microwave region [17]. Intensive research has been made to improve the Q of BST capacitor in the microwave region. Paper [18] reported an BST interdigital capacitor having a zero bias Q of 50 at 30 GHz. A circular BST parallel plate capacitor revealed a Q of 100 at 10 GHz and better than 40 up to 45 GHz, which is the best ever reported Q of BST capacitors in the microwave region [13].

The total unloaded quality factor of a lossy resonator considering losses from all parts can be derived as

$$\frac{1}{Q_u}=\frac{1}{Q_c}+\frac{1}{Q_{BST}}+\frac{1}{Q_{sub}}+\frac{1}{Q_{rad}} \tag{5.9}$$

where Q_c, Q_{BST}, Q_{sub} and Q_{rad} stand for the loss contribution from the conductors, BST film, substrate dielectric loss and radiation respectively. For a resonator with 500 nm thick gold as top electrode, 300 nm platinum as bottom electrode, and BST loss tangent of 0.05, the total Q_u of the resonator is 9.5 derived from equation (5.9) for a fixed BST dielectric constant of 500. The loss from the MgO substrate and radiation loss is small and negligible in this case (Q > 1000). The dissipation of a bandpass filter can be estimated from the resonator Q as follows

$$\mathrm{IL}_{f_0} = 4.343 \sum_{i=1}^{n} \frac{\Omega_c}{\mathrm{FBW}\, Q_i} g_i \ (\mathrm{dB}) \tag{5.10}$$

where IL_{f0} is the insertion loss in dB at the centre frequency of the filter, $\Omega_c = 1$, FBW is the fractional bandwidth of the filter, g_i is the normalised element value of the Chebysev lowpass prototype filter and Q_i is the unloaded quality factor of the resonator corresponding to element g_i. Substituting the unloaded resonator Q of 9.5 into the equation (5.10), the insertion loss of the 5 % FBW, 0.02 ripple 2-pole filter is estimated to be 9.2 dB at the centre frequency of the filter (for a BST dielectric constant of 500). For the 9 % FBW, 0.02 ripple 3-pole filter, the insertion loss at the centre frequency of the filter is estimated to be 12.6 dB (for a BST dielectric constant of 500).

However, the resonator Q also changes with the dielectric constant of the BST film. For instance, when only the loss from the top electrode is considered in the resonator simulation and the top electrode is assumed to be 500 nm thick gold, the resonator quality factors decreases with the dielectric constant of the BST film as summarised in Table 5- 4. This can be explained by an aggravating electric field concentration in the conductors with the increased effective dielectric constant, hence an inferior loss performance.

BST film permittivity	Resonator Q		
	Top electrode Au t = 500 nm	Bottom electrode Pt t = 300 nm	BST tanδ = 0.05
$\varepsilon_r = 200$	44.3	65.7	30.0
$\varepsilon_r = 500$	32.8	31.1	23.2
$\varepsilon_r = 1200$	23.2	16.9	21.6

Table 5- 4 A summary of resonator Q for BST film dielectric constant (ε_r) of 200, 500 and 1200 for a fixed metal thickness (t) or a fixed BST loss tangent (tanδ).

Lossy 2-pole and 3-pole filters are simulated and the simulated results as a function of BST dielectric constant are shown in Fig.5- 16 and Fig.5- 17 respectively. In the simulation, the top metal layer is set as 500 nm thick gold and the bottom metal layer is 300 nm platinum. The loss tangent of BST thin film is set as 0.05. For the 2-pole and 3-pole filters, the simulated passband insertion loss is 8.6 dB and 11.4 dB respectively for a BST dielectric constant of 500, which are close to the estimation using equation (5.10). The simulated filters with higher dielectric constant have an inferior insertion loss as a result of fading Q and matching. It should be noted that the increasing in insertion loss with the increasing of dielectric constant is consistent with the change of Q in Table 5- 4.

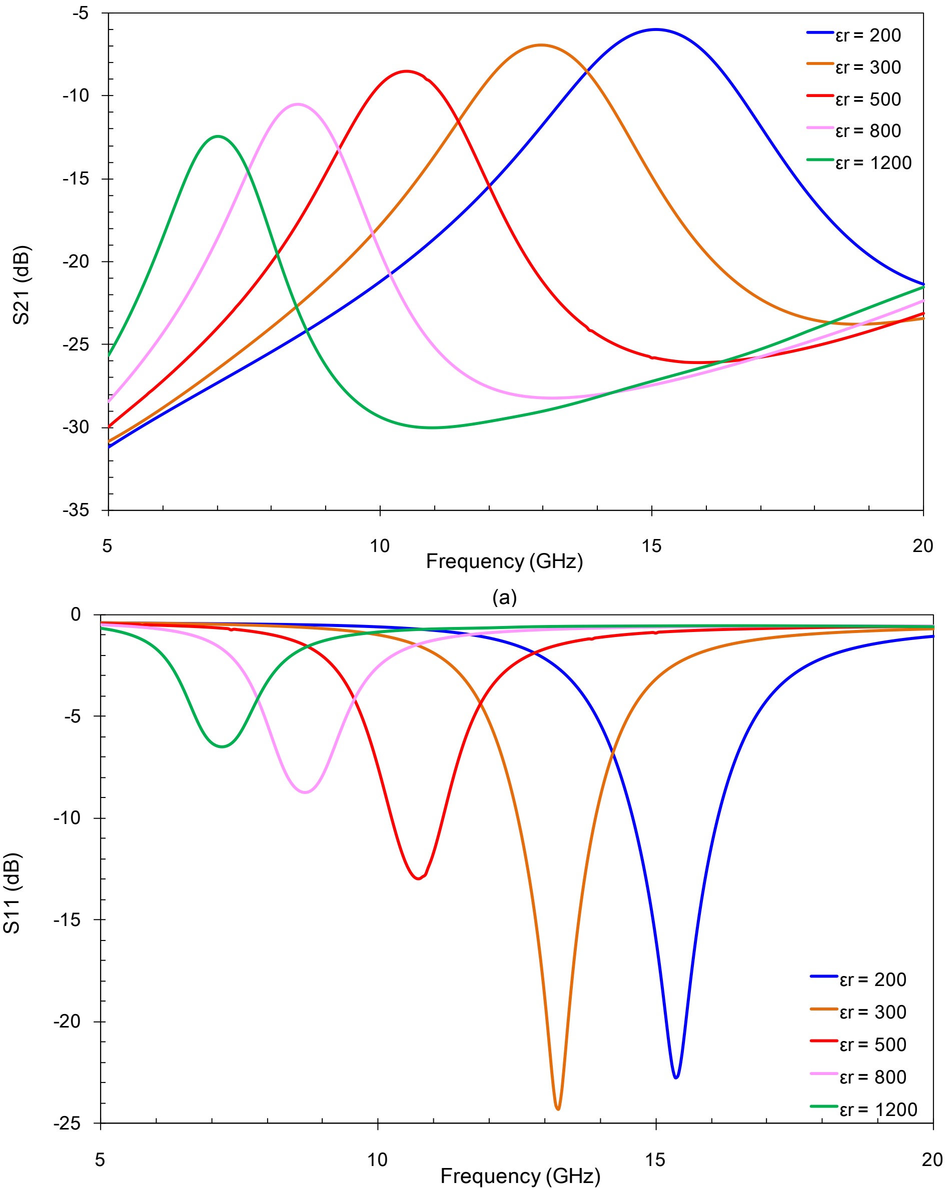

(a)

(b)

Fig.5- 16 The simulated transmission (a) and reflection (b) of the lossy 2-pole filter with BST film dielectric constant changing from 200 and 1200.

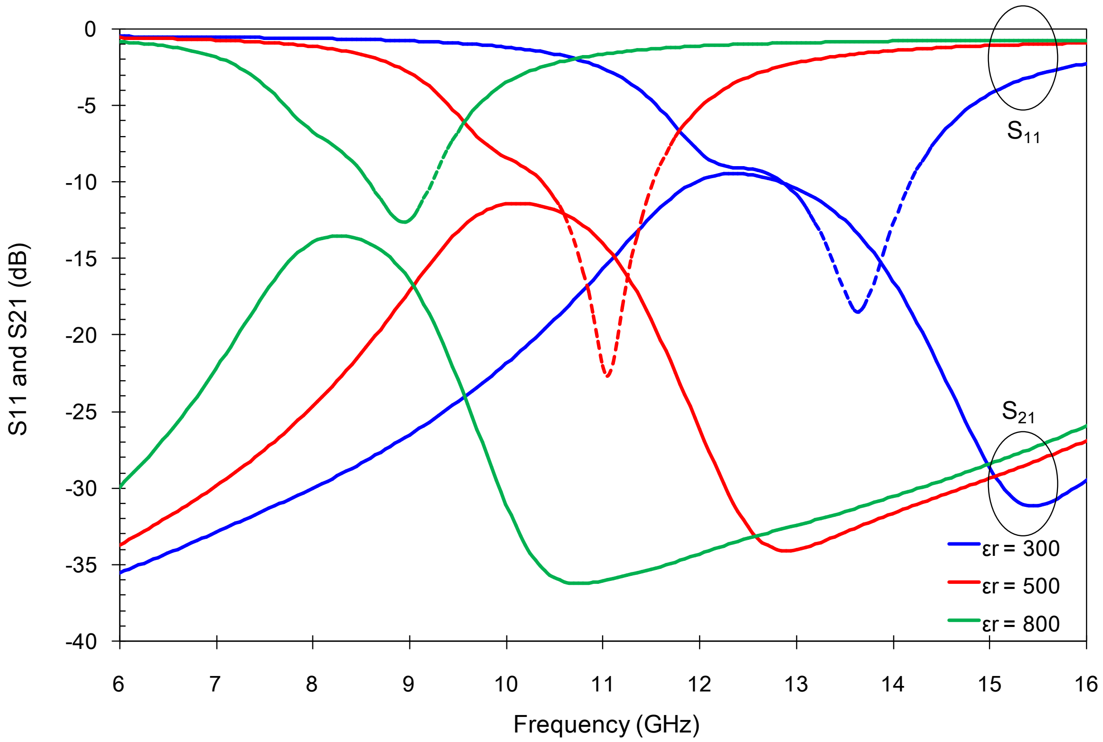

Fig.5- 17 The simulated transmission (solid lines) and reflection (dashed lines) of the lossy 3-pole filter with BST film dielectric constant of 300, 500 and 800.

5.5 Fabrication

The fabrication process of the BST bandpass filters is shown in the process flow diagram with corresponding sectional schematics in Fig.5- 18. A thin layer of platinum was deposited on 0.5 mm thick MgO substrate as bottom electrode of the filters by RF magnetron sputtering. The bottom electrode was defined by ion beam milling with positive imaging photoresist, Shipley 1813. Pulsed laser deposition was then used to deposit 500 nm of $Ba_{0.6}Sr_{0.4}TiO_3$ film on the metallised MgO substrate, with a laser repetition rate of 50 Hz, 50000 pulses. The deposition temperature was maintained at 650 °C. The O_2 pressure in chamber was 0.3 mbar and O_2 flow rate was 10 sccm. The sample was cooled down to room temperature at a rate of - 4 °C/min in 800 mbar static oxygen ambient. After the BST deposition, the top metal, which was gold (with a chromium buffer layer not shown in the figure), was deposited by RF magnetron sputtering on top of the BST film and patterned by UV photolithography and ion beam milling. In the final step, part of the BST film was removed by ion beam milling to uncover the bottom electrode. A photo of the enlarged area of the BST parallel plate capacitor taken with an optical microscope is shown in Fig.5- 19.

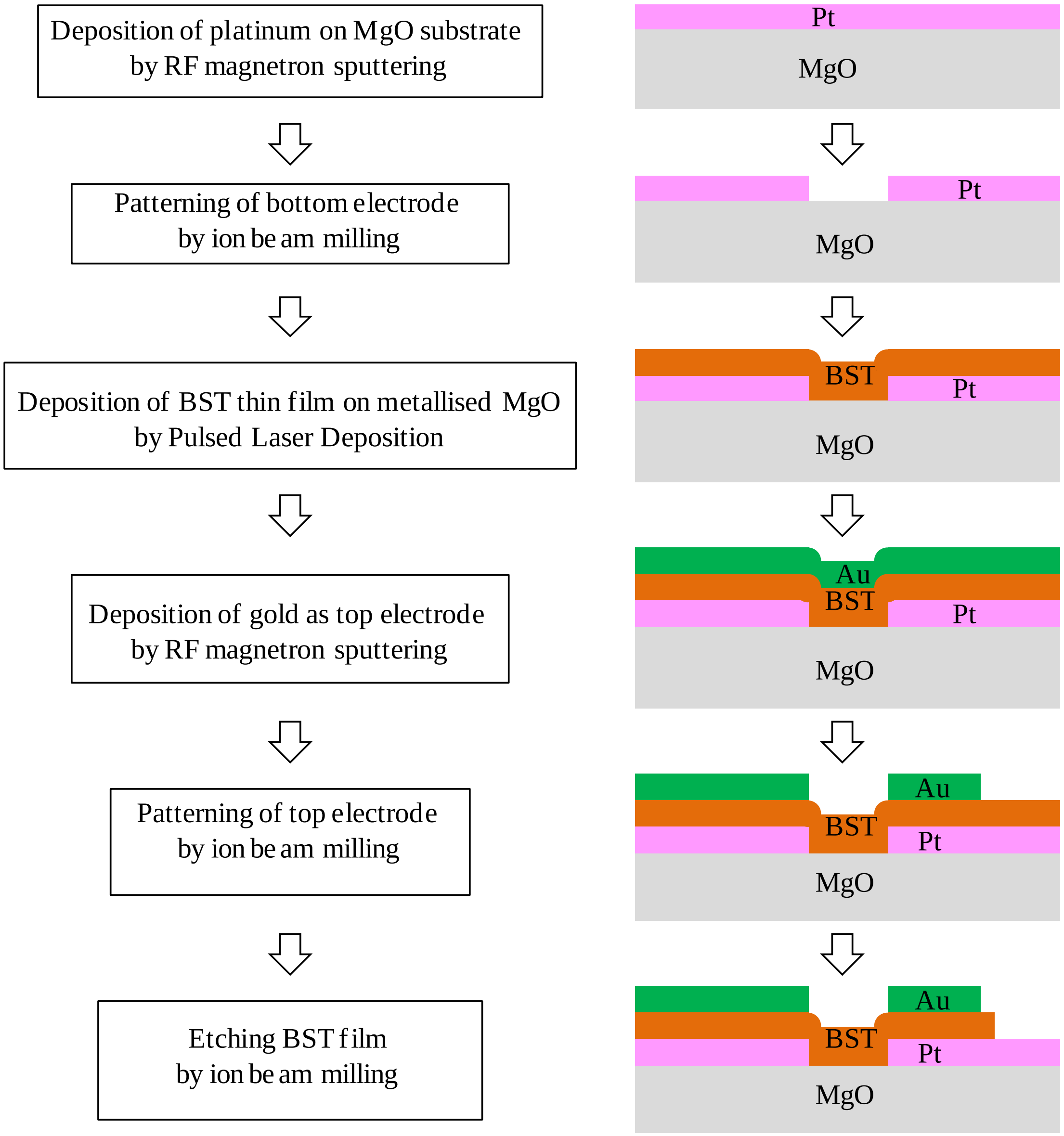

Fig.5- 18 The fabrication process of the BST bandpass filters shown in flow diagrams with corresponding sectional schematics.

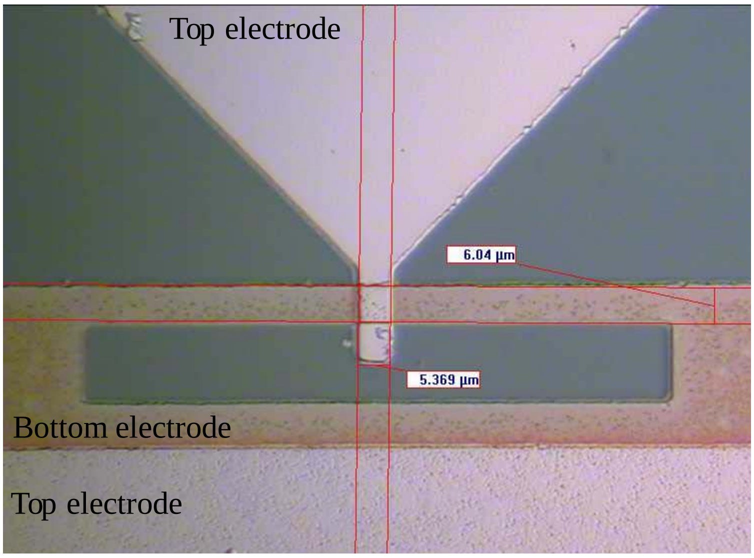

Fig.5- 19 Photo of the BST parallel plate capacitor area of a filter, taken with an optical microscope.

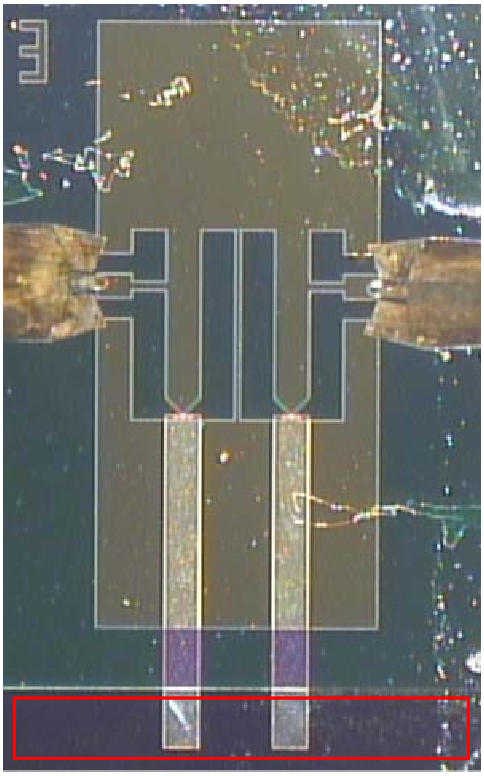

Fig.5- 20 A 2-pole BST filter under test, BST film in the area surrounded by the red box was removed. DC probes were located on the ground in the top metal layer and the bias lines in the bottom metal layer.

The 2-pole and 3-pole BST filters were designed to have a tapped line to ground distance of 0.3 mm and 0.38 mm respectively for a BST film dielectric constant of 500. However, in the practical fabrication, as the permittivity of BST film is not likely to be precisely controlled, three filters with different tapped line positions were fabricated on the same sample to adapt to possible BST film permittivity.

Compared with the BST lowpass filters discussed in chapter 4, an extra step of etching BST film is required in the fabrication of BST bandpass filters, which increases the fabrication complexity substantially. As indicated in Fig.5- 20, BST film in the enclosed area was removed by ion beam milling whereas the rest part of the circuit was protected by photoresist. However, etching of BST film by either ion beam milling or chemical etching can cause damage to the electrodes and substrate underneath and leads to a poor quality of the device [19]. Besides, the large capacitance between the upper ground and bottom bias line is connected in parallel with the BST parallel plate capacitor for DC signals. As shown in Fig.5- 20, any hillock, hole or imperfection of the BST film on top of the bias line area may leads to breakdown with bias and DC short circuit between the bias line and the top electrode. The BST capacitor can not be biased and the filter can not be properly tuned in this case. The problems above make the fabrication of BST filters very difficult.

5.6 Measurement

The BST integrated capacitors based bandpass filters were tested on a probe station using an Agilent 8722ES S-parameter Network Analyser. The devices were probed by microprobes in a ground-signal-ground (GSG) configuration, as shown in Fig.5- 20, via 3.5 mm coaxial cables and bias tees to protect the network analyser. The DC bias was applied to the top electrode and the bias lines respectively, via DC probes using a voltage source. Although the resonators can be independently biased, the same bias voltage was applied to the resonators in a filter. A full two port calibration was performed using Cascade 101-190B Impedance Standard Substrate over 0.05 GHz to 20 GHz.

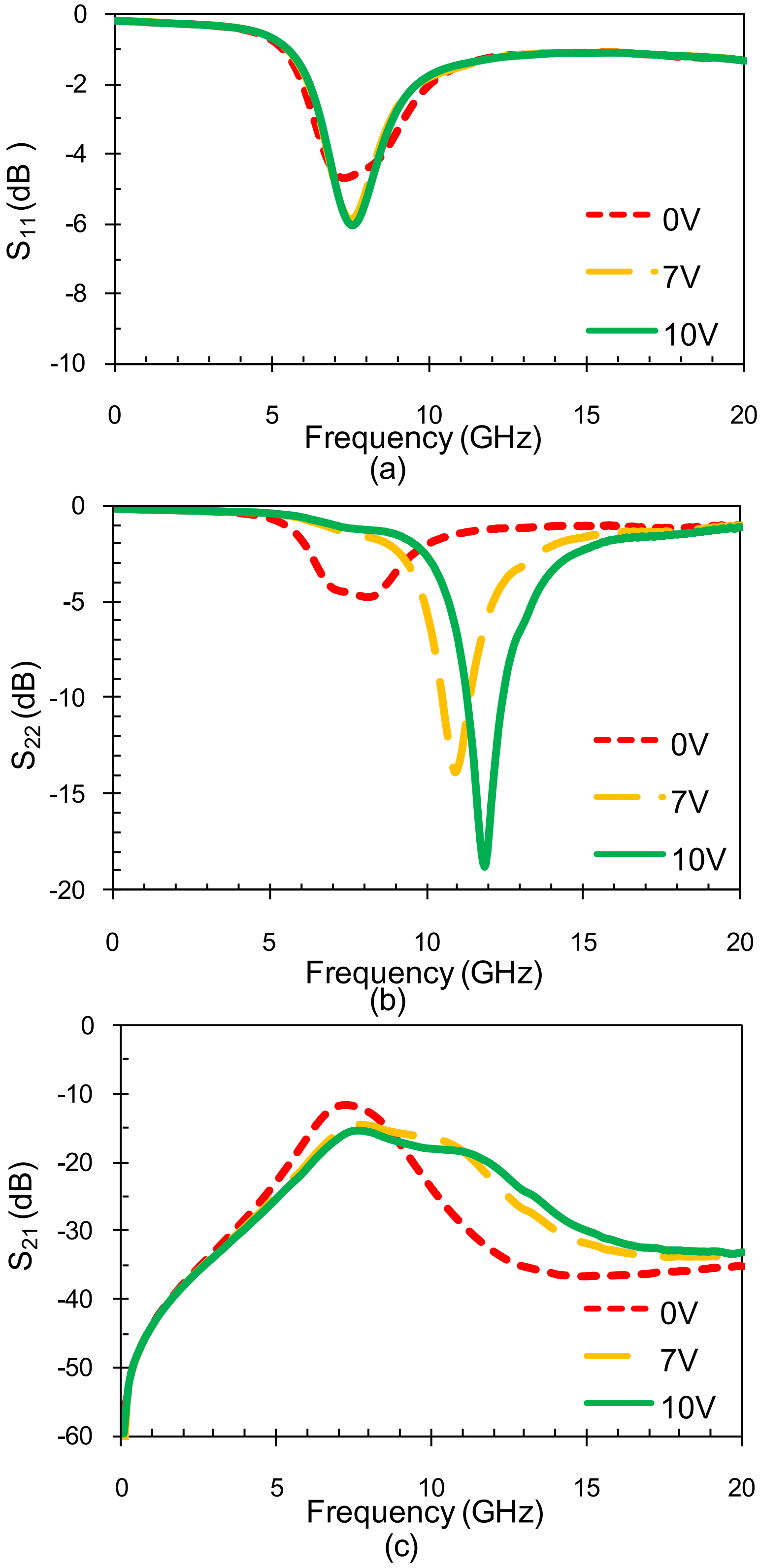

Fig.5- 21 The measured S_{11} (a), S_{22} (b) and S_{21} (c) of a two pole BST filter versus frequency at bias voltages of 0 V, 7 V and 10 V.

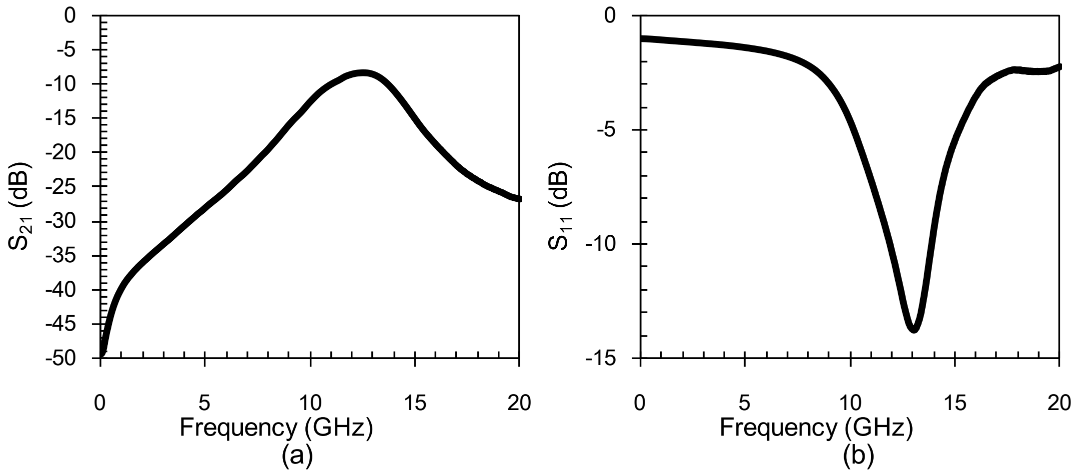

Fig.5- 22 The measured insertion loss (a) and return loss (b) of a 2-pole BST bandpass filter at 0 V

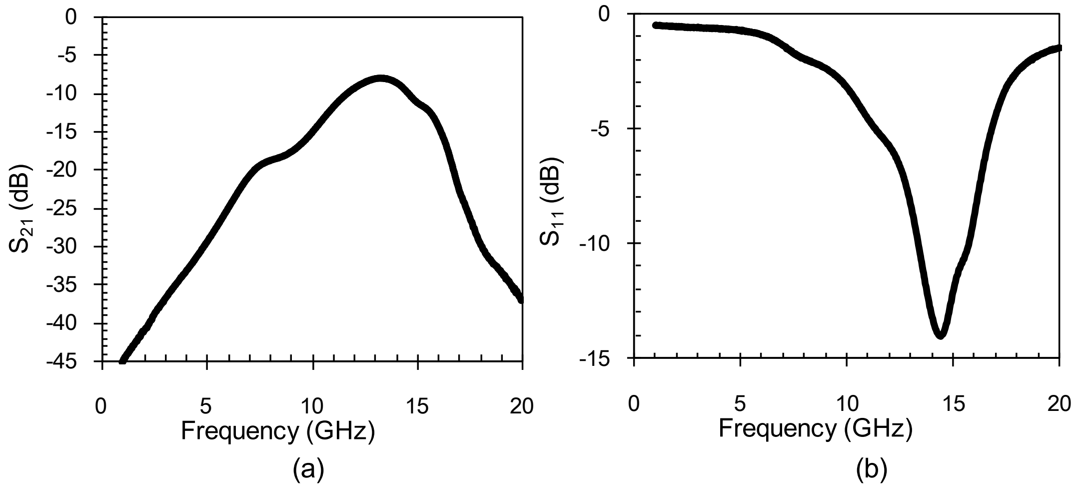

Fig.5- 23 The measured insertion loss (a) and return loss (b) of a 3-pole BST bandpass filter at 0 V

Unfortunately, most of the bandpass filters fabricated have the problem of no tuning with bias, which is the result of short circuit between the two metal layers discussed in the previous section. The measured results of a 2-pole BST bandpass filter were shown in Fig.5- 21. The non-reciprocal behaviour in S_{11} and S_{22} with bias indicates that only one resonator is tunable. The first resonator is not tunable, which indicates a short circuit between the bias line of the first resonator and the top electrode. The second resonator showed reasonable tuning from about 8 GHz to 12 GHz with 10 V bias. The dielectric constant of the BST film was estimated by comparing the measured results with the simulated resonant frequency of a resonator given in Fig.5- 4. The BST film dielectric constant was approximately 1000 at zero bias and tuned to 400 with 10 V bias. The insertion loss at 0 V was 11.6 dB. The high insertion loss of the measured filter is partly due to the loss of BST film and the conductor loss, and partly due to the high reflection in the passband. As the top and bottom metal layers are very thin (several hundred nanometres, smaller than its skin depth at the operating frequency) and the current concentration in the narrow lines is severe, the conductor loss can be serious. The quality of metal film might also be degraded during the etching process of BST film. The filter also exhibits a high reflection as only one resonator is tunable with bias hence the filter is not matched.

The measured results of some BST filters at zero bias are given in Fig.5- 22 and Fig.5- 23. The 2-pole BST bandpass filter shown in Fig.5- 22 has a zero bias insertion loss of 8.5 dB at a centre frequency of 12.5 GHz. The 3-pole BST bandpass filter shown in Fig.5- 23 has a zero bias insertion loss of 8.1 dB at a centre frequency of 13.3 GHz. These filters are not tunable with bias due to the short circuit between the two metal layers.

5.7 Summary

In this chapter X-band or Ku-band combline bandpass filters based on integrated BST parallel plate capacitors were designed and fabricated on MgO substrate. The filters were in a multilayer structure: the BST thin film was sandwiched between two metal films and part of the BST film was required to be etched out. However, most of the filters fabricated failed to be tuned with bias as a consequence of short circuit between the two metal layers. A 2-pole filter with only one resonator tunable demonstrated a good tuning range from about 8 GHz to 12 GHz with 10 V bias. Given time to re-fabricate the device, filters with good tuning performance should be demonstrated.

Reference

[1] G.L.Matthaei, L.Young, and E.M.T.Jones, Microwave filters, impedance matching networks, and coupling structures, Artech House, 1980.

[2] J.-S. Hong and M. J. Lancaster, Microstrip Filters for RF/Microwave Applications, John Wiley & Sons,Inc., 2001.

[3] Y. H. Shu, J. A. Navarro, and K. Chang, "Electronically switchable and tunable coplanar waveguide-slotline band-pass filters", *IEEE Transactions on Microwave Theory and Techniques*, vol. 39, no. 3, pp. 548-554, 1991.

[4] J. S. Wong, "Microstrip Tapped-Line Filter Design", *IEEE Transactions on Microwave Theory and Techniques*, vol. 27, no. 1, pp. 44-50, 1979.

[5] "Sonnet User's Guide, Release 10": Sonnet Softerware, Inc., 2004.

[6] T. K. Ishii, Handbook of Microwave Technology, Volume 1, Components and Devices, Academic Press, Inc., 1995.

[7] J. Papapolymerou, C. Lugo, Z. Zhiyong, X. Wang, and A. Hunt, "A Miniature Low-Loss Slow-Wave Tunable Ferroelectric BandPass Filter From 11-14 GHz", in *IEEE MTT-S International Microwave Symposium Digest*2006, pp. 556-559.

[8] G. Subramanyam, N. Mohsina, A. Al Zaman, F. Miranda, F. Van Keuls, R. Romanofsky, and J. Warner, "Ferroelectric thin-film based electrically tunable Ku-band coplanar waveguide components", in *IEEE MTT-S International Microwave Symposium Digest*2001, pp. 471-474.

[9] J. Sigman, C. D. Nordquist, P. G. Clem, G. M. Kraus, and P. S. Finnegan, "Voltage-Controlled Ku-Band and X-Band Tunable Combline Filters Using Barium-Strontium-Titanate", *Microwave and Wireless Components Letters*, vol. 18, no. 9, pp. 593-595, 2008.

[10] R. E. Collin, Foundations for Microwave Engineering, McGraw-Hill, 1992.

[11] K. Leong, J. Mazierska, and J. Krupka, "Measurements of unloaded Q-factor of transmission mode dielectric resonators", in *IEEE MTT-S International Microwave Symposium Digest*1997, pp. 1639-1642.

[12] J. Nath, D. Ghosh, J. Maria, M. B. Steer, A. Kingon, and G. T. Stauf, "Microwave properties of bst thin film interdigital capacitors on low cost alumina substrates", in *the 34th European Microwave Conference*2004, pp. 1497-1500.

[13] A. Vorobiev, P. Rundqvist, K. Khamchane, and S. Gevorgian, "Silicon substrate integrated high Q-factor parallel-plate ferroelectric varactors for microwave/millimeterwave applications", *Applied Physics Letters*, vol. 83, no. 15, pp. 3144-3146, 2003.

[14] A.K.Tagantsev, V.O.Sherman, K.F.Astafiev, J.Venkatesh, and N.Setter, "Ferroelectric materials for microwave tunable applications", *Journal of Electroceramics*, vol. 11, no. pp. 5-66, 2003.

[15] A. Vorobiev, P. Rundqvist, K. Khamchane, and S. Gevorgian, "Microwave loss mechanisms in $Ba_{0.25}Sr_{0.75}TiO_3$ thin film varactors", *Journal of Applied Physics*, vol. 96, no. 8, pp. 4642-4649, 2004.

[16] J. Nath, D. Ghosh, J. P. Maria, A. I. Kingon, W. Fathelbab, P. D. Franzon, and M. B. Steer, "An electronically tunable microstrip bandpass filter using thin-film Barium-Strontium-Titanate (BST) varactors", *IEEE Transactions on Microwave Theory and Techniques*, vol. 53, no. 9, pp. 2707-2712, 2005.

[17] P. Bao, T. J. Jackson, X. Wang, and M. J. Lancaster, "Barium strontium titanate thin film varactors for room-temperature microwave device applications", *Journal of Physics D: Applied Physics,* vol. 41, no. p. 063001, 2008.

[18] M. Al Ahmad, M. Brunet, S. Payan, D. Michau, M. Maglione, and R. Plana, "Wide-Tunable Low-Field Interdigitated Barium Strontium Titanate Capacitors", *Microwave and Wireless Components Letters,* vol. 17, no. 11, pp. 769-771, 2007.

[19] C. K. Ong and P. Wang, "Microwave tunable devices based on patterned ferroelectric thin film", in *17th IEEE International Symposium on the Applications of Ferroelectrics*2008, pp. 1-4.

CHAPTER 6

TUNABLE BANDPASS FILTERS USING DISCRETE BST AND GaAs VARACTORS

The previous chapters focus on miniaturised tunable lowpass and bandpass filters monolithically integrated with BST parallel plate varactors. Such integrated BST filters may suffer from a high insertion loss of more than 5 dB [1-3], partly due to the severe current crowding in the conductors. In this chapter, discrete BST interdigital and parallel plate varactors were fabricated and integrated into microwave laminate circuits in a hybrid manner to form two pole and four pole bandpass filters. The same filters were also made using commercially available GaAs varactors to give a direct comparison between semiconductor and BST tuning technologies in an application environment.

6.1 Filter design

6.1.1 Filter synthesis

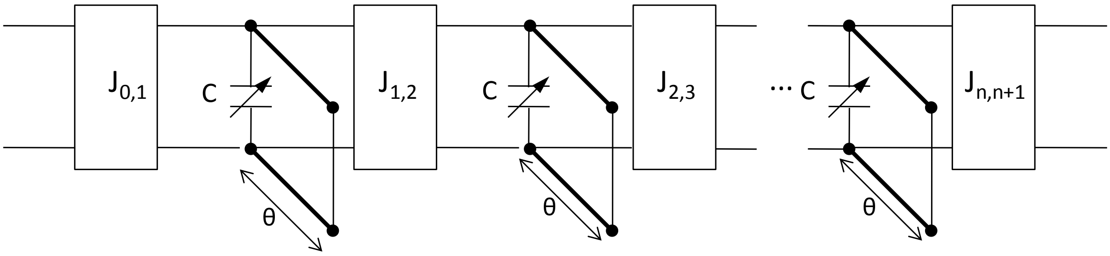

Fig.6- 1 Circuit diagram of coupled resonator filter

A tunable bandpass filter comprised of coupled resonators is shown in Fig.6- 1, where the J-inverters represent the couplings to input/output ports and between resonators. These couplings were implemented by tapped lines as shown in Fig.6- 2. This eased the application of DC bias as all resonators were connected directly to the measurement ports which eliminated the need for extra bias networks. The required coupling could be achieved by carefully adjusting the position, the length and width of the tapped line.

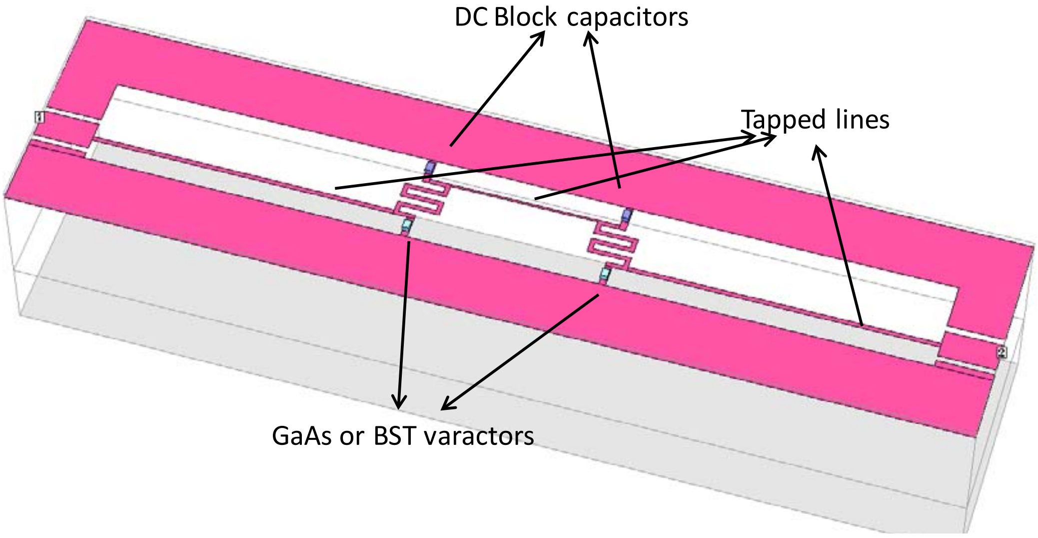

Fig.6- 2 The schematic layout of a two pole bandpass filter (size of 84.6 mm × 20.4 mm)

As shown in Fig.6- 2, the circuit was designed in coplanar waveguide (CPW) configuration with coupled resonators and the discrete elements were assembled onto the circuit in a hybrid manner. The shunt resonators were implemented by quarter-wavelength transmission lines loaded with variable capacitors. The resonator lines were meandered to minimise the size. Each resonator line was grounded via a DC block capacitor at one end while loaded by a varactor between the other end and the ground plane. The DC block capacitors separated the signal line from the ground plane for DC bias. The lumped varactors were the tuning elements of the filter. Three types of varactors, BST interdigital capacitors (IDCs), BST parallel plate capacitors, or GaAs varactors were used in this work to compare the BST tuning technology with the semiconductors in an application environment. The capacitance of the BST and GaAs varactors decreases with the applied bias, hence the filter is tuned to higher frequency with the increasing of bias.

The filters were simulated using Netlist Project Analysis in Sonnet [4]. Netlist project enables modelled elements, such as resistors, capacitors, inductors and transmission lines, or S-, Y-, Z-parameter data files to be combined with geometry subprojects [4]. Netlist project provides a convenient way to combine subprojects and saves the simulation time. The circuits were analysed by geometry full wave electromagnetic (EM) simulation, in which the DC block capacitors and varactors were combined with the circuits as modelled elements or S-parameter data files.

The filter synthesis commences by calculating the element values of the prototype filter as described in chapter 3. The g-values for second order and fourth order Chebyshev lowpass prototype filters with a passband ripple of 0.1 are listed in Table 6- 1. A two pole bandpass filter with a fractional bandwidth (FBW) of 9 % and a four pole filter with a FBW of 24 % are designed in this work. The desired coupling coefficient M_{ij} and external Q_e for the two filters are calculated and given in Table 6- 2. As discussed in the design of coupled resonator filters in chapter 3, the desired coupling coefficients and external quality factors can be determined against the physical dimensions of the filter by EM simulation.

Filter order	ripple (dB)	Reflection (dB)	g_0	g_1	g_2	g_3	g_4	g_5
two pole	0.1	16.428	1	0.843	0.622	1.355		
four pole	0.1	16.428	1	1.109	1.306	1.770	0.818	1.355

Table 6- 1 The element values of Chebyshev lowpass prototype filters

Filter order	FBW	Q_e	M_{12}	M_{23}	M_{34}
two pole	9 %	9.367	0.124		
four pole	24 %	4.62	0.199	0.158	0.199

Table 6- 2 The required coupling coefficients and external quality factors

6.1.2 Determining the resonant frequency

Before determining the coupling coefficients, the capacitance dependence of the resonant frequency was first investigated by simulation. The schematic layout of a meandered resonator is shown in Fig.6- 3. The total length of the resonator line was about 19.7 mm. The width of the line was 0.4 mm and the space between adjacent lines was 0.6 mm. The same dimensions of the resonator lines are used in all the simulations and implements. In practice, there were gaps between the resonator line and ground planes for lumped elements assembly.

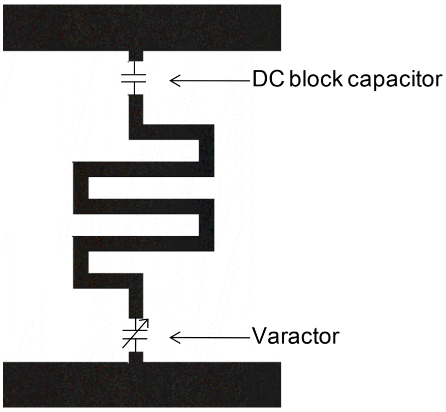

Fig.6- 3 The schematic layout of a meandered resonator (this figure is not to scale).

The resonator was simulated by Sonnet Netlist Project Analysis with different loaded capacitance. In the simulation, the DC block was modelled as a 120 pF capacitance, and the varactor was modelled by capacitance from 0.1 pF to 3 pF at a step of 0.1 pF. The dots in Fig.6- 4 show that the resonant frequency decreases dramatically from about 3.3 GHz to 0.8 GHz with the loaded capacitance increasing from 0.1 pF to 3 pF, especially when the capacitance is less than 1 pF. The electrical length of the resonator line as a function of the loaded capacitance is also shown in Fig.6- 4: the larger the loaded capacitance, the smaller the electrical length of the resonator line. The electrical length of a transmission line is defined as follows [5]

$$\theta = \beta l = \frac{2\pi f \sqrt{\varepsilon_r}}{\mathrm{c}} l \tag{6.1}$$

where f is the resonant frequency, ε_r is the effective relative permittivity, c is the velocity of light in vacuum and l the length of the line.

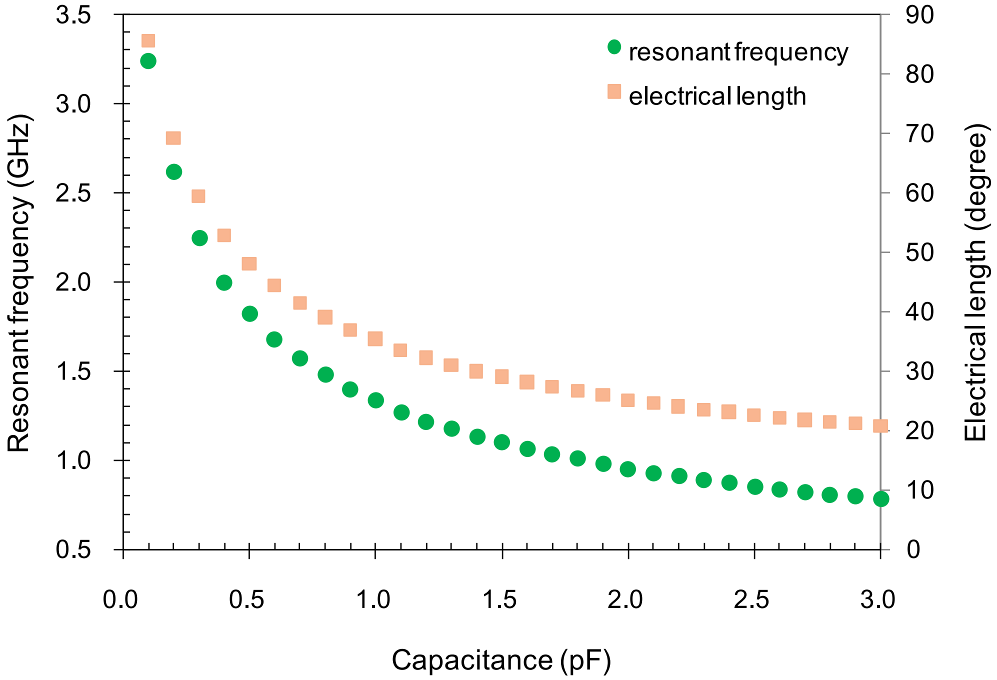

Fig.6- 4 The resonant frequency of a single resonator and the electrical length of the resonator line versus the loaded capacitance.

6.1.3 Investigating the coupling coefficient

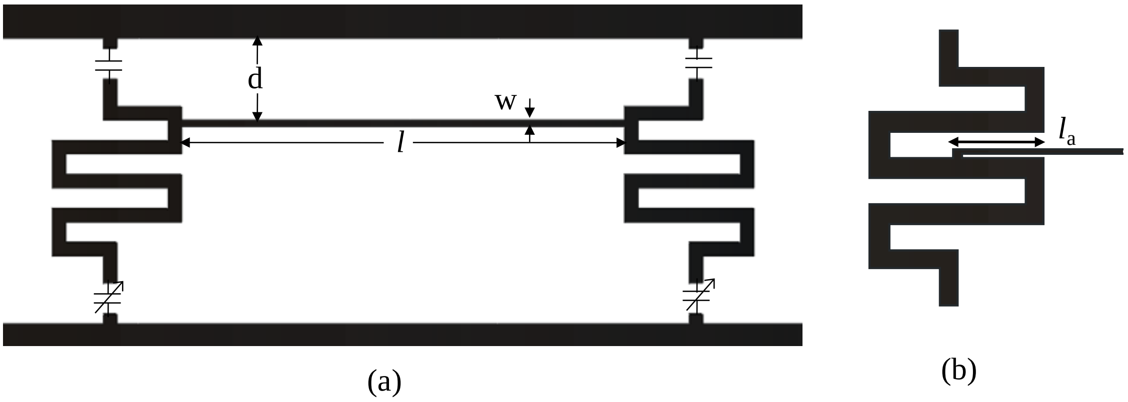

(a) (b)

Fig.6- 5 Parameters (d, *l*, w) defining the position of the tapped line for coupled resonators (a) and l_a defining the overlap length of the tapped line and resonator (b). (this figure is not to scale)

The schematic layout of the coupled resonators is shown in Fig.6- 5. The coupling between the two resonators was implemented by a tapped line. Physical dimensions defining the tapped line were the distance from the tapped line to the virtual ground d, the length of the tapped line *l* and the width of the tapped line w, as denoted in Fig.6- 5 (a). When the tapped line was inserted into the resonator, l_a defined the overlap length as shown in Fig.6- 5 (b).

To find the desired coupling coefficient, coupled resonators loaded by 0.3 pF capacitors but with different positions of the tapped lines were simulated. The coupling coefficient M_{12} can be extracted from the simulated frequency response of the coupled resonators as given in chapter 3 as [6]

$$M_{12} = \pm \frac{f_2^2 - f_1^2}{f_1^2 + f_2^2} \tag{6.2}$$

where f_1 and f_2 are the two split resonances. The relations between the coupling coefficient and the position parameters were studied. Among them, the relationship between the coupling coefficient M_{12} and the distance d for a tapped line length of 13 mm and 0.2 mm wide is investigated and shown in Fig.6- 6. The coupling coefficient is proportionally related to the distance d, which means that the coupling is increased with the tapped line moving far away from the virtual ground. However, the coupling between the resonators not only affects the coupling coefficient but also shifts the centre frequency (defined as the mathematical mean of the two resonance peaks). The centre frequency shift is defined as the frequency difference between the centre frequency of the coupled resonators and the resonant frequency of a single resonator loaded by the same value capacitance. The resonant frequency of a single resonator loaded by a 0.3 pF capacitor is 2.25 GHz. As shown in Fig.6- 6, the coupled resonators have a centre frequency shift up to 0.18 GHz, which is 8 % shift. The data in Fig.6- 6 is not complete because the resonator is meandered and some of the positions are not available.

The length *l* and width w of the tapped line also affect the coupling coefficient and centre frequency, which should be considered as well. The position parameters d, *l*, w and l_a are determined for the desired coupling coefficients of the two pole and four pole filters, and are given in Table 6- 3. The achieved coupling coefficients are very close to the desired ones.

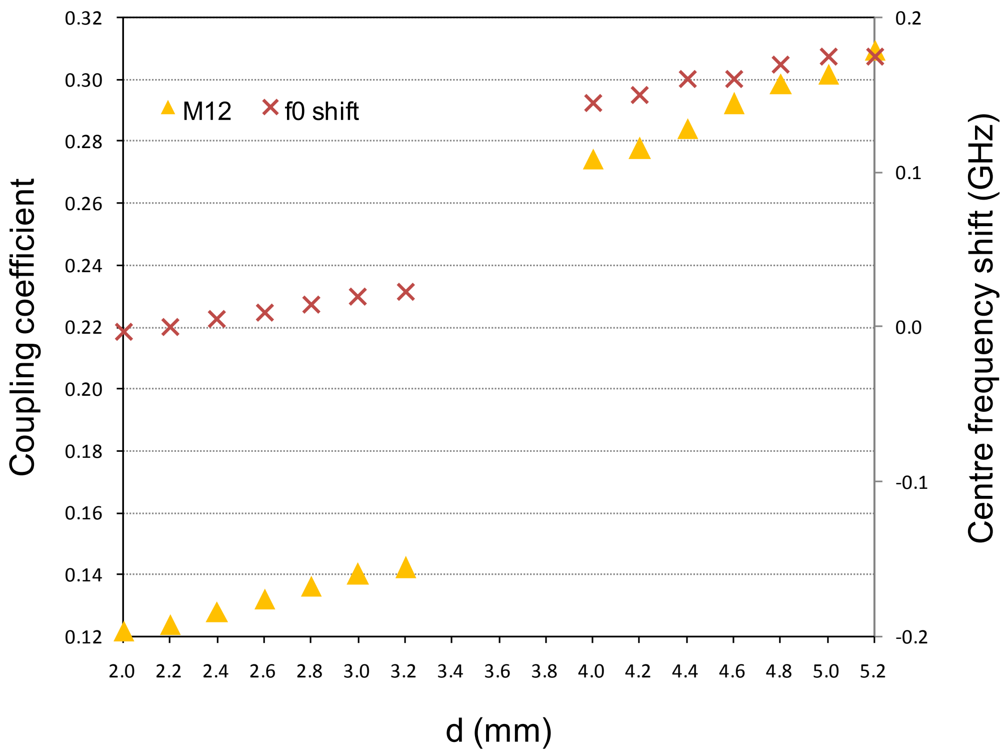

Fig.6- 6 The coupling coefficient (triangles) and resonance shift (crosses) as a function of position parameter d when *l* = 13 mm, w = 0.2 mm and loaded capacitance = 0.3 pF.

Filter order	d (mm)	*l* (mm)	w (mm)	l_a (mm)	M_{ij}	f_0	Desired M_{ij}
two pole	2.0	13.0	0.2		M_{12}=0.124	2.25	M_{12}=0.124
four pole	3.6	24.5	0.2	1.0	M_{12}=0.202	2.25	M_{12}=0.199
four pole	3.0	20.0	0.2		M_{23}=0.159	2.25	M_{23}=0.158

Table 6- 3 Physical dimensions for desired coupling coefficients

The above coupling coefficients M_{ij} were investigated as functions of position parameters when the loaded capacitance was fixed to 0.3 pF. However, M_{ij} also changed with the loaded capacitance, as the capacitors were directly connected to the tapped lines. The capacitance dependence of M_{ij} was studied by simulating coupled resonators with different loaded capacitance. The dimensions of the resonator were as depicted in the previous section. As shown in Fig.6- 7, when the position of the tapped line is fixed, i.e. a 13 mm long, 0.2 mm wide tapped line is used and its distance to virtual ground is fixed to 2 mm, the coupling coefficient M_{12} increases with the decreasing of the loaded capacitance. The centre frequency shift with the loaded capacitance is small.

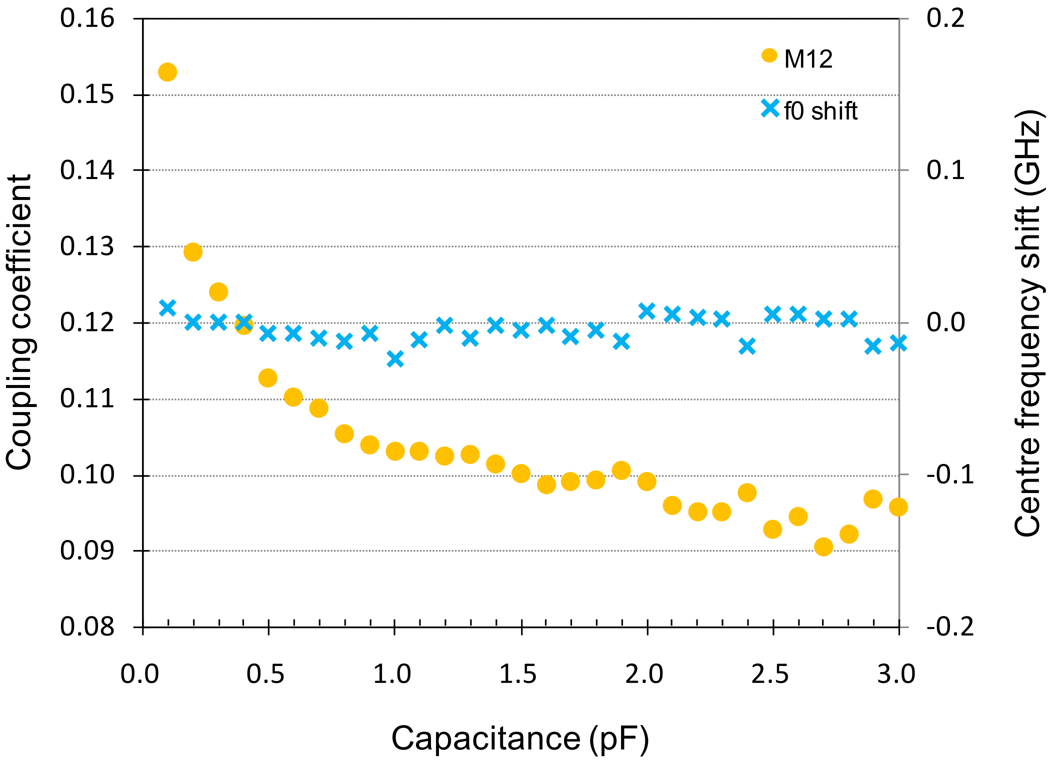

Fig.6- 7 The coupling coefficient (dots) and centre frequency shift (crosses) as a function of the loaded capacitance for a fixed tapped line dimensions of *l* = 13 mm, w = 0.2 mm, d = 2 mm.

6.1.4 Investigating the external quality factor

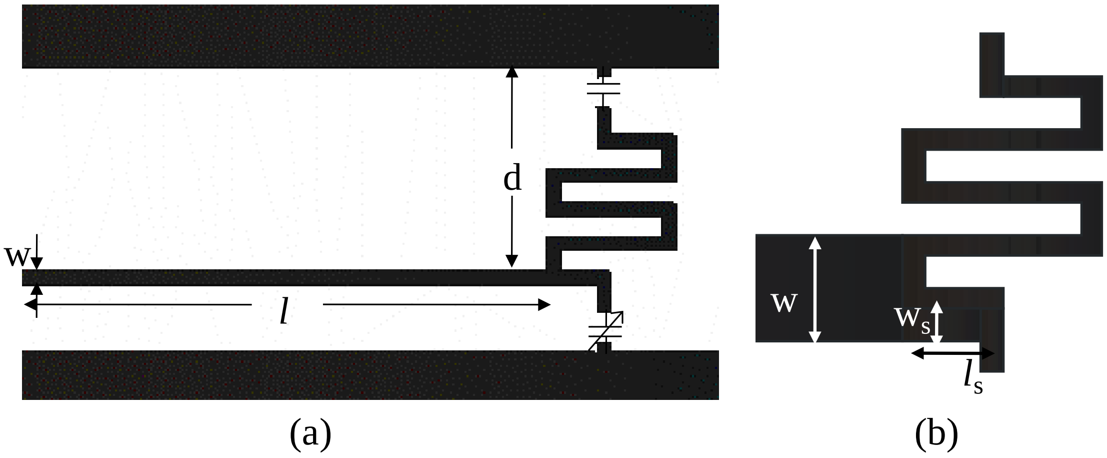

(a) (b)

Fig.6- 8 The schematic layout of an external coupled resonator (a) and an extra wide tapped line to achieve enhanced coupling (b). (this figure is not to scale).

The coupling to the input/output ports was implemented by tapped lines as shown in Fig.6- 8. Physical dimensions defining the tapped line include the length of the tapped line *l*, the width w and the distance to virtual ground d. External coupled resonators loaded by a 0.3 pF capacitance were simulated with different positions of the tapped lines to find appropriate Q_e. Q_e can be extracted from the simulated frequency response as discussed in chapter 3 as [6]

$$Q_e = \frac{\omega_0}{\Delta\omega_{3dB}} \tag{6.3}$$

where ω_0 is the resonant frequency, $\Delta\omega_{3dB}$ is the 3dB attenuation bandwidth. A smaller Q_e value means a stronger external coupling to the input/output ports. For an input/output coupling tapped line of 27 mm long and 0.4 mm wide, the dependence of Q_e on the distance d was investigated by simulation. As shown in Fig.6- 9, when moving the tapped line towards the virtual ground (i.e., d decreasing), the strength of the external coupling decreases dramatically. The resonance shifts very little with the influence of external coupling. The resonance shift here is defined as the difference between the centre frequency of an external coupled resonator and the resonance of a single resonator. The tapped line can be widened (see Fig.6- 8 (b)) to achieve the very strong external coupling (Q_e of 4.62) required by the four pole filter. The required physical dimensions for the appropriate Q_e for the two pole and four pole filters are listed in Table 6- 4. For the two pole filter, the achieved value of Q_e (10.57) is bigger than the desired Q_e (9.367), which results in weaker external coupling. For the four pole filter, the achieved Q_e is 4.51 and is close to that of the requirement, which is 4.62. The values in Fig.6- 9 and Table 6- 4 are obtained when the loaded capacitance is fixed to 0.3 pF.

Filter order	d (mm)	*l* (mm)	w (mm)	$l_s \times w_s (mm^2)$	Q_e	f_0	Desired Q_e
two pole	6.0	27.0	0.4		10.57	2.25	9.367
four pole	5.0	29.0	2.0	1.5 × 0.6	4.51	2.25	4.620

Table 6- 4 Physical dimensions of the two pole and four pole filters for appropriate Q_e

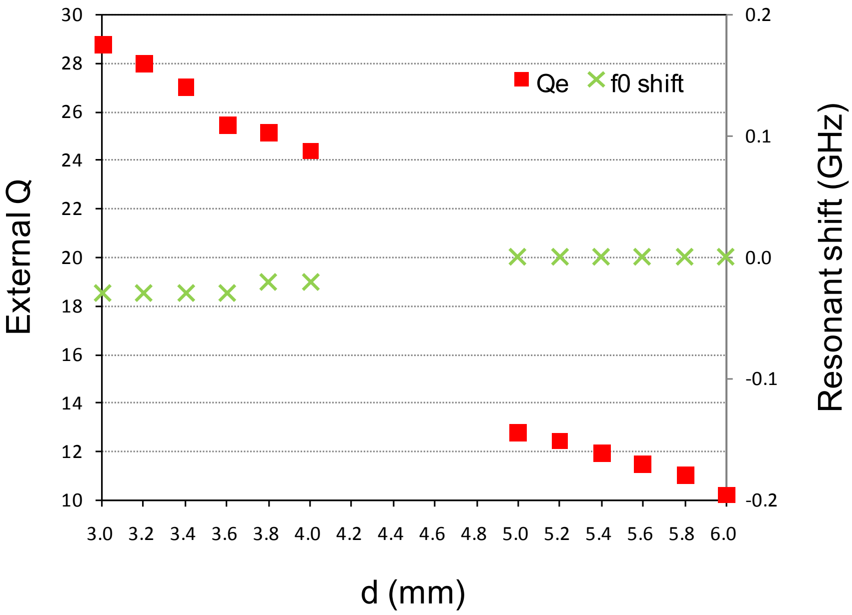

Fig.6- 9 The external quality factor (squares) and resonant frequency shift (crosses) as a function of the distance d when the tapped line *l* = 27 mm, w = 0.4 mm, and loaded capacitance = 0.3 pF.

The external quality factor Q_e strongly depends on the loaded capacitance. This is because the varactors are directly connected to the meandered resonators and tapped lines. The tuning of the varactor capacitance will lead to changing of the electromagnetic field distribution on the resonator line, hence affecting the couplings. As shown in Fig.6- 10, when the physical dimensions of the tapped line are fixed (i.e. the tapped line is 27 mm long, 0.4 mm wide, and is 6 mm away from the virtual ground), Q_e reaches a peak value of 12.8 at a capacitance of 0.8 pF, which means the weakest external coupling. The external coupling rises significantly when the loaded capacitance decreases from 0.8 pF to 0.1 pF, which leads to a much stronger external coupling when tuning to higher frequencies. The resonance shift of the external coupled resonator is also shown in Fig.6- 10. When the loaded capacitance is less than 0.3 pF, the resonance shifts noticeably to lower frequency with the decreasing of the loaded capacitance. When the capacitance is more than 0.3 pF, the centre frequency of an external coupled resonator is about 0.1 GHz higher than its original resonance.

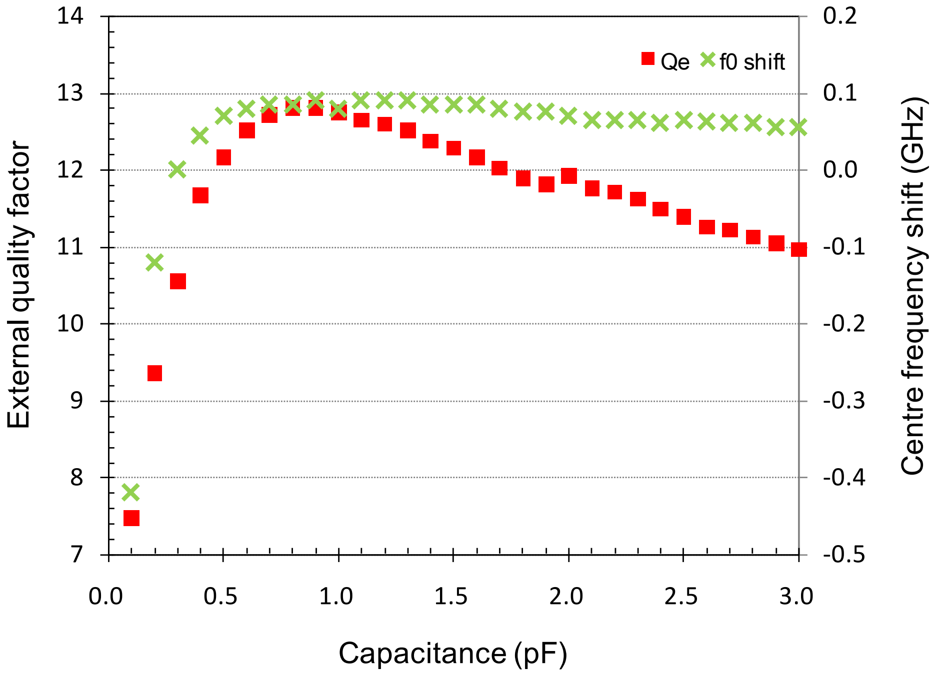

Fig.6- 10 The external Q (squares) and centre frequency shift (crosses) as a function of the loaded capacitance for a fixed tapped line dimensions of *l* = 27 mm, w = 0.4 mm, d = 6 mm.

6.1.5 Completed filter design

In the above investigation, the physical dimensions of the tapped lines were determined for the desired external Q_e and coupling coefficients M_{ij} when the loaded capacitance is 0.3 pF. However, the filter performance (especially the four pole filter) will be degraded when the loaded BST/GaAs varactor capacitance is tuned far away from 0.3 pF, as both Q_e and M_{ij} change with the loaded capacitance, making the circuit no longer perfectly matched.

The two pole and four pole bandpass filters circuits were designed and implemented in a coplanar waveguide configuration on Rogers RT/duroid 5870 laminate. The filters were simulated using Netlist Project Analysis in Sonnet using the following parameters. The substrate thickness was 0.787 mm and the dielectric constant was 2.33. The width of the CPW signal line was 4 mm and the gap was 0.1 mm. The simulated characteristic impedance of the CPW input/output lines was 51.9 Ω at 1 GHz. To obtain an impedance of 50 Ω, a gap less than 0.1 mm was required which exceeded the precision of fabrication, or, a much wider signal line was required but this would cause difficulty in final assembly. The filters were simulated in boxes with 10 mm air below and above the circuit.

(i) Two pole filter

A two pole filter was implemented and simulated using the tapped line physical dimensions given in Table 6- 3 and Table 6- 4. The filter layout is shown in Fig.6- 2. The size of the filter was 84.6 mm × 20.4 mm. The filter circuit was analysed by full wave EM simulation, in which DC blocks and varactors were combined with the circuit as modelled elements. In the simulation, the DC blocks were modelled as 120 pF capacitors and the varactors capacitance was changed from 0.1 pF to 3 pF. The simulated frequency response of a lossless two pole filter is shown in Fig.6- 11. The filter can be tuned widely from 2.68 GHz to 0.85 GHz with the loaded capacitance changing from 0.1 pF to 3 pF. The passband reflection is higher than 10 dB for the capacitance less than 1 pF as a result of the weak external coupling of the two pole filter. It can be seen from Fig.6- 11 that when the capacitance is 0.5 pF the passband reflection is highest which indicates the weakest external coupling. This is consistent with what predicted in Fig.6- 10 despite a little shift of the maximum Q_e point. When tuning to higher frequency (i.e., smaller loading capacitance), the bandwidth becomes wider but the 3 dB fractional bandwidth remains about 14 %.

The centre frequency and fractional bandwidth variation of the simulated two pole tunable filter as a function of the loaded varactor capacitance changing from 0.1 pF to 3 pF is summarised in Fig.6- 12, compared with the resonant frequency tuning of a single resonator. When the capacitance is smaller than 0.5 pF, the centre frequency of the two pole filter is slightly smaller than the resonance of a single resonator. When capacitance is bigger than 0.5 pF, the filter centre frequency is a bit higher than the resonance of a single resonator. Such frequency shift is mainly caused by the external coupling and is in accordance with Fig.6- 10. The 3 dB fractional bandwidth of the simulated filter remains about 14 %.

The filter response could be also calculated from the coupling coefficients M_{ij} and external Q as describe in chapter 3. The M_{ij} and Q_e given in Table 6- 2 were used in the calculation to predict the ideal response of a two pole filter. The calculated response is shown in Fig.6- 13, and is compared with the simulated response of the two pole filter with 0.3 pF loaded capacitance. The simulated response compares well with the calculation despite the higher passband reflection of the simulated filter, which is due to the weak external coupling of the implemented two pole filter. The difference between simulation and calculation away from the passband is because in the calculation the coupling are considered as frequency invariable, however, this approximation is only valid close to the centre frequency in practical implementations such as distributed transmission lines.

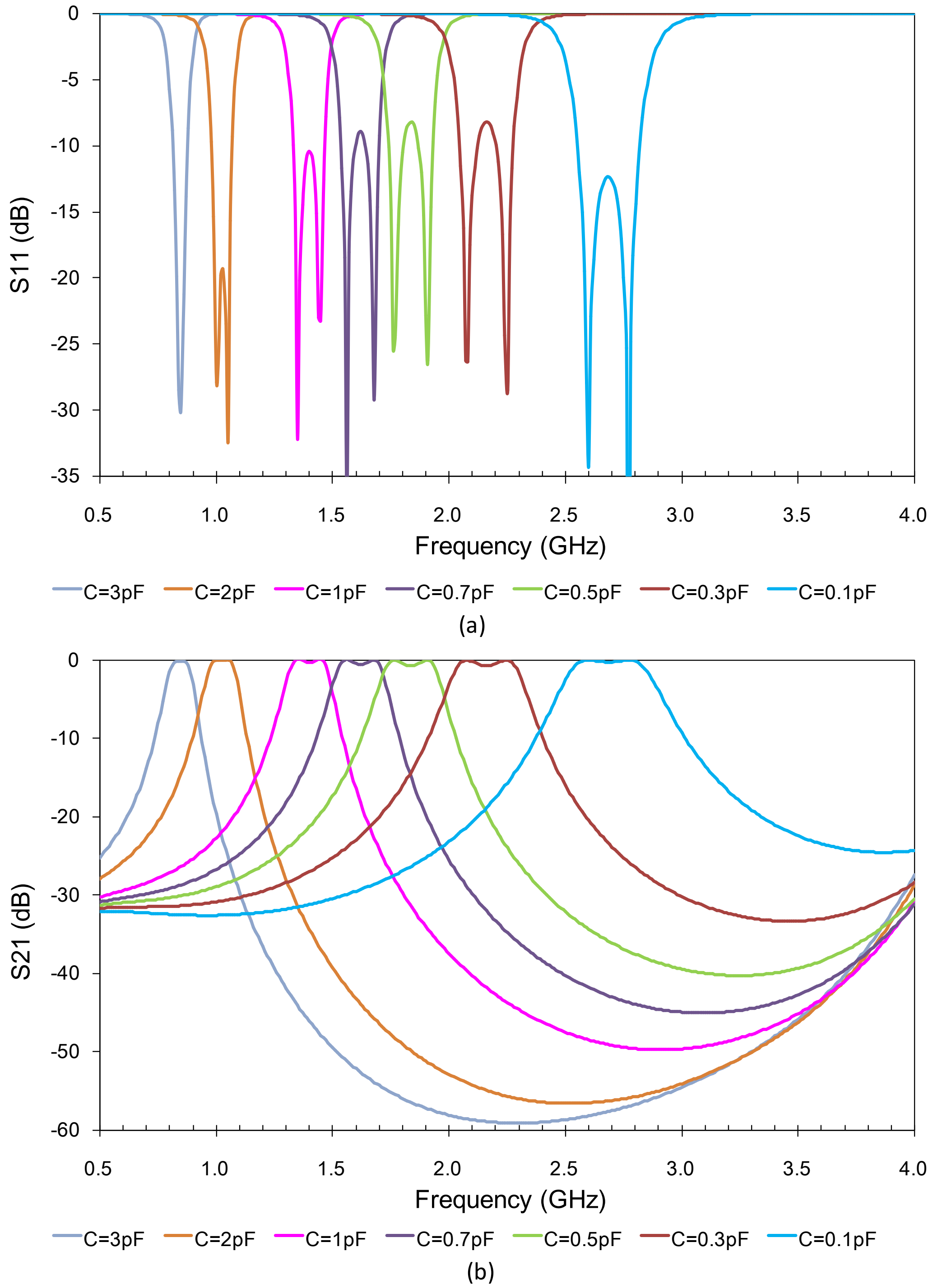

Fig.6- 11 Simulated S_{11} (a) and S_{21} (b) of a two pole filter with loaded varactor capacitance being 0.1 pF, 0.3 pF, 0.5 pF, 0.7 pF, 1 pF, 2 pF and 3 pF.

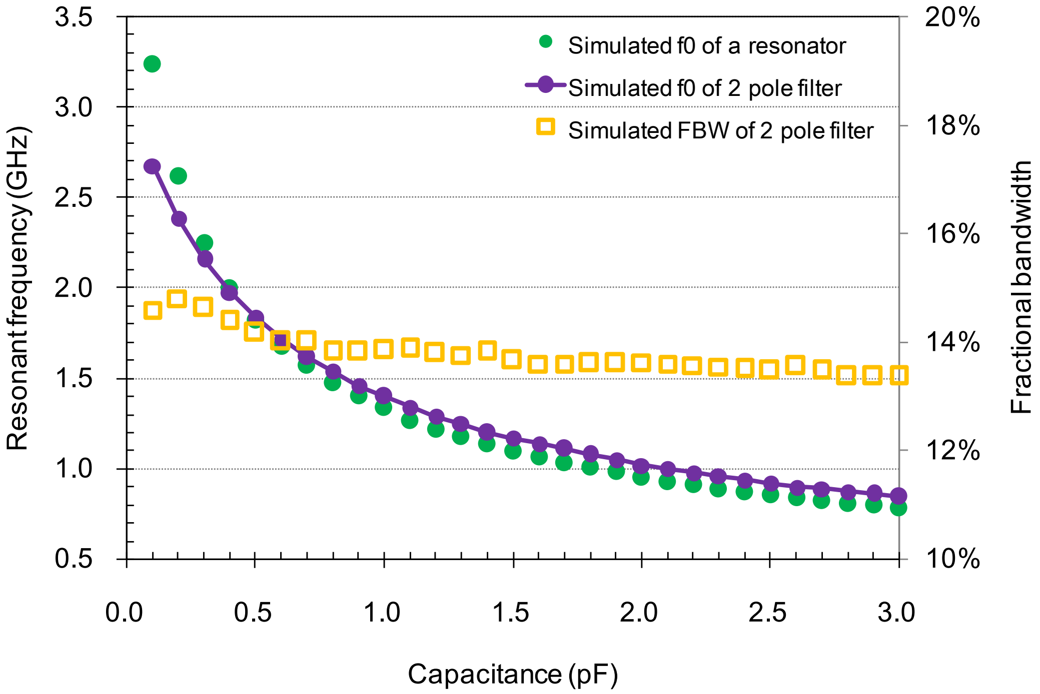

Fig.6- 12 The simulated centre frequency and 3 dB fractional bandwidth of a two pole filter, and the resonance of a single resonator with loaded capacitance from 0.1 pF to 3 pF.

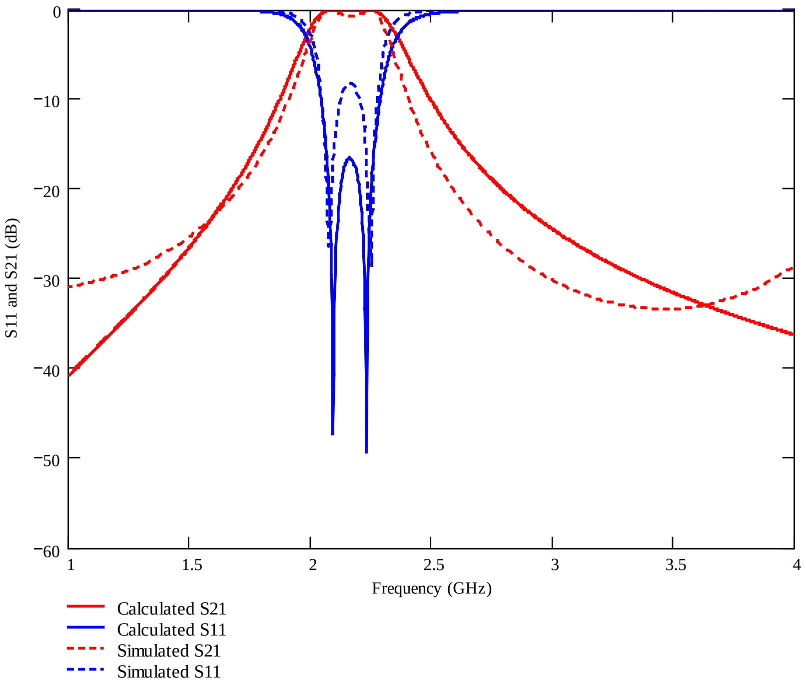

Fig.6- 13 Simulated and calculated response of the two pole bandpass filter with 0.3 pF loaded capacitance. Solid lines represent the calculation results and dashed lines the simulation results.

(ii) Four pole filter

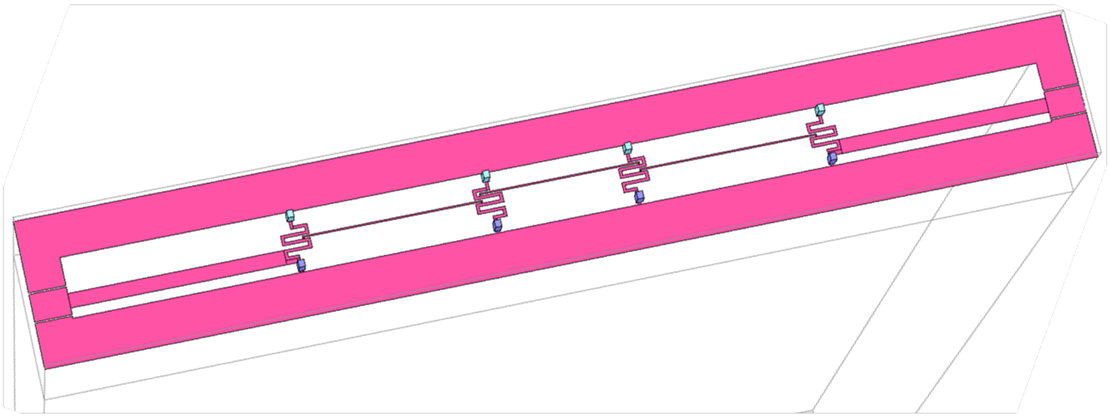

Fig.6- 14 The schematic layout of a four pole bandpass filter (size of 144.2 mm × 20.4 mm)

A four pole filter was also designed and implemented using the physical dimensions listed in Table 6- 3 and Table 6- 4. Further optimisation was performed by simulation to lower the passband reflection by adjusting the position of the coupling line between the second and third resonators. The final dimensions of the tapped line for M_{23} were l = 22 mm, w = 0.2 mm, d = 2.6 mm, l_a = 3 mm. The four pole filter had a similar configuration as the two pole filter but longer, having a length of 144.2 mm. The four pole filter was simulated by Netlist in Sonnet with loaded capacitance of 0.2 pF, 0.3 pF and 0.4 pF. The simulated results of a lossless four pole filter are shown in Fig.6- 15. The filter exhibits degraded return loss performance when the loaded capacitance is tuned far away from 0.3 pF as the coupling coefficients M_{12}, M_{23}, M_{34} and external Q_e all change with the loaded capacitance.

The comparison of the calculated and simulated response of the four pole filter is shown in Fig.6- 16. The calculation is based on the coupling coefficients and external quality factors given in Table 6- 2 and represents an ideal case. The simulated response compares well with the calculation except a smaller bandwidth and dispersion at frequencies away from the passband, which is similar to case of the two pole filter.

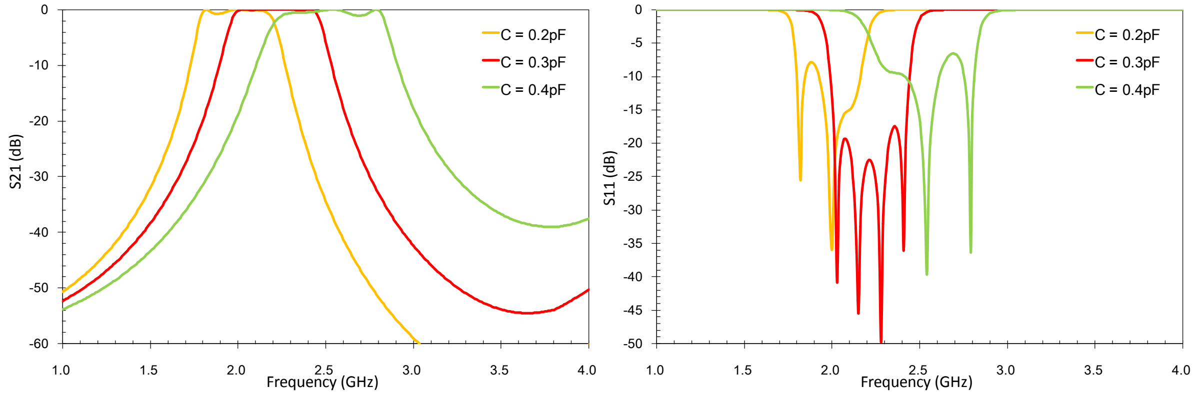

(a)

(b)

Fig.6- 15 Simulated S_{21} (a) and S_{11} (b) of a four pole filter with the loaded capacitance of 0.2 pF, 0.3 pF and 0.4 pF.

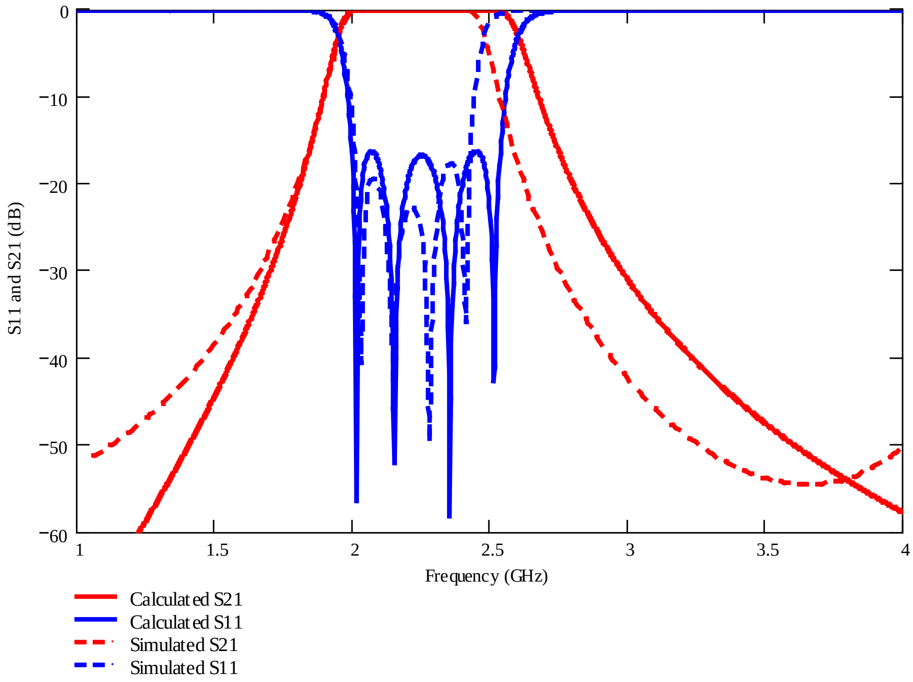

Fig.6- 16 Comparison of the calculated response (represented by solid lines) and simulated results (dashed lines) of a four pole bandpass filter with 0.3 pF capacitors.

6.2 Fabrication, assembly and packaging

The circuits were designed on Rogers RT/duroid 5870 laminate with a thickness of 0.787 mm. The thickness of the copper cladding was 17 µm. The gap between one end of the resonator line and ground plane for DC blocks assembly was 0.4 mm and the gap at the other end for varactors was 0.3 mm. The circuits were imaged and etched by photochemical etching at Advanced Chemical Etching Ltd. The circuits of the two pole and four pole bandpass filters are shown in Fig.6- 19 (a).

The DC blocks, GaAs varactors and BST varactors were assembled to the circuits in a flip chip manner using silver epoxy glue. Fig.6- 19 (b) shows a photo of several 120 pF broadband DC blocking capacitors obtained from Dielectric Laboratories Inc. The size of the capacitors is about 1 mm × 0.5 mm and 0.6 mm. The capacitors are surface mountable with Ni/Au termination.

MV39003 flip chip GaAs hyperabrupt junction varactors sourced from Microwave Device Technology Ltd. are shown in Fig.6- 19 (c). The GaAs varactor diode has a large tuning range from 2.80 pF at 0 V to 0.11 pF at 15 V and a Q of 3500 specified at 4 V, 50 MHz. The varactor diodes are in a flip chip package which eases assembling onto the planar circuits. The size of GaAs varactor is approximately 0.7 mm × 0.4 mm and 0.1 mm. The gold bond pads are 0.2 mm × 0.1 mm and connect to cathode and anode of the diode respectively. GaAs varactors were used in the two pole and four pole filter circuits to form GaAs filters.

The BST interdigital capacitors (IDCs) and parallel plate capacitors were made in house on MgO substrates. The substrate is optically transparent from the back which makes the flip chip assembly easier. The fabrication methodology of the BST capacitors is shown in the process flow diagram in Fig.6- 17, and a simplified diagram of the construction of the BST capacitors is shown in Fig.6- 18.

For the BST IDCs, a $Ba_{0.5}Sr_{0.5}TiO_3$ thin film was grown epitaxially on a 0.5 mm thick MgO substrate by the pulsed laser deposition (PLD) method. The BST thin film was grown at 750 °C in a 10 sccm oxygen flow to provide an oxygen pressure of 0.1 mbar. The laser spot size on the target was 8 mm^2 and the laser fluence was 1.5 J/cm^2. The repetition rate was 5 Hz. The target to substrate distance was 6.5 cm. The film was annealed in-situ at 650 °C for 1 hour under an oxygen pressure of 800 mbar immediately after the deposition. The film was cooled down to room temperature at a rate of - 30 °C/min. The thickness of the BST thin film was measured in the scanning electron microscope (SEM) to be 400 ± 30 nm. 400 nm silver was then deposited on the BST thin film by RF magnetron sputtering and the electrode was defined by UV photolithography and ion beam milling. A photograph of a BST IDC, taken in an optical microscope, is shown in Fig.6- 19 (d). The number of fingers is 12. The length of finger is 0.11 mm, the width of the finger is 0.01 mm and the gap between the fingers is 0.01 mm. The size of the contact pad is 0.6 mm × 0.4 mm. 22 BST IDCs were fabricated on a 10 mm × 10 mm MgO substrate, characterised by an impedance analyser, and then cut into 2 mm × 1 mm individual chips with a diamond saw. BST IDCs with similar capacitance were chosen and mounted in the two pole and four pole filter circuits to form BST IDC filters.

For the BST parallel plate capacitors, a 8 nm Ti adhesion layer followed by 200 nm platinum were deposited onto a 0.5 mm thick MgO substrate as bottom electrode by RF magnetron sputtering. The bottom electrode was patterned by photolithography and ion beam milling. PLD was then used to deposit 500 nm of $Ba_{0.25}Sr_{0.75}TiO_3$ thin film onto the patterned Pt/Ti/MgO substrate, using a laser fluence of 1.5 J/cm^2, at a laser repetition rate of 20 Hz with a substrate temperature of 650 °C. The lower growth temperature is required to avoid damage to the bottom electrode. The target to substrate distance was 5.5 cm, and the laser spot size on the target was 1.5 mm^2. The oxygen pressure in the chamber was 0.1 mbar and the oxygen flow rate was 10 sccm. The film was annealed in-situ at 650 °C for 1 hour under an oxygen pressure of 800 mbar. The sample was cooled down to room temperature at a rate of -30 °C/min. The thickness of the BST thin film is about 500 nm. After BST deposition, the top metal, 1400 nm ± 10 nm gold, (which was measured with a DEKTAK surface profiler), was evaporated onto the BST film and patterned by the ion beam milling. As shown in the photograph of the overlap area of the parallel plate capacitor in Fig.6- 19 (e), the capacitor is formed by two 10 µm × 10 µm parallel plate capacitors in series. The size of the contact pad is about 0.8 mm × 0.5 mm. 24 BST parallel plate capacitors were fabricated on a 10 mm × 10 mm MgO sample, characterised by an impedance analyser, and then cut into 2 mm × 1 mm single chips by the dicing saw. Capacitors with similar capacitance were chosen and mounted in the two pole and four pole filters to form BST parallel plate filters.

After the lumped elements assembly, the circuits were mounted into brass box carriers with 10 mm air both below and above them. 3.5mm SMA connectors with tab contact were used to connect the circuit and the coaxial cable. The connection between the input/output ports and SMA connector tab was made by silver epoxy. The junctions of the ground planes with the box side walls were sealed with silver glue to balance the ground planes. It was verified in the experiments that the ground planes must be grounded along their sides to avoid spurious modes. A photograph of the assembled two pole filter in the box is shown in Fig.6- 19 (e).

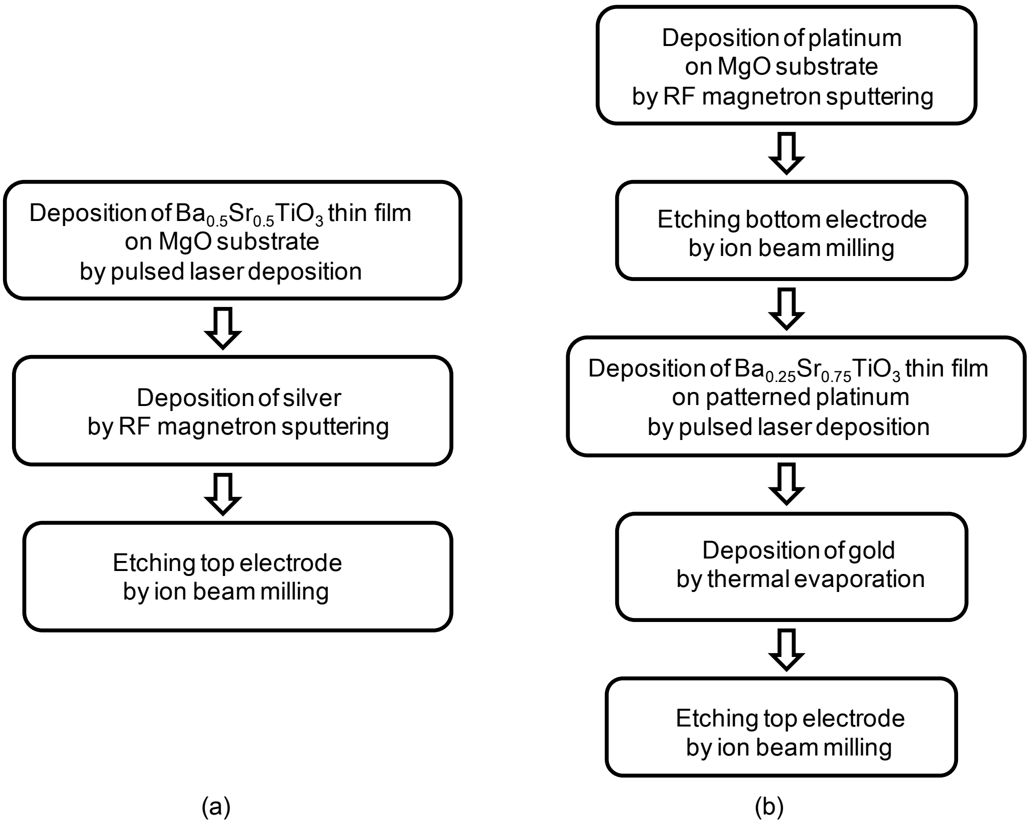

(a) (b)

Fig.6- 17 Process flow of the fabrication procedure of BST interdigital capacitors (a) and BST parallel plate capacitors (b).

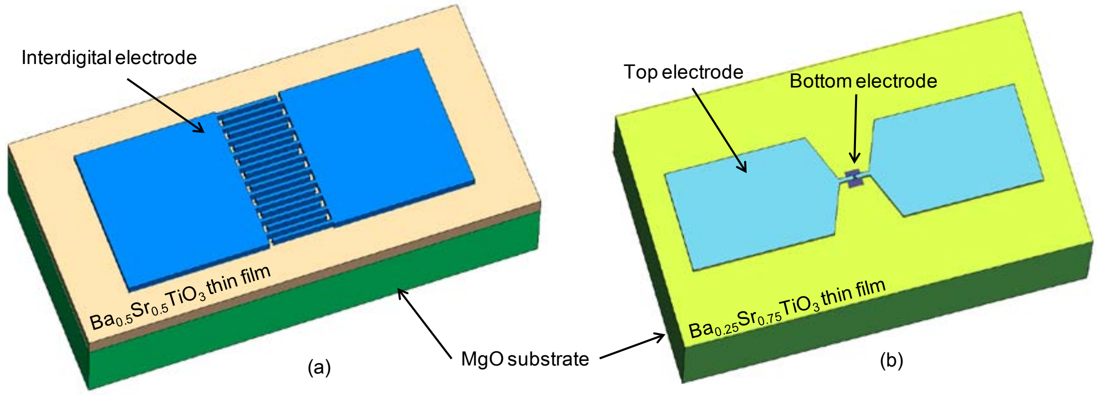

Fig.6- 18 Schematics of a BST IDC (a) and a BST parallel plate capacitor (b)

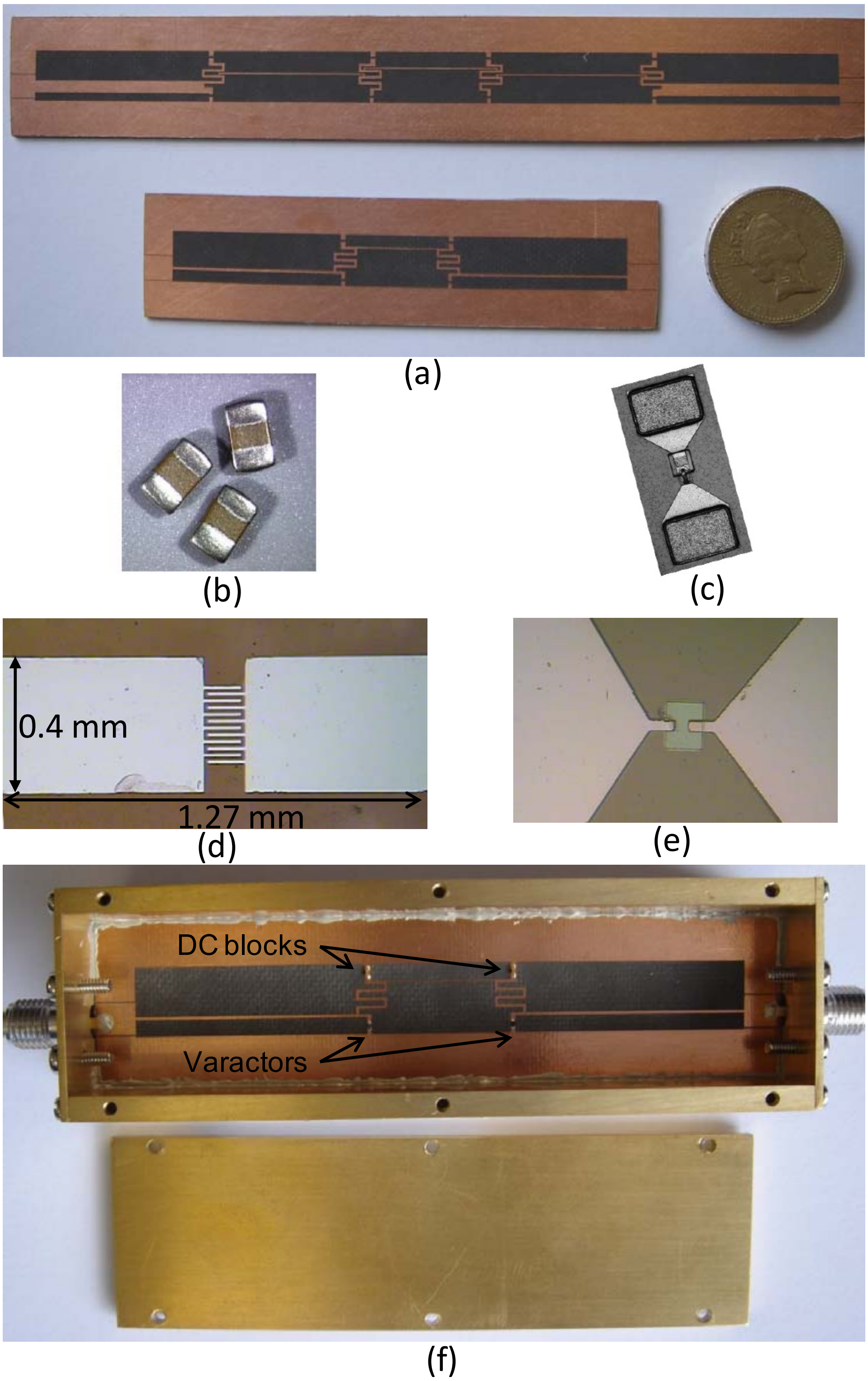

Fig.6- 19 Photo of two pole and four pole filter circuits on duroid 5870 laminate (a); Photo of DC block capacitors (b) and GaAs flip chip varactor (c); Photo of BST interdigital capacitor (d) and enlarged overlap area of parallel plate capacitor (e); and an assembled two pole filter in a brass box (f).

6.3 Measurement results and comparison with simulation

6.3.1 Measurement set-up and calibration

Fig.6- 20   Measurement set-up of bandpass filters in box

The filters were measured using Agilent 8722ES network analyser with 3.5 mm coaxial cables. The DC bias was applied to the circuit using a voltage source via external bias tees to protect the network analyser. A full two port calibration was performed using 3.5 mm 85052D calibration kit over 0.5 GHz - 4 GHz.

6.3.2 The two pole bandpass filters

Two pole bandpass filters with DC blocks mounted at one end of the resonators, and GaAs varactors, or BST interdigital capacitors, or BST parallel plate capacitors at the other end of the resonators were assembled in boxes and measured by network analyser. The measurement results of the two pole filters are given below and compared with simulation results.

(i) 2-pole GaAs filter

The capacitance tuning curve of GaAs varactor is shown in Fig.6- 21. The GaAs varactor has a very large tunability of 24 (which is a relative tunability of 96 %) with 14 V bias, where the tunability is defined as the ratio of zero bias capacitance (which is 2.8 pF) to the capacitance with bias (which is 0.12 pF). A two pole bandpass filter with GaAs varactors as tuning elements was measured with the application of 0 - 14 V bias. The measured S_{21} and S_{11} of the 2-pole GaAs filter after calibration are shown in Fig.6- 22. The tuning of the 2-pole GaAs filter is summarised in Table 6- 5. The filter can be tuned over a frequency range of 1.5 GHz, from 0.94 GHz at zero bias to 2.44 GHz at 14 V. The passband insertion loss (IL) varies from 4.2 dB at zero bias to 0.8 dB at 14 V. The smaller insertion loss after tuning is due to the improved of quality factor of the GaAs varactor with bias, which will be discussed later. The minimal passband return loss (RL) is better than 13.5 dB at all bias states. Although the bandwidth (BW) became wider with bias, the 3 dB fractional bandwidth (FBW) remains about 14 % in all bias cases. The measured second harmonic occurs at about 4.5 GHz and is close to that of the simulation.

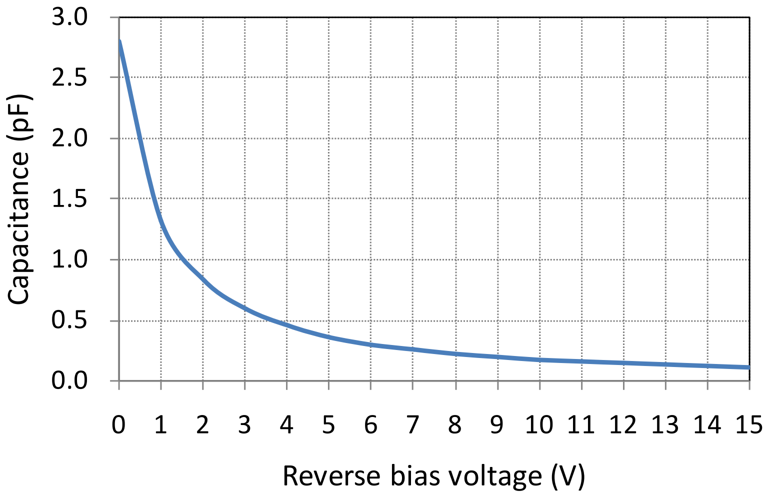

Fig.6- 21 Capacitance versus reverse bias of the GaAs varactor [7]

Bias (V)	Capacitance (pF)	f_0 (GHz)	IL (dB)	RL (dB)	3dB BW (GHz)	3dB FBW (%)
0	2.80	0.94	4.2	21.2	0.13	13.88
2	0.82	1.44	2.6	13.5	0.20	14.07
4	0.45	1.78	1.7	15.2	0.25	13.92
6	0.30	2.01	1.2	18.9	0.28	13.82
8	0.22	2.18	1.0	42.1	0.32	14.69
10	0.17	2.29	0.9	29.5	0.33	14.49
12	0.14	2.37	0.8	23.0	0.35	14.73
14	0.12	2.44	0.8	19.2	0.35	14.39

Table 6- 5 Summary of the tuning of the 2-pole GaAs filter versus bias

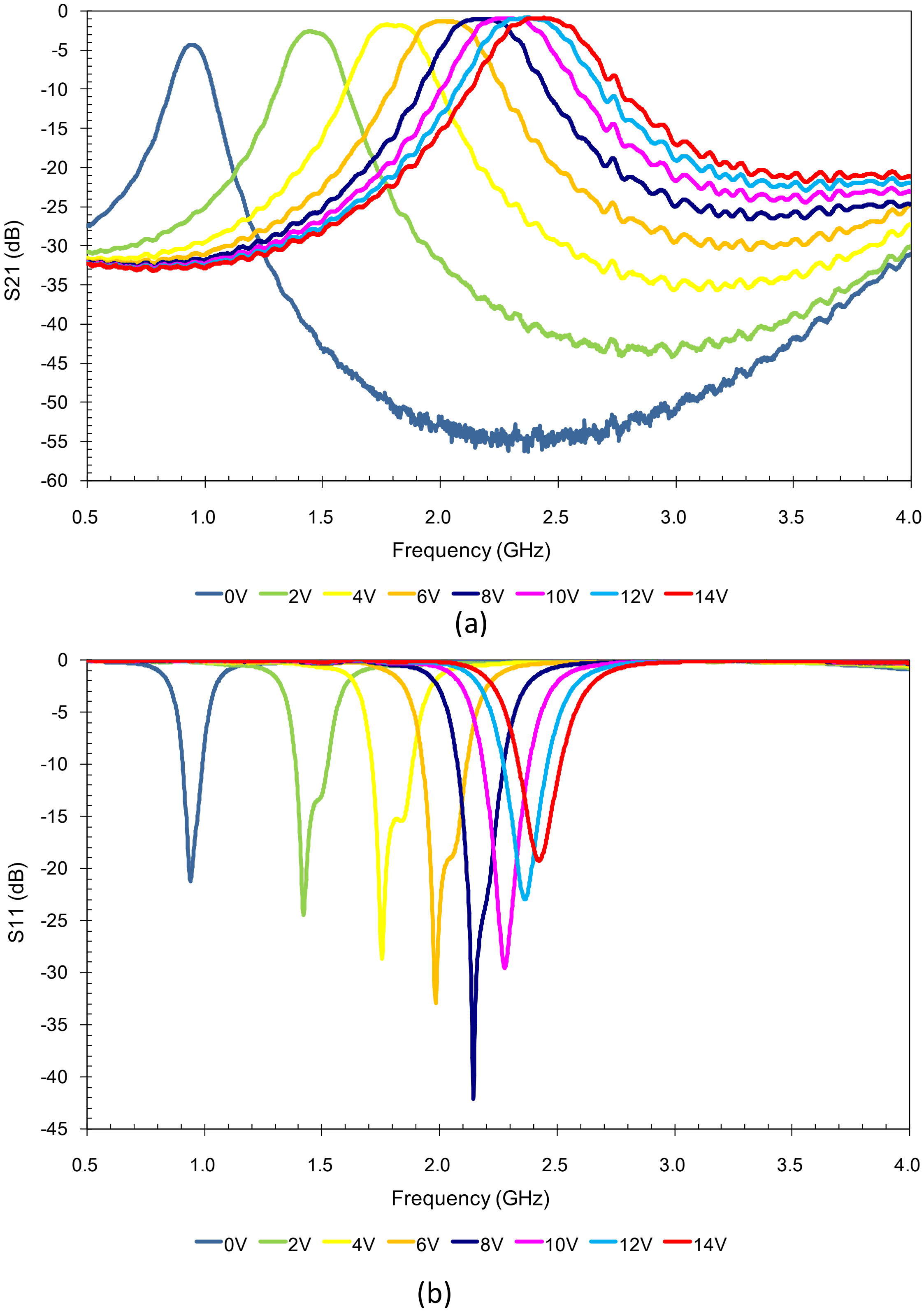

Fig.6- 22 Measured S_{21} (a) and S_{11} (b) of the 2-pole GaAs filter versus frequency as a function of bias voltages.

The measured frequency response of the 2-pole GaAs filter at 0 V, 6 V and 14 V are compared with the simulation in Fig.6- 24. In the simulation, the losses from the circuit and lumped elements were taken into account. The circuit was simulated in a copper box with 10 mm air above and below it. The thickness of copper cladding was set as 17 µm. The thickness of the substrate was 0.787 mm and loss tangent was 0.0012. The lossy circuit was simulated by full wave EM simulation in Sonnet. The GaAs varactor diode considering parasitic effects of package, substrate and loss was modelled as shown in Fig.6- 23. In the modelling, the diode representing the ideal varactor was reverse biased. The diode capacitance was 2.8 pF at 0 V, 0.3 pF at 6 V and 0.12 pF at 14 V (see Table 6- 5). The parasitic inductance L_s was 0.1 nH and substrate capacitance C_p was 0.02 pF, and the series resistance was 2.05 Ω at all bias conditions according to its data sheet [7]. The modelling circuit of the GaAs varactor was simulated using the Advanced Design System (ADS) [8]. The generated S-parameter data file was combined with the lossy filter circuit instead of the simple element values in the lossless assumption.

As shown in Fig.6- 24, the centre frequency of the measured response shifts about 0.1 GHz from the simulated response. This can be explained by the inaccurate estimation of the parasitic inductance L_s and substrate capacitance C_p in the varactor diode modelling, or other parasitic reactance caused by the varactor mounting or packaging. The length of the fabricated resonator line is slightly different with the simulation to leave space for varactor assembling. The tuning of the measured GaAs filter will be shown later in Fig.6- 41 with comparison with the BST filters. It can be also seen from the comparison that the fabricated filter exhibits a stronger external coupling than that of the simulation.

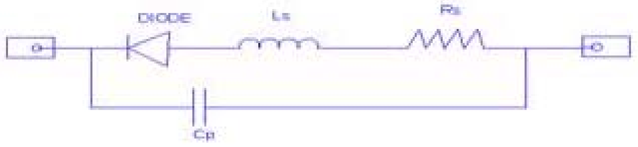

Fig.6- 23 The spice model for GaAs varactor diode (taken from [7])

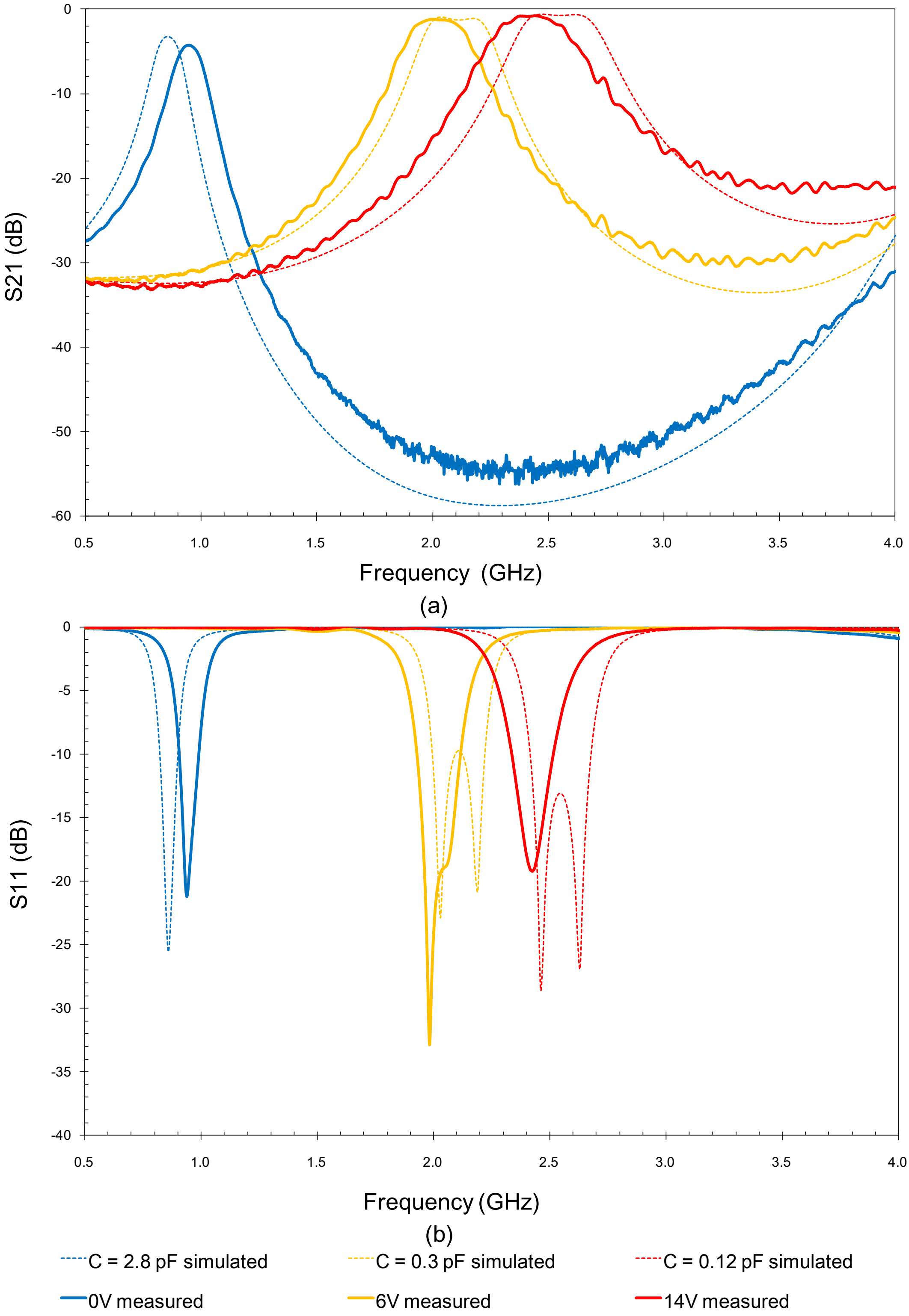

Fig.6- 24 Comparison of the simulated (dashed lines) and measured (solid lines) S_{21} (a) and S_{11} (b) of the 2-pole GaAs filter at 0 V, 6 V and 14 V respectively.

(ii) 2-pole BST IDC filter

Before measuring the 2-pole BST IDC filter, the electrical properties of the $Ba_{0.5}Sr_{0.5}TiO_3$ thin film IDCs were characterised on wafer with an Agilent 4294A impedance analyser using a 42941A impedance probe together with a Cascade Microtech ACP40 GS200 microprobe. Open-short-load calibration and fixture compensation was performed prior to the measurement. The interdigital fingers were designed to be 10 µm wide with 10 µm gaps between adjacent fingers. The dimensions of the fabricated fingers were measured with an optical microscope and were very close to that of the design, as shown in the photo in Fig.6- 25. The measured capacitance tuning and effective loss tangent curves of a BST IDC as a function of the applied bias voltage are shown in Fig.6- 26. A tunability of 1.7 (40 %) was recorded for 40 V (4 V/µm) bias at 1 MHz. The effective loss tangent at zero bias was 0.012 and decreased to 0.005 at 40 V bias. This indicates an improved filter loss performance with the application of bias. The frequency dependence of the capacitance and effective loss tangent of the BST IDC up to 110 MHz is shown in Fig.6- 27. The BST IDCs on the same sample have slightly different capacitance (a range of 0.83 pF - 0.99 pF at zero bias was observed) due to the inhomogeneous thickness or permittivity of BST thin film.

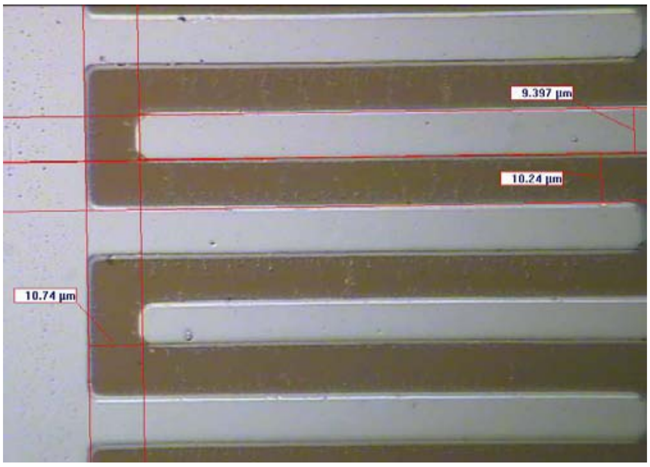

Fig.6- 25 Enlarged photo of the interdigital fingers (taken with an optical microscope)

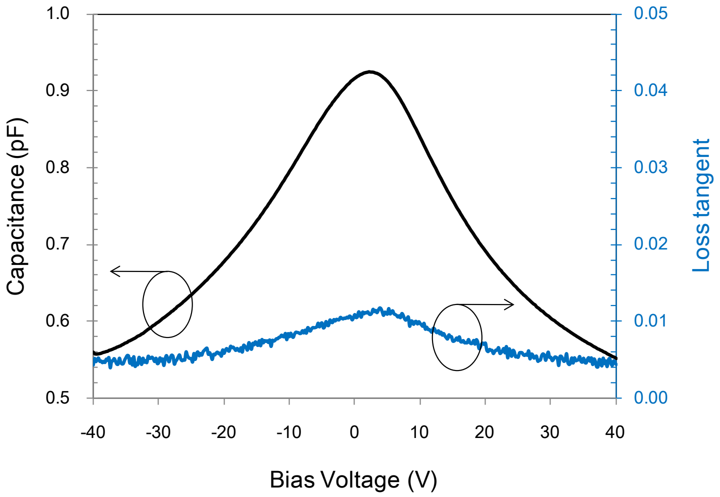

Fig.6- 26 Typical capacitance tuning and effective loss tangent curves of a $Ba_{0.5}Sr_{0.5}TiO_3$ thin film IDC as a function of DC bias voltage at 1 MHz.

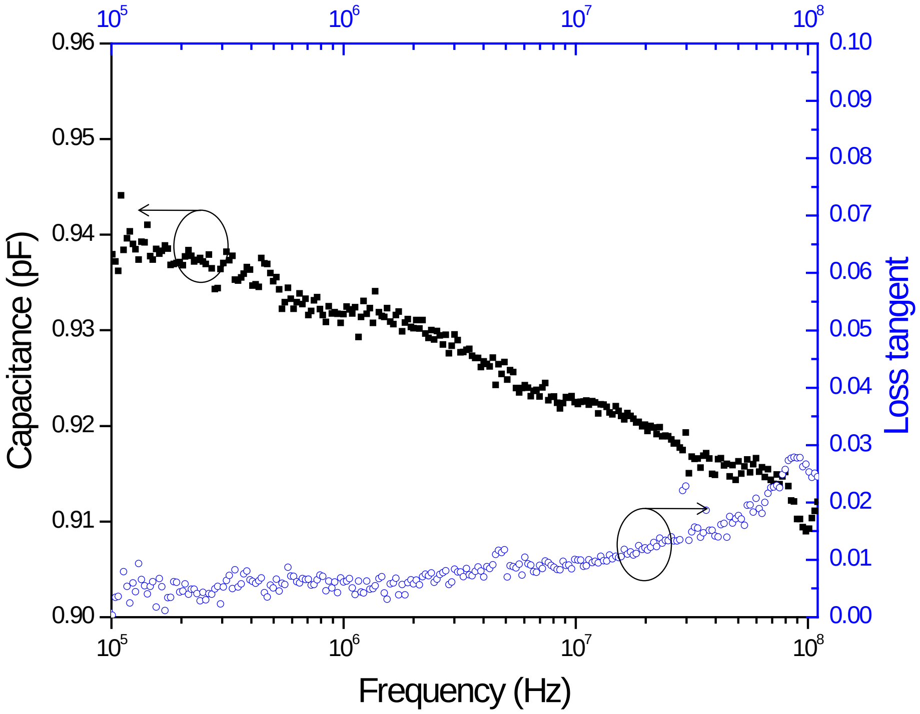

Fig.6- 27 Typical capacitance and effective loss tangent curves of a $Ba_{0.5}Sr_{0.5}TiO_3$ thin film IDC as a function of frequency up to 110 MHz.

After on wafer characterisation of the properties of the BST IDCs, the sample was cut into individual chips by dicing saw and BST IDCs chips were mounted to the circuits in a flip chip manner. A two pole bandpass filter using BST interdigital varactors as the tuning elements was measured. The measured response is shown in Fig.6- 28. The tuning of the 2-pole BST

IDC filter is summarised in Table 6- 6. The filter is tuned 0.47 GHz (23.3 %) from 1.55 GHz at zero bias to 2.02 GHz at 65 V, which is an electric field of 6.5 V/µm. The passband insertion loss is 3.7 dB without bias and is improved to 1.1 dB with 6.5 V/µm electric field due to an improved quality factor of the BST IDC with bias. The return loss is also improved with bias and is better than 14.4 dB at all bias states. The 3 dB fractional bandwidth of the filter remains around 14 - 15 %.

Bias (V)	Electric field (V/um)	f_0 (GHz)	IL (dB)	RL (dB)	3dB BW (GHz)	3dB FBW (%)
0	0.0	1.55	3.7	14.4	0.24	15.48
10	1.0	1.66	2.6	14.9	0.24	14.50
20	2.0	1.78	1.8	15.5	0.25	14.06
30	3.0	1.87	1.4	16.5	0.27	14.48
40	4.0	1.94	1.2	17.2	0.29	14.73
50	5.0	1.95	1.1	18.1	0.30	15.11
60	6.0	1.99	1.1	18.0	0.30	15.09
65	6.5	2.02	1.1	18.3	0.30	14.71

Table 6- 6 Summary of the tuning of 2-pole BST IDC filter

In the simulation, the BST IDCs were modelled by a parallel capacitance resistance model. The capacitance can be estimated by comparing the simulation with the measurement results. The simulated result of the 2-pole BST IDC filter agrees well with the measurement as shown in Fig.6- 29. The solid lines represent the measurement results and the dashed lines simulation results. A capacitance of 0.75 pF at zero bias and 0.38 pF with bias was used in the simulation. The extracted capacitance at zero bias (which is 0.75 pF) is slightly smaller than the measured capacitance at 1 MHz using the impedance analyser (which is 0.873 pF). This can be explained by the decreasing frequency dependence of the IDC capacitance as shown in Fig.6- 27. The permittivity of the $Ba_{0.5}Sr_{0.5}TiO_3$ thin film was estimated using the IDC capacitance equations provided in chapter 3, changing from 1680 at zero bias to 780 at 65 V, which was 53.6 % tuning. The resistance represented the dielectric loss of the BST film and was calculated by $R = 1/\tan\delta\omega C$, where ω was the centre angular frequency and $\tan\delta$ was set as 0.012 at zero bias and 0.005 at maximum bias, the same as the measured effective loss tangent of the BST IDC at 1 MHz. The metal loss was not concluded in the model as the BST film loss was considered to dominate in the BST IDC. As also shown in Fig.6- 29, the practical filter exhibits a stronger external Q_e compared with the simulation, which is similar to the case of the 2-pole GaAs filter.

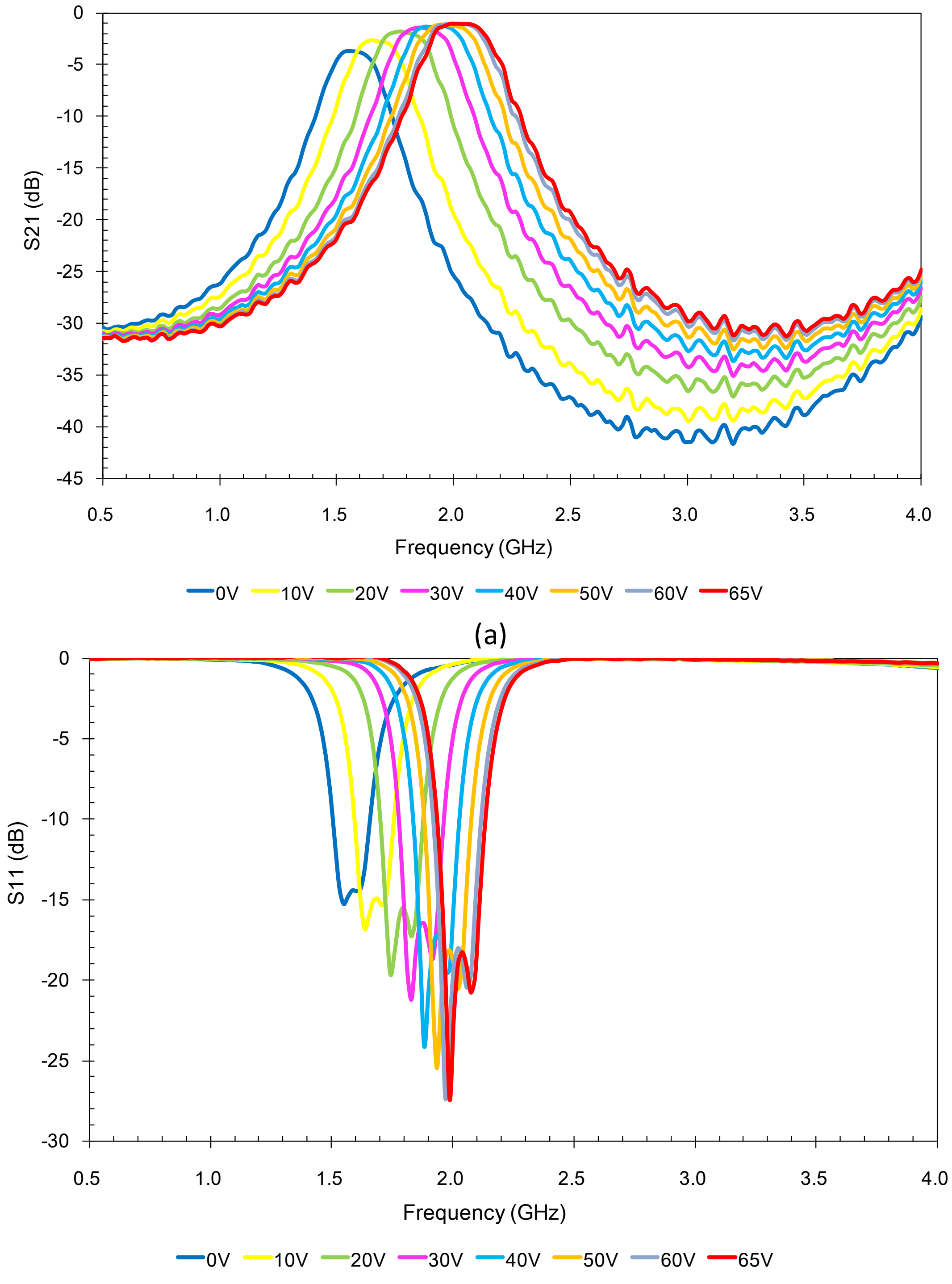

(a)

(b)

Fig.6- 28 Measured S_{21} (a) and S_{11} (b) of the 2-pole BST IDC filter versus frequency as a function of bias voltage.

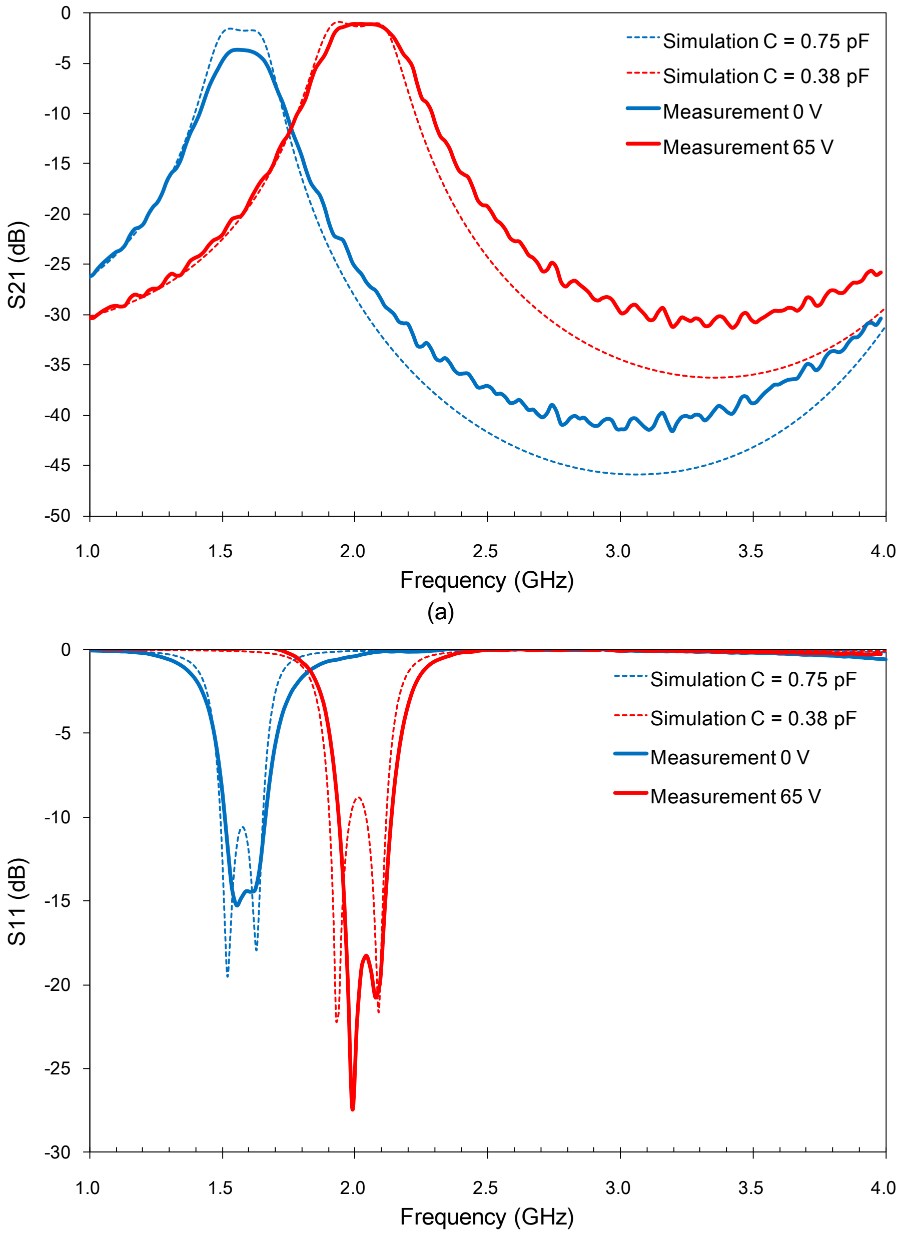

(a)

(b)

Fig.6- 29 Comparison of simulated (dashed lines) and measured (solid lines) S_{21} (a) and S_{11} (b) of the 2-pole BST IDC filter at two bias ends.

(iii) 2-pole BST parallel plate filter

$Ba_{0.25}Sr_{0.75}TiO_3$ thin film parallel plate capacitors were characterised on wafer with an Agilent 4294A impedance analyser using 42941A impedance probe together with ACP40 GS200 microprobe. Standard open-short-load calibration and fixture compensation was performed before the measurement.

The capacitor was designed as two 10 µm × 10 µm capacitors in series so each capacitor shared half of the applied DC bias. However, as shown in the photo in Fig.6- 30, the precise fabrication of the overlap area of the capacitor is difficult due to over-etching or slight mis-alignment of the mask. This leads to small capacitance difference of each of the parallel plate capacitors. For example, 24 parallel plate capacitors on a sample measured showed an average value of 0.32 pF with 7 % standard deviation. These capacitors were measured with about 8 mm air beneath them (by placing the capacitors on an empty plastic box) to remove the coupling capacitance between the pads and metal platform of the probe station. This coupling capacitance is about 0.06 pF - 0.07 pF.

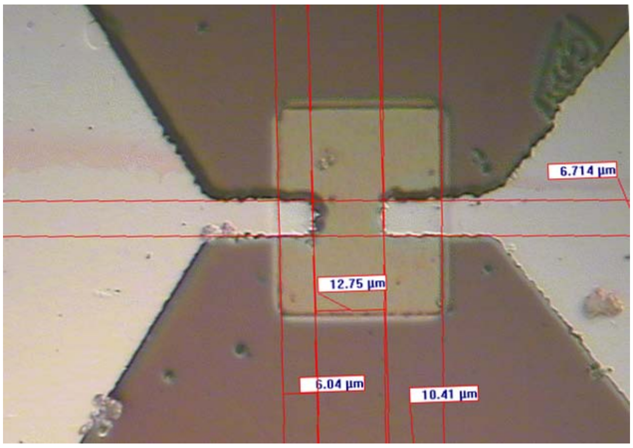

Fig.6- 30 Enlarged photo of the overlap area of a $Ba_{0.25}Sr_{0.75}TiO_3$ parallel plate capacitor (taken with an optical microscope)

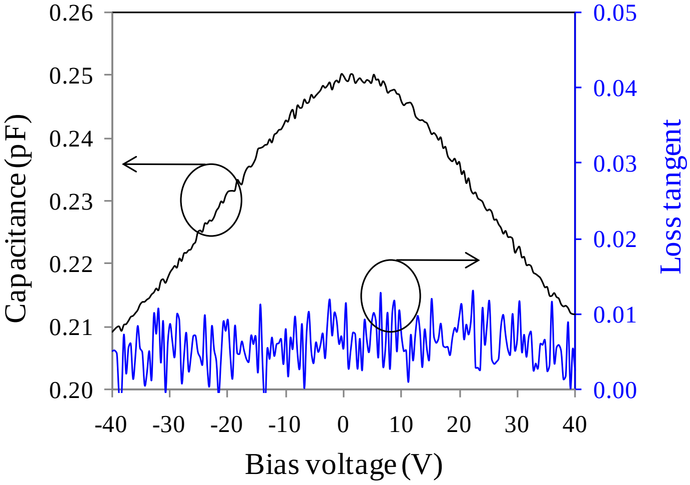

Fig.6- 31 Typical capacitance tuning and effective loss tangent of a $Ba_{0.25}Sr_{0.75}TiO_3$ thin film parallel plate capacitor versus bias at 1 MHz.

The measured capacitance tuning and effective loss tangent of a BST parallel plate capacitor is shown in Fig.6- 31. The typical $Ba_{0.25}Sr_{0.75}TiO_3$ parallel plate capacitor has a tunability of 1.2 (0.25 pF / 0.21 pF) (relative tunability 16.0 %) for 40 V bias, which corresponds to an electric field of 40 V/µm, measured at 1 MHz. This tunability is small compared with the $Ba_{0.5}Sr_{0.5}TiO_3$ thin film IDC discussed in the previous section. In theory BST capacitors in the parallel plate configuration can have a higher tunability than that of in the interdigital configuration as the tuning capability of the BST films can be more effectively used [9]. However, for this particular case, the BST film used in the parallel plate capacitor (Ba/Sr ratio of 25/75) has lower Ba concentration compared with the film in the IDC (Ba/Sr ratio of 50/50). The lower Ba concentration was chosen in order to reduce the capacitance to a useful value at room temperature. Another reason might be the growth temperature effect on the BST film properties. The lower growth temperature might also contribute to the lower permittivity and tunability [10]. The parallel plate capacitors were found to exhibit a bias independent loss tangent as shown in Fig.6- 31. This agrees well with the constant insertion loss of the measured filter with the application of bias (see Fig.6- 32 (a)).

After capacitors characterisation, the sample was cut into individual chips with a dicing saw and BST parallel plate capacitors were assembled to the filter circuit in a flip chip manner. A 2-pole BST parallel plate filter in a copper box was measured. The measurement result is shown in Fig.6- 32. The tuning of the two pole filter with BST parallel plate capacitors is summarised in Table 6- 7. The centre frequency is tuned 7.9 % from 2.32 GHz to 2.52 GHz with the application of 45 V bias, which is an electric field of 45 V/µm. The passband insertion loss is about 1.4 dB - 1.3 dB in the whole tuning range, which is the lowest insertion loss for BST room temperature filters from the author’s knowledge [11-14]. The return loss is better than 20.2 dB at all bias states. The 3 dB fractional bandwidth of the filter remains about 15 % with tuning.

Bias (V)	Electric field (V/um)	f_0 (GHz)	IL (dB)	RL (dB)	3dB BW (GHz)	3dB FBW (%)
0	0	2.32	1.4	24.5	0.35	15.09
20	20	2.40	1.4	27.1	0.36	15.00
40	40	2.50	1.3	21.9	0.36	14.40
45	45	2.52	1.3	20.2	0.38	15.08

Table 6- 7 Summary of the tuning of the 2-pole BST parallel plate filter

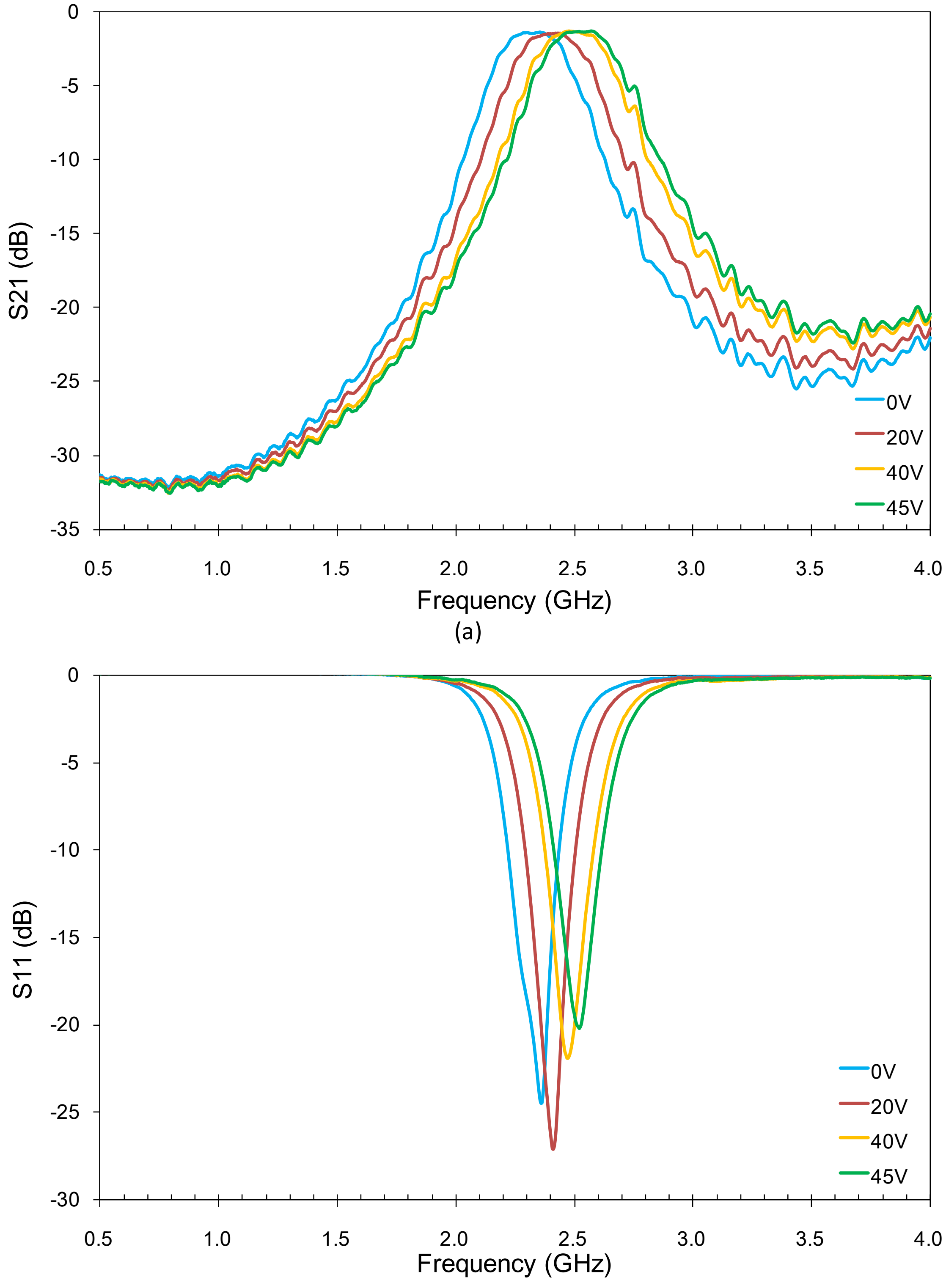

(a)

(b)

Fig.6- 32 Measured S_{21} (a) and S_{11} (b) of a 2-pole BST parallel plate filter

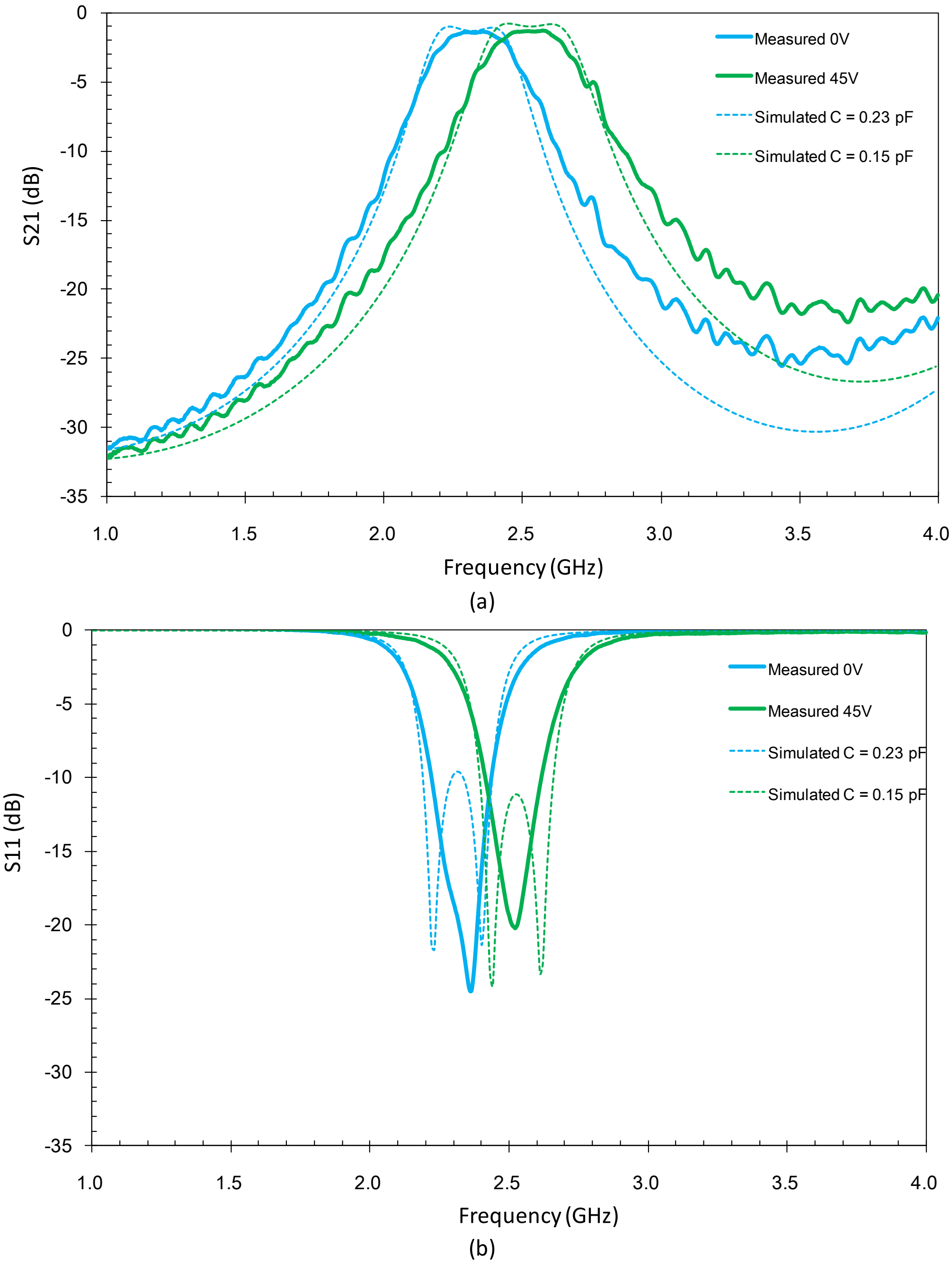

Fig.6- 33 Comparison of the simulated (dashed lines) and measured (solid lines) S_{21} (a) and S_{11} (b) of the two pole filter using BST parallel plate varactors.

The capacitance of the parallel plate capacitors used in the filter was estimated by comparing the simulation with the measurement results. In the simulation, the BST parallel plate varactor was modelled as a parallel capacitance resistance model and the resistance was calculated by $R = 1/\tan\delta\omega_0 C$, where ω_0 was the centre frequency of the filter and $\tan\delta$ was assumed to be

0.01 with and without bias. The simulated response compares well with the measurement as shown in Fig.6- 33. The estimated capacitance was 0.23 pF at 0 V and 0.15 pF at 45 V. The practical filter had a stronger external coupling compared with the simulation.

6.3.3 The four pole bandpass filters

Four pole filters with GaAs varactors, or BST interdigital varactors, or BST parallel plate varactors as tuning elements were assembled in brass boxes as the two pole filters. The BST IDCs and parallel plate capacitors were fabricated and characterised as described in previous sections. The measurement results of the four pole filters are shown below and compared with the simulation.

(i) 4-pole GaAs filter

The measured S_{21} and S_{11} of a 4-pole GaAs filter in a plain box (no tuning screws) is shown in Fig.6- 34. The filter is tuned from about 0.92 GHz at zero bias to 2.49 GHz at 15 V bias. This tuning range is similar to that of the 2-pole GaAs filter (0.94 GHz - 2.44 GHz).

However, the filter performance can be severely degraded when the tuning range is large. At zero bias, the filter insertion loss is 18 dB and the minimal return loss is 3 dB. The poor loss performance is due to the unmatched couplings of the 4-pole filter at zero bias. The GaAs capacitor has a zero bias capacitance of 2.8 pF. As mentioned in the design of the four pole filter, the external quality factor and coupling coefficients all change with the loaded capacitance and the filter performance can be degraded when the loaded capacitance is tuned far away from 0.3 pF. This can be improved by mounting tuning metal screws on the box lid, aligned to the top of each resonator and coupling lines, as shown in Fig.6- 35. The passband reflection can be reduced by carefully adjusting the tuning screws and the insertion loss can be improved in this way. Appendix B gives the tuning of the four pole GaAs filter with bias after adjusting the tuning screws for good return loss at 3 V, 6 V, 9 V, 12 V and 15 V respectively. Once the tuning screws have been set, they are no longer altered; the tuning in these figures is solely from the varactor. At each bias voltage, the return loss can be tuned to better than 15 dB by adjusting the metal screws.

The best case is for 6 V, the tuning of the filter with bias after adjusting the tuning screws for good S11 at 6 V is shown in Fig.6- 36 and summarised in Table 6- 8. The return loss can be reduced from 3.7 dB to 21.7 dB and the insertion loss is improved from about 8.5 dB to 2.8 dB at about 1.9 GHz by adjusting the tuning screws. The improvement in insertion loss is due to an improved matching and passband shape. The return loss is better than 6.3 dB in most bias range. The 4-pole GaAs filter with tuning screws shows a tuning range of 0.9 GHz - 2.21 GHz with 15 V bias. The 3 dB fractional bandwidth is 19.31 % at 6 V and decreases when tuning away from 6 V due to degraded matching. The spurious resonances at higher frequencies are caused by the coupling between the tuning screws and circuits.

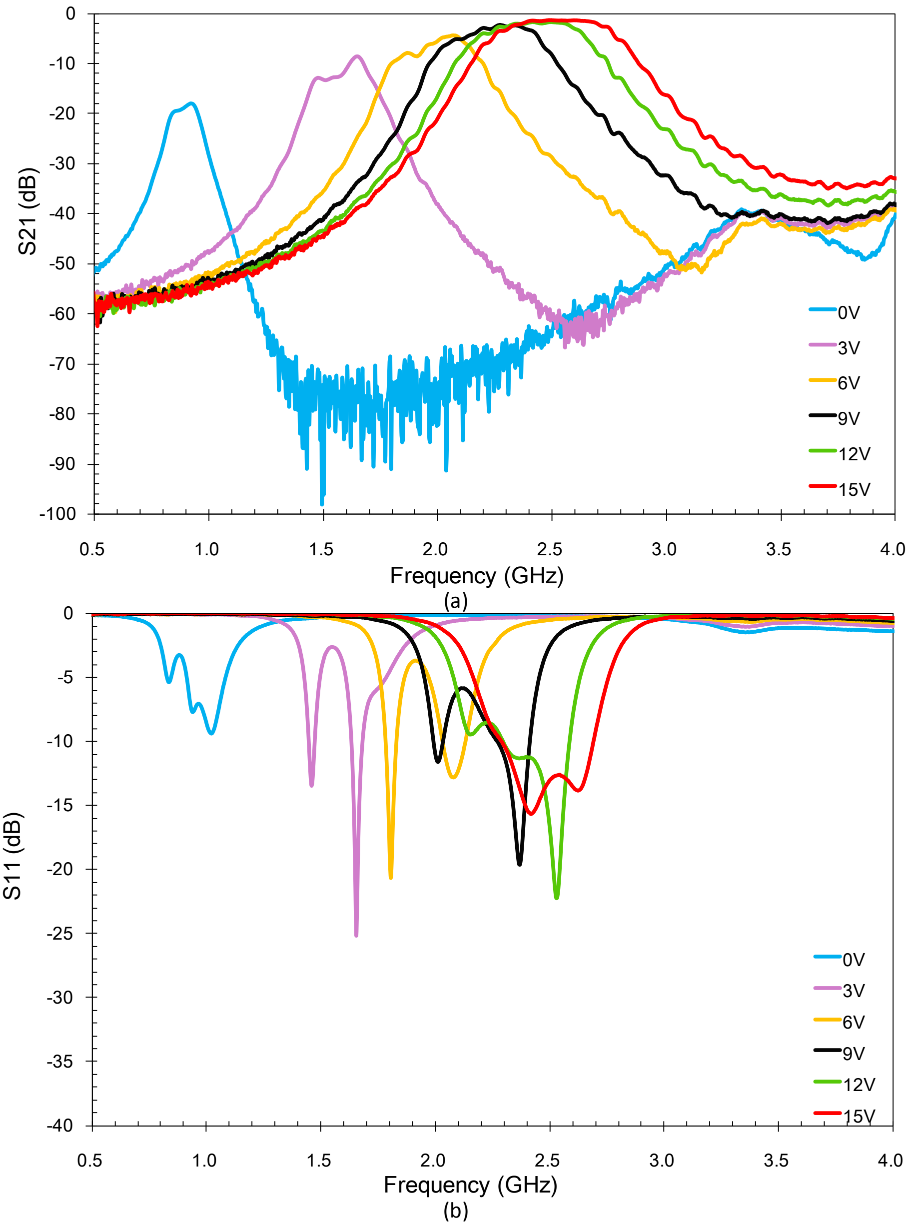

Fig.6- 34 Measured S_{21} (a) and S_{11} (b) of a 4-pole GaAs filter without tuning screws.

Fig.6- 35 A box with tuning screws for the four pole filter

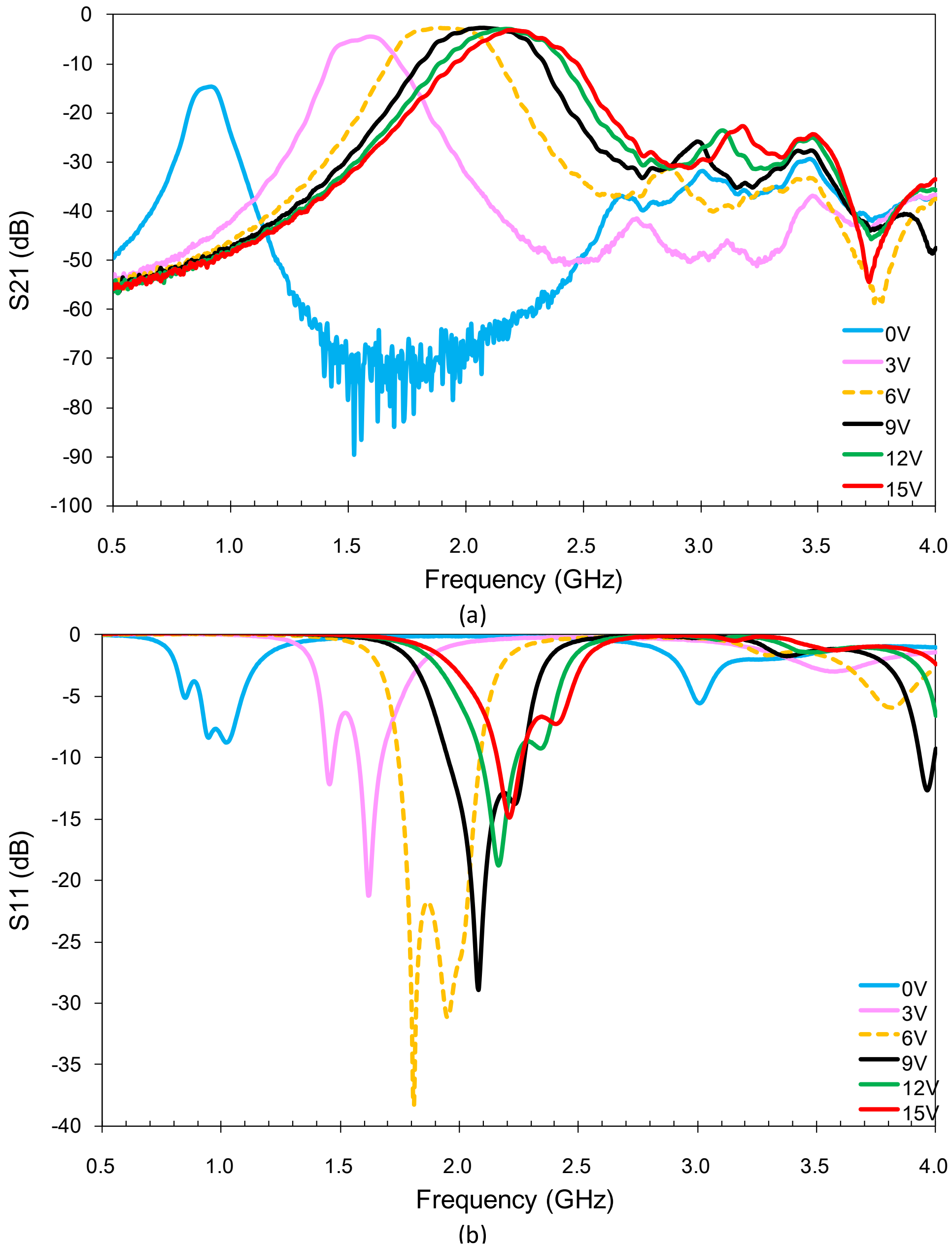

Fig.6- 36 Measured S_{21} (a) and S_{11} (b) of the 4-pole GaAs filter as a function of bias after adjusting the tuning screws for good S_{11} at 6 V.

Bias (V)	Capacitance (pF)	f_0 (GHz)	IL (dB)	RL (dB)	3dB BW (GHz)	3dB FBW (%)
0	2.80	0.90	14.6	3.8	0.12	13.72
3	0.58	1.56	4.5	6.3	0.25	15.78
6	0.30	1.91	2.8	21.7	0.37	19.31
9	0.19	2.07	2.6	12.9	0.39	18.95
12	0.14	2.17	2.8	8.7	0.35	16.21
15	0.11	2.21	3.0	6.7	0.31	14.06

Table 6- 8 The tuning of the 4-pole GaAs filter after adjusting the metal screws for good S_{11} at 6 V

The measurement results of the 4-pole GaAs filter with tuning screws at 6 V is compared with the simulation in Fig.6- 37. In the simulation, the circuit model of the GaAs varactor was analysed by ADS and the generated S-parameter data file was combined with full wave EM simulation of the circuit by Netlist. The losses from the duroid substrate and copper cladding were included in the simulation as well. The measured filter has a smaller centre frequency and bandwidth than the simulation, which is similar to the case of the 2-pole GaAs filter.

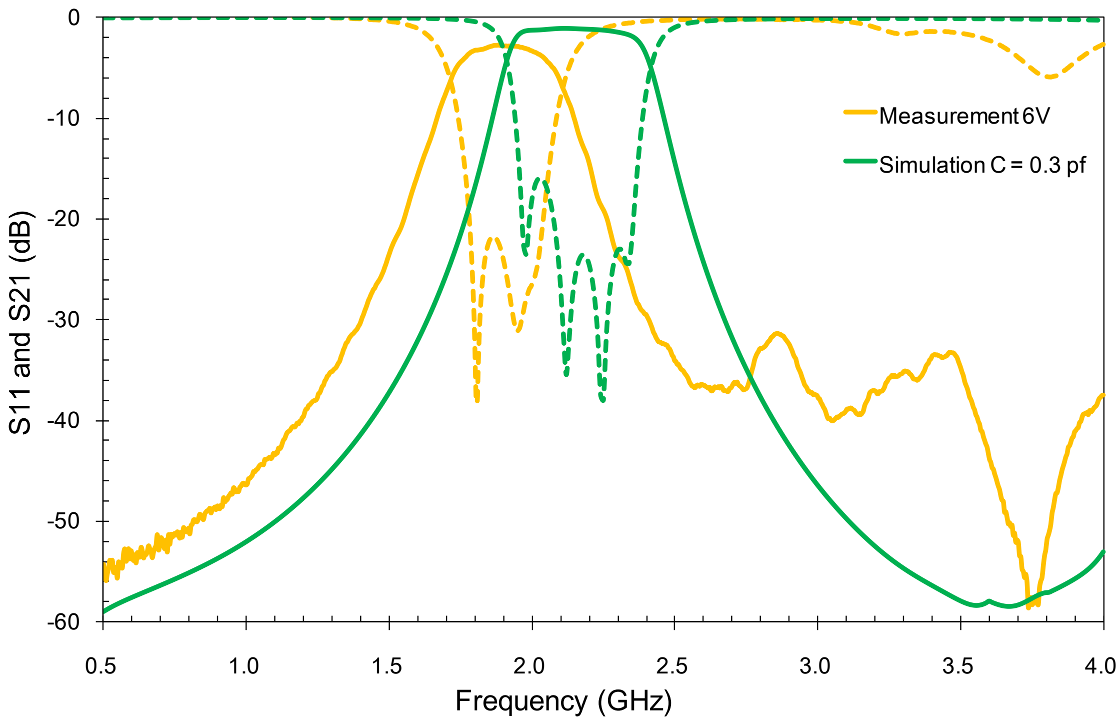

Fig.6- 37 Comparison of the simulation and measurement of the 4-pole GaAs filter with tuning screws at 6V

(ii) 4-pole BST IDC filter

BST IDCs with a zero bias capacitance of 0.94 pF, measured at 1MHz, were used in the 4-pole BST IDC filter. The tuning of the 4-pole BST IDC filter assembled in a plain box is shown in Fig.6- 38 and is summarised in Table 6- 9. The filter is tuned from 1.49 GHz at 0 V to 1.85 GHz at 25 V, which is 19.5 % tuning. The passband insertion loss at 0 V is 9.2 dB and is improved to 4.2 dB at 25 V. This is in part due to the improved quality factor of BST IDCs with bias (see Fig.6- 26) and in part due to the reduced return loss. The 3 dB fractional bandwidth remains about 17 % at all bias states.

Bias (V)	Electric field (V/μm)	f_0 (GHz)	IL (dB)	RL (dB)	3dB BW (GHz)	3dB FBW (%)
0	0.0	1.49	9.2	5.9	0.25	16.40
10	1.0	1.62	7.0	6.6	0.27	16.86
15	1.5	1.73	5.7	7.3	0.30	17.52
25	2.5	1.85	4.2	8.7	0.33	17.86

Table 6- 9 Summary of the 4-pole BST IDC filter

The filter performance at 0 V can be improved by using tuning screws. By changing the plain box lid to the lid with tuning screws and adjusting the screws at 0 V, the passband reflection of the 4-pole BST IDC filter at 0 V is improved from 5.9 dB to 17.6 dB, and the insertion loss is improved from 9.2 dB to 6.3 dB. The comparison of the 4-pole BST IDC filter before and after the tuning screw adjusting at 0 V is shown in Fig.6- 39 and concluded in Table 6- 10. The fractional bandwidth is increased to 18.65 % with the tuning screws. However, the tuning with bias after the tuning screw adjusting is not available because of the breakdown of the BST IDCs at 30 V in the previous measurement. The BST IDC 4-pole filter will be compared with the GaAs 4-pole filter directly in section 6.4.

	f_0 (GHz)	IL (dB)	RL (dB)	3dB BW (GHz)	3dB FBW (%)
no screws	1.49	9.2	5.9	0.25	16.40
with screws	1.54	6.3	17.6	0.29	18.65

Table 6- 10 The comparison of the 4-pole BST IDC filter at 0 V with and without tuning screws.

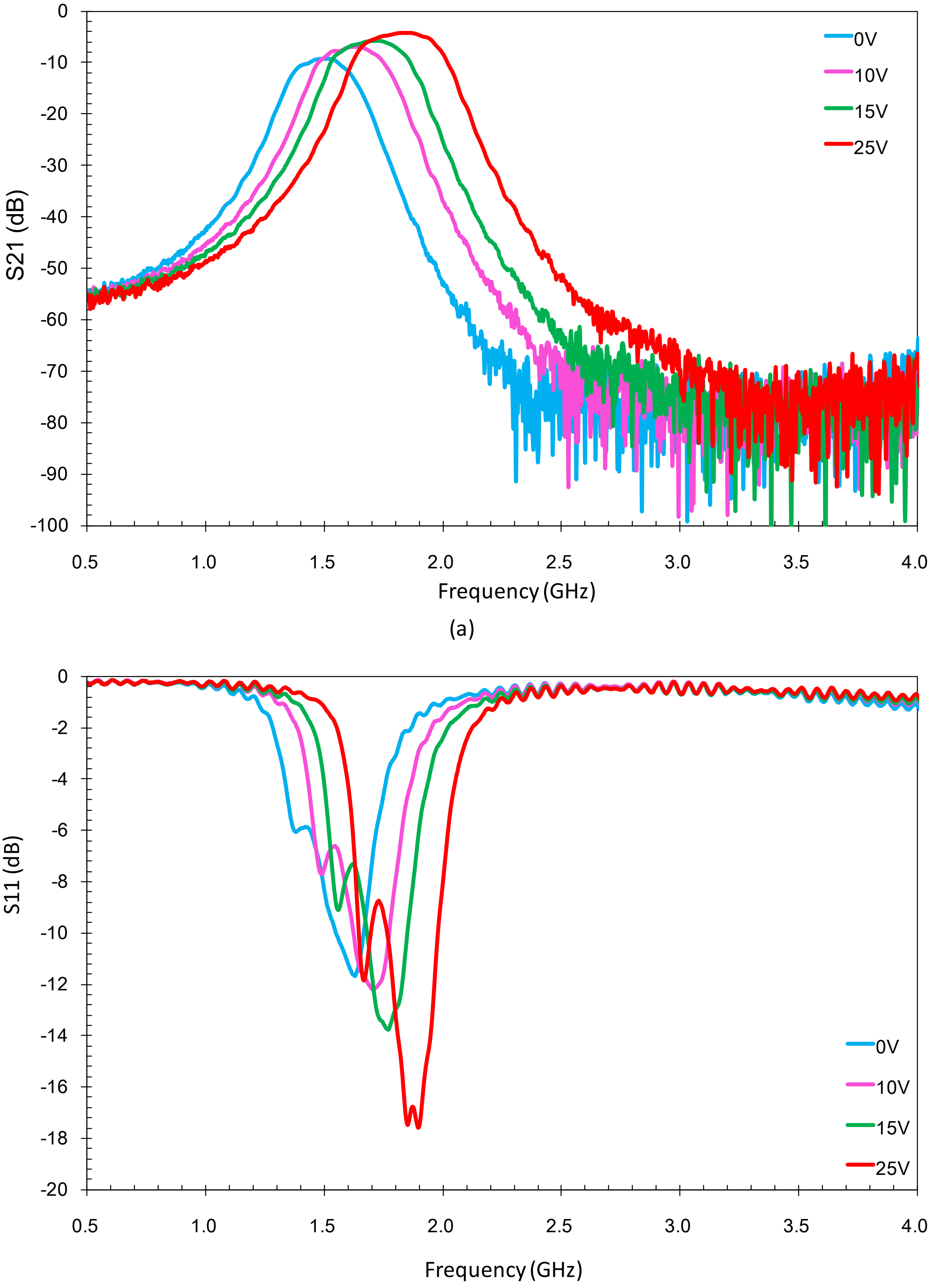

(a)

(b)

Fig.6- 38 Measured S_{21} (a) and S_{11} (b) of a 4-pole BST IDC filter with no tuning screws.

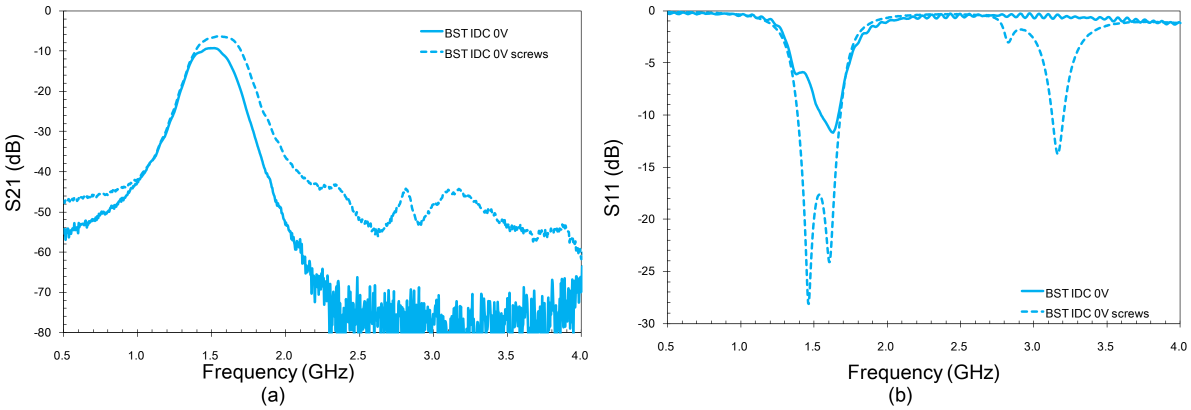

(a)

(b)

Fig.6- 39 The S_{21} (a) and S_{11} (b) of the 4-pole BST IDC filter with (dashed lines) and without (solid lines) tuning screws at 0 V.

(iii) 4-pole BST parallel plate filter

A 4-pole BST parallel plate filter was measured in a plain box and shown in Fig.6- 40. The tuning of the 4-pole BST parallel plate filter is summarised in Table 6- 11. As the BST parallel plate capacitors have an average capacitance of 0.32 pF, which is close to that of the design (0.3 pF), the filter shows an acceptable return loss perfermance in the whole tuning range so that tuning screws are not used. The filter is tuned 9 % from 2.22 GHz at zero bias to 2.44 GHz at 35 V bias (which is an electric field of 35 V/μm). This tuning range is close to that of the 2-pole BST parallel plate filter (2.32 GHz - 2.52 GHz). The passband insertion loss remains about 2.8 dB in all bias states. The almost constant insertion loss in the tuning range is a result of the bias independent loss tangent of BST film in the parallel plate capacitors (see Fig.6- 31). The passband reflection is better than 14.7 dB at zero bias and is better than 9.4 dB in the whole tuning range. The 3 dB fractional bandwidth is about 20 % in all bias states. This filter will also be compared with the 4-pole GaAs filter in the following section.

Bias (V)	Electric field (V/μm)	f_0 (GHz)	IL (dB)	RL (dB)	3dB BW (GHz)	3dB FBW (%)
0	0	2.22	2.8	14.7	0.47	21.04
10	10	2.29	2.9	13.6	0.46	20.19
20	20	2.37	2.9	11.6	0.47	19.97
30	30	2.44	2.8	10.4	0.49	20.22
35	35	2.44	2.8	9.4	0.50	20.38

Table 6- 11 Tuning of the 4-pole BST parallel plate filter

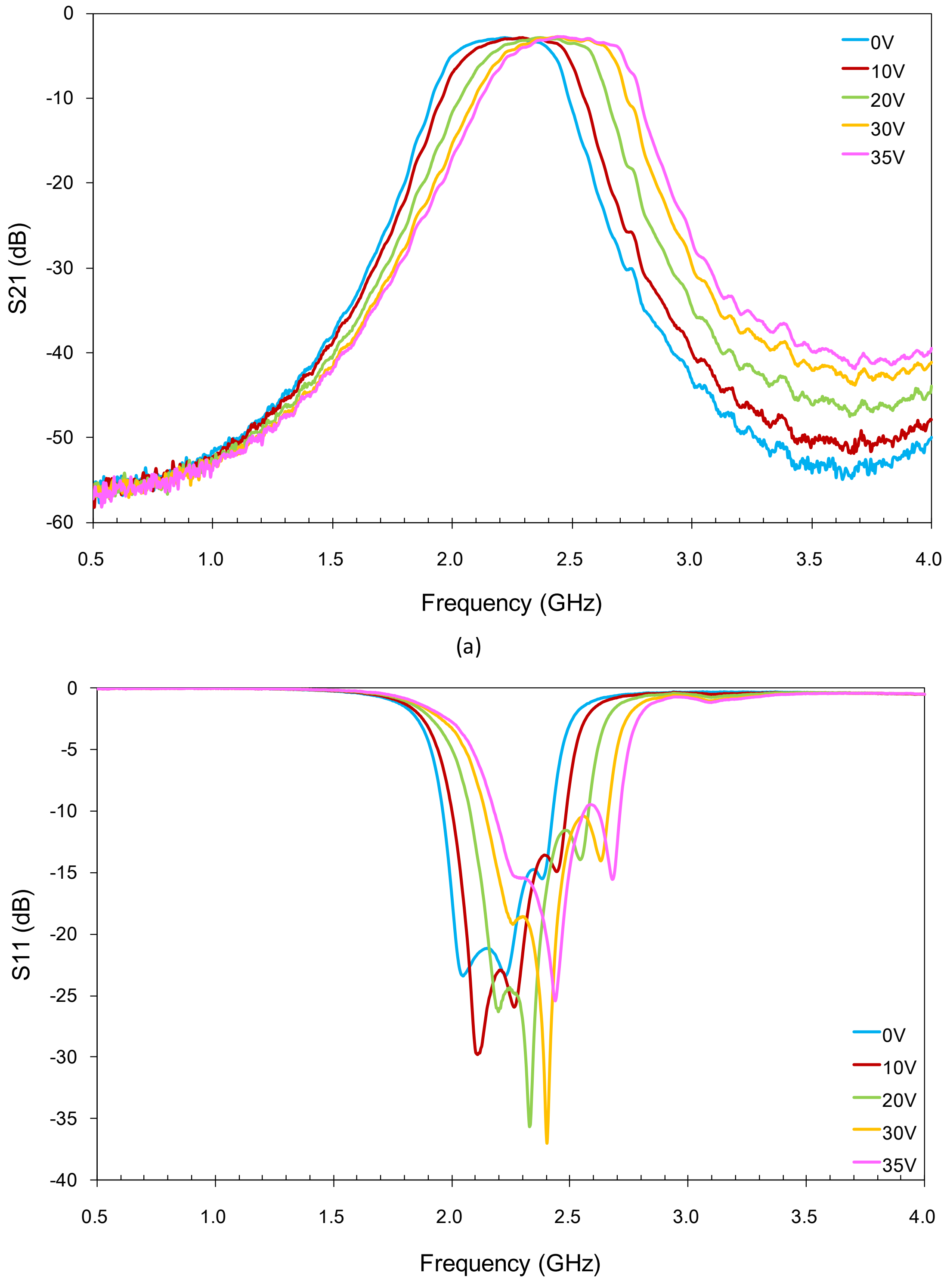

(a)

(b)

Fig.6- 40 Measured S_{21} (a) and S_{11} (b) of the 4-pole BST parallel plate filter with no tuning screws.

6.4 Comparison of GaAs, BST IDC and BST parallel plate filters

6.4.1 Tunability

The tuning of the measured centre frequencies of the 2-pole GaAs filter, BST IDC filter and BST parallel plate filter as a function of the loaded varactor capacitance are shown in Fig.6-41 and compared with the simulation of a lossless 2-pole filter. The tuning of each filter is clear in this figure.

The 2-pole GaAs filter has largest tuning range from 0.94 GHz to 2.44 GHz owing to the very high tunability of GaAs varactors (a tunability of 24 for 0 V - 14 V bias). The 2-pole BST IDC filter is tuned 0.47 GHz (30.3 %) from 1.55 GHz to 2.02 GHz with an electric field of 6.5 V/µm, which is the highest tunability among the BST filters. Such a tunability is better than or comparable to other published BST filters in a similar frequency region [2], [12-15]. The BST IDCs used have been tuned from 0.87 pF at zero bias to 0.38 pF at 65 V, which is 56.3 % relative tunability. The 2-pole BST parallel plate filter is tuned 0.2 GHz (8.6 %) from 2.32 GHz to 2.52 GHz with the application of 45 V/µm electric field. The BST parallel plate capacitors used have been tuned 34.8 % from 0.23 pF to 0.15 pF. The 4-pole filters experience similar tuning range with the 2-pole ones using the same set of varactors and are not plotted in Fig.6- 41.

As mentioned in a previous section, in theory the BST parallel plate capacitors can have a higher tunability than that of in the interdigital configuration. However, in this case, the BST parallel plate capacitors have a smaller tunability compared with the BST IDC due to a lower Ba concentration of the BST film and a lower growth temperature is used in the BST film deposition. It should be noted that the tunability of BST filters can be further improved by reducing the gap of the IDC or using optimised BST parallel plate capacitors. As mentioned in chapter 2, Pervez [16] reported a BST parallel plate capacitor with a tunability of 13.7 (92.7 %) at 400 V/µm, which was the highest tunability ever reported for BST varactors. BST parallel plate capacitors with more than 70 % tunability were also reported [17], [18]. The breakdown field of BST film is 6.5 V/µm in the IDCs and 45 V/µm in the parallel plate capacitors. In theory the breakdown field of BST thin film can reach 800 V/μm, which leaves plenty room for improvement [19]. Therefore, the BST filters demonstrated in this work could be expected to yield better tuning performance on condition that a high quality BST film is fabricated and capacitor layout is optimised.

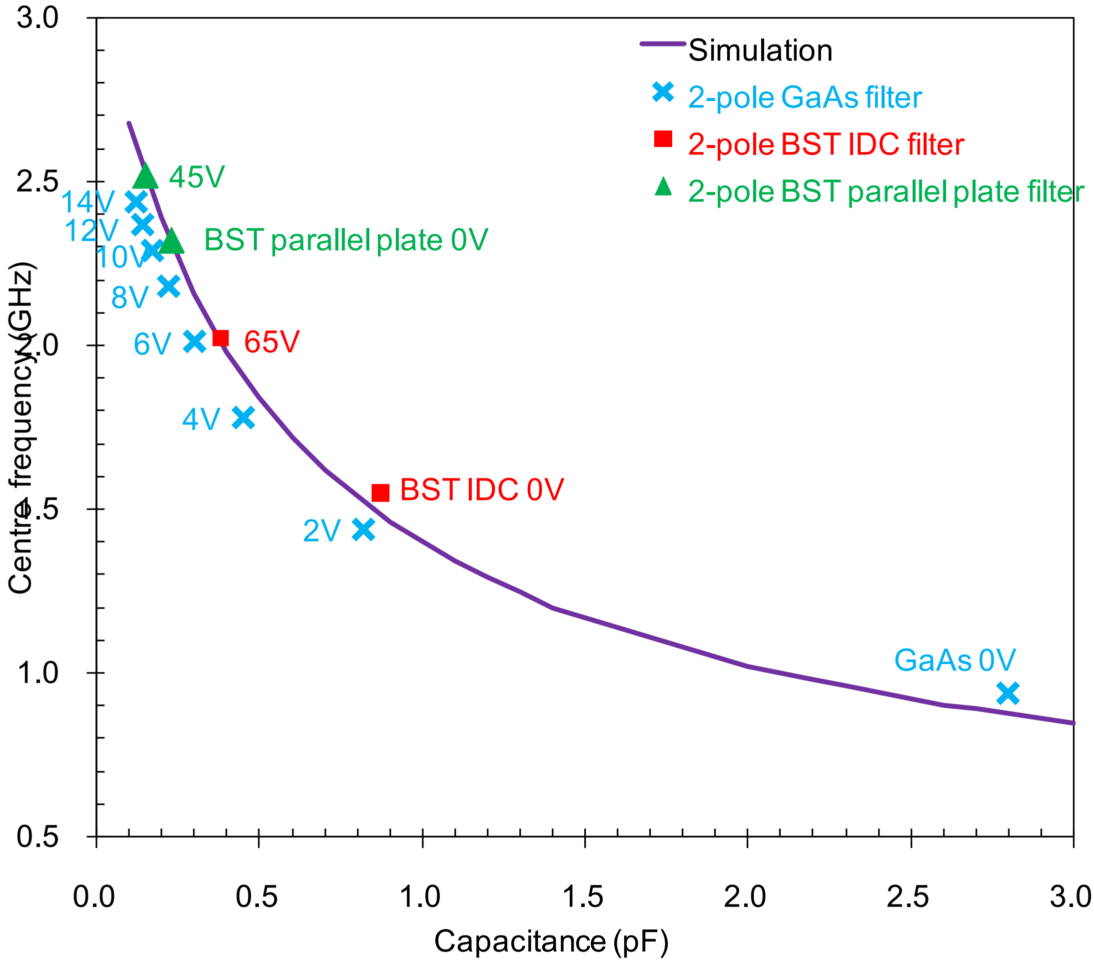

Fig.6- 41 The tuning range of the measured 2-pole GaAs filter (crosses), BST IDC filter (squares) and BST parallel plate filter (triangles) versus loaded varactor capacitance. The simulated tuning range of a lossless 2-pole filter (solid line) is also shown in figure.

6.4.2 Loss

The high loss of room temperature microwave devices based on BST varactors used to be a significant drawback limiting their microwave applications [20]. Intensive research effort has been made to improve the quality factor of BST varactors [18], [21], [22]. A comparison of the quality factor of BST varactor, Si abrupt junction varactor, and GaAs heterostructure barrier varactor in the microwave region showed that advantages of BST varactors emerges at frequencies above 10 GHz [23]. This is because the quality factor of varactor diode is inversely proportional to the frequency. For instance the Q of the GaAs varactor used in this work is about 170 at 1 GHz and this is reduced to only 17 at 10 GHz, which will considerably degrade the loss performance [7].

In this work, the loss contribution from the varactors (GaAs, BST IDC and BST parallel plate varactors) are separated from the filter circuit losses. Besides, a direct comparison of the loss performance of the 4-pole GaAs filter and BST filters is given for the first time.

The losses from different parts of the filter were investigated by simulating a resonator with only the loss from the substrate (which had a dielectric loss tangent of 0.0012), copper cladding (which was 17 µm copper), or varactors taken into account. The loaded quality factor can be found from the simulation, expressed as [5]

$$\mathrm{Q_L} = \frac{f_0}{\mathrm{BW_{3dB}}} \tag{6.4}$$

where f_0 is the resonant frequency and $\mathrm{BW_{3dB}}$ is the 3 dB attenuation bandwidth. The total loaded $\mathrm{Q_{toal}}$ of a lossy resonator loaded with varactors is comprised of the loss contributed from the substrate, copper cladding and varactors as

$$\frac{1}{\mathrm{Q_{total}}} = \frac{1}{\mathrm{Q_{substrate}}} + \frac{1}{\mathrm{Q_{copper}}} + \frac{1}{\mathrm{Q_{var\,actor}}} \tag{6.5}.$$

As discussed in chapter 3, the loaded Q can be used as the unloaded Q as long as the external coupling is weak [24]. The dissipation of a bandpass filter can be estimated from the unloaded quality factor of the resonator as [6]

$$\mathrm{IL}_{f_0} = 4.343\sum_{\mathrm{i}=1}^{\mathrm{n}} \frac{\Omega_\mathrm{c}}{\mathrm{FBW\,Q_i}}\mathrm{g_i}\ \mathrm{dB} \tag{6.6}$$

where IL_{f_0} is the insertion loss in dB at centre frequency of the filter, $\Omega_c = 1$, FBW is the ripple fractional bandwidth of the filter and g_i is the normalised element value of the

Chebyshev lowpass prototype filter. Q_i is the unloaded quality factor of the resonator corresponding to g_i. Here the loaded Q_{total} of the resonator extracted from equations (6.4) and (6.5) is used instead of the unloaded Q.

For the 2-pole GaAs filter, the resonator with loss from only the varactor diode, the copper cladding, or the substrate is simulated at 0 V, 6 V and 14 V bias. In the simulation, the varactor diode is modelled as shown in Fig.6- 23 and the parameters are specified according to the data sheet [7]. The simulated resonator quality factors corresponding to loss from different part of the filter are summarised in Table 6- 12. In the table, the total Q of the resonator is calculated using equation (6.5). The calculated insertion loss is estimated from the Q_{total} using equation (6.6) and is compared with the simulated and measured insertion loss. It can be seen that the diode loss is dominant, especially when the insertion loss is high. The Q_{diode} is improved from 21.4 to 285.0 with the loaded capacitance decreasing from 2.8 pF to 0.12 pF. This is expected as the unloaded Q is inversely proportional to the capacitance C and resistance R_s if the loss resistance is modelled in series with the reactance [5]

$$Q_u = \frac{1}{\omega C R_s} \tag{6.7}$$

where ω is the angular frequency. The Q_{total} is improved from 18.0 when the loaded capacitance is 2.8 pF to 96.5 when the capacitance changes to 0.12 pF. The calculated insertion loss decreases from 3.9 dB to 0.7 dB with the decreasing of the loaded capacitance, and is very close to the simulated insertion loss. The measured insertion loss is about 0.3 dB higher than the estimation as the loss from the DC blocks and silver epoxy is not taken into account in the estimation and simulation. Both the calculation and measurement show that the dissipation is reduced when the filter is tuned to higher frequencies (i.e., smaller loading capacitance) because of the improved Q of the varactor diode.

Bias (V)	Capacitance (pF)	Q_{diode}	Q_{copper}	$Q_{substrate}$	Q_{total}	Calculated IL (dB)	Simulated IL (dB)	Measured IL (dB)
0	2.80	21.4	115.2	5161.5	18.0	3.9	3.29	4.2
6	0.30	147.1	185.6	2165.7	79.1	0.9	0.97	1.2
14	0.12	285.0	187.2	661.9	96.5	0.7	0.56	0.8

Table 6- 12 The quality factors and insertion loss of the 2-pole GaAs filter

For the 2-pole BST IDC filter, the BST IDC was represented by a parallel capacitance resistance model and the resistance was calculated by R = 1/tanδωC, where ω was the centre angular frequency. The BST thin film loss was predominated in the IDC compared with the conducting loss, which was not included in the model. Table 6- 13 concludes the simulated quality factors from different part of the filter at two bias ends. The quality factor of the BST IDC is 86.3 and is dominant at zero bias when a loss tangent of 0.012 is assumed (according to the measured properties at 1 MHz, see Fig.6- 26). The Q_{BST} is improved to 230.3 at 65 V when a loss tangent of 0.005 is assumed, and this is comparable to the conducting loss (loss from copper cladding). The Q_{copper} is above 150. The Q from substrate loss is high, over 1000. The total Q increases from 53.0 to 97.2 with the deceasing of BST loss tangent with bias.

The passband insertion loss was also estimated using equation (6.6) from the total Q of a resonator, changing from 1.3 dB to 0.7 dB with the improved BST loss tangent with bias. The simulated lossy filter was shown in Fig.6- 29 and the passband insertion loss changed from 1.6 dB to 0.9 dB with bias. The estimated insertion loss is close to that of the simulated insertion loss but is smaller compared with the measured insertion loss (3.7 dB - 1.1 dB) as loss from silver epoxy, DC blocks and IDC electrodes are not taken into account in the simulation. The insertion loss is reduced with bias due to the reduced loss tangent of BST thin film with bias. The difference between the simulated insertion loss (1.6 dB) and measured IL (3.7 dB) at 0 V might indicates that the BST loss tangent is under estimated at 0 V. This is possible as the BST loss tangent is directly proportional with the frequency [25], [26]. The loss tangent of a BST IDC measured from 0.1 MHz to 110 MHz also shows an increase with frequency (see Fig.6- 27).

Bias (V)	Capacitance (pF)	tanδ	Q_{BST}	Q_{copper}	$Q_{substrate}$	Q_{total}	Calculated IL (dB)	Simulated IL (dB)	Measured IL (dB)
0	0.75	0.012	86.3	155.2	1177.1	53.0	1.3	1.6	3.7
65	0.38	0.005	230.3	180.8	2406.9	97.2	0.7	0.9	1.1

Table 6- 13 The quality factors and insertion loss of the 2-pole BST IDC filter

The BST parallel plate capacitor was also modelled as a parallel capacitance resistance model and the resistance was calculated by R = 1/tanδω_0C, where ω_0 was the centre angular frequency of the filter. BST film tanδ was assumed to be 0.01 with and without bias. For the BST parallel plate filter, the losses from different parts of the resonator were analysed in a similar way and concluded in Table 6- 14. The substrate Q is high, over 800. The copper cladding Q is about 190. The BST capacitor Q is about 150 and is dominant. The total Q is about 77 with and without bias. The calculated insertion loss is 0.9 dB and this is very close to the simulated IL. The measured IL is a bit higher as the loss from silver epoxy, DC blocks and BST varactor electrodes are not included in the simulation.

Bias (V)	Capacitance (pF)	tanδ	Q_{BST}	Q_{copper}	$Q_{substrate}$	Q_{total}	Calculated IL (dB)	Simulated IL (dB)	Measured IL (dB)
0	0.23	0.01	135.6	190.0	1352.4	74.8	0.9	1.0	1.4
40	0.15	0.01	154.1	190.6	836.0	77.3	0.9	0.8	1.3

Table 6- 14 The quality factors and insertion loss of the 2-pole BST parallel plate filter

The above tables show that BST varactors quality factors over 100 are achieved in this work and these are comparable with the GaAs diodes. The 2-pole BST filters show a small passband insertion loss close to that of the GaAs filter. The measured response of the 4-pole BST filters is compared directly with the 4-pole GaAs filter with a similar centre frequency.

The 4-pole BST IDC filter with tuning screws at 0 V has a centre frequency of 1.54 GHz, and this is close to that of the 4-pole GaAs filter after adjusting tuning screws for optimal S_{11} at 3 V, which is 1.56 GHz. The 4-pole BST IDC filter at 0 V is compared with the GaAs filter with tuning screws at 3 V in Fig.6- 42. The GaAs filter has a smaller insertion loss (3.6 dB) than the BST IDC filter (6.3 dB). However, as the Q of BST IDC is improved with the application of bias, the insertion loss difference between the filters using GaAs varactors and BST IDCs should be decreased when the filters are tuned to higher frequency.

The 4-pole BST parallel plate filter at 0 V is also compared with the 4-pole GaAs filter with tuning screws at 9 V in Fig.6- 43. The performance of the GaAs filter is tuned by adjusting the tuning screws for optimal S_{11} at 9 V. The two filters have a similar centre frequency and bandwidth. The insertion loss of BST parallel plate filter (2.8 dB) is very close to that of the GaAs filter (2.3 dB).

The 2-pole BST parallel plate filter has an insertion loss of 1.4 dB - 1.3 dB and the 4-pole BST parallel plate filter has an insertion loss of 2.8 dB in the full tuning range. Both of these are lower than insertion loss reported for other published BST room temperature filters [11-14] and are very close to that of the GaAs filters demonstrated in the same configuration. This indicates that high quality BST films (for instance Q > 100) promote the filter loss perfermance significantly and the BST tuning technology in the low gigahertz range is already competitive with semiconductors in terms of loss.

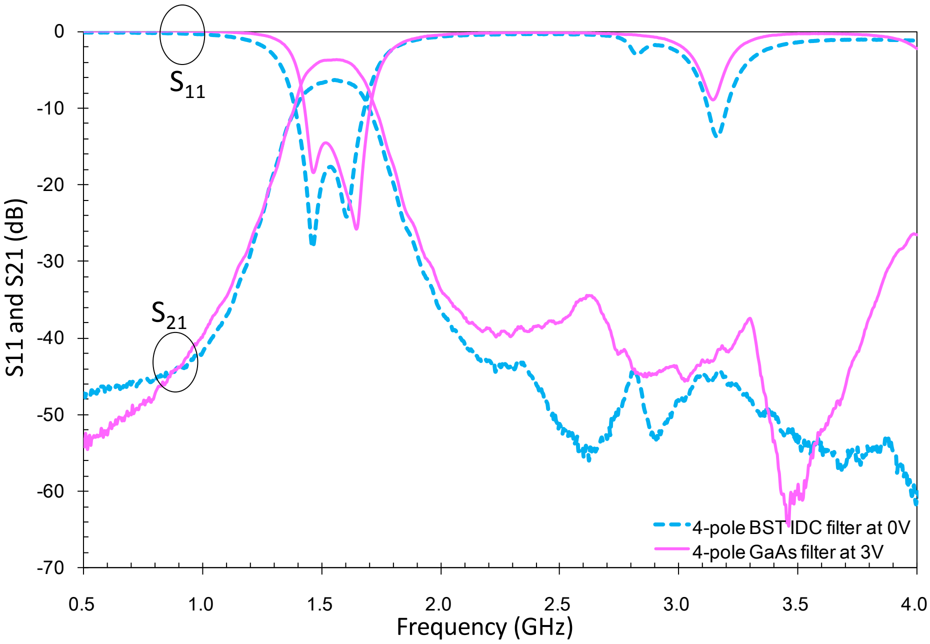

Fig.6- 42 The comparison of the 4-pole BST IDC filter at 0 V (dashed lines) and 4-pole GaAs filter at 3 V (solid lines), both with tuning screws.

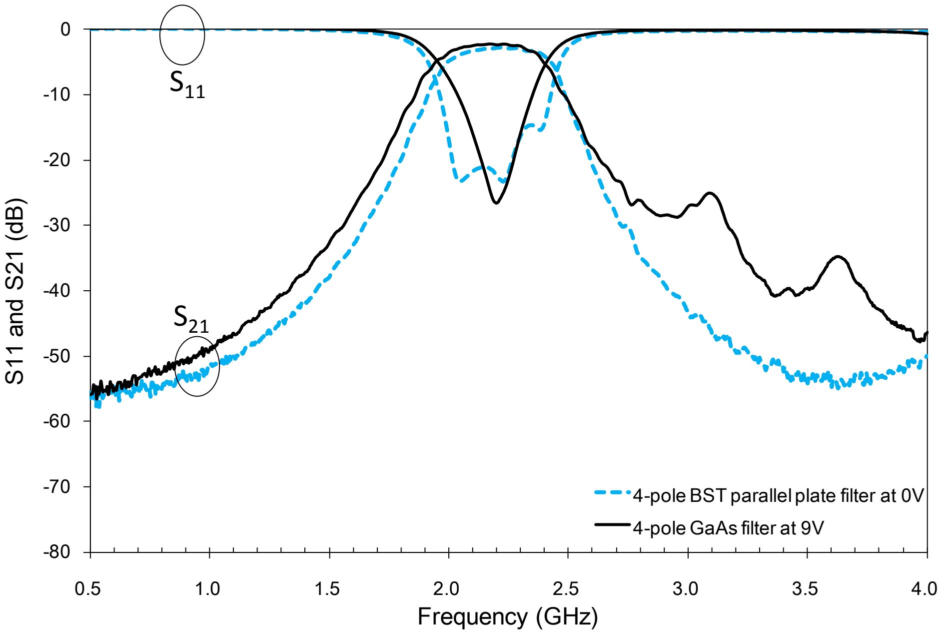

Fig.6- 43 Comparison of the 4-pole BST parallel plate filter at 0 V (dashed lines) and the 4-pole GaAs filter with tuning screws at 9 V (solid lines)

6.4.3 Figure of Merit

The figure of merit (FoM) of a tunable bandpass filter is defined as [27]

$$\mathrm{FoM} = \frac{f_2 - f_1}{\sqrt{\Delta f_1 \Delta f_2}} \frac{1}{\sqrt{\mathrm{IL}_1 \mathrm{IL}_2}} \qquad (\mathrm{dB}^{-1}) \tag{6.8}$$

where f_1, f_2 are the centre frequency of the two states, Δf_1, Δf_2 are the bandwidth and IL_1, IL_2 are the passband insertion loss at the two bias states. FoM provides a comprehensive way to compare tunable filters, taking both tunability and loss into account. The FoM is also related to filter order. Filters with higher order will have lower FoM [28]. The tuning range, passband insertion loss and reflection, and figure of merit of 2-pole and 4-pole filters demonstrated in this chapter are concluded in Table 6- 15.

Filter order	Varactor type	Bias /Electric field	Centre frequency (GHz)	Tunability	Insertion loss (dB)	Return loss (dB)	FoM (dB^{-1})
2	GaAs	14 V	0.94~2.44	2.6	4.2~0.8	13.5	3.84
2	BST IDC	6.5 V/μm	1.55~2.02	1.3	3.7~1.1	14.4	0.87
2	BST parallel plate	45 V/μm	2.32~2.52	1.1	1.4~1.3	20.2	0.41
4	GaAs	15 V	0.9~2.21	2.5	14.6~3	3.8	1.03
4	BST IDC	2.5 V/μm	1.49~1.85	1.2	9.2~4.2	5.9	0.20
4	BST parallel plate	35 V/μm	2.22~2.44	1.1	2.8~2.8	9.4	0.16

Table 6- 15 Summary of the 2- and 4-pole, GaAs, BST IDC and BST parallel plate filters. The 4-pole GaAs filter is measured after adjusting the tuning screws for optimal S_{11} at 6 V. The other filters are measured in plain boxes.

As shown in Table 6- 15, the GaAs filters have the highest FoM, which is 3.84 dB^{-1} for the 2-pole and 1.03 dB^{-1} for the 4-pole filter. This is mainly due to the large tunability of the GaAs varactors. Among the BST filters, the 2-pole BST IDC filter has the largest tuning range and the best FoM of 0.87 dB^{-1} owing to the good tunability (56.3 %) and low loss tangent (0.012 at 0 V and 0.005 with bias) of BST IDC. The 2-pole BST parallel plate filter has the lowest insertion loss (1.4 dB - 1.3 dB) in the BST filters. The 2-pole BST parallel plate filters has a FoM of 0.41 dB^{-1} as a result of the high quality BST parallel plate capacitors (Q > 100) used. Both FoM of the 2-pole BST IDC filter and 2-pole BST parallel plate filter are better than other published results of BST room temperature filters in microwave region as summarised in chapter 1 [1-3], [11-14], [29]. The 4-pole BST IDC filter has a FoM of 0.2 dB^{-1} and the 4-pole BST parallel plate filter has a FoM of 0.16 dB^{-1}.

The GaAs filters performed better than the BST filters in this work, however, the use of superior BST films would close the gap. The BST IDC filters demonstrated a good tunability and the BST parallel plate filters showed a low loss performance in line with the GaAs filters. The simultaneous high tunability and low loss of BST filters could be demonstrated by the use of optimised BST varactors as the technology matures.

6.5 Summary

In this chapter, 2-pole and 4-pole coupled resonator bandpass filters were designed on duroid. BST IDCs and BST parallel plate capacitors were fabricated in house, characterised by an impedance analyser, and diced into individual chips. GaAs varactor diodes or BST varactors were integrated into the circuits in a hybrid manner. Full sets of measurement results of the 2-pole and 4-pole filters using GaAs varactors, or BST interdigital capacitors, or BST parallel plate capacitors as tuning elements were presented and discussed in detail. Direct comparison of the GaAs filters and BST filters with exactly the same circuit configurations was made for the first time. The 2-pole GaAs filter showed the largest tuning range (0.94 GHz - 2.44 GHz) and the best FoM (3.84 dB^{-1}) as a result of the large tunability of the GaAs varactors. The 4-pole GaAs filter was tuned from 0.9 GHz to 2.21 GHz and showed a FoM of 1.03 dB^{-1}. Among the BST filters, the 2-pole BST IDC filter had the largest tuning range from 1.55 GHz to 2.02 GHz (which is 30.3 % tuning) and the highest FoM of 0.87 dB^{-1}, which is best FoM of BST room temperature filter ever reported. The 4-pole BST IDC filter was tuned 24.2 % from 1.49 GHz to 1.85 GHz and had a FoM of 0.2 dB^{-1}. The insertion loss of the BST IDC filters was improved with bias as a result of the improved loss tangent of BST film with bias. The 2-pole BST parallel plate filter had an insertion loss of 1.4 dB - 1.3 dB in the whole tuning range, which was comparable to the GaAs filter and was the smallest insertion loss of BST room temperature filters reported till date. The filter was tuned from 2.32 GHz to 2.52 GHz and showed a FoM of 0.41 dB^{-1}. The 4-pole BST parallel plate filter showed a constant insertion loss of 2.8 dB in the whole tuning range from 2.22 GHz to 2.44 GHz, resulting in a

FoM of 0.2 dB^{-1}. Comparison between BST and GaAs filters showed that in the low gigahertz range, the BST tuning technology is already comparable with the semiconductors in terms of loss performance.

References

[1] D. Kuylenstierna, A. Vorobiev, and S. Gevorgian, "40 GHz lumped element tunable bandpass filters with transmission zeros based on thin $Ba_{0.25}Sr_{0.75}TiO_3$ (BST) film varactors", in *Topical Meeting on Silicon Monolithic Integrated Circuits in RF Systems*, 2006, pp. 342-345.

[2] V. Pleskachev and I. Vendik, "Tunable microwave filters based on ferroelectric capacitors", in *15th International Conference on Microwaves, Radar and Wireless Communications*2004, pp. 1039-1043.

[3] G. Subramanyam, N. Mohsina, A. Al Zaman, F. Miranda, F. Van Keuls, R. Romanofsky, and J. Warner, "Ferroelectric thin-film based electrically tunable Ku-band coplanar waveguide components", in *IEEE MTT-S International Microwave Symposium Digest*2001, pp. 471-474.

[4] "Sonnet User's Guide, Release 10": Sonnet Softerware, Inc., 2004.

[5] T. K. Ishii, Handbook of Microwave Technology, Volume 1, Components and Devices, Academic Press, Inc., 1995.

[6] J.-S. Hong and M. J. Lancaster, Microstrip Filters for RF/Microwave Applications, John Wiley & Sons,Inc., 2001.

[7] Microwave Device Technology Ltd., http://www.microwavedevicetechnology.com.

[8] "Advanced Design System (ADS), Agilent Technoligies, Palo Alto, USA. http://eesof.tm.agilent.com".

[9] Y. Liu, "MEMS and BST technologies for microwave applications", Doctor of Philosophy thesis, Electrical and Computer Engineering, University of California, Santa Barbara, 2002

[10] X. H. Zhu, D. N. Zheng, H. Zeng, W. Peng, J. G. Zhu, X. W. Yuan, L. P. Yong, J. Miao, J. Li, H. Y. Tian, and X. P. Xu, "Effects of growth temperature and film thickness on the electrical properties of $Ba_{0.7}Sr_{0.3}TiO_3$ thin films grown on platinized silicon substrates by pulsed laser deposition", *Thin Solid Films*, vol. 496, no. 2, pp. 376-382, 2006.

[11] A. Tombak, J. P. Maria, F. T. Ayguavives, Zhang Jin, G. T. Stauf, A. I. Kingon, and A. Mortazawi, "Voltage-controlled RF filters employing thin-film barium-strontium-titanate tunable capacitors", *IEEE Transactions on Microwave Theory and Techniques*, vol. 51, no. 2, pp. 462-467, 2003.

[12] J. Nath, W. M. Fathelbab, P. G. Lam, D. Ghosh, S. Aygiin, K. G. Gard, J. P. Maria, A. I. Kingon, and M. B. Steer, "Discrete Barium Strontium Titanate (BST) Thin-Film Interdigital Varactors on Alumina: Design, Fabrication, Characterization, and Applications", in *IEEE MTT-S International Microwave Symposium Digest*2006, pp. 552-555.

[13] J. Papapolymerou, C. Lugo, Z. Zhiyong, X. Wang, and A. Hunt, "A Miniature Low-Loss Slow-Wave Tunable Ferroelectric BandPass Filter From 11-14 GHz", in *IEEE MTT-S International Microwave Symposium Digest*2006, pp. 556-559.

[14] C. Lugo, G. Wang, J. Papapolymerou, Z. Zhao, X. Wang, and A. T. Hunt, "Frequency and Bandwidth Agile Millimeter-Wave Filter Using Ferroelectric Capacitors and MEMS Cantilevers", *IEEE Transactions on Microwave Theory and Techniques*, vol. 55, no. 2, pp. 376-382, 2007.

[15] J. Nath, D. Ghosh, J. P. Maria, A. I. Kingon, W. Fathelbab, P. D. Franzon, and M. B.

Steer, "An electronically tunable microstrip bandpass filter using thin-film Barium-Strontium-Titanate (BST) varactors", *IEEE Transactions on Microwave Theory and Techniques,* vol. 53, no. 9, pp. 2707-2712, 2005.

[16] N. K. Pervez, P. J. Hansen, and R. A. York, "High tunability barium strontium titanate thin films for rf circuit applications", *Applied Physics Letters,* vol. 85, no. 19, pp. 4451-4453, 2004.

[17] E. Marsan, J. Gauthier, M. Chaker, and K. Wu, "Tunable microwave device: status and perspective", in *IEEE-NEWCAS Conference*2005, pp. 279-282.

[18] A. Tombak, J. P. Maria, F. Ayguavives, Zhang Jin, G. T. Stauf, A. I. Kingon, and A. Mortazawi, "Tunable barium strontium titanate thin film capacitors for RF and microwave applications", *Microwave and Wireless Components Letters,* vol. 12, no. 1, pp. 3-5, 2002.

[19] F. D. Morrison, P. Zubko, D. J. Jung, J. F. Scott, P. Baxter, M. M. Saad, R. M. Bowman, and J. M. Gregg, "High-field conduction in barium titanate", *Applied Physics Letters,* vol. 86, no. 15, p. 152903, 2005.

[20] O. G. Vendik, E.K.Hollmann, A. B. Kozyrev, and A. M. Prudan, "Ferroelectric tuning of planar and bulk microwave devices", *Journal of Superconductivity,* vol. 12, no. pp. 325-338, 1999.

[21] M. S. Tsai, S. C. Sun, and T.-Y. Tseng, "Effect of bottom electrode materials on the electrical and reliability characteristics of (Ba, Sr)TiO_3 capacitors", *IEEE Transactions on Electron Devices,* vol. 46, no. 9, pp. 1829-1838, 1999.

[22] M. Ouaddari, S. Delprat, F. Vidal, M. Chaker, and Ke Wu, "Microwave characterization of ferroelectric thin-film materials", *IEEE Transactions on Microwave Theory and Techniques,* vol. 53, no. 4, pp. 1390-1397, 2005.

[23] A. Vorobiev, P. Rundqvist, K. Khamchane, and S. Gevorgian, "Silicon substrate integrated high Q-factor parallel-plate ferroelectric varactors for microwave/millimeterwave applications", *Applied Physics Letters,* vol. 83, no. 15, pp. 3144-3146, 2003.

[24] K. Leong, J. Mazierska, and J. Krupka, "Measurements of unloaded Q-factor of transmission mode dielectric resonators", in *IEEE MTT-S International Microwave Symposium Digest*1997, pp. 1639-1642.

[25] A. Vorobiev, P. Rundqvist, K. Khamchane, and S. Gevorgian, "Microwave loss mechanisms in $Ba_{0.25}Sr_{0.75}TiO_3$ thin film varactors", *Journal of Applied Physics,* vol. 96, no. 8, pp. 4642-4649, 2004.

[26] P. Bao, T. J. Jackson, X. Wang, and M. J. Lancaster, "Barium strontium titanate thin film varactors for room-temperature microwave device applications", *Journal of Physics D: Applied Physics,* vol. 41, no. p. 063001, 2008.

[27] V. Pleskachev and I. Vendik, "Figure of Merit of Tunable Ferroelectric Planar Filters", in *the 33rd European Microwave Conference*2003, pp. 191-194.

[28] V. Pleskachev and I. Vendik, "Tunable microwave filters based on ferroelectric capacitors", in *Microwaves, Radar and Wireless Communications, 2004. MIKON-2004. 15th International Conference on*2004, pp. 1039-1043.

[29] J. Nath, W. Fathelbab, P. D. Franzon, A. I. Kingon, D. Ghosh, J. P. Maria, and M. B. Steer, "A tunable combline bandpass filter using barium strontium titanate interdigital varactors on an alumina substrate", in *IEEE MTT-S International Microwave Symposium Digest*2005, pp. 595-598.

CHAPTER 7
CONCLUSION AND FUTURE WORK

7.1 Conclusion

This thesis investigated the frequency agile microwave applications of ferroelectric thin films. Ferroelectric thin films exhibit a high dielectric constant (10^2 - 10^3) and the dielectric constant can be controlled by an external electric field, which is the basis for frequency agile applications.

The motivations for developing frequency agile devices have been discussed. Several technologies for frequency agility have been studied and some important parameters of these technologies have been compared. Fundamental properties of ferroelectric materials have been reviewed, with emphasis on certain desirable features of BST thin films for microwave tuning applications. Fabrication issues such as deposition methods, substrate and metallisation choices have been discussed. Pulsed laser deposition (PLD) has been used to deposit the BST thin films in this work. Most of the main challenges in material and device fabrication have been overcome successfully, but more work is required to further optimise the materials and capacitor structures. Two BST varactors topologies, interdigital and parallel plate, have been compared. Surveys of the development of BST varactors and filters in the literature have been provided.

In this work, several novel structure ferroelectric thin film filters were designed and demonstrated in a frequency range between 1 GHz and 25 GHz: (i) ferroelectric lowpass filters based on integrated BST varactors were implemented on high resistivity silicon substrates using a lumped element approach; (ii) ferroelectric combline bandpass filters based on integrated BST varactors were implemented on MgO substrates, using distributed lines loaded by varactors as resonators; and (iii) tunable bandpass filters using discrete BST varactors as tuning elements were implemented on microwave laminates and compared with the same filters using GaAs varactors.

A miniaturised ferroelectric lumped element lowpass filter based on integrated thin film BST varactors was demonstrated in the K-band. The filter incorporated integrated meander lines as series inductors, and 5 µm × 5 µm or 10 µm × 10 µm BST parallel plate varactors as shunt capacitors and tuning elements. The filter was implemented in a coplanar waveguide (CPW) configuration on a high resistivity silicon substrate, showing possibility of monolithic integration of BST devices with silicon based MMICs. The lowpass filter demonstrated 32.1 % tuning of the 10 dB cut-off frequency, changing from 18.52 GHz at 0 V to 24.47 GHz at 15 V. Several lowpass filters using different sized inductors or capacitors showed zero bias cut-off frequencies in a range between 4 GHz and 17 GHz. These ferroelectric lowpass filters have demonstrated a good tunability at a relatively low bias voltage. The main limitation of these filters is the relative high insertion loss, in which the metal film loss is dominant, as a consequence of very thin metal film (thickness smaller than skin depth) and narrow lines which resulting severe current concentration in the conductors. High conductivity metal and thick metal electrodes can be used to reduce the conductor loss. A modified layout aiming at reducing the metal loss was also presented. In future work, effort on making thicker electrodes will lead to better loss performance of ferroelectric devices based on integrated BST varactors.

Miniaturised combline bandpass filters based on integrated BST capacitors were implemented in CPW configuration on MgO substrates. The filters consisted of shunt resonators which were comprised of transmission line elements loaded by 5 µm × 5µm BST parallel plate capacitors. Each resonator was independently biased. The filter was in a multilayer structure and BST film was sandwiched between the top and bottom metal layer. Etching of BST film was required to contact the bottom electrode, however, this increased the fabrication difficulty substantially. A two pole BST bandpass filter showed a tuning of about 4 GHz with 10 V bias of only one resonator. The other resonator failed to tune with bias as the top and bottom metal layers were shorted, which was probably due to damage during the BST film etching. The process of etching BST film on selected area not only enables contacting the bottom electrodes for bias application, but also reduces the loss in the BST film. This process is not yet well controlled in the group at Birmingham and requires more research effort on it.

As the semiconductors suffer from poor Q at frequencies above about 10 GHz, the merits of

BST devices are expected to emerge there. The BST integrated filters demonstrated in this work have miniaturised size, large tuning range at a relative low bias voltage, and operate at frequencies over 10 GHz. These filters developed in this thesis exhibit an insertion loss of 8 - 10 dB. One way to reduce the device loss is to fabricate discrete BST varactors and integrate them into filter circuit laminates in a hybrid manner. The discrete BST filters can have a much lower insertion loss as results of thicker transmission line conductors, larger filter size and lower operating frequency compared with the BST integrated filters.

Therefore, a significant part of this research work focused on tunable bandpass filters based on discrete BST varactors. The filter circuits consisted coupled resonators loaded with BST or GaAs varactors, and were implemented on duriod 5870 laminate. BST interdigital and parallel plate capacitors were fabricated on MgO substrates, characterised by an impedance analyser, and cut into 2 mm × 1 mm individual chips. These BST varactors and commercially available GaAs varactors were assembled onto the two pole and four pole filter laminate circuits to form different filters. Hence, a direct comparison between semiconductor and BST tuning technologies in an application environment is given for the first time in this work. The GaAs filters had the largest tunability as a result of the very high tunability (23) of GaAs varactors. The two pole BST IDC filter showed 30.3 % tuning from 1.55 GHz to 2.02 GHz with 65 V bias, with an insertion loss from 3.7 dB to 1.1 dB. Such a tunability is better than or comparable with other published BST filters in a similar frequency range. The four pole BST IDC filter was tuned from 1.49 GHz to 1.85 GHz with 25 V bias. The two pole BST parallel plate filter was tuned from 2.32 GHz to 2.52 GHz with an insertion loss of 1.4 dB - 1.3 dB. The four pole BST parallel plate filter showed an insertion loss of 2.8 dB in the full tuning range. Both of these insertion losses are lower than other published BST filters and these values are very close to that of the GaAs filters at the same frequency. It is clear that in the gigahertz range, the GaAs filters perform better than the BST filters in the term of tunability, but the BST filters are already in line with the GaAs filters in the term of loss performance. The simultaneous high tunability and low loss of BST filters could be demonstrated by the use of optimised BST varactors and superior BST films.

In this work, advanced microwave filters based on integrated or discrete BST varactors have been successfully demonstrated. The BST tuning technology has showed tremendous potential for frequency agile application. Some suggestions for future research work will be outlined in the next section.

7.2 Future work

Future research effort should be directed toward improving the ferroelectric device quality factor at frequencies over 10 GHz. A good understanding of the material properties and their dependence on fabrication parameters is essential for material optimisation for simultaneous high tunability and low loss. The BST film used in this work has a loss tangent as low as 0.01 at lower gigahertz range. However, the loss tangent tends to increase with frequency and gets around 0.1 over 20 GHz (as depicted in appendix A), which results in inferior loss performance of ferroelectric devices for microwave/millimetre applications. Meanwhile, the conductor loss can be reduced by making the metal electrodes thicker or using high conductivity metal such as Cu, Au as base electrodes. In addition, the patterning technique of BST film, by which the BST film presents on the selected area only instead of on the entire surface, is not well controlled in the group at Birmingham and requires more research effort and experience on it. Other problems such as lifetime, failure mechanisms, and temperature dependence property of ferroelectric materials are out of the scope of this thesis, but they are also important for the development of ferroelectric devices and need further studies. With the advance in material fabrication, as well as the optimised device electronic design, advanced system capability could be created, and ferroelectric devices could come to commercialisation.

APPENDIX A

BST AND METAL FILM CHARACTERISATION

An experimental method to characterise the properties of BST and metal thin films using parallel plate capacitor structures is described as follows.

(1) BST thin film characterisation

To extract the properties of BST thin films, several square parallel plate capacitors using a $Ba_{0.25}Sr_{0.75}TiO_3$ thin film were grown on a high resistivity silicon substrate, following the same fabrication procedure as the ferroelectric lowpass filters presented in chapter 4. The layout and cross sectional view of the varactor is shown in Fig. 1. The dimension of the square central patch is 10 µm or 20 µm, and the length of the outer electrode is 0.8 mm. As the area of the outer electrode is much bigger (over 1500 times) than the central patch, the capacitance between the outer electrode and the uniform bottom electrode is much bigger than that of the central patch. The large capacitance of the outer top electrode provides effective microwave ‘connection’ to the bottom metal and allows the DC bias to be applied between the top and bottom layer.

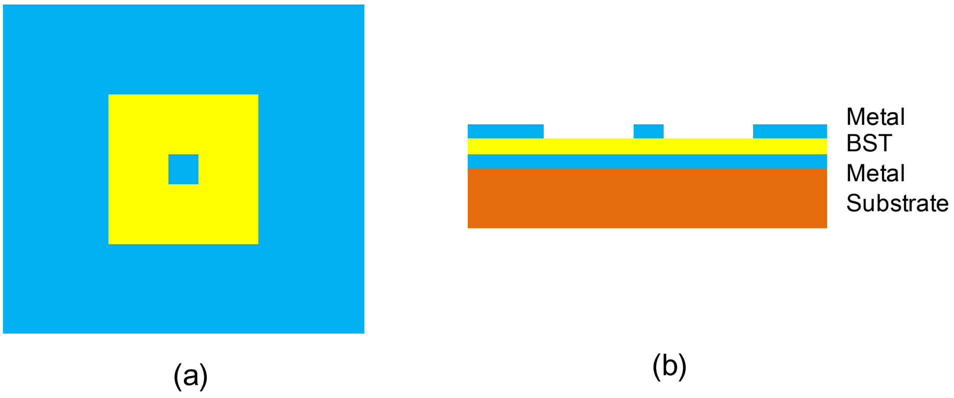

Fig. 1 Top view (a) and cross sectional view (b) of a BST parallel plate capacitor

The complex reflection coefficient S_{11} of the varactors was measured on a probe station using an Agilent E8361A PNA Network Analyser through ACP50-GSG-150 microprobes at frequencies up to 30 GHz. A two-port line-reflect-reflect-match (LRRM) calibration was performed before measurement. The varactor can be modelled by a parallel resistance capacitance at lower frequency end. In this case, the admittance Y of the varactor can be expressed in term of S_{11} as

$$Y = G + j\omega C = \frac{1}{Z_0}\left(\frac{1 - S_{11}}{1 + S_{11}}\right) \tag{9}$$

where G and C are the conductance and capacitance of the varactor and Z_0 = 50 Ω. The effective loss tangent of the device under test can be derived from the following expression as

$$\tan\delta_{DUT} = \frac{G}{\omega C} \tag{10}$$

The capacitance and effective loss tangent of a 10 µm × 10 µm parallel plate capacitor is derived from the measured reflection coefficient S_{11} using the above equations and is plotted as a function of bias at 2 GHz in Fig. 2. A relative tunability of 30 % is achieved at 13 V (corresponding to an electric field of 32.5 V/µm) and the effective loss tangent is about 0.02, which is mainly the BST loss. The dielectric constant of the BST thin film can be derived directly from the capacitance following the expression

$$\varepsilon_r = \frac{C\,t}{\varepsilon_0 A} \tag{11}$$

The extracted dielectric constant of the BST film at 2 GHz varies from 738 at zero bias to 514 at 13 V.

However, the above modelling is not adequate at higher frequencies, where the parasitic inductance and resistance from the probe/device contact and series resistance from the electrode should be taken into account to estimate the properties of BST film accurately. The calibration procedure may also introduce a negative inductance to calibrate the sliding of the probe [1]. To solve this problem, series inductance L_s and resistance R_s representing parasitic effects of the electrode and probe contact are taken into account in the modelling as shown in Fig. 3. Variable C represents the true capacitance and R_d characterizes the loss from dielectric material.

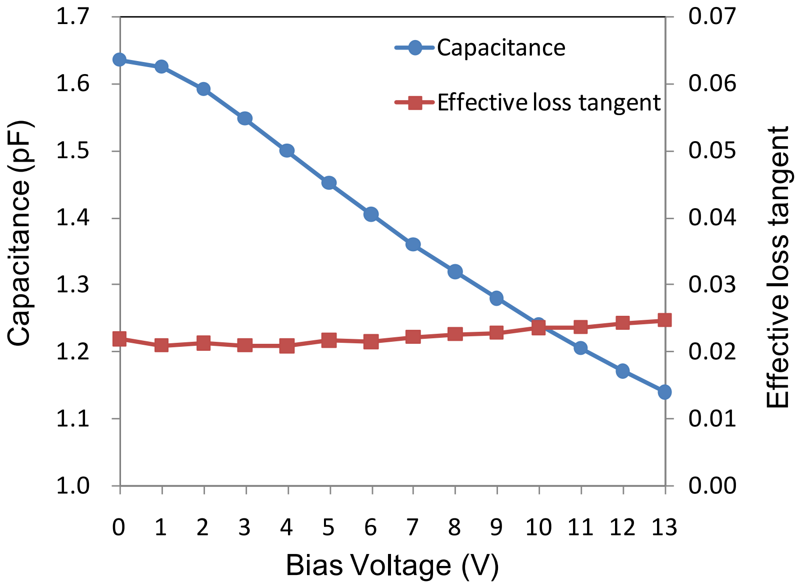

Fig. 2 The measured capacitance and effective loss tangent versus frequency of a 10 µm × 10 µm BST parallel plate capacitor at 2 GHz

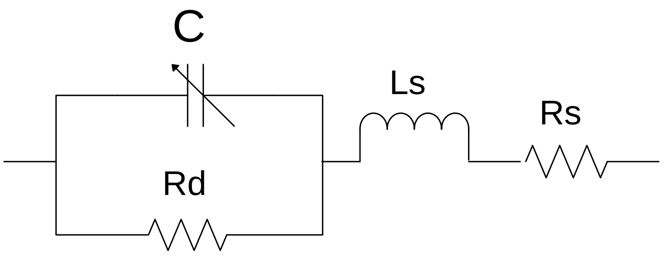

Fig. 3 Modeling of the parallel plate varactor

To extract the true capacitance and separate the BST loss with the metal loss, two different size capacitors with central patch of 10 µm × 10 µm and 20 µm × 20 µm were measured. Assuming that the L_s and R_s are the same in the two cases, the characteristic impedance of the two capacitors is

$$Z_1 = \frac{1}{G_1 + j\omega C_1} + j\omega L_s + R_s \tag{12}$$

$$Z_2 = \frac{1}{G_2 + j\omega C_2} + j\omega L_s + R_s \tag{13}$$

where subscript 1 and 2 denote the capacitor 1 which is 10 µm × 10 µm and capacitor 2 which is 20 µm × 20 µm respectively. Subtracting (5) from (4) yields

$$Z_1 - Z_2 = \frac{1}{G_1 + j\omega C_1} - \frac{1}{G_2 + j\omega C_2} \tag{14}$$

As we know from (2),

$$G = \omega C \tan\delta \tag{15}$$

By substituting (7) into equation (6), it can be re-written as

$$Z_1 - Z_2 = \frac{1}{\omega C_1 \tan\delta + j\omega C_1} - \frac{1}{\omega C_2 \tan\delta + j\omega C_2} \tag{16}$$

where tanδ represents the true loss tangent of BST thin film. The real part and imaginary part of (Z_1-Z_2) are

$$\mathrm{Re}(Z_1 - Z_2) = \frac{1}{1+\tan^2\delta}\left(\frac{1}{\omega C_1} - \frac{1}{\omega C_2}\right)\tan\delta \tag{17}$$

$$\mathrm{Im}(Z_1 - Z_2) = -\frac{1}{1+\tan^2\delta}\left(\frac{1}{\omega C_1} - \frac{1}{\omega C_2}\right) \tag{18}$$

The true capacitance and loss tangent of BST thin film can be derived as

$$\tan\delta = -\frac{\mathrm{Re}(Z_1 - Z_2)}{\mathrm{Im}(Z_1 - Z_2)} \tag{19}$$

$$C_1 = \frac{1-\gamma}{\omega\left(1+\tan^2\delta\right)} \frac{1}{\mathrm{Im}(Z_1 - Z_2)} \tag{20}$$

where $\gamma = C_1/C_2$. The ratio of C_1/C_2 can be obtained by the capacitance at lower frequency end where it is not affected by the parasitic inductance ($\omega L_s \ll 1/\omega C$). The parasitic inductance L_s and resistance R_s can be also extracted in this way. The L_s is about - 48 pH in the whole frequency range. The L_s is negative when the absolute value of the negative calibration inductance is bigger than the parasitic inductance of the electrode and a decreasing capacitance frequency curve may be observed in this case [1]. The extracted R_s is less than 0.1 Ω. The extracted capacitance and loss tangent as a function of frequency is shown in Fig. 4 and Fig. 5 respectively. The uncorrected measured capacitance decreases with frequency noticeably due to the effect of parasitic inductance L_s, while the extracted capacitance shows little dissipation up to 30 GHz. The extracted BST film loss tangent is less than 0.03 up to 6 GHz and is around 0.1 up to 30 GHz, which is comparable to other published quality factor of BST film in a similar frequency range [2], [3].

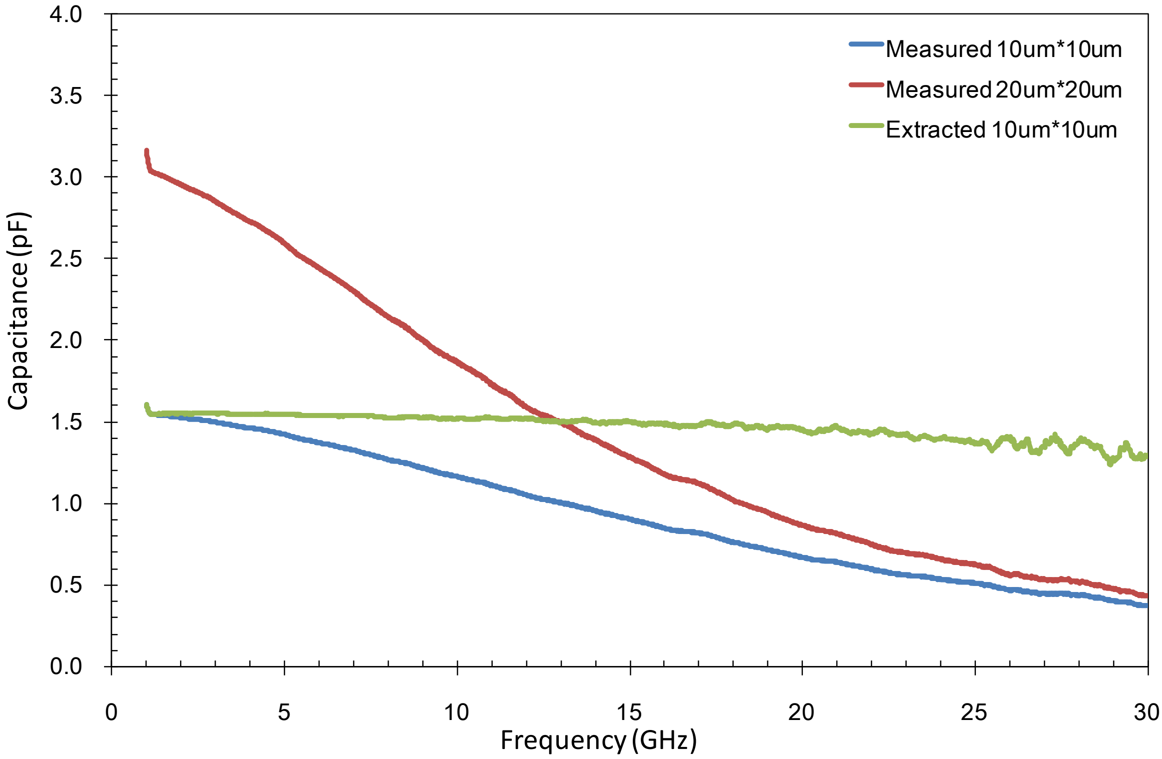

Fig. 4 The extracted capacitance for a 10 µm × 10 µm BST parallel plate capacitor versus frequency

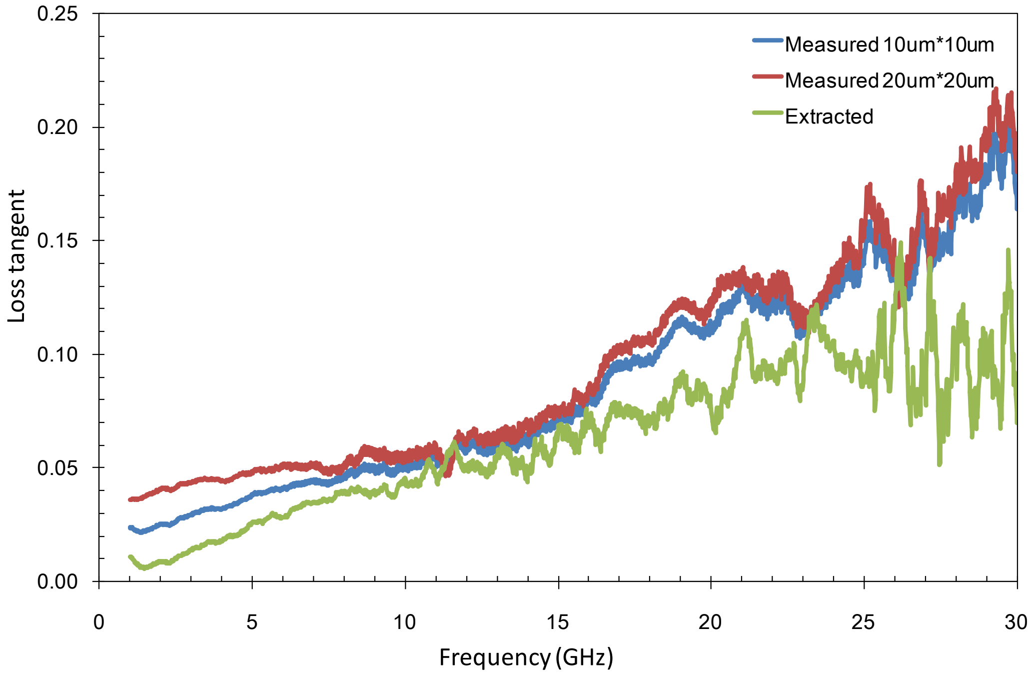

Fig. 5 The extracted loss tangent of BST film versus frequency

(2) Metal film characterization

In practice, the metal is not perfect and the conductivity can be seen to degrade by a factor of k (k<1) from its ideal case

$$\sigma_{real} = k\sigma_{ideal}$$

This effect is well known in metal film deposition [4]. To determine the actual conductivity of the metal film, the resistivity of a silver film grown on BST/MgO substrate was measured using a four-point DC resistivity probe. The four probes were arranged in a linear fashion as shown in Fig. 6, where the two outer probes are connected to a current supply, and the inner probes to a voltmeter. As current flows between the outer probes, the voltage drop across the inner probes is measured. The resistivity ρ is derived as

$$\rho = \frac{\pi}{\ln 2}\left(\frac{V}{I}\right)t$$

where $\pi / \ln 2$ is the geometric factor of the four-point probe, V/I is the measured resistance (which was 14 mΩ), and t is the thickness of the film (which was 400 nm). Thus, the actual conductivity of the silver film is derived as

$$\sigma_{real} = \frac{1}{\rho} = 39.68 \times 10^6\ \mathrm{S/m}$$

which is 64.3% of the ideal conductivity of silver ($\sigma_{ideal} = 63.01 \times 10^6$ S/m) [5].

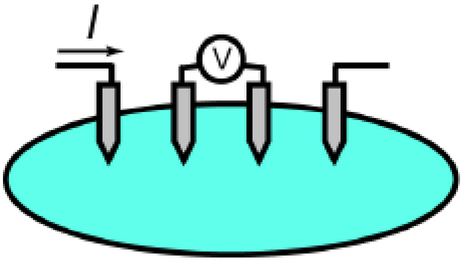

Fig. 6 Schematic of the four-point probe configuration

The properties of BST and metal thin films were characterised experimentally up to 30 GHz. This information is helpful for analysing the loss factors of ferroelectric filters presented in this thesis.

References

[1] A. Vorobiev, D. Kuylenstierna, P. Rundqvist, and S. Gevorgian, "Broadband Microprobe Characterization of the Ferroelectric Films and Varactors", in *36th European Microwave Conference*2006, pp. 843-846.

[2] E. Marsan, J. Gauthier, M. Chaker, and K. Wu, "Tunable microwave device: status and perspective", in *IEEE-NEWCAS Conference*2005, pp. 279-282.

[3] D. C. Dube, J. Baborowski, P. Muralt, and N. Setter, "The effect of bottom electrode on the performance of thin film based capacitors in the gigahertz region", *Applied Physics Letters*, vol. 74, no. 23, pp. 3546-3548, 1999.

[4] D. Ghosh, "Tunable Microwave Devices using BST (Barium Strontium Titanate) and Base Metal Electrodes", Doctor of Philosophy thesis, North Carolina State University, 2005

[5] D.M.Pozar, Microwave Engineering, 2nd ed. New York, USA, John Wiley & Sons, Inc., 1998.

APPENDIX B

THE FOUR POLE GaAs FILTER WITH TUNING SCREWS

The fabricated four pole GaAs filter exhibits high passband reflection as a result of the unmatched external coupling and coupling coefficient. This can be improved by using tuning screws. The graphs below show the measured response of the filter as a function of bias, with adjusting the tuning screws at 3 V, 6 V, 9 V, 12 V and 15 V for optimal S_{11} at each bias voltage respectively. The return loss can be tuned to better than 15 dB at each bias voltage. However, this will be degraded with the changing of bias voltage. The tuning in all the following figures is solely from the varactor. For instance, the tuning screws were adjusted for optimal S_{11} at 3 V and the filter response at 3 V (dashed lines) was recorded in Fig. 7. After the tuning screws have been set, they are no longer altered and full set of response for different bias voltages (solid lines) was also recorded in Fig. 7. The best set of results is shown in Fig. 8 (adjusting screws at 6 V) with a passband return loss better than 6.3 dB in most tuning range. The graphs are shown in the same scale for the ease of comparison.

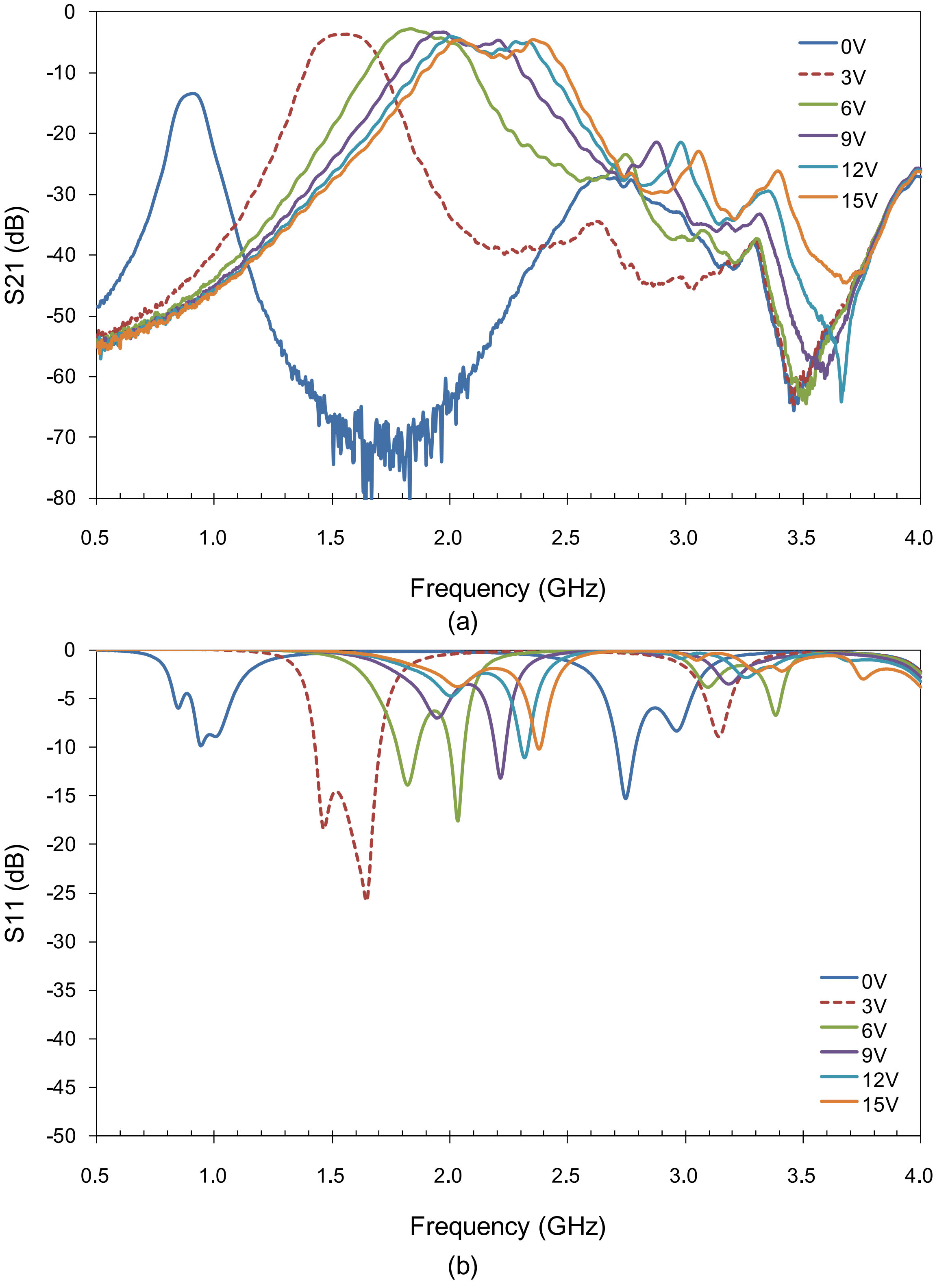

(a)

(b)

Fig. 7 Measured response of the 4-pole GaAs filter as a function of bias after adjusting the tuning screws for optimal S_{11} at 3 V.

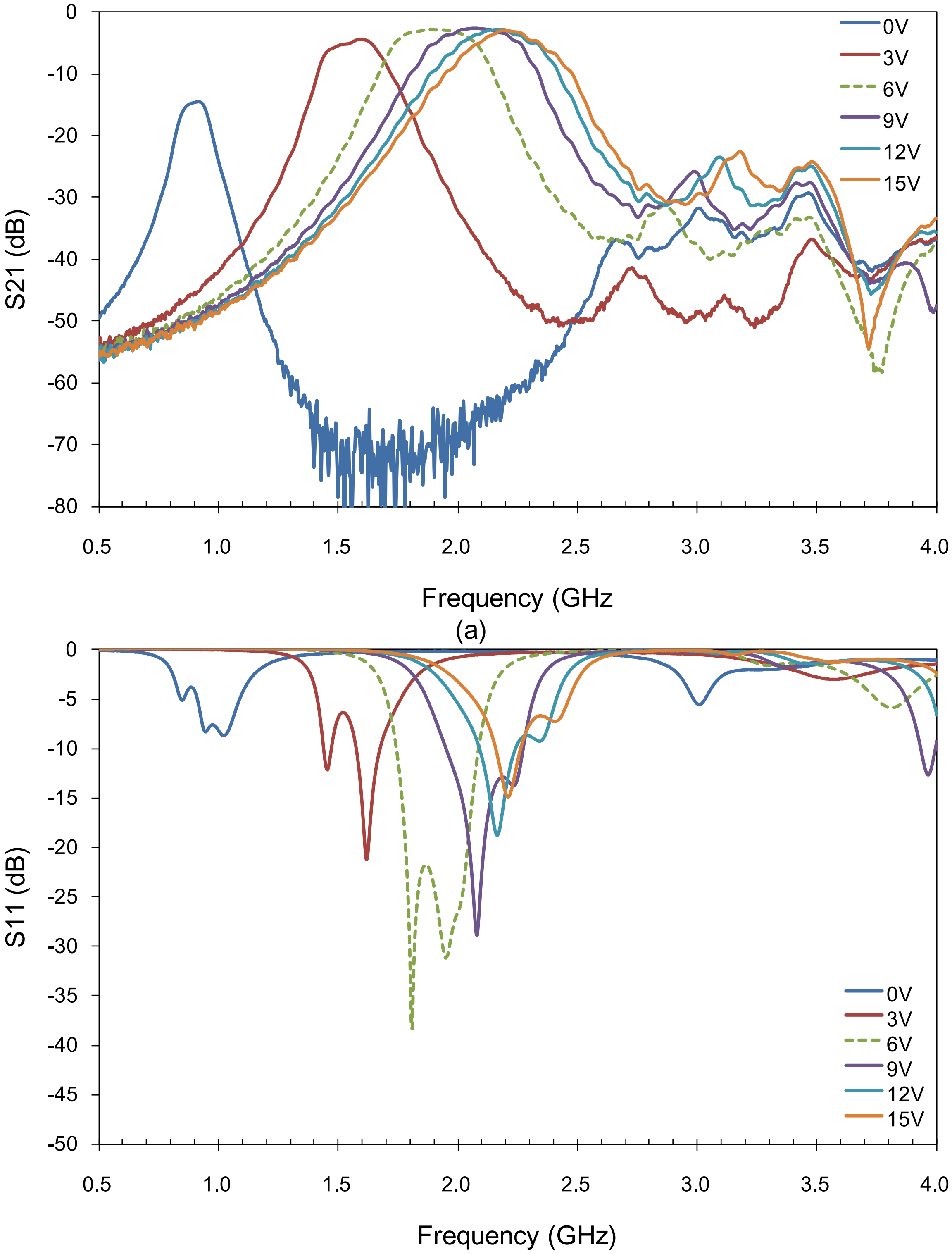

(a)

(b)

Fig. 8 Measured response of the 4-pole GaAs filter as a function of bias after adjusting the tuning screws for optimal S_{11} at 6 V

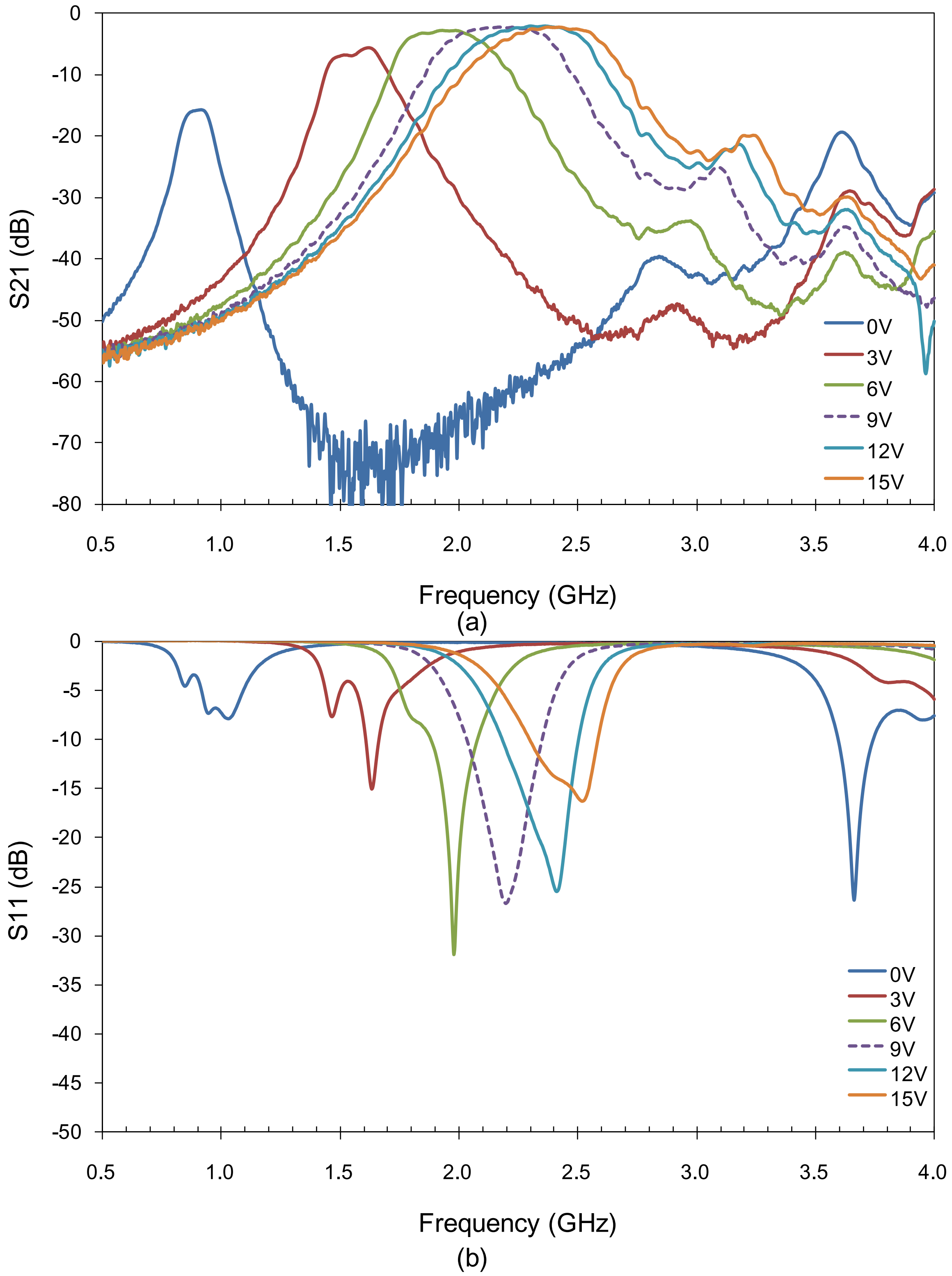

Fig. 9 Measured response of the 4-pole GaAs filter as a function of bias after adjusting the tuning screws for optimal S_{11} at 9 V

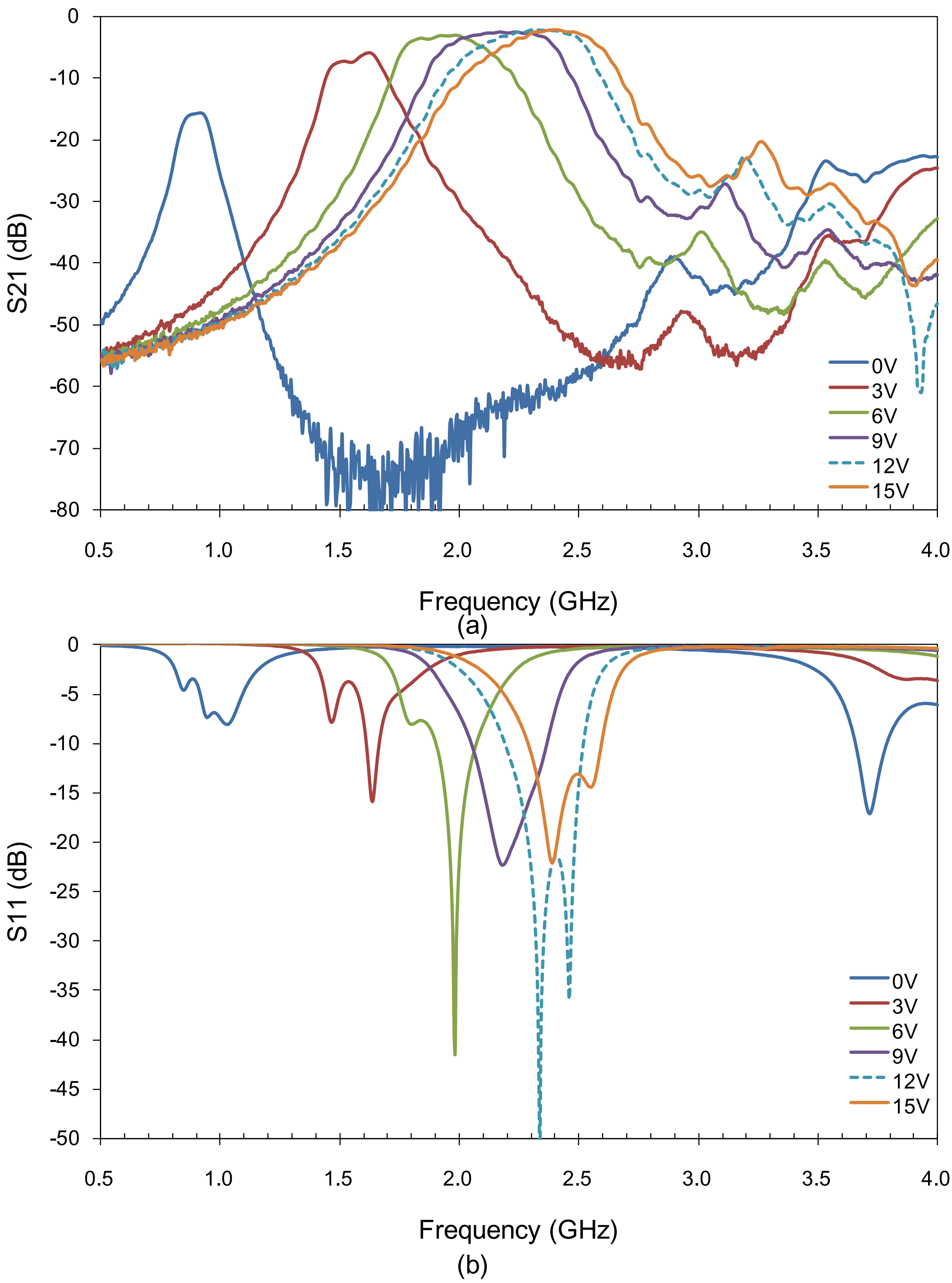

Fig. 10 Measured response of the 4-pole GaAs filter as a function of bias after adjusting the tuning screws for optimal S_{11} at 12 V.

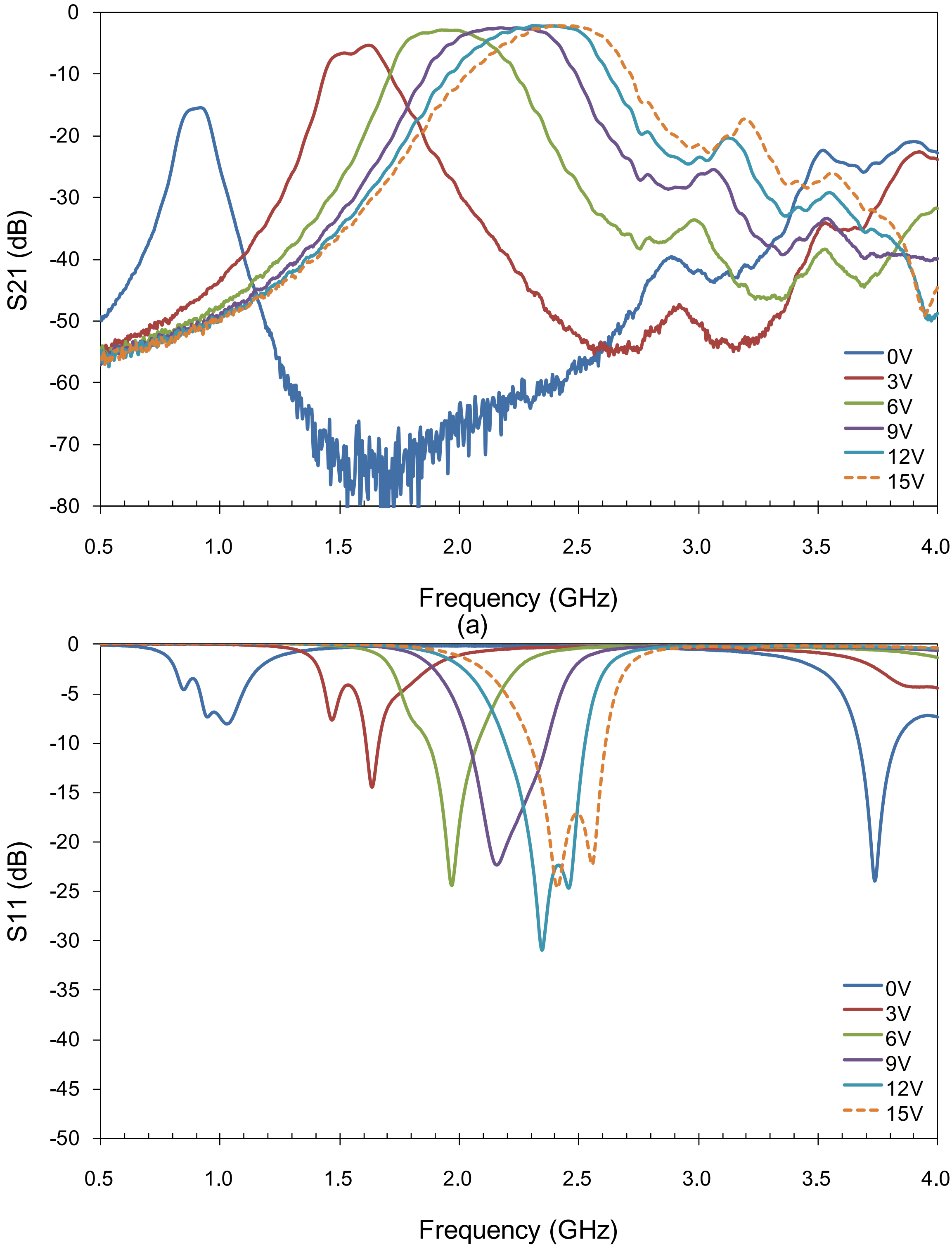

(a)

(b)

Fig. 11 Measured response of the 4-pole GaAs filter as a function of bias after adjusting the tuning screws for optimal S_{11} at 15 V.

APPENDIX C

LIST OF PUBLICATIONS

[1] P. Bao, T. J. Jackson, X. Wang and M. J. Lancaster, "Barium strontium titanate thin film varactors for room-temperature microwave device applications", *Journal of Physics D: Applied Physics*, vol. 41, 21 pp, Feb. 2008.

[2] X. Wang, P. Bao, M. J. Lancaster, T. J. Jackson, "Ferroelectric lumped element filter/switch for microwave applications", in *the Proceedings of the 38th European Microwave Conference*, pp. 43-46, Oct. 2008. (Attached)

Submitted

[1] X. Wang, P. Bao, T. J. Jackson and M. J. Lancaster, "Tunable microwave filters based on discrete ferroelectric and semiconductor varactors", submitted to *IEEE Transactions on Microwave Theory and Techniques*.